Robust control of shakers for mechanical qualifications of spacecraft

Samsul Arefin

To cite this version:

Samsul Arefin. Robust control of shakers for mechanical qualifications of spacecraft. Automatic. Université Paris-Saclay, 2022. English. NNT : 2022UPASG042 . tel-03883262

HAL Id: tel-03883262
https://theses.hal.science/tel-03883262v1

Submitted on 3 Dec 2022

Robust control of shakers for mechanical qualifications of spacecraft

Contrôleur robuste d'un vibreur pour la qualification mécanique des satellites

Thèse de doctorat de l'université Paris-Saclay

École doctorale n° 580, Sciences et Technologies de l'information et de la communication (STIC)
Spécialité de doctorat : Automatique
Graduate School : Sciences de l'ingénierie et des systèmes. Référent : • CentraleSupélec

Thèse préparée dans l'unité de recherche **Laboratoire des Signaux et Systèmes (Université Paris-Saclay, CNRS, CentraleSupélec**), sous la direction de **Didier DUMUR**, Professeur, le co-encadrement de **Sihem TEBBANI**, Professeur, la co-supervision de **Alain BETTACCHIOLI**, Ingénieur chez Thales Alenia Space, la co-supervision de **Aurélien HOT,** Ingénieur CNES

Thèse soutenue à Paris-Saclay, le 24 Juin 2022, par

Samsul AREFIN

Composition du Jury

Nicolas LANGLOIS Professeur, ESIGELEC	Président, rapporteur et examinateur
Daniel ALAZARD Professeur, ISAE-Supaero	Rapporteur et examinateur
Sami TLIBA Maître de conférences, Laboratoire des Signaux et Systèmes	Examinateur
Estelle COURTIAL Maître de conférences, Université d'Orléans	Examinatrice
Didier DUMUR Professeur, CentraleSupélec	Directeur de Thèse

THESE DE DOCTORAT

NNT : 2022UPASG042

université PARIS-SACLAY

ÉCOLE DOCTORALE
Sciences et technologies
de l'information et de
la communication (STIC)

Acknowledgement

This study was carried out under the financial support of Thales Alenia Space, Cannes and French Space Agency (CNES), Toulouse.

My very special thanks to my industrial supervisor Dr. Alain Bettacchioli, control and simulation expert at Thales Alenia Space, Cannes, for our hour-long discussions about the thesis topics and scientific challenges of the research work, which motivated me to leave my engineering position at the AOCS department and start my P.hD Thesis, and also for opening this interesting thesis topic and later on, all of his contributions in my Thesis concerning to the supervision, transmission of all necessary references and information about the research. In addition, my extreme gratitude to Jean-Marie Pasquet, Technical Director at Thales Alenia Space, Cannes, for all of his assistance throughout all phases of my Thesis, including the funding of the research and all sorts of paper works linked to the Thesis.

This work would not have been possible without the sincere guidance, the assistance of my thesis director Didier Dumur, director of the study at CentraleSupelec, Paris. Being very far from the Campus, without his unprecedented care, whether about the administrative issues or academic writing, I would not be able to terminate the Thesis. I've learned a lot from him about academic writing and the amazing final touches. I would like to express my gratitude to my academic supervisor from CentraleSupelec, Sihem Tebbani, for her valuable technical suggestions and all her recommendations throughout my thesis writing.

Without forgetting Aurélien Hot, my industrial supervisor from CNES, his very fine suggestions about mechanical modeling and information related to the vibration testing systems helped me a big time to realize my Thesis. The work presented here is based on the Vibration testing system of Thales Alenia Space, Cannes. Therefore, my very most appreciation goes to all team members of the AIT department of Thales Alenia Space for their warm welcome, valuable time and information, and the opportunity to participate in vibration testing campaigns of different scientific and commercial satellites.

Finally, my heart is full of acknowledgment to my late mother, without her encouragement and inspiration, it would have been impossible to complete my Thesis.

université
PARIS-SACLAY

ÉCOLE DOCTORALE
Sciences et technologies
de l'information et de
la communication (STIC)

Titre : Contrôleur robuste d'un vibreur pour la qualification mécanique des satellites

Mots clés : Qualification satellite, Suivi dynamique robuste, Mécanique structurelle, Contrôle actif des vibrations, Variation paramétrique

Résumé : L'objectif de cette thèse est d'éliminer le phénomène de battement du système d'essais vibratoires lors de la qualification mécanique de satellite. Les essais en qualification mécanique consistent à appliquer, à l'interface du satellite, une accélération résultant d'un balayage sinusoïdal à des fréquences et amplitudes données, en fonction des besoins du lanceur. Cependant, la structure de la commande utilisée pour cette qualification est souvent non satisfaisante en termes de performances de suivi de la référence au voisinage des modes structuraux et des modes réservoir du satellite. Des interruptions peuvent également se produire pendant les tests en raison de dépassements inacceptables. En effet, l'algorithme de commande non linéaire actuellement utilisé s'avère peu adapté aux dynamiques ayant des modes de vibration très peu amortis. Le travail proposé consiste donc à développer une stratégie de contrôle capable d'éviter les instabilités du modèle composite qui comprend l'actionneur, l'interface et le satellite. Après une étude portant sur le phénomène d'oscillation et sur la littérature dans le domaine du contrôle actif de vibrations, la recherche a été menée avec l'objectif de faire évoluer l'architecture de commande actuelle vers une stratégie de commande robuste. Le système d'essais en vibration nécessite en effet de satisfaire des performances de précision strictes en suivi dynamique pour une très large bande de fréquence. De plus, la stratégie développée doit s'affranchir du conservatisme des commandes robustes habituellement constaté lorsque la dynamique du système contient des modes faiblement amortis.

Dans un premier temps, une étude de faisabilité sur un système simplifié faiblement amorti montre la suppression des vibrations du système via une commande robuste. Ensuite, un modèle identifié d'un satellite commercial réel est utilisé pour démontrer les performances supérieures obtenues par l'architecture de commande proposée. Finalement, afin de surmonter l'un des principaux défis lié à la sensibilité de la commande robuste vis-à-vis de toute variation des paramètres modaux, une reformulation de la structure de commande permet la désensibilisation de la commande robuste face à ce type de variations paramétriques.

Cette étude se termine par la mise en œuvre d'une architecture Model In the Loop (MIL) du système d'essai de vibration afin de valider l'ensemble des travaux via des simulations dans les domaines temporel et fréquentiel, connus sous le nom d'essai en vibration virtuel. Une formulation adaptée de la stratégie de commande développée dans le cadre de l'architecture matérielle industrielle utilisée permet son implémentation avec des composants matériels et logiciels existants.

université
PARIS-SACLAY

ÉCOLE DOCTORALE
Sciences et technologies
de l'information et de
la communication (STIC)

Title: Robust control of shakers for mechanical qualifications of spacecraft

Keywords: Spacecraft qualification, Robust dynamic tracking, Structural mechanics, Active vibration control, parameter variation

Abstract: The aim of this thesis is to eliminate the beating phenomenon of the vibration testing systems during the mechanical qualification of the spacecraft. Mechanical qualification tests consist in applying, at the spacecraft interface, a sine sweep acceleration at given frequencies and magnitudes, depending on the launcher's requirements. However, the shaker control used for this qualification is often unsatisfying in terms of tracking performance in the neighborhood of spacecraft's structural modes and tank modes. Inopportune aborts may also happen during tests due to unacceptable overshoots. The reason for these troubles is the nonlinear control algorithm currently used, inappropriate for spacecrafts with very lightly damped vibrational modes. Therefore, the proposed work consists in developing a control strategy able to avoid the instabilities of the composite model, which includes shaker, interface, and spacecraft chain. Following a preliminary study of the phenomenon of oscillation and current literature on the topic of active vibration control, the research is conducted, moving the current control architecture towards a robust control strategy. The vibration testing system indeed imposes strict performance in terms of dynamic tracking for a very large frequency range. The developed robust control strategy also needs to overcome the usual conservatism noticed when the plant dynamics contain lightly damped modes.

Firstly, a feasibility study conducted on a simplified lightly-damped system highlights the elimination of vibration via robust control. Then an identified model of a real commercial satellite is used to demonstrate the superior performance of the proposed control architecture.

Finally, in order to overcome one of the main challenges related to the sensitivity of the robust control against any modal parameter variation, a reformulation of the control structure allows the desensitization of the robust control against these kinds of variations in the system.

This work ends with a model in the loop architecture of the vibration testing system in order to validate the control study via both time and frequency domain simulations known as the virtual shaker test. In the frame of the used industrial hardware architecture, the newly defined strategy formulation allows the implementation based on the existing hardware and software components.

1. TABLE OF CONTENTS

2. NOTATION

$\mathbb{R}$	The set of real number
$\mathbb{R}^{m\times n}$	Real matrix space of $m \times n$ dimension
$\mathbb{C}$	The set of complex number
$\mathbb{C}^{m\times n}$	Complex matrix space of $m \times n$ dimension
$[a,b],]a,b[$	For $(a,b) \in \mathbb{R}^2$, with $a \leq b$, a close interval and an open interval bounded by a and b, respectively
i	Imaginary number
$Re(a)$	Real part of the complex number a
$Im(a)$	Imaginary part of the complex number a
a^*	Complex conjugate of the complex number a
A^*	Complex conjugate of the matrix A
A^T	The transpose of a matrix A
$\|x\|$	The absolute value of x
$\|X\|_2$	The Euclidian norm of X
$\|X\|_q$	The q-norm of X
$\|X\|_\infty$	The infinite norm of X

$\dot{x}$	The derivative of x
$\lambda_i(A)$	The i^{th} eigen value of matrix A
$\sigma_i(A)$	The i^{th} singular value of matrix A
μ	Structured singular value

3. LIST OF ACRONYMS

A

ARE
  Algebric Ricatti Equation, 61
AVC
  Active Vibration Control, 42

B

BST
  Balanced Stochastic Model Trancation, 85

C

CLA
  Coupled Load Analysis, 2
CNES
  Centre Nationale d'Etude Spatiale, 6
cola
  Constant Output Level Adaptator, 19

D

DoF
  Degree of Freedom, 9
DVF
  Direct Velocity Feedback, 46

F

FEM
  Finite Element Modeling, 2
FOH
  First Order Hold, 81

H

HAC
  High Authority Control, 46

L

L2S

4. LIST OF FIGURES

5. LIST OF TABLES

1 INTRODUCTION

Qualifying large space structures such as satellites require numerous qualification tests, among which, tests in a vacuum thermal environment corresponding to the space environment, radiofrequency tests and mechanical environment tests. This research project focuses on the mechanical environment tests of large space structures, particularly those related to the qualification of a spacecraft under severe vibrations. Given the very specific environment that a spacecraft is exposed to from its launch up to the final destination orbit, it is imperative to test all the equipment as well as the satellite itself. The qualification to mechanical environments of a large space structure is mainly based on two types of tests: acoustic test for qualification at medium-high frequency behavior and vibration tests on a shaker table for its low-frequency range qualification. The first one takes place in a reverberation chamber and its objective is to put the satellite structure and equipment into an environment equivalent to which it will experience during takeoff. The pressure oscillation under the cover due to the vibration of the cover itself generating the acoustic environment, which is in fact, very dimensioning. The satellite is thus subject to spectral distribution between 20 to 2kHz, depending on the launcher, which can reach up to the magnitude of 142 dB. On the other hand, vibration tests qualify the satellite at a lower frequency range, which is between 5 and 100 Hertz for typically geostationary satellites. They are justified by the mechanical conduction of low-frequency structure-borne vibrations, but also to identify the modal signature of the specimen through low-level tests.

1.1 MECHANICAL STRENGTH VERIFICATION

The spacecraft is subject to face severe mechanical environments and its mechanical strength must be checked after the integration process (Lalanne, 2014) (Wijker, 2004) (Girard & Roy, 2007). A qualification or acceptance campaign is carried out in an environment which aims to prove the satisfactory structural resistance of spacecraft and equipment (McConnell, 1995). The qualification demonstrates the ability of the spacecraft to withstand the stresses it will experience during launch x 1.25, while the acceptance is limited to the flight expected value. Qualification therefore implies a concept of oversizing, while acceptance is limited to the flight expected value excitation level of the mechanical structure without any risk of unnecessary fatigue. Obviously, the level of qualification or acceptance is never immediately applied to the specimen but through several stages starting from low amplitude and then successively attaining higher amplitude levels. Therefore, a very low-level test is carried out with an amplitude level usually in the order of one-eighth of the qualification level. This step allows to verify the relevance of the test strategy (chapter 2 for details) which mainly includes the speed of the frequency increase (or decrease) of the reference known as sweep rate. It also contains the amplitude near the modal parameters in order to verify the relevance of the reference amplitude around spacecraft modes. Therefore, the goal is to avoid all sorts of excitation during the higher amplitude levels and proper selection of control parameters to assure the reference tracking while avoiding aborts. When the parameters seem consistent and safe, this level is doubled to reach the low testing level and successively reaches the intermediate and qualification level (Bettacchioli, 2014b). To be noted that the choice to stop at an acceptance level or to continue until a qualification falls under the commitment agreed between the mechanical analysts, the launcher authority and the client.

1.2 MODAL SIGNATURE VERIFICATION FOR COUPLED LOAD ANALYSIS

A coupled dynamic load analysis has to be carried out in order to observe the response behavior of the spacecraft and launch vehicle together during the liftoff, atmospheric flight, engine ignition and shutdowns, staging and separation events (ECSS, 2013) (Arianespace, 2011) (Wijker, 2007). The spacecraft model is achieved via FEM modeling and then validated via the vibration testing to use for CLA.

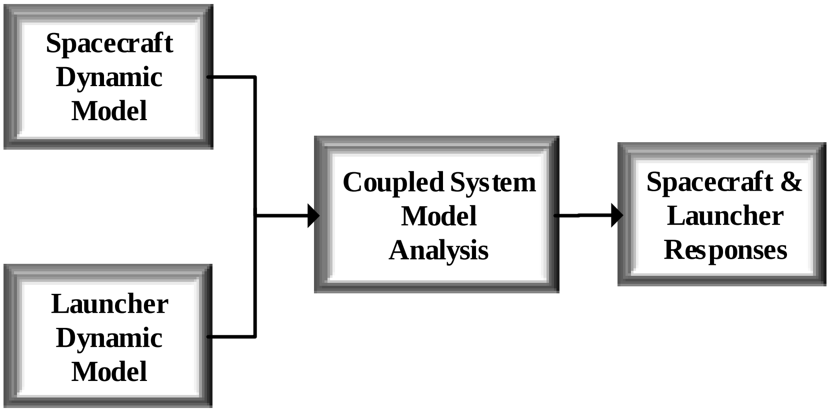

Figure 1-1 - Process of CLA (Wijker, 2007)

The verification of the modal signature is particularly important to overcome the risks of mechanical coupling analyzed through the process of CLA (Figure 1-1) (Arianespace, 2011). Since the modal damping of the main modes of the launcher and the satellite is very low (around 0.03), any coupling of launcher and satellite modes would result in severe oscillations if they are excited, therefore it is important to avoid any coupling between them. Indeed, any coupling of lightly damped launcher and satellite modes might cause partial damage during the flight. Moreover, the launcher authority which guarantees the absence of resonance due to spacecraft modes requires proof that there is no resonance of the satellite capable of causing coupling (Ewins, 2000). Another point to mention is that the identification of the modal signature of a satellite is necessary to verify the validity of its theoretical model achieved via FEM (Lalanne, 2014) (Wijker, 2004) (Girard & Roy, 2007).

1.3 CONTEXT OF THE RESEARCH

The large space structures are subject to the vibration qualification test. One among the large space vibration testing facilities in France is possessed by Thales Alania Space, Cannes. This facility is used to qualify a very diverse range of space structures such as scientific observational satellites, commercial geostationary satellites as well as the equipment level tests of solar panels, antennas, payloads etc. In Figure 1-2, a commercial geostationary satellite is on the shaker's table for its mechanical qualification.

Figure 1-2 Satellite on the vibration testing facility at Thales Alenia Space

The vibration system – Laredo Moving & Storage (LMS) testing solution by Siemens presents some issues. One of the major issues is the performance of the current closed-loop control algorithm of the vibration testing system which is incapable of tracking the reference signal with precision when the reference signal passes through the satellite vibrational modes, resulting in local overshoots as well as strong oscillations. The overshoot can cause the premature abort of the test and strong oscillations can bring fatigue to the structure (Soucy & Coté, 2002) (Calvi & Nali, 2007), consequently requiring the recalibration of control parameters (for details, see the section 2.2.5) to resume the test or in the worst-case scenario, may lead to an eventual damage of the structure (Naisse & Bettacchioli, 2012). The following figure shows the closed-loop tracking performance of a typical vibration test of a spacecraft.

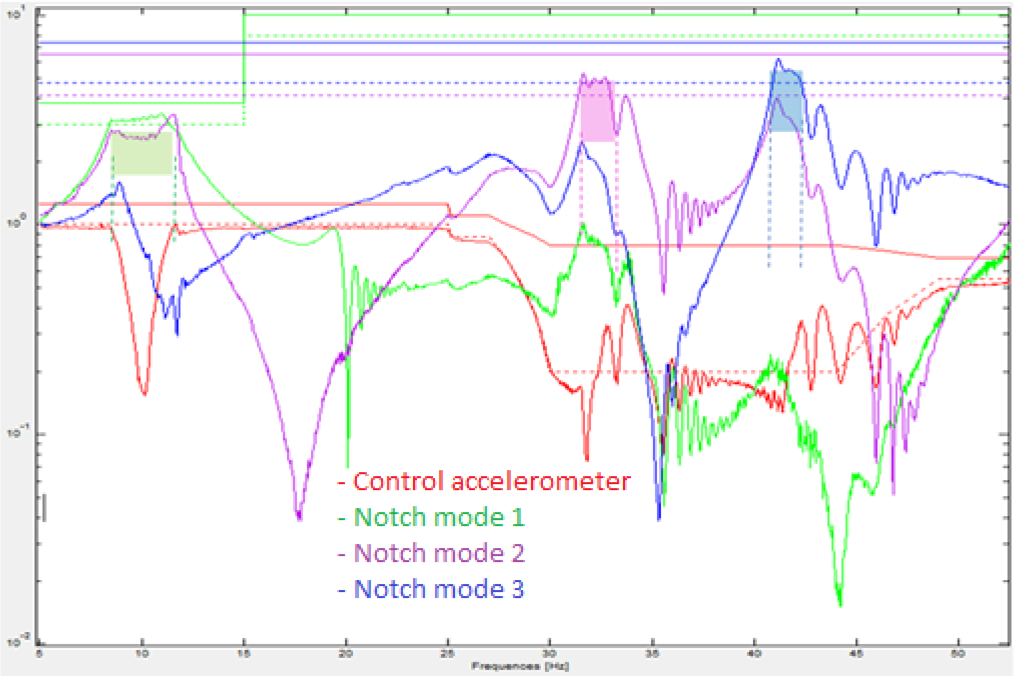

Figure 1-3 - Frequency response of the spacecraft with reference acceleration (Naisse, 2012) (Bettacchioli & Nali, 2015)

Figure 1-3 shows the response of three measurement accelerometers (in green, violet and blue), the vibration imposed on the satellite via the shakers table (in red) capturing the output acceleration of a geostationary satellite between 5 and 55 Hz where undesired oscillations are observed in all frequency ranges. The reference signals for each output acceleration are given in the same color while the dotted lines represent corresponding tracking references and the straight lines are the upper limit known as abort threshold. The green, violet and blue blocks correspond to the tracking of earth deck, upper and lower tank mode positions respectively. The figure illustrates the overshoot in the neighborhood of modes and oscillations during and after mode frequencies. While analyzing the vibration command (dotted red), the output command tracks ideally from 5 to 25 Hz and limits the first mode amplitude below the abort. After 25 Hz up to the end of the test, the reference signal amplitude is reduced significantly in order to limit the overshoot and oscillation of the second and third modes (in violet and blue). In the ideal scenario, the reference signal would be a single value of amplitude and the controller must generate such command that the response acceleration follows the exact tracking while avoiding overshoot and oscillation.

This research work deals with the deep analysis of the current vibration system to find out the causes of those issues in order to give appropriate implementable solutions enabling fine tracking, eliminating oscillation of the current vibration testing system at Thales Alenia Space. Therefore, this project is a result of the joint collaboration between Thales Alenia Space and the French space agency CNES (Centre National d'Etudes Spatiales). The thesis work has been led under the supervision of L2S laboratory of CentraleSupelec, Paris-Saclay University.

1.4 MOTIVATION AND SCIENTIFIC-TECHNOLOGICAL CHALLENGES

This research project is based on the real-world industrial challenge which needs a high knowledge of the vibration testing system. Therefore, the expertise of the system is acquired through experiences during the test campaign of different large space structures in the TAS facility as this subject is rarely developed in the literature. Since this project requires sound knowledge of spacecraft mechanical system as well as modern control algorithms, enables to work on a purely industrial level system, and to make a bridge between those two-engineering domains, it is a great opportunity to gain expertise of both sides and to experience the work in the integration and test facilities of mostly sophisticated space industry. In terms of scientific challenges, the major objective is to define the control system that ensures a tracking performance on a very large frequency range (from 5 to 100 Hz), whether most literature on control systems concern a very short frequency range in the neighborhood of the crossover frequency of the controller (Balas, 1990). Moreover, the system requires a very fine tracking performance when applying a reference signal which vibrates the structure and the control strategy must avoid all types of oscillations caused by vibrational modes. As the system works at very high sampling frequency (up to 12.8 kHz), the control design must assure the minimum complexity for the implementation issues.

1.5 DEVELOPED METHODOLOGY, AIMS AND OBJECTIVES

The vibration control system has several parameters to be calibrated depending on the speed and amplitude of the reference signal, the dynamics of spacecraft (details are given in the section 2.2.3) (Bettacchioli, 2018) (Bettacchioli, 2014b). Therefore, the current vibration testing campaign consists of several stages starting from a very low-level reference amplitude test in order to calibrate all control parameters and then, increasing the amplitude of the reference at each step to avoid all damages of the space structure due to overshoots and strong oscillations resulting from the current control algorithm (Bettacchioli, 2014b). Moreover, there is no possible way to ensure the stability performance of the closed-loop vibration test throughout the frequency domain stability analysis (Bettacchioli, 2014b), therefore the need of the current four-level vibration test to go from very low amplitude to qualification level amplitude in order to avoid any outcome which damages the satellite structure. The aim of the research is to provide a robust control algorithm, which can successfully track the reference signal of the vibration system while eliminating all overshoot and oscillations due to the structural modes of the satellite under variation of the modal parameters. The goal also includes the development of a simulator corresponding to the real vibration system scenario to ensure, prior to the testing campaign, the validity of the control design through time domain and frequency domain simulations. This work will not only ensure the performance of the vibration testing system, but also reduce the cost of the testing campaign by cutting off several stages of tests intended to calibrate the current control structure as the new robust control algorithm should be free from any parameter dependency.

In order to achieve those goals, the research includes the following objectives:

- A thorough analysis of the current control algorithm via constructor's manual, literature review, experience of several testing campaigns in order to evaluate all flaws and advantages of the current control architecture. Development of a simulator based on current control architecture to further compare the current performance with newly proposed architectures.

- Literature review on the modern control algorithms in order to select possible solutions for the study.
- Study of different control algorithms and comparison of the efficiency of the proposed algorithms.
- Design of a minimum order satellite model from a higher-order identified model and determination of the modal parametric variables-based synthesis model.
- Application of control algorithms based on previously studied system on the real satellite model
- Robustification of the control algorithms
- Analysis of the tractability of the control algorithm in the real system
- Development of the time domain simulator corresponding to the real testing scenario as well as frequency domain analysis to validate the control strategy.
- The procedure must ensure the ease of use and user friendliness as the technicians and engineers of the testing campaign may have a minimum control systems background.

The research study not only solves the industrial problem but also gives perspective to some original questions related to both modern control systems and structural mechanics.

- High precision dynamic signal tracking and controlling satellites vibrational modes as well as filtering the noises and disturbances while most literatures study the regulation problem where the need is to attenuate the vibrations caused by only disturbances and noises (Preumont, 2018).
- Precision tracking of variable frequency pseudo-periodic signal
- Distributed control action to a very large interval of frequency (5

to 100 Hz)

- Robustification of a large structure against modal parametric variation which is a real dilemma in this domain and very few literatures can be found concerning this subject.

1.6 STRUCTURE OF THE THESIS

The research work is structured in a series of successive chapters to understand the industrial problem and the developed strategies during the project. The following paragraph outlines the chapter-wise summary of the thesis.

Chapter one introduces the context of the project, the motivation of the study as well as fixing aims and objectives to attain. The conference and journal publications derived from the project are also cited.

Chapter two is dedicated to the analysis of the industrial problem, where the first section describes the current vibration system architecture. Its second part briefly analyses the encountered issues with this system and points out the scientific keywords for the research.

Chapter three introduces a one-DoF simplified dynamic model of the structure used for preliminary study case. Lately, an analysis of different control strategies found in the literature let us choose the appropriate control architecture to cope with modern control algorithms in order to find the right direction of the thesis.

Chapter four studies a real multi DoF composite model of the vibrator and satellite to procure a modal parameter-based synthesis model. By taking into account industrial constraints, a new control algorithm has been studied as explained in the previous chapter. The time and frequency domain analysis has been illustrated to show the efficiency as well as limitations of the new algorithm.

Chapter five tackles with the robustness issues and develops new strategies to overcome this problem, satisfying the industrial needs. A robustness analysis is provided to validate the efficiency of studied algorithms.

Chapter six is dedicated to the development of an industrial level simulator to create the realistic vibration testing scenario including the implementable solutions and the validation of the procedure.

The manuscript ends with a brief conclusion on the research and perspectives for further development.

1.7 PUBLICATIONS DURING THE PHD

Three articles have been published based on this work to disseminate its scientific contents.

Pub.	Title	Issue
1.	Sine Sweep Tracking Control of a Lightly-Damped Spacecraft	ICSTCC, Oct 2020, Romania.
2.	Robust Dynamic Tracking Control of a Modal Parameter Varying Spacecraft avoiding Vibration	ICSC, Nov 2021, France.
3.	Vibration Test of a Spacecraft via Virtual Shaker based on Robust Switching Control Architecture	ICARCV, Dec 2022, Singapore <submitted>

2 VIBRATION TESTING SYSTEM

This chapter is dedicated to the study of the current mechanical vibration testing system at Thales Alenia Space, developed by LMS Siemens. The hardware-level description stands at the beginning of the chapter, then, the software-level description such as the closed-loop system architecture is explained with the related algorithms. Lately, the focus is given on the analysis, in order to explore the limitations of the actual system. A simplified simulator has been introduced to clarify those limitations in terms of the system architecture. The main purpose of this chapter is to briefly understand the actual system in order to define scientific challenges for the Ph.D. work, which will be addressed in later chapters.

2.1 HARDWARE-LEVEL DESCRIPTION

The vibration plant roughly includes a table which supports the load to be tested (the satellite) and a vibrator which sets it in motion. The vibrator's operation is similar to that of a loudspeaker and it is actuated by a strong current delivered by amplifiers. The physical description of the different elements of the vibration test system is detailed below, with all necessary characteristics needed for the analysis of the closed-loop system.

2.1.1 Actuator

The vibrator is operated by a very intense alternating current, up to 3000 A peak, to vibrate the composite system including the satellite and the satellite holder. A cooling system of de-ionized water (to avoid electromagnetic shortcuts) assures the proper functioning of the system. Generated force $F(t)$ is given by Laplace's law, i.e, proportional to the delivered intensity of the current $I(t)$ (Brennan, n.d.).

$$F(t) = BLI(t) \qquad \textit{Eq. 2-1}$$

where B is the constant magnetic field and L is the coil length. The frequency and the amplitude can be controlled independently via the control signal. The spacecraft can be placed in two different configurations, either the longitudinal setup, where the spacecraft is positioned directly on the actuator (left of the Figure 2-1) or the transversal setup via the table (right of the Figure 2-1) (Naisse, 2012) (Charles, n.d.). The whole actuator-shaker setup is installed on a seismic mass (~150 tons) which is mounted on spring boxes to isolate the building from produced vibration.

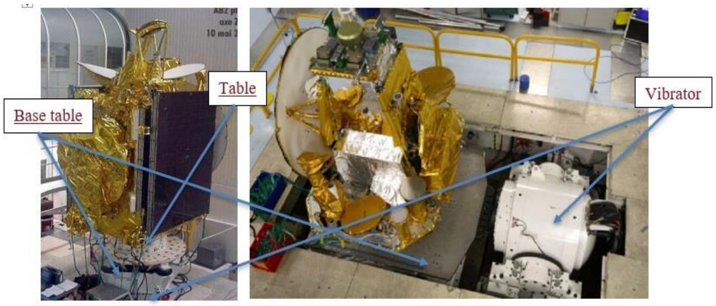

Figure 2-1 - Spacecraft in longitudinal & transversal configuration (Charles, n.d.)

The interface between the adapter and the satellite is called the "table" and the control accelerometers are placed at this level. The functioning range of this installation is between 5 to 1700 Hz (Ellero, 2014) where the actuator can deliver the following vibration characteristics:

Table 2-1 - Characteristics of the actuator (Ellero, 2014)

Vibration type	Max effort (kN)	Max. acceleration (g)
Random	267	60g
Sinus	289	75g
Shock	801	180g

2.1.2 Amplifier

The amplifier bridges between the numerical control output and the actuator input. The control output is a numerical acceleration signal, which is therefore needed to be converted into appropriate electrical signal to command the actuator, which is basically done by the amplifier. In addition, it may amplify the current supply if necessary. A large set of amplifiers is needed to convert the analog output voltage (±10 volts peak) of the control system into a proportional current of several amps (3000 A peak) (Ellero, 2014) (LMS FAQ, n.d.).

2.1.3 Main limitations of the installation

Maximum produced shaker force is limited by:

- Low frequency - Stroke of coil
- Mid frequency - Amplitude of induced force (B, L and I)
- High frequency - Internal shaker resonance (Reduces with size of the shaker)

Transmitted force by the vibrator is unidirectional but, despite many correctly distributed bearings, the eccentricity of the load's Center of Gravity induces moments that generate parasitic movements in other degree of freedom (Brennan, n.d.).

2.1.4 Sensor

The measurement of a vibration test is carried out with more than 400 accelerometers, up to 640, and even much more with the new range of satellites. Among this large set of channels, no more than 128 can be dedicated to the control. They are approximatively distributed in three groups: one third (~40 channels or less) for the satellite longitudinal z-axis test control, another third for the transverse x-axis and the last third for the transverse y-axis (Ellero, 2014) (PLM Software, 2013). In each group, four channels are dedicated to controlling the vibrator table and the other ones to the notching (this notion will be explained in the next section)

The four accelerometers placed on the vibrator's table are triaxial sensors and, during a run-test, only the four identically oriented channels are used. These four measurements allow control at the satellite's base. In addition to the redundancy aspect, their location at the four corners of the table makes it possible to take into account the table's deformations. In the absence of deformation, these four sensors' measurements should be identical except for noise. However, local deformations lead to deviations and the adopted procedure of testing requires that the control effort always generated from the highest amplitude channel. Consequently, the acquisition channel sometimes gets changed during several periods corresponding the highest amplitude.

The other sensors are placed on key locations of the satellite's structure, typically where the structure modes are the most critical. These sensors are called "notching accelerometer". They make it possible to verify that the local excitations of the equipment or structures (Ellero, 2014) are still in a safe domain.

Several types of accelerometers are used for the vibration test in particular PCB, Endevco, DJB, Bruel & Kjaer, etc. are common in industry (PCB 356B21, Website) (DJB A/131/V, n.d.) (Endevco 2222C, n.d.). A typical example of an accelerometer is PCB356B21, whose frequency operating range mentioned in the constructor's datasheet (PCB 356B21, Website) is compatible with the full functional range of the actuator as well as current system's architecture.

2.1.5 Notching

The qualification level vibration test consists of applying the sine sweep acceleration signal of almost 1g magnitude at the satellite's base but, because of the very weak damping of the dominant modes, holding such a level all along the run-test is unthinkable as it inevitably causes the destruction of the specimen. In order to overcome this drawback, and knowing that moreover the launcher’s specifications are designed with margins, the excitation level at the base of the satellite is reduced so that each dominant mode’s amplitude never exceeds a given threshold. In the reality, each mode of the satellite has its corresponding threshold limit and there are several sensors fixed in the satellite body, known as notchers. During the vibration test when the reference frequency reaches a mode frequency of the satellite, the amplitude of the output acceleration measured by notchers exceeds control sensors. The moment it attains the threshold fixed for the given mode, the control effort is then computed from the measured data from notchers. This strategy is called ”Classical notching” (or ”automatic notching”) and the main goal of this strategy is to limit the vibration of the satellite near modes in order to keep it safe from structural fatigue or any damage (Ellero, 2014) (Naisse & Bettacchioli, 2012) (Simcenter Notching, 2019).

In addition, another type of notching called ”Manual notching” is also used in some cases, which consists of not using the control based on a conventional notching but by modifying the reference amplitude in a lower value at the satellite’s base. In this case, the control effort is computed from the control sensors measurement without using any notchers and each mode reaches its maximum authorized threshold without overshoot. Classic notching is then relegated to the rank of security. This strategy is mostly applied for higher frequency modes where the classical notching fails to limit the vibration under the threshold. These strategies are detailed via illustration in Figure 1-3 and Figure 2-9 and the corresponding sections.

2.2 SYSTEM ARCHITECTURE

This section explains the general software level architecture of the closed-loop system and briefly describes each principal block of the system with necessary algorithms. Figure 2-2 shows the current architecture.

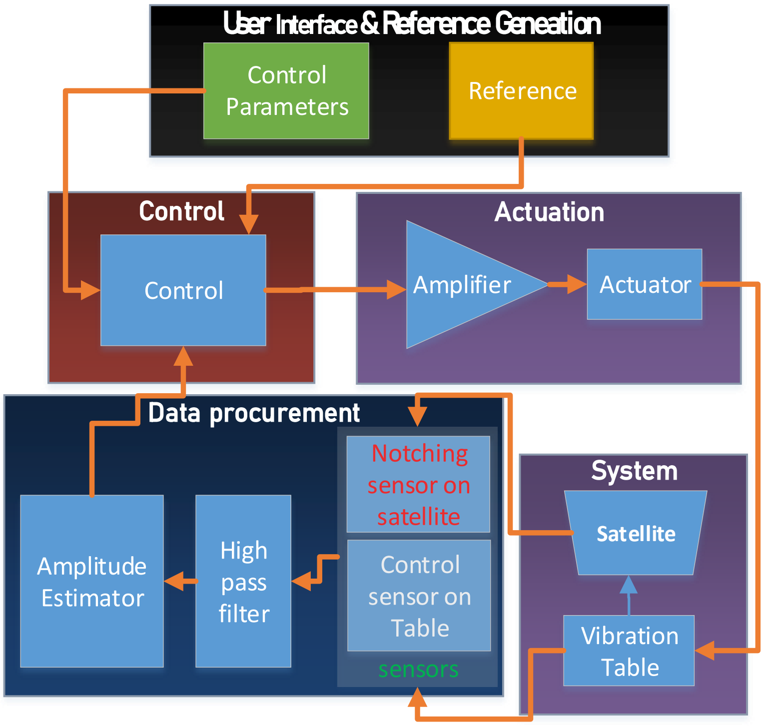

Figure 2-2 - Closed-loop system

The current control structure is quite different from a classic one as it is not carried out on a position (or a speed or an acceleration) but on the acceleration amplitude with an error which is defined as the ratio of the reference amplitude and the real applied amplitude. The control then requires expressions depending on whether this error is less or greater than 1. Moreover, a single parameter entitled “Compression factor” allows to adjust the control loop dynamics: The smaller this factor, the more responsive the control is but leads to instability, the larger it is, the more stable the system is, but the dynamic is slower. The mechanical analyst must tune this factor and find a compromise between stability and performance, which is then adjusted to even more appropriate values during low-level preliminary tests. The architecture of Figure 2-2 is simplified in Figure 2-3 to illustrate the way a vibration testing system works numerically (Bettacchioli & Nali, 2015).

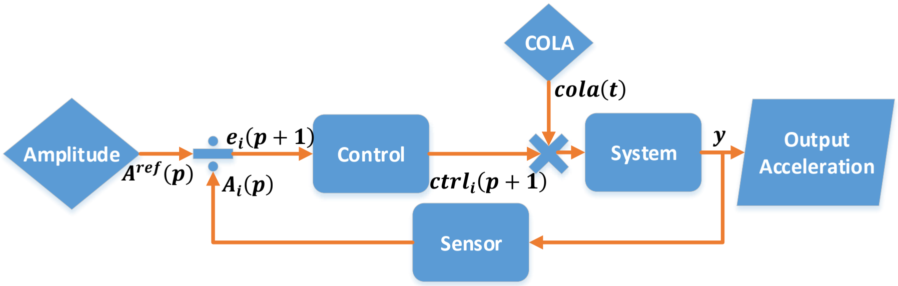

Figure 2-3- Closed-loop numerical system

Figure 2-3 represents the simplified numerical closed-loop system architecture of the VTS where $A^{ref}, A, e, ctrl, cola$ and y correspond respectively to the reference amplitude, measured amplitude, error, the periodic reference and the output acceleration, where p is the pseudo-period number, i the sensor number. The details of the terms are given in the following section.

2.2.1 Reference "$\boldsymbol{cola}$"

The reference signal applied to the system is a pseudo-sinusoidal acceleration, it has two distinct parts, the amplitude of the sine wave expressed in "g" (the gravitational constant) and its frequency that varies with time within a given interval and at a rate expressed by the unit of octave per minute (Arefin, 2020). The following parameters and expressions define the signal $\ll cola \gg$

2.2.1.1 Sweep rate

The sweep rate $\ll s \gg$ is positive if the frequency increases as a function of time or negative otherwise. The sweep rate can be linear in frequency but it is most often exponential and is expressed in octave per minute (Nali & Bettacchioli, 2014a). It is typically exponential as the objective of the test may stay longer in low-frequency modes and sweep rapidly in high-frequency modes to avoid structural fatigue due to vibration.

$$f(t) \;=\; f_0 \times 2^{\frac{S}{60}t} \;=\; f_0\, e^{\alpha t} \qquad \text{Eq. 2-2}$$

$$with\;\; \alpha = \frac{\ln(2)}{60}\, s$$

The upper and lower limits of the frequency variation are expressed by $[f_{\min}\,;\,f_{\max}]$

2.2.1.2 Expression of $\boldsymbol{cola}$

By definition, the frequency of a periodic signal is the derivative of its phase (SUA, 2017) (Bettacchioli, 2014b).

$$\omega(t) \;=\; 2\pi\, f(t) \;\triangleq\; \frac{d\varphi(t)}{dt} \qquad \text{Eq. 2-3}$$

$$\varphi(t) : phase\ of\ cola$$

With this condition, we obtain,

$$\varphi(t) = \int_0^t 2\pi\, f_0\, e^{\alpha\tau}\, d\tau \;=\; 2\pi\, \frac{f_0}{\alpha}\, (e^{\alpha t} - 1) \qquad \text{Eq. 2-4}$$

As a result,

$$cola(t) = \sin\left(2\pi\, \frac{f_0}{\alpha}\, (e^{\alpha t} - 1) + \varphi_0\right)\; for\ all\ t\, \in [0, t_{end}] \qquad \text{Eq. 2-5}$$

In practice, the process starts at a frequency f_0, remains at f_0 until the output stabilizes and then the sweeping starts. As the beginning of the sweep is the start time for us, the phase φ_0 is not necessarily zero. Therefore, we define the beginning of the $cola$ $t = 0$ and the end of the test at $t = t_{end}$. In addition, Eq. 2-5 gives the unitary $cola$ signal. If A is the amplitude of the periodic signal, then in the Eq. 2-5 $A * cola(t)$ gives the periodic signal with the reference amplitude.

2.2.1.3 Other important parameters

From relations [Eq. 2-5] defining $cola$, we can deduce other characteristic parameters, such as the duration of the test and the duration of each pseudo-period.

2.2.1.3.1 Maximum duration

The duration t_{max} of the signal $cola$, is the time to reach the maximum frequency, excluding the initial rise time to reach the reference at the frequency f_0, given by:

$$t_{max} = \frac{1}{\alpha} \ln\left(\frac{f_{max}}{f_0}\right) \qquad \text{Eq. 2-6}$$

This parameter determines the duration of the vibration test (Arefin, 2020), which is equivalent to t_{end} of the contituous time $cola$ given by the Eq. 2-5.

2.2.1.3.2 Pseudo-period duration

The duration of the P^{th} pseudo-period expressed by τ_K, is the difference between the total time of the $(P-1)^{th}$ and the P^{th} periods from the beginning of the $cola$ (at $t = 0$), respectively t_P and t_{P-1}. As each complete period adds 2π to the total phase, the phase at the end of P^{th} period can be written:

$$\varphi_p(t) = 2\pi \frac{f_0}{\alpha}\left(e^{\alpha t_P} - 1\right) = 2P\pi \qquad \text{Eq. 2-7}$$

Here, t_P is the total time of the test from first period to end of the P^{th} pseudo period of the $cola$. By using Eq. 2-7, the expression of t_P can be obtained:

$$t_P = \frac{1}{\alpha} \ln\left(1 + \frac{\alpha\, P}{f_0}\right) \qquad \text{Eq. 2-8}$$

By extending the reasoning to the instant t_{P-1}, we can obtain the duration of the P^{th} pseudo-period τ_P.

$$\tau_P = t_P - t_{P-1} = \frac{1}{\alpha}\ln\left(\frac{f_0 + \alpha P}{f_0 + \alpha(P-1)}\right) = \frac{1}{\alpha}\ln\left(1 + \frac{\alpha}{f_0 + \alpha(P-1)}\right) \qquad \textit{Eq. 2-9}$$

The final form of the Eq. 2-9 is obtained by simply adding a term into the numerator of the log function. And consequently, the apparent frequency of the P^{th} pseudo-period is expressed by:

$$f_P = \frac{1}{\tau_P} = \frac{\alpha}{\ln\left(1 + \frac{\alpha}{f_0 + \alpha(P-1)}\right)} \qquad \textit{Eq. 2-10}$$

Figure 2-4 shows a typical example of a $cola$ reference signal, generated with 1g magnitude, starting from 1 Hz and ending at 6 Hz, with a sweep rate of 20 octave/min. These parameterizations have been chosen to illustrate the change of frequency of the periodic signal.

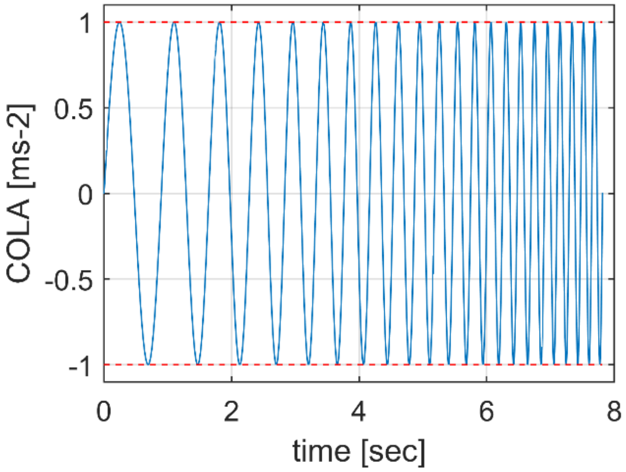

Figure 2-4 -Example of a $cola$ reference signal

2.2.2 Amplitude estimation

The response amplitude of each accelerometer is calculated using 120 to 240 samples depending on the acquisition frequency and the current instantaneous frequency (PLM Software, 2013). Several estimation methods can be used to estimate the maximum amplitude of each pseudo-period, from which we detail the main four calculation ones used by LMS (Simcenter Estimation, 2019) in the following paragraphs.

2.2.2.1 Maximum value estimation

This method consists in assimilating the amplitude of the response to the maximum value of the signal over each cola pseudo-period. Figure 2-5 illustrates this principle.

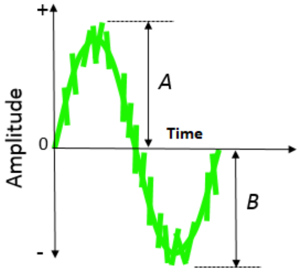

Figure 2-5 – Estimated amplitude equal to the maximum measurement during a $cola$ pseudo-period (Simcenter Estimation, 2019)

The maximum value is then:

$$A_{\max}(P) = \max_{j}\left(\left|a_P^j\right|\right) \qquad \textit{Eq. 2-11}$$

Here, a_P^j denotes the j^{th} sample magnitude in the P^{th} pseudo-period of $cola$. In this method, the measurements are not filtered, therefore, if the measurements are noisy, we would likely have a maximum value noticeably higher than the actual value of the amplitude. A control which is based on such estimation will therefore tend to minimize the actual output of the system and, depending on the nature of the measurement noise, to produce a choppy command.

2.2.2.2 *Average value estimation*

This method is based on the average of the absolute values of the signal a_P^j over a pseudo-period of $\boldsymbol{cola}$. We therefore have for the P^{th} pseudo-period of cola:

$$A_{\text{average}}(P) \;=\; \frac{\pi}{2}\frac{1}{N_P}\sum_{j=1}^{N_P}\left|a_P^j\right| \qquad \textit{Eq. 2-12}$$

where N_P represents the number of samples of the P^{th} pseudo-period cola and the factor $\frac{\pi}{2}$ is the ratio between the peak value and the absolute value of a sinusoidal signal. This estimator has the advantage of filtering out high-frequency noise.

2.2.2.3 *RMS estimator*

This estimator computes the amplitude $A_{\text{RMS}}(P)$ of the sinusoidal signal having the same energy as the real signal (see the Figure 2-6). Using N_P samples over the P^{th} pseudo-period of the $cola$, the RMS value has the following expression:

$$A_{\text{RMS}}(P) = \sqrt{2}\sqrt{\frac{1}{N_P}\sum_{j=1}^{N_P}(a_P^j)^2} \qquad \textit{Eq. 2-13}$$

In the Figure 2-6, the sampled magnitude $a_{1,\dots,N}$ corresponds to $a_P^{1,\dots,N}$ of the Eq. 2-13.

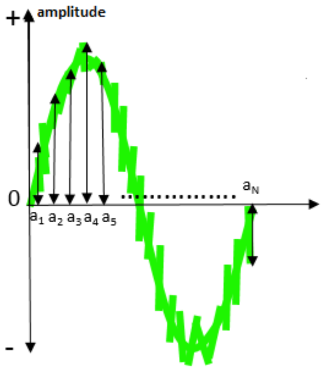

Figure 2-6 - RMS value over a $cola$ period (Simcenter Estimation, 2019)

Similar to the average estimation method, the RMS estimation also attenuates high frequency noise. Typically, the amplitude estimated by this method is slightly below the mean value and the one of the first harmonic approximation (Simcenter Estimation, 2019).

2.2.2.4 First harmonic estimator

This method is based on the Fourier decomposition of a signal (Charles, n.d.) (Ellero, 2014). Any recurrent signal can be decomposed into an infinite sum of sinusoids of different frequencies.

Let $x(t)$ be a periodic signal of period T_0 : $x(t) = x(t + T_0)$

Using Fourier decomposition, we can write:

$$x(t) = a_0 + \sum_{n=1}^{\infty} a_n \cos(2\pi f_n t) + \sum_{n=1}^{\infty} b_n \sin(2\pi f_n t) \qquad \textit{Eq. 2-14}$$

a_n and b_n are the coefficients which characterize the amplitude of the sinusoidal component of frequency $f_n = n\frac{1}{T_0}$. Knowing the apparent frequency of each pseudo-period of $cola$, we assimilate it to that of the first harmonic, so that:

$$y(t) = A\,sin(2\pi f t + \varphi_e) \tag*{Eq. 2-15}$$

φ_e is the phase shift of the output signal with respect to the phase of the input signal $cola$ denoted by φ in Eq. 2-4.

This relation can also be written:

$$y(t) = A\,[sin(2\pi f t)\,cos(\,\varphi_e) + \,cos(2\pi f t)\,sin(\,\varphi_e)] \tag*{Eq. 2-16}$$

In a matrix form:

$$y(t) = \,[sin(2\pi f t) \quad cos(2\pi f t)] \begin{bmatrix} A\cos(\,\varphi_e) \\ A\sin(\,\varphi_e) \end{bmatrix} \tag*{Eq. 2-17}$$

By substituting for t the discrete instants $k.T_s$ (T_s : sampling period) for k varying from 1 to N_P which is the number of samples of the P^{th} pseudo-period of the $cola$ estimated by the accelerometer m, we obtain the matrix form:

$$\underbrace{\begin{bmatrix} y^m(1\,.T_s) \\ y^m(2\,.T_s) \\ \vdots \\ y^m(N_P\,.T_s) \end{bmatrix}}_{Y^m} = \underbrace{\begin{bmatrix} sin(2\pi f T_s) & cos(2\pi f T_s) \\ sin(2\pi f(2)T_s) & cos(2\pi f(2)T_s) \\ \vdots & \vdots \\ sin(2\pi f(N_P)T_s) & cos(2\pi f(N_P)T_s) \end{bmatrix}}_{\Phi} \underbrace{\begin{bmatrix} A\cos(\,\varphi_e) \\ A\sin(\,\varphi_e) \end{bmatrix}}_{\Theta} + \underbrace{\begin{bmatrix} \varepsilon(1.T_s) \\ \varepsilon(2.T_s) \\ \vdots \\ \varepsilon(N_P.T_s) \end{bmatrix}}_{\varepsilon} \tag*{Eq. 2-18}$$

where Y^m is the vector of the measured outputs and ε the measurement error. In this equation, we find the estimated $\widehat{\Theta}$ of the signal Θ in order to deduce the amplitude A and the phase shift φ_e. Solving this system by the least mean square method allows us to write:

$$\widehat{\Theta} = \begin{bmatrix} \hat{A}cos(\hat{\varphi}) \\ \hat{A}sin(\hat{\varphi}) \end{bmatrix} = \Phi^{\#}\, Y^m \qquad \textit{Eq. 2-19}$$

where $\Phi^{\#} \triangleq [\Phi^t\Phi]^{-1}\,\Phi$ is the pseudo inverse of Φ.

Remark that:

$$\|\Theta\|^2 = \Theta^t\Theta = [A\cos(\varphi_e)]^2 + [A\sin(\varphi_e)]^2 = A^2 \qquad \textit{Eq. 2-20}$$

We obtain:

$$\widehat{\mathrm{A}} = \|\widehat{\Theta}\| = \sqrt{\widehat{\Theta}^2(1) + \widehat{\Theta}^2(2)} \qquad \textit{Eq. 2-21}$$

Remark:

1) In the presence of a constant offset, it would normally be necessary to consider the following model:

$$y(t) = A\,[\sin(2\pi ft)\cos(\,\varphi_e) + \cos(2\pi ft)\sin(\,\varphi_e)] + offset$$

That can also be written in the form of a scalar product:

$$y(t) = [\sin(2\pi ft) \quad \cos(2\pi ft) \quad 1] \begin{bmatrix} A\cos(\,\varphi_e) \\ A\sin(\,\varphi_e) \\ offset \end{bmatrix}$$

2) Among the four methods that have just been presented, it is the first harmonic one which makes it possible to obtain the most representative amplitude and phase of the signal.
3) A high pass filter of 0.5 Hz bandwidth removes the low frequency

noise of the measured signal.

2.2.3 Control structure

The closed-loop control architecture is shown in Figure 2-3 and the control algorithms used in the current vibration testing system are detailed in this section (Bettacchioli, 2014b) (Arefin, 2020) (Simcenter Control, 2019). Its principle is to weight the $cola$ with the correction which is calculated at the start of each pseudo-period, by comparing the reference amplitude and that already reached, provided that its frequency is not too high. Otherwise, higher frequencies would have less samples within a period and the measured data will be less accurate to capture the periodicity. We thus calculate $ctrl_i$ from the measurement of each sensor. To achieve such controller, the error is defined as the ratio of the reached amplitude $A_{i\in[1,N]}(P)$ to that of the setpoint $A_i^{ref}(P)$ for a sensor $i \in [1\ to\ N]$, we therefore have N associated errors, given by:

$$e_{i\in[1,N]}(P+1) = \frac{A_{i\in[1,N]}(P)}{A^{ref}(P)} \qquad \textit{Eq. 2-22}$$

where P is the indice of the elapsed pseudo-period.

We notice that, if the amplitudes follow the reference exactly, then the error is equal to 1. This control method computes the control effort by differentiating the values of error either superior or less or equal to 1, by considering the same notations as previously, we have:

$$ctrl_i(P+1) = ctrl(P)\frac{1+W}{e_i(P+1)+W} \quad \text{if } e_i > 1$$

$$ctrl_i(P+1) = ctrl(P)\frac{\frac{1}{e_i(P+1)}+W}{1+W} \quad if\ e_i \leq 1 \qquad \textit{Eq. 2-23}$$

The weighting factor W influences the dynamics of the correction (see section 2.2.3.7). In the Eq. 2-2, we can see that when $A_{i\in[1,N]}(P) > A^{ref}(P)$, then the error $e_i > 1$. This case corresponds to an overshoot and, for the biggest value of e_i, we get the smallest value of $ctrl_i(P+1)$ from the Eq. 2-23. Consequently for N sensors, we therefore calculate N control signals and the final correction which is applied to the system is the one with minimum value.

$$ctrl(P+1) = \min_{i\in[1,N]}\left(ctrl_i(P+1)\right) \qquad \textit{Eq. 2-24}$$

2.2.3.1 SISO control strategy

The index $i \in [1, N]$, mentioned in the previous section, represents the accelerometers used for control. Although there is a large number of accelerometers for measurement, according to Eq. 2-24, the control algorithm uses only the accelerometer with the highest acceleration as explained in the previous section (therefore the displacement), which may be considered as the worst-case scenario. Even in the presence of multiple measurement channels, the control architecture is a SISO system (Bettacchioli, 2018) (Arefin, 2020). As mentioned in section 2.2.3, the control law uses the control accelerometers throughout the whole frequency range of sine sweep. The exception happens in the neighborhood of the satellite mode, as the spacecraft starts to oscillate and the control accelerometer reaches the upper bound, the control shifts from control accelerometer to notch accelerometers (Simcenter Notching, 2019). After the passage of the mode, control shifts back to control accelerometer when the output acceleration gets smaller than the limit. Later in this chapter, an example is given to illustrate the strategy.

2.2.3.2 Weighting factor

The weighting factor W of Eq. 2-23 is calculated (PLM Software, 2015) (Arefin, 2020) by the following equation:

$$W = \frac{40 \times \left(K_f - 1\right)}{T_{loop}} \qquad \textit{Eq. 2-25}$$

with $\boldsymbol{K_f}$ being the compression factor which can be taken from 1 to 20 in order to vary W and $\boldsymbol{T_{loop}}$ is the loop time defined in the next section.

This weight is introduced to tune the rapidity of the control and the stability. When $\boldsymbol{W} = \mathbf{0}$, then Eq. 2-23 can be written as $\boldsymbol{ctrl_i}(\boldsymbol{P}+\mathbf{1}) = \boldsymbol{ctrl}(\boldsymbol{P})\frac{\mathbf{1}}{\boldsymbol{e_i}(\boldsymbol{P}+\mathbf{1})}$ meaning the correction of total error in the next period. Higher the $\boldsymbol{W}$ lower the $\boldsymbol{ctrl_i}(\boldsymbol{P}+\mathbf{1})$ gets, meaning the slower but smoother correction of the error.

2.2.3.3 Loop time $\boldsymbol{T_{loop}}$

The loop time T_{loop}, introduced in the Eq. 2-26 is the time which separates two consecutive control signals (PLM Software, 2015) (Arefin, 2020). In other words, it is the total time needed for the signal to propagate from a given point of the closed-loop system to return to the same point. Typically, it can be defined as the sum of the measurement acquisition and processing times.

$$T_{loop} = T_{acq} + T_{proc} \qquad \text{Eq. 2-26}$$

2.2.3.4 Processing time

The processing time T_{proc} is the time required for data processing or in other word, the necessary time to run all algorithms in the closed-loop system. This parameter depends on the number of sensors. For a given on board computer capacity, it is constant. In order to avoid any lag in the real time system, T_{proc} is very small and in Siemens VTS, it is 17 msec (PLM Software, 2013).

2.2.3.5 Acquisition time

As it can be seen in the definition of loop time that it is constituted of processing time and propagation time from one point of the closed loop to return back to the same point. The acquisition time T_{acq} is therefore the time required to propagate the signal in the loop without the processing time. This time varies with the frequency of the $cola$ as at a slower frequency, the signal also propagates slowly, but in higher frequency of the $cola$, acquisition time must be smaller to match the need of real-time closed-loop system. The time is greater than or equal to one period but does not exceed two periods of $cola$.

2.2.3.6 Comparison between $\boldsymbol{T_{acq}}$ and $\boldsymbol{T_{proc}}$

At low frequency, T_{proc} is negligible compared to T_{acq} and we can consider that T_{loop} is almost equal to the last one. On the other hand, when the frequency of cola increases, T_{proc} becomes predominant (see Figure 2-7). At 20 Hz, T_{acq} is 0.05 sec and T_{proc} is 0.01 sec where at 5 Hz, T_{acq} is 0.2 sec and T_{proc} is 0.01 sec. At low frequency (5 Hz), T_{proc} is 1/20th of the T_{acq} whereas at high frequency (20 Hz), it becomes 1/5th of the T_{acq}.

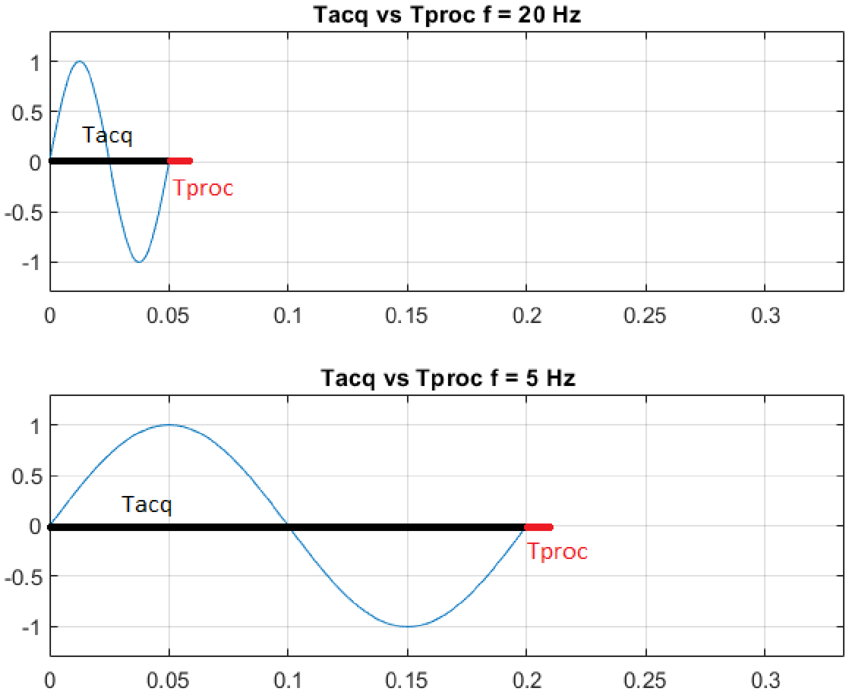

Figure 2-7- Tproc (red) and Tacq (blue) for different frequencies

2.2.3.7 Compression factor

The compression factor K_f determines the responsiveness of the controller as well the stability of the closed-loop system. On the most common applications of vibration tests, it is chosen between 1 to 20 and then, we can obtain the weighting W defined by Eq. 2-25.

$$For\ K_f = 1\ \rightarrow W = 0\ \rightarrow ctrl(P+1) = \frac{ctrl(P)}{e(P+1)}$$

In other words, lower the K_f is, faster to the correction of the error but it tends to destabilize the system, while higher values of K_f slow down the dynamics for the benefit of stability. It is unnecessary to take a K_f more than 20 as the effect of a much bigger value will not be noticeable.

2.2.4 User interface

The user interface allows users to enter the following parameters that defines the strategy of the test (Bettacchioli, 2014b):

Parameters of the reference:

- the direction (either the increase or decrease of the frequency of $cola$) and the sine sweep speed (in octaves / min)
- The amplitude of the $cola$ and abort thresholds (Abort thresholds are limits of measurement accelerations, which, if exceeded, cause the test to be stopped)
- Frequency interval of the test

Parameters of the control algorithm:

- Compression factor

Installation instruction:

- The control/notching accelerometer selection instructions

2.2.5 Vibration testing campaign

The vibration testing procedure is mainly based on 4 main steps, characterized by the amplitude of the reference $cola$ (SUA, 2017) (Arefin, 2020). After fixing control and notching accelerometers on the shakers table and at different locations of the satellite, all other parameters of the user interface are also provided by the mechanical analyst. Figure 2-8 shows the different steps of the vibration test of a Spacecraft.

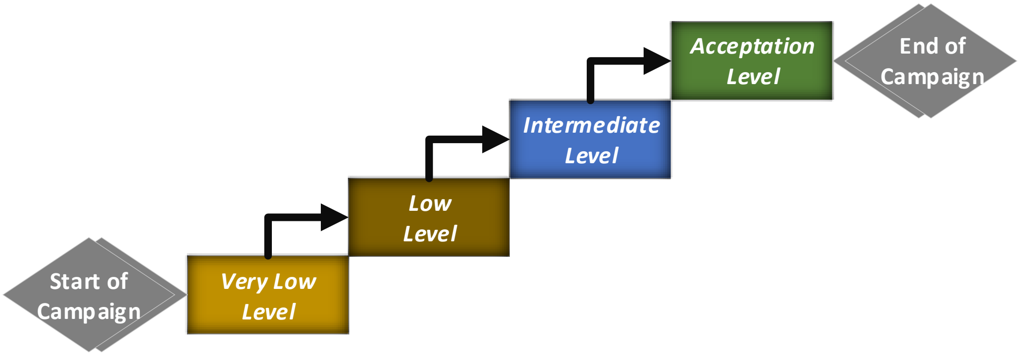

Figure 2-8- Vibration campaign steps

The campaign begins with a very low-level test, defined by the amplitude of $cola$, typically ${}^{1}/_{8}$th of the amplitude of qualification (or acceptation) level. This step ensures the relevance of all parameters defined for the campaign, if not, they can be adjusted as necessary. Usually the initial control parameters need some readjustments so that the accelerations of the shakers table better follow the reference $cola$. At this stage, modal parameters of the spacecraft are also known. As the level of amplitude is very low, eventual damage of spacecraft is not expected. Once the very low-level test has been accomplished, the next step is to test at low-level amplitude, twice the amplitude of the very low-level test. This test uses the parameters fixed during the previous level. If the output acceleration doesn’t follow the $cola$ with the required precision, the control parameters would go through a manual retuning procedure, and the test would be carried out repeatedly until the expected results are observed. In the same way, the next two levels are carried out by increasing twice of the amplitude level each time.

2.3 ISSUES OF LMS-SIEMENS VIBRATION ANALYSIS SYSTEM

Current system presents several issues in terms of architecture and also questions the practicality of the campaign. Lots of those issues have been studied in (Bettacchioli & Nali, 2015) we give hereafter a brief overview of them, and limitations are addressed throughout the manuscript.

2.3.1 System architecture-related issue

The closed-loop system tracks the reference $cola$, which typically sweeps through a frequency range of 5 to 100 Hz. Although the tracking is far from being perfect, it becomes worse in the neighborhood of the satellite vibrational modes, as in most of the cases strong oscillations can be observed. These oscillations are known as beating phenomena in the literature (Nali & Bettacchioli, 2014a), which are stronger at higher frequencies. Figure 2-9 shows a typical result of the satellite vibration test from 5 to 50 Hz frequency range (x axis) and the y axis represents the amplitude measured by accelerometers (in g).

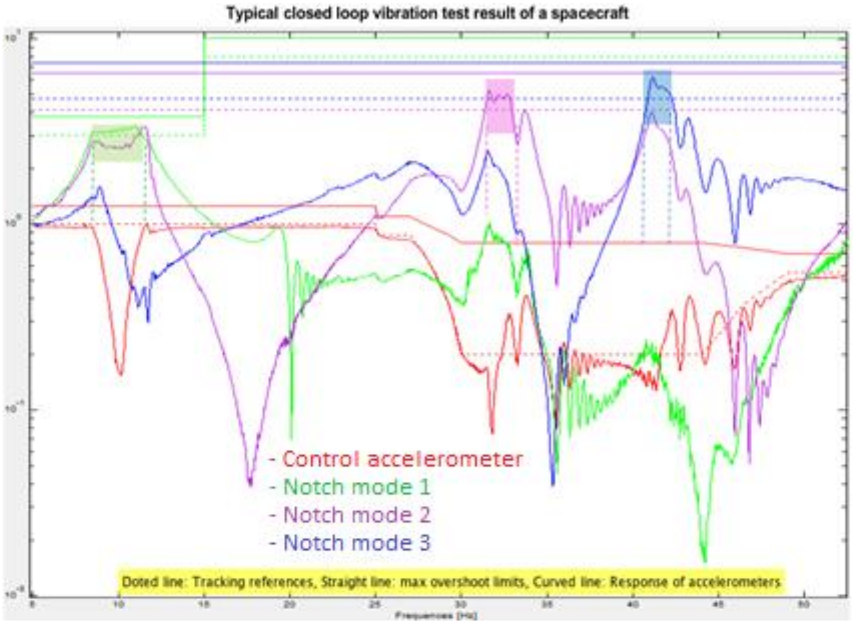

Figure 2-9- Typical performance of the current vibration testing

system (Bettacchioli & Nali, 2015)

Figure 2-9 contains the response of a control accelerometer (red curve) and three notch accelerometers (green, magenta and blue curves). Each accelerometer comes with its own reference (dotted lines) and an abort limit (straight lines) presented with the same color as the response. As mentioned in the section 2.2.3, the control uses only one measurement signal at a time (the worst-case signal among all measurement channels) to generate the command. In the neighborhood of the vibrational modes where the notch accelerometers reach their limit, the control is done by those accelerometers. The rest of the time, the command takes the control accelerometer for the measurement. At the beginning of the test, the control accelerometer tracks the reference (red curve with red dotted line) with acceptable error (5%). While approaching the first mode, a notch accelerometer captures an increase of acceleration and when it attains its reference (first intersection between green curve with green dotted line), the control shifts from the control accelerometer to this notch in order to limit the vibration of the satellite as this channel becomes the worst case in terms of magnitude (green rectangle zone). In the green rectangle, an overshoot (almost 8%) and also oscillations can be observed. Later, the control accelerometer takes the control back, and similarly to the first mode, the second and third modes are controlled by the other two-notch accelerometers (the magenta and blue rectangle, successively). Unlike the first mode, the tracking of the last two modes presents strong overshoots and oscillations. At the same time, the tracking after the second mode (from 33 Hz) with the control accelerometer (red curve) shows continuous beating, a very degraded tracking performance.

In addition to the issues mentioned in the last paragraph, if we observe the reference of the control accelerometer (red dotted line), from 25 Hz the amplitude has been significantly reduced to limit the notch accelerometer response below the acceptation limit (This is called manual notch, the description is given is the section 2.1.5). If the control performance was able to track the reference accurately without any risk of overshoot and oscillation, the control reference could have been kept to a constant amplitude.

2.3.2 The practicality of the current campaign

The control parameters are readjusted manually by an assembling, integration and test (AIT) expert during operation. As there is no existing way to analytically verify the relevance of those parameters (such as the frequency domain stability analysis), the current strategy is to go through four levels of vibration testing level increasing little by little the reference amplitude in order to avoid any structural damage of the spacecraft. Furthermore, the reiterated values of the control parameters are taken from totally intuition of the expert, therefore no guarantee to have better performance than the previously fixed values. This procedure takes extra time and the reiteration on the real satellite with overshoots and beating, may bring extra stress to the spacecraft. In fact, this whole procedure may take between three to four weeks of work for a commercial spacecraft, may need longer period of time for scientific spacecraft, making the vibration testing procedure quite expensive.

2.4 ANALYSIS OF THE CURRENT CONTROL ALGORITHM

The highlighted issues explained in the previous section are related to the current control law as well as the architecture of the current system. A systematic analysis is needed to further investigate the encountered problems. A simplified simulator has been developed to study the behavior of the current control algorithm. Figure 2-10 illustrates the structure of the simulator.

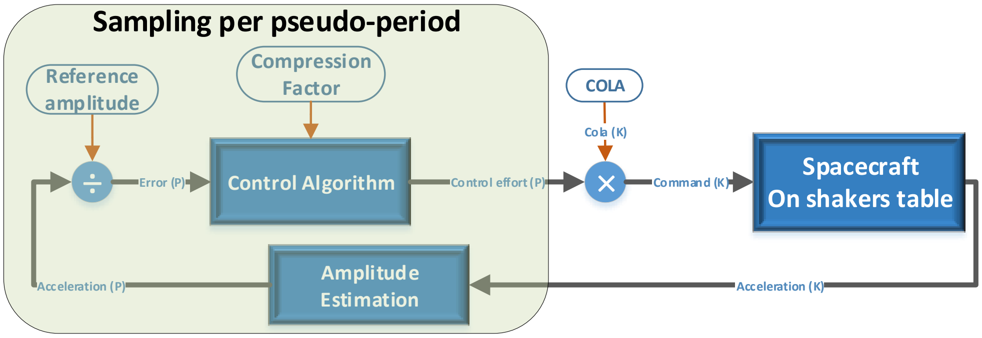

Figure 2-10: Simplified study simulator with the current control law

2.4.1 Description of the study simulator

In this section, the model we consider is a single DoF model corresponding to the satellite's first mode (Detail the S-DoF model is given in section 3.3) where the dynamics of the vibration installation is supposed to be perfect (no modes in the range of [5, 100] Hz) and the control law is the current one (see section 2.2.3 for control algorithm). In order to simplify the simulation and only focus on the tracking performance, sensors are taken as perfect without introducing any noise and it takes acceleration as input and the output corresponds to the estimated max magnitude of each pseudo-period of $cola$. To be mentioned that, as we just want to analyze the behavior of the current nonlinear control structure causing issues, and the objective of the analysis is not to demonstrate the accurate real-world performance of the LMS-Siemens control loop, therefore the single DoF system is sufficient for the purpose. Furthermore, the principle of the two different sampling periods in the same closed-loop system (P: pseudo period of $cola$, K: sampling time of the command) has been integrated, where the correction is updated at each period P of $cola$ based on the amplitude attained in the previous period $(P-1)$ (see the section 2.2.3 for details of the control algorithm). Additionally, the command applied to the actuator is the correction of the amplitude for a given pseudo period multiplied by the $cola$ with a magnitude equal to 1, given by the following equation.

$$command(k) = ctrl(P) * cola(K)$$

Eq. 2-27

In Figure 2-10, the transparent green block uses the variable sampling period (P), whether the rest of the system is sampled with the period K. In addition, the estimated amplitude over the period P is the maximum absolute value (see section 2.2.2.1).

2.4.2 Simulation scenario

The parameters are taken in such a way that results would correspond to a real-world problem. The vibrational mode is fixed at 10 Hz, which is similar to the first satellite mode, therefore, the simulation starts at 5 Hz and ends at 20 Hz, to analyze the behavior only in the neighborhood of this spacecraft mode. The amplitude has been fixed to the unity (1 g) and the sampling frequency k of the system is fixed to 1.6 k Hz.

2.4.3 Result analysis

In the figures below, we can see the effect of the damping ratio (Figure 2-11), sweep speed (Figure 2-13) and compression factor (Figure 2-12) in the output acceleration (See section 3.3 for the details of the dynamic of the satellite).

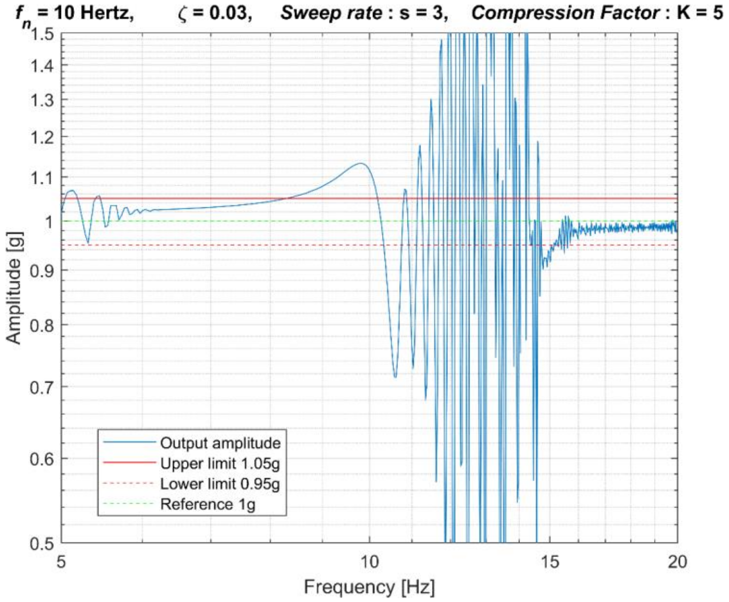

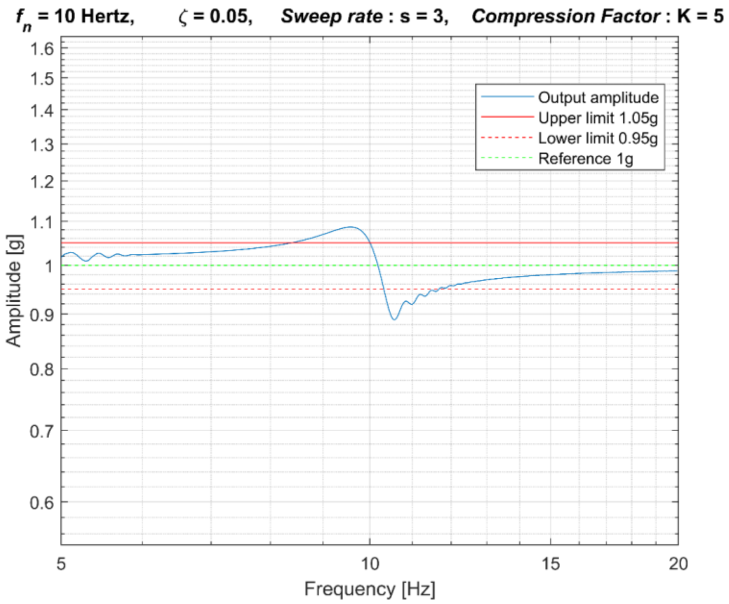

Figure 2-11 - Influence of the damping ratio of the satellite on the tracking performance

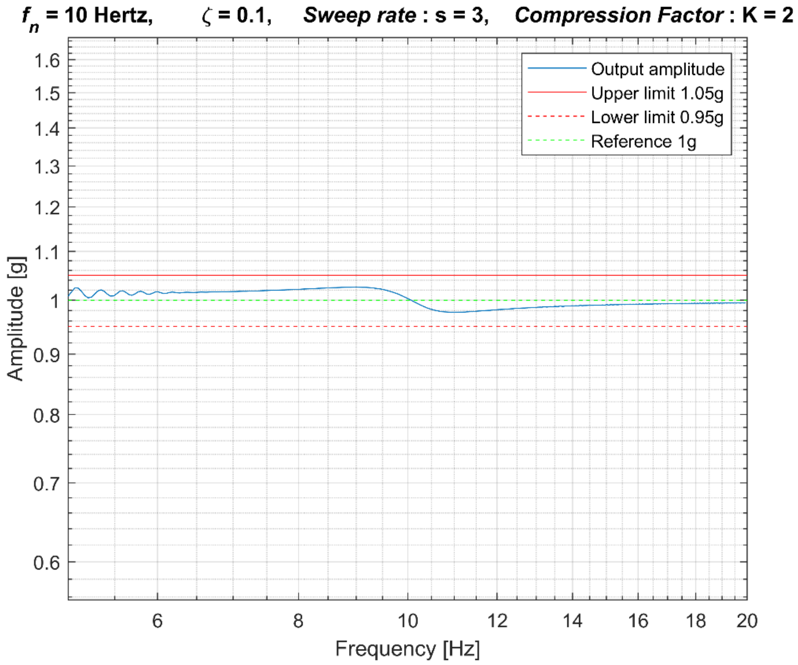

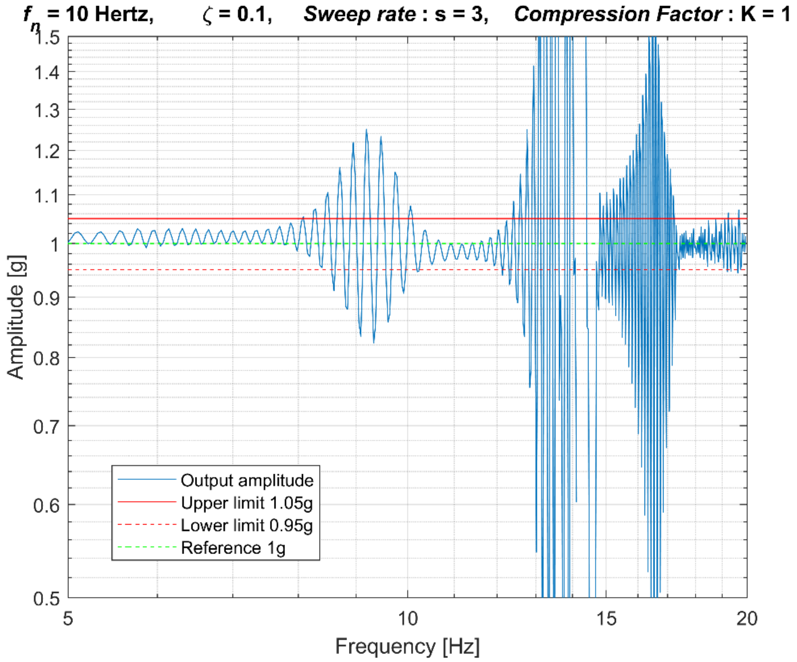

Figure 2-12 - Influence of the compression factor of the satellite on the tracking performance

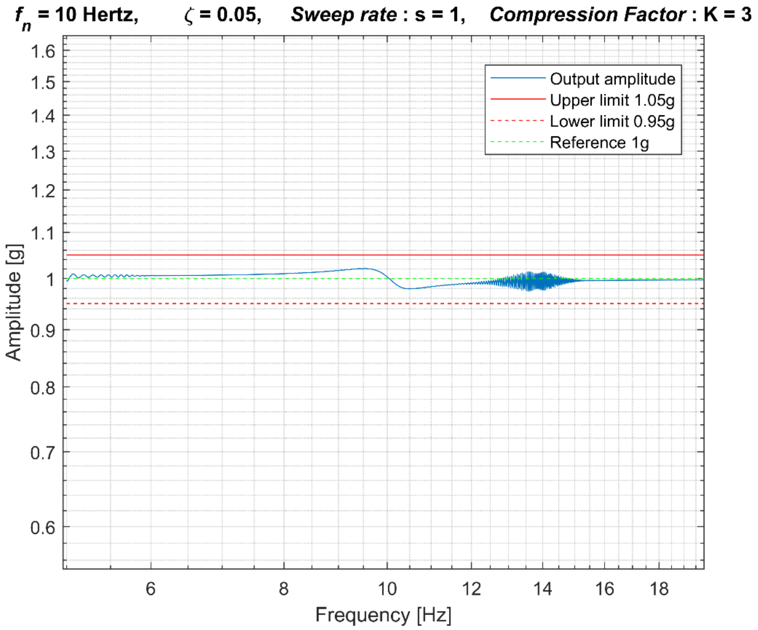

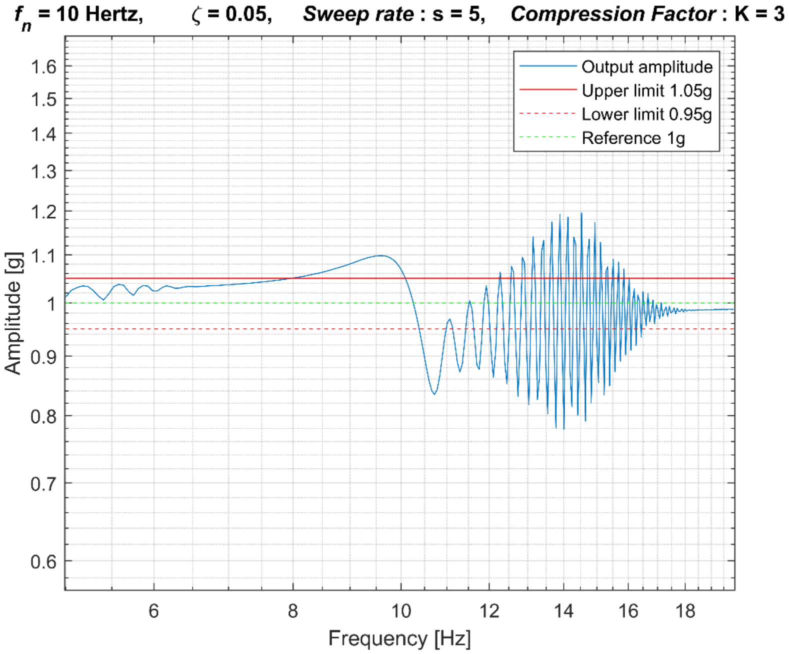

Figure 2-13 - Influence of the sweep rate of the satellite on the tracking performance

The simulations show that the control only gives satisfactory results for a sufficiently damped system, in this case, when the damping ratio is greater than 0.1 and for a carefully chosen compression factor (generally between 3 and 5). Otherwise, the results are acceptable only if the sweep speed is chosen below 3 octaves per minute (for example, 1 octave per minute). On the other hand, such sweep speed is obviously not acceptable in the case of satellite tests because of the risk of structural fatigue, as the lower speed indicates the longer period of vibration while sweeping through the mode frequency (Girad & Roy, 2012). With a speed of 3 octaves per minute, no result is satisfactory, furthermore, all the stable responses show significant overshoots and beats. Those less degraded results are obtained with a compression factor between 7 and 20.

In conclusion, the closed loop system stays permanently in the transient state as the frequency of the $cola$ changes, therefore, the transient behavior dominates the performance of the closed-loop system. Hence, the analysis focuses on the dynamical error of the closed-loop system rather than the steady-state error, commonly used in the classical control system analysis (Arefin, 2021). In addition, the lightly damped mode causes the system to oscillate more, moreover, combined with a higher sweep rate which brings system to stay more on transient state because of the rapid shift of the $cola$ frequency, bring strong overshoot and beatings. Lastly, as there is no analytical way to evaluate the stability of the nonlinear control law, the arbitrary chosen value of the compression factor can further degrade the performance.

2.4.4 Limitations of the study simulator

The results are very severe compared to a real-world test (see the Figure 1-3). Due to the fact that the LMS system lets the user select different compression factors for different frequency ranges during the test, this increases the performance. Choosing a smaller compression factor for a better correction when the frequency of tracking is far from mode frequencies and increasing the compression factor just after the mode frequency limits the overshoot of the system in a real vibration testing campaign (Bettacchioli, 2014b). This feature is not present in the study simulator, making the difference in terms of performance. Furthermore, the LMS user interface allows users to reduce the amplitude of the $cola$ (see the Figure 1-3) at higher frequencies, in order to limit the beating and overshoot, which is absent in the study simulator.

However, in order not to unnecessarily complicate the simulator, it is limited to control a single channel, avoiding any notching, causing less nonlinearities in the closed-loop system. In addition, the simulation doesn't show the effect of the modal parameter variations of the plant model and the sensor noises are absent as well.

2.5 CONCLUSION

This chapter gives a detail of the current vibration testing architecture, the functional explanation of the current control system as well as the vibration testing campaign. The issues of the current system are detailed via an example of a typical vibration test of a commercial satellite. Later in the chapter, a simplified study simulator has been developed and the simulation results have been used to analyze the influence of different parameters of the current system. The performance of the current nonlinear control algorithm is limited when the satellite contains very lightly damped modes, higher sweep rate. Both of these terms are linked to rapid change of the gain of the system and the incapacity of the controller to respond faster to compensate error. Moreover, rapidity can be obtained by decreasing the compression factor, but it may completely loose the stability performance. There is no stability assessment to determine the limit of the compression factor during the vibration test. Therefore, the next chapter is dedicated to find a new approach of control to overcome those limitations…

3 FEASIBILITY STUDY ON A SINGLE DEGREE OF FREEDOM SYSTEM

3.1 INTRODUCTION

The current chapter presents the state of art of the Vibration Testing System (VTS) issues and different perspectives of existent control strategies. The research has been conducted focusing on active vibration control (AVC) and robust control strategies, as well as literature on the application of robust control strategies on AVC problems. Different strategies exhibit promising features and also show considerable drawbacks. Therefore, the motivation of the research goes to the elaboration of a control strategy demonstrating the potential of satisfying superior performance criterion of VTS, at the same time, lowering the design complexity for further implementation in an industrial environment. The first part of this chapter includes the literature review, followed by a feasibility study. A simple Single Degree of Freedom plant model is considered to demonstrate the obtainable performances compared to the existing VTS control algorithm via time domain and frequency domain simulations. The main objective of this part of the research is to start with a simplified case to illustrate feasible performance via appropriate control algorithms, which will be used for further improvement for application to a real case of VTS.

3.2 LITERATURE REVIEW

The vibration testing system presents some unique features in the domain of automatic control system and vibration control system. In contrast to the VTS, vibration control of structures containing lightly damped modes, such as satellites, planes, bridges/buildings, focuses mainly on the regulation problem where the system has to compensate noises and disturbances with a constant reference signal (Genta, 2009) (Shahravi & Azimi, 2014) (Seto & Preumont, 2008) (Le Ballois, 1994). In most cases, a simple low-pass filter which reduces the gain of vibrational modes, can satisfy the specification of a regulation problem by the suppression of gain of vibrational modes (Gagne, et al., 1995) (Miljković, 2009). The literature of robotics and agile satellites also mentions a tracking problem via prefiltering the reference signal to avoid exciting vibrational modes (Doherty & Tolson, 2013) (Newman, 2020) (Jatunitanon, et al., 2009). However, this strategy comes with the cost of slowing down the reference by cutting of several frequency components by selective pass band filters, which can be realized on a VTS (Pai & Sinha, 2011). In the case of a VTS, the system tracks the $cola$ signal and the system gets highly excited when the reference passes through the satellite’s vibrational modes and also during the change of reference amplitude (Bettacchioli & Nali, 2015). Consequently, the low pass filtering with a lower corner frequency (lower than the frequencies of the modes), can no longer satisfy the tracking performance as the system needs a very high bandwidth controller for high-frequency tracking. Another uniqueness of the research study is to deal with very specific types of tracking error found in the VTS of a large structure spacecraft. The frequency of the reference $cola$ changes constantly and the system never reaches steady-state compared to any other classical control problems (Nali & Bettacchioli, 2014a). Therefore, the constant change of frequency keeps the system permanently in a transient regime. So in this study, the control problem deals with a dynamic tracking error issue (Bettacchioli & Nali, 2015).

The current control method can be considered as part of the Sliding Mode Control (SMC) , including an amplitude estimator (see section 2.2), which slides on the surface of the error signal via two nonlinear control laws (Eq. 2-23) (PLM Software, 2015) (Liu & Wang, 2011). Firstly, we may notice that the command is updated at each variable period of the $cola$ starting from 5 to 100 Hz, which is considerably very low compared to 12 kHz sampling frequency of the system. Consequently, the correction frequency is quite low and the lightly-damped modes introduce a significant gain variation in a very small period of time during the tracking, where this slower control response is inadequate to compensate the tracking error. Especially when the frequency of $cola$ shifts towards higher frequencies, this slow controller will exhibit bad performances as shifting towards the direction of higher frequency modes needs faster control response compared to the first mode. Secondly, the controller slides through the surface of the error greater than one and smaller than or equal to one (the error is basically the ratio between the reference and estimated amplitude) (Bettacchioli, 2014b), as the two nonlinear control laws contain the error along with a weight to tune the rapidity of the controller (complexity of the control law is considered as first-order, therefore no derivative of the error is used in the control law (Bandyopadhyay, et al., 2009), the command to the actuator generated by these control laws are non-smooth due to the non-linearity of the control laws, therefore the output accelerations are not smooth at all. This non-smoothness phenomenon is well known in the domain of SMC, called the chattering problem, and increases the noises in higher frequencies when the control law covers varied ranges of frequencies with a single controller (Bartolini, et al., 2008) (Lee & Utkin, 2006). Literature on sliding mode control shows a very prominent performance of SMC of a system with varying parameters and tracking of periodic signal (Reinfrank, et al., 1993) (Sabanovic, et al., 1999), such as the lower order SMC based linearized feedback loop or low pass filtering (Liu & Wang, 2011) (Kacprzyk, 2019). As being a part of nonlinear control, all those methods exhibit a certain level of non-smooth behavior while generating the command (Lee & Utkin, 2006). Notably, in the case of VTS, the chattering phenomenon introduces non-smoothness in higher frequencies, which contributes to the oscillations (see Figure 1-3), therefore the tracking performance in higher frequencies is degraded at such level that it no more follows the reference. Some advanced strategies such as higher-order SMC based on LMI (Bandyopadhyay, et al., 2009), backstepping control (Bartolini, et al., 2008), adaptive control (Kacprzyk, 2019) show a very significant reduction of chattering phenomena using higher-order controller and a higher-order estimator (Liu & Wang, 2011) for very fast parameter varying systems, which induces a significant amount of computing complexity. Consequently, it becomes challenging to implement such methods in a real-time very fast systems (Hernández, et al., 2014). Moreover, the non-smoothness of command introduced by the control algorithm can be severe to the well-functioning of the actuator (Lee & Utkin, 2006). In addition, due to the lack of the proper stability assessment of the controlled system, such algorithms would always need the four-stage VTS procedure (see section 2.2.5). In regards to those above issues, the focus of the research goes to other types of control algorithms, which will be explained in the following paragraphs.

In the domain of vibration control, mainly two strategies can be found in the literature (Seto & Preumont, 2008). The first one is the passive vibration control or vibration suppression problem, where the vibration is reduced from the system by adding materials to increase the damping ratio of the system (Preumont, 2018). This system does not come with any actuation, which therefore explains the name, passive control, based on the intrinsic property of the constituent materials. On the other hand, in the active vibration control (AVC), an actuator actively rejects or attenuates the vibration, with a closed-loop system architecture (Genta, 2009). There is a third type of system, named hybrid vibration control, where the system is conceived with both active and passive vibration control strategies (Genta, 2009). In the classical mechanics, the active vibration control strategies are based on mainly the root locus methods, where the desired behavior of the closed-loop system is converted in terms of the increase of the damping ratio, which would result in reduction of total vibration in the system. The control laws are visually determined from the root locus diagram (Preumont, 2018).

In the AVC, the control systems are categorized into two different architectures based on the position of the sensors and actuators (Shahravi & Azimi, 2014). Firstly, the collocated systems, where the sensors and actuators are attached to the same degree of freedom, not sufficient to be attached to the same location (Balas & Doyle, 1990). Additionally, they must also be dual, meaning the product between actuator and control signal represent energy exchange between the structure and the control system (Seto & Preumont, 2008). On the other hand, the non-collocated system stands for the system with right half plane zeros but it does not cause any trouble to control engineers as these zeros lie well outside of the desired bandwidth (Seto & Preumont, 2008). Therefore, the collocated systems can result in higher bandwidth-controlled system by reducing each vibration mode influence in the system, whether the non-collocated systems reduce the system vibration in general, without being precise to each mode, and result in a lower bandwidth-controlled system which is less precise than its counterpart (Preumont, 2018). In the literature of structural mechanics, most of the active vibration damping strategies depend on increasing the negative real part of the system poles. Those are called low authority control (LAC) as those strategies use very little control effort (Aubrun & Margulies, 1982) (Seto & Preumont, 2008). On the other hand, the high authority control (HAC), where the system does not impose any limitation on control effort, depends on relocating closed-loop poles of the system (Preumont, 2018). One of such method is the lead control (LC) where active damping of the system is carried out by the phase-lead controller. In this strategy, we can only consider a very limited range of frequencies of the system dynamics, for example, a single vibrational mode. In order to solve this issue, a developed version of the strategy called direct velocity feedback (DVF) considers a control algorithm which allows a wider range of the frequency of system dynamics (Fuller, et al., 1997). Although this method does not consider the number of poles of the system's dynamics, resulting more often in an improper closed-loop system (Seto & Preumont, 2008). Therefore, an evolved version of the DVF can be found in the literature, called positive position feedback (PPF) where the control structure allows the closed-loop dynamics to have the number of poles superior to zeros (Moon, et al., 2017). Though most of the mechanical systems with several lightly damped modes include alternating poles and zeros, where all above strategies cannot be used (Seto & Preumont, 2008). Integral force feedback gives the perspective for such problem (Fleming & Yik, 2014), although the system containing several modes cannot be controlled precisely by this type of control algorithm as it emphasizes a single-mode and a tradeoff has to be done for all other modes (Preumont, 2018). According to the definition, the VTS can be considered as a non-collocated hybrid system as the control system contains an electromagnetic actuator without any regard to the position of vibrational mode coordinates and having an AVC structure with a passive vibration isolation strategy to protect the building from its vibration (refer to the section 2.1). All above mechanical mode control strategies solve regulation problems without mentioning any further possibilities to extend to the multimode tracking problem. Moreover, those methods do not accommodate the possibilities to a parameter varying system. When it comes to the implementability and user-friendliness, those methods need profound knowledge of control engineering and perfect knowledge of system dynamics, whereas in VTS system, we may not dispose of those options, making classic mechanical control system quite challenging to implement in the VTS.

Apart from these previous approaches, let consider some general aspects of vibration control found in the literature that should be regarded in the control synthesis. Firstly, the spillover problem has been hugely addressed in the literature, which is basically the consequence of designing a controller based on a reduced-order plant in order to limit the computational complexity (Liu & He, 2019). Therefore, the higher and lower frequency neglected plant dynamics that are not taken into account during the control synthesis may affect the closed-loop behavior as well as the closed-loop systems performance (Genta, 2009). Especially the degradations are observed in the neighborhood of the fastest and the latest frequency of the VTS. The classical methods rarely address this issue (Seto & Preumont, 2008) and the SMC may give the perspective of this issue while degrading the performance and also at the cost of non-linearity on the actuator command (Nonami & Ito, 1997). Secondly, we may refer to the crosstalk issue of a mechanical system can be found in the literature (Holterman & Vries, 2001) (Bettacchioli & Nali, 2015) (Seto & Preumont, 2008). The crosstalk stands for the case where the vibrational modes communicate each other as well as the cross-axis excitation issues in the closed-loop system (Habtour, et al., 2017) (Nelson & O'Malley, 2014). More often in mechanical systems, when the vibration mode frequencies are very close to each other, the adjacent mode can participate into the excitation of the system while controlling a separate mode (Preumont, 2018). In a multi-variable system, the control synthesis considers one input-output channel at a time to avoid the complexity of a multivariable system (Jain & Alleyne, 2009). While evaluating the time domain and frequency domain performances in a closed-loop multivariable plant with mono-variable separate controllers, a single axis controller of a given axis excites the vibrational mode of another axis as they are not linked together (Zenga, 2005). The time-domain analysis gives the degraded performance of such system and the analysis consists of determining whether the performance can be accepted or not.

While considering all those factors, state-space feedback controls are hugely used as advanced strategies in the literature of AVC (Seto & Preumont, 2008). Most of the literature use optimal control strategies such as linear quadratic control (LQR) as a standard procedure to design a controller (Gabbert, et al., 2006) (Zhang, et al., 2008). The performance of a LQ controller is far superior than all above-mentioned strategies for a well-known system dynamic (Preumont, 2018). Main drawback of this type of controller is the necessity of measuring all states of the plant, which may not be possible in an industrial system (Xue, et al., 2007). In this case, we may compute an optimal Kalman estimator in order to estimate the missing states and an optimal LQ controller separately, although the separation principal states the optimality of combined estimator-controller system called Linear Quadratic Gaussian (LQG) controller (Green & Limebeer, 2012) (Tewari, 2002). We may refer to the literature of AVC, where the use of a LQG controller has been well demonstrated with superior performances than any classical methods (Preumont, 2018). Nevertheless, the synthesis procedure of LQ and LGQ controllers needs to specify weight, in addition to covariance matrices. In general, they are determined arbitrarily without any way to specify the performance criteria (Xia & Mahmoud, 2012). In order to obtain the necessary performance criteria, the tuning of those matrices as well as the time domain verification has to be considered and the procedure continues until the required performance has been achieved (Seto & Preumont, 2008). In (Barrera-Cardenas & Molinas, 2012) (Yasuo, et al., 2018), the reiteration and verification procedure has been done automatically via an algorithm where the synthesis initiates from random weights and then the time domain simulation is used to achieve the performance criteria and again the reiteration procedure starts by changing the weights until the required performance has been achieved. Yet it is quite challenging to process an industrial-grade system via this procedure as the plant dynamics would be very complex, which will lead to consequent time delay, therefore the increase of cost (Leguiller, 2015). Therefore, the suitable optimal control algorithm must be capable of introducing different performance criteria for user-friendliness.

The development of the H_∞ norm-based sub-optimal controllers are widely introduced in industrial systems for the possibility of directly introducing the performance measures via the controller synthesis (Lundstrøm, et al., 1991). In the literature of structural control as well as optimal control (Preumont, 2018) (Seto & Preumont, 2008) (Alazard, et al., 1999), the different H_∞ controllers are not commonly used as LQG because of the comprehension of mathematical complexities among engineers without the knowledge of advanced control systems background (wikipedia Hinfinity, n.d.) of such control, though a few research works show very prominent result of H_∞ control (Khan & Khot, 2015) (Tliba & Abou-Kandil, 2003) (Alazard, et al., 2003). From an industrial point of view where the plant dynamics fall into a similar criterion for different product families and performance requirements are similar for all products, we may investigate a model-based H_∞ control for the whole product family. Once the architecture has been fixed, an automated tool can overcome the complexity, so that engineers with a very little knowledge of control engineering may follow the procedure and obtain necessary analysis. This is the case of the VTS, where most of the satellite dynamics (in terms of the modal parameters) fall into a similar range and the requirements stay similar for all product ranges. The intrinsic robustness properties is the main advantage of H_∞ control methods versus the LQG control for a given industrial environment (Zhou, et al., 1996) (Xing & Bainum, 2012). In addition, a research work at Thales Alenia Space already demonstrates the superior performance of using optimal control algorithms such as LQR and LQG control for a nominal identified satellite model (Leguiller, 2015). Yet, difficulties of selecting the covariance matrices of model and measurement noises as stated in the previous paragraphs have been observed in the control design and the procedure starts with arbitrary matrices and a lot of iteration in time domain analysis is needed to tune the controller in order to achieve the desired performance (Bettacchioli, 2018). By definition, LQG control is a particular case of the H_2 control, where H_2 optimal norm is one of the solutions of H_∞ optimization (Skogestad & Postlethwaite, 2001). Therefore, both solutions may often bring similar performances. Though, the small gain theorem (Zhou, et al., 1996) gives an advantage to H_∞ norm, which leads to a result superior in terms of performance as well as robustness (Skogestad & Postlethwaite, 2001). Furthermore, we may include the spillover problem as neglected dynamics through the additive uncertainty in the procedure of obtaining H_∞ control (Aström & Murray, 2009). While considering the crosstalk issue, the SISO synthesis of the H_∞ control can easily be extended to MIMO synthesis while keeping the SISO performance criteria via frequency-domain constraints.

Having in mind the drawback of above-mentioned control strategies, the focus of the research work goes to the H_∞ control. The main motivation for that goes to the industrial level implementability, the superior performance, robustness features, spillover solution, MIMO synthesis capability and also the intrinsic robustness property of the H_∞ control. In the literature, the H_∞ optimization problems are solved via different methods and the selection among those methods depends on the type and the requirement of the system (Skogestad & Postlethwaite, 2001) (Apkarian, 1993).

The symbol "H_∞" stands for hardy space (space of analytical functions on the unity disk of $\mathbb{D}$ of the complex plane (Ross & Cima, 2000)) of a complex variable limited in open right half complex plane (Skogestad & Postlethwaite, 2001) (Bartoszewicz, 2011). The H_∞ norm is the largest singular value of the transfer matrix of a LTI plant (Mahmoud & Xia, 2012). Therefore, H_∞ optimal control theory is based on several decades of developments of a generalized control problem against the worst-case scenario derived by unknown additive disturbances, noise filtering, tracking issues (Skogestad & Postlethwaite, 2001). The first development of a design problem using the H_∞ norm was done by George Zames by solving an optimization problem (Zames, 1981). At the early stages of the development of this theory, problems have been introduced in frequency domain and the synthesis procedure used the approximation theory (simplification of the complexity of a function (Achiezer, 1956)), spectral factorization (Masani & Wiener, 1957), (Youla, et al., 1976) resulting in a very complicated high dimensional near optimal controller (Doyle, et al., 1990). The follow up major research of the domain was finding of a link between the time domain characterization of those controllers and the Riccati equation, leading to a general formulation for time varying plant in the finite horizon (Zhou, et al., 1996). The development concerns dynamic differential game theory of a min-max optimal problem where the controller is considered to be minimized with regards to disturbances considered as the maximizing factor (Bartoszewicz, 2011). When it comes to the application of H_∞ controller of an AVC problem, one of the first application can be found in (Le Ballois, 1994), where the Glover and McFarlane synthesis approach has been applied to the attitude control of a satellite with flexible modes (Glover, et al., 1990). The main focus of this research is to satisfy the highest performance and robust stability without introducing structured uncertainties. This approach introduces pre and post compensator in the open-loop to shape the required constraints and then solving the optimization problem to obtain H_∞ controller, therefore it is known as loop-shaping synthesis (Apkarian, 1993). The main advantage of the loop-shaping synthesis is the desensitization of the controller without defining the structured uncertainties. It leads to achieve a further robust controller against the flexible appendices (Le Ballois, 1994). However, this method seems complicated and less user friendly for an industrial usage and the attitude control problem is just a regulation problem without the tracking options (Giuliano, 2019) (Le Ballois, 1994). A further development of a H_∞ synthesis of fixed structure controllers using non-smooth optimization has been discussed in the literature (Apkarian, et al., 2005), where the structure of the controller is imposed depending on the computing capacity of the computer. This strategy might seem interesting as the synthesized controller is already in an implementable structure without any order reduction. Although the limitation of the non-smooth optimization is that the user must know the right form control structure adapted to the optimization problem to solve, otherwise it would compute a non-zero value for the prefixed given structure of the controller creating pole-zero compensation problem (Gahinet & Apkarian, 2011). Therefore, this non-zero values may induce the unnecessary pole-zero compensation issue resulting very often in numerical instabilities. As the fixed structure is considered as a constraint for optimization, different fixed structures can give different optimization solutions for similar performance criteria. A loop can be introduced to start the design from a small structure and incrementally increase the controller order for a better solution of the optimization, which may lead to enormous computing delay. This method may be very useful for simple systems without vibrational modes where an optimal PID structure may satisfy all requirements, but for complex systems like VTS, above mentioned fixed structure constraint may impose issues to solve the optimization problem of other performance constraints. In that case, it is necessary to know the controller structure or an iteration can be used to start the synthesis from a minimum order to increase the complexity until the correct structure is found.

A major work at Caltech and NASA has been done in the domain of AVC, where an H_∞ based mixed sensitivity has been applied for an identified plant dynamic to a disturbance and noise reduction problem (Balas, 1990). In (Preumont, 2018) (Alazard, et al., 1999), several case studies show optimal performance of an H_∞ mixed sensitivity synthesis of typical regulation problem. The mixed sensitivity method seems to generalize the regulation problem and the tracking problem through the definition of generalized frequency domain constraints (Skogestad & Postlethwaite, 2001). Moreover, we may extend the SISO constraints to a MIMO structure to above-mentioned AVC related issues with the typical robustness features of an H_∞ control. Due to these prominent features, the development of the research focuses on the mixed sensitivity H_∞ control.

3.3 SIMPLIFIED STUDY MODEL

As a first step, a S-DoF second-degree dynamics is considered below to characterize the satellite-actuator-interface model where the single vibration mode corresponds to the first mode of a typical geostationary satellite with modal parameters such as the mode frequency and damping ratio. Though, this model does not come with any information about the configuration of real satellite such as the mass and inertia, but only with modal parameters, which is sufficient for the study of vibration control problem. This simplified model has been selected to keep the complexity as low as possible to determine the feasibility of the control structures for controlling oscillations while reducing the tracking error. Therefore, the absence of the actuator and interface dynamics does not reduce the conclusions of this study as corresponding modes of those equipment are out of the studied frequency range (5 to 100 Hz) of the VTS.

Figure 3-1 shows the damped S-DoF spring-mass system corresponding the satellite fixed on the vibrator. The object of mass m represents the satellite linked to spring (k stiffness) and damper (c damping constant) attached to a base, where the excitations will be applied. This system can be commanded by either an input force F_0 or acceleration $\ddot{x}_0$ at the base where x_0 is the base position. The output of the system is either the acceleration $\ddot{x}$ (where x is the position of mass) or force F. In the case of VTS, system is commanded by acceleration $\ddot{x}_0$, therefore $F_0 = F = 0$.

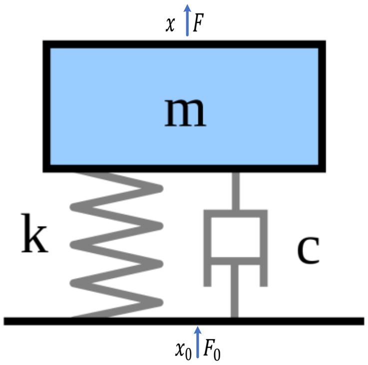

Figure 3-1- S-DoF spring-mass system

The dynamic equation of this spring-mass system is derived from the Newton equation of law:

$$m\ddot{x} + c(\dot{x} - x_0) + k(x - x_0) = 0 \qquad \textit{Eq. 3-1}$$

Eq. 3-1 is written in the Galilean referential linked to the ground, where x_0 and x correspond to the position where the excitation is applied and the position of the mass.

Eq. 3-1 can be written as follows:

$$m\ddot{x} + c\dot{x} + kx = c\dot{x}_0 + kx_0 \qquad \textit{Eq. 3-2}$$

The change of variable in Eq. 3-2 let us write the following form:

$$\ddot{x} + 2\frac{c}{2\sqrt{mk}}\sqrt{\frac{k}{m}}\dot{x} + \left(\sqrt{\frac{k}{m}}\right)^2 x = 2\frac{c}{2\sqrt{mk}}\sqrt{\frac{k}{m}}\dot{x}_0 + \left(\sqrt{\frac{k}{m}}\right)^2 x_0 \qquad \textit{Eq. 3-3}$$

By the following change of variable to $\frac{c}{2\sqrt{mk}} = \zeta$ et $\sqrt{\frac{k}{m}} = \Omega_n$, we find the differential equation of the S-Dof system:

$$\ddot{x} + 2\zeta\Omega_n\dot{x} + {\Omega_n}^2 x = 2\zeta\Omega_n\dot{x}_0 + {\Omega_n}^2 x_0 \qquad \textit{Eq. 3-4}$$

In Eq. 3-4, Ω_n and ζ represent respectively the modal angular frequency in rad/sec and the modal damping of the system. Laplace transform of the Eq. 3-4 gives us the following form. By rearranging terms of both sides, we find the transfer function:

$$\frac{\ddot{X}(s)}{\ddot{X}_0(s)} = \frac{2\zeta\Omega_n s + {\Omega_n}^2}{s^2 + 2\zeta\Omega_n s + {\Omega_n}^2} \qquad \textit{Eq. 3-5}$$

where is s the Laplace variable.

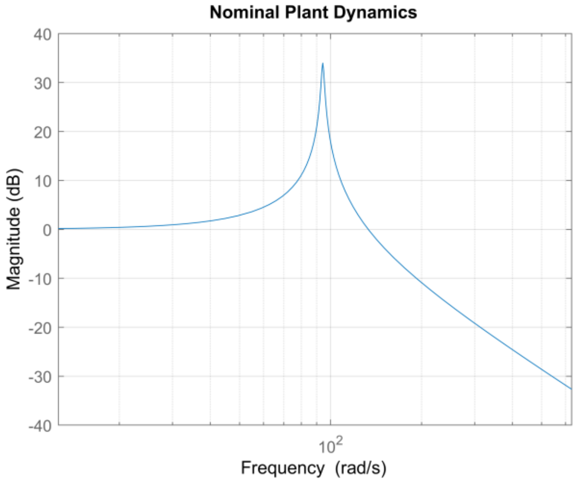

Figure 3-2 - S-Dof model representing the first mode of a satellite

The frequency response of the dynamics is defined from the Eq. 3-5 with the mode frequency at $15\,Hz$ ($\cong 94.25\,rad/sec$) and the corresponding damping $\zeta = 1\%$ is depicted in Figure 3-2. The dynamic response of the model illustrates a single mode corresponding to the first mode of the satellite, therefore the model does not contain any anti-resonance. The main objective of this preliminary study is the feasibility of sine sweep acceleration tracking via H_∞ control, while the reference signal passes through mode frequency. For this purpose, the study concerns the frequency interval of 5 to 20 Hz, generally the mode and the neighborhood frequencies.

3.4 REFORMULATION OF THE CLOSED-LOOP SYSTEM

The current control scheme of the Figure 2-3 is based on a nonlinear control algorithm where the architecture cannot accommodate the standard control loop of any existent optimal control strategies. Therefore, two parts of the reference signal (amplitude and the unitary periodic signal) need to be combined within a unique signal. Figure 3-3 shows the reformulated control loop and the first benefit of this structure is the use of very high sampling period (which can be selected from 6.4 kHz to 12.8 kHz) of the computed command compared to the variable sampling period of the nonlinear control (which varies from 5 Hz to 100 Hz), generating command after each pseudo period of the $cola$. Consequently, the bandwidth of the control can be increased significantly to reduce the tracking error. In addition, the new control architecture does not use the estimator as the input and measured output of the system are both pseudo-periodic acceleration signals (consequently reducing computing complexity) and it will reduce a significant amount of noise in the system (due to current estimation strategies, see the section 2.2.2), resulting in a superior performance. Secondly, the stability margin could be determined by using different methods applied on a LTI system.

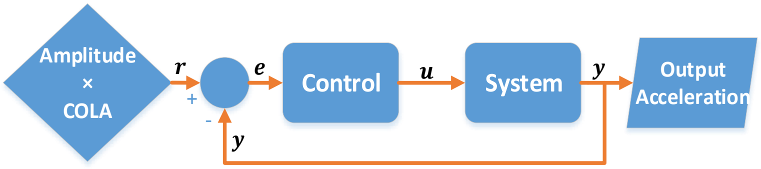

Figure 3-3 - New closed-loop system of the VTS

The reference of the system r is an acceleration and the standardized unity is expressed by g. The control block uses the acceleration error e and outputs the control effort u as an acceleration, then the output acceleration is given by y. The system block contains combined dynamics of the actuator, satellite and the interface, it will be denoted as plant. To be noted that even the simplified system has only one output, though the plant model is taken as the worst-case among all sensor outputs of the real VTS system (see section 2.2.3).

3.4.1 Generalities of mixed sensitivity H_∞ control design

The main advantage of the mixed sensitivity-based design is the generalization of the tracking issue with the regulation issues such as the noise and perturbation compensation as well as the stability criterion via appropriate frequency domain constraints (Skogestad & Postlethwaite, 2001). Those constraints can be directly formulated from industrial specifications and the whole synthesis and analysis procedure can be reproduced for all satellite product lines, which will ease the use of such analysis. Therefore, engineers with a little knowledge of control systems would be able to follow the procedure with proper user manual. The following part will explain the general procedure of mixed sensitivity-based synthesis and then the feasibility study on the study case.

3.4.2 $\boldsymbol{H}_\infty$ control synthesis

Consider the closed-loop SISO feedback structure of Figure 3-4, where signals denoted by $r(t)$, $y(t)$, $e(t)$, $u(t)$, $w_i(t)$, $w_0(t)$, $n(t)$ respectively correspond to the reference acceleration, output acceleration, tracking error, command generated by the control algorithm, plant input disturbance, plant output disturbance and measurement noise.

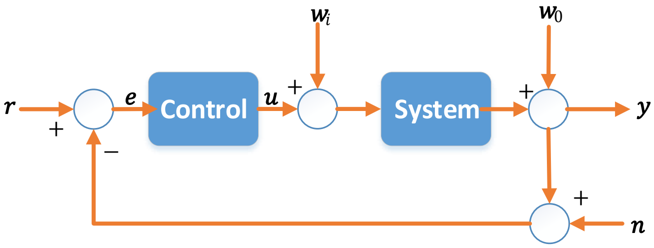

Figure 3-4 - Feedback tracking control scheme with noise and disturbance

3.4.2.1 Sensitivity analysis

As denomination states, mixed sensitivity-based synthesis is based on the implication of different sensitivity functions of a closed-loop system in terms of performance criteria (Zhou, et al., 1996). From Figure 3-4, we can derive different closed-loop transfer functions from different inputs to output y:

$$\begin{aligned} Y(s) = {} & \big(1 + G(s)K(s)\big)^{-1} W_0(s) + \big(1 + G(s)K(s)\big)^{-1} G(s)W_i(s) \\ & + \big(1 + G(s)K(s)\big)^{-1} G(s)K(s)\big(R(s) - N(s)\big) \end{aligned} \qquad \text{Eq. 3-6}$$

The transfer function from different inputs to control error e:

$$E(s) = \big(1 + G(s)K(s)\big)^{-1}\big(R(s) - N(s) - W_0(s)\big) + \big(1 + G(s)K(s)\big)^{-1}G(s)W_i(s) \qquad \textit{Eq. 3-7}$$

The transfer function from different inputs to command u:

$$U(s) = (1 + K(s)G(s))^{-1}K(s)(R(s) - N(s) - W_0(s)) - (1 + K(s)G(s))^{-1}K(s)G(s)W_i(s) \qquad \textit{Eq. 3-8}$$

In Eq. 3-6, Eq. 3-7, Eq. 3-8, G(s) and K(s) denote the plant and controller transfer function respectively. Signals in the frequency domain are represented in capital letter $(E, Y, R, N, U, W_0, W_i)$, where small letters represent time domain signal $(e, y, r, n, u, w_0, w_i)$. The definition of principal sensitivity functions used in the mixed sensitivity synthesis can be obtained from Eq. 3-9 to Eq. 3-11.

The sensitivity function $S(s)$ represents the transfer function between the reference *r* and the error *e*, given by:

$$S(s) = \big(1 + G(s)K(s)\big)^{-1} \qquad \textit{Eq. 3-9}$$

The complementary sensitivity function $T(s)$, as its name says, is mainly the complement of the input sensitivity function, which represents the influence of the noise on the system error:

$$T(s) = 1 - S(s) = \big(1 + G(s)K(s)\big)^{-1}G(s)K(s) \qquad \textit{Eq. 3-10}$$

The sensitivity function on the command represents the energy of the control signal *u*:

$$K(s)S(s) = K(s)\big(1 + G(s)K(s)\big)^{-1} \qquad \textit{Eq. 3-11}$$

The main advantage of using these sensitivity functions is to impose constraints on them to shape the open-loop transfer function $G(s)K(s)$ (Apkarian, 1993) to satisfy the design criteria. According to the Eq. 3-10, $S(s) + T(s) = 1$ and the implication of this relation states that, generally it is not possible to satisfy constraint imposed on both S and T at same frequency (Skogestad & Postlethwaite, 2001). Therefore, it is mandatory to separate the bandwidth of the control from the noise filter. The bandwidth of the control which reduces the tracking error is at low frequencies and the noises are at high frequencies. Thus, it is possible to minimize tracking error and reject the sensor noise at the same time by constraining $S(s)$ at low frequency and $T(s)$ at high frequency (Duc & Font, 1999). In the reality, the good performance of the system depends on the quality of sensors which do not introduce any noise at low frequencies where we want to minimize the error.

3.4.2.2 Weight selection

Industrial specifications are taken into account by means of frequency-domain transfer functions, called weighting functions. These frequency domain specifications can be directly imposed on closed-loop sensitivity functions (S, KS and T). Though the success of the control design depends mostly on the appropriate choice of weighting functions, in order to satisfy the specifications mentioned in Section 3.5.1 (Dulau & Oltean, 2020). These weighting functions, denoted $w_1(s)\, w_2(s)\, and\, w_3(s)$ are represented in Figure 3-5.

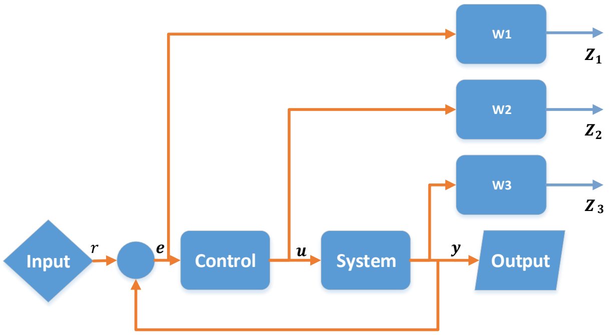

Figure 3-5 – Weighting functions definition for H∞ control synthesis

Figure 3-5 can be represented via a generalized scheme, with an augmented model containing plant and filter dynamics with a separate block containing the controller to be synthesized. In Figure 3-6, $P(s)$ is the augmented plant model, $K(s)$ is the controller to be synthesized, u is the command, e the error signal, r and $Z = [z_1\ z_2\ z_3]^T$ are the exogenous input and outputs.

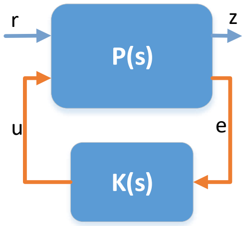

Figure 3-6 - Upper LFT of standard H∞ control

The augmented model $P(s)$ containing weights without the control block $K(s)$ illustrated in Figure 3-6, is given by:

$$\begin{bmatrix} Z(s) \\ E(s) \end{bmatrix} = P(s) \begin{bmatrix} R(s) \\ U(s) \end{bmatrix} = \begin{bmatrix} P_{11}(s) & P_{12}(s) \\ P_{21}(s) & P_{22}(s) \end{bmatrix} \begin{bmatrix} R(s) \\ U(s) \end{bmatrix}$$

Eq. 3-12

In Eq. 3-12, $P(s)$ corresponds to:

$$P = \left[\begin{array}{cc} w_1 & -w_1 G \\ 0 & w_2 \\ 0 & w_3 G \\ \hline I & -G \end{array}\right]$$

The augmented plant is looped via the relation $u = K(s)e$ and the closed-loop transfer function between r to z is given by the linear fractional transformation (LFT) and denoted as $F(P, K)$. There are two possibilities to represent the problem, either by upper or lower LFT. Here, we keep the lower LFT as upper LFT is mostly used to represent the uncertainties (Apkarian, 1993).

$$F(P, K) = P_{11} + P_{12} K (I - P_{22})^{-1} P_{21}$$

Eq. 3-13

The computation of the H_∞ robust controller can be achieved by minimizing $\|F(P, K)\|_\infty$, over the set of all controllers $K(s)$ which stabilize the internal states of the system. The minimum gain is called H_∞ optimal gain expressed by γ_{opt}. This can be also realized in a sub-optimal way, that is, for $\gamma > 0$, find the controller that stabilizes the internal states of the system and satisfies $\|F(P,K)\|_{\infty} < \gamma$. As previously mentioned, the error signal can be minimized and the sensor noise rejected at the same time by constraining $S(s)$ at low frequencies and $T(s)$ at high frequencies, assuming that the sensors perform perfectly at low frequencies and will not introduce noise in the frequency band where the tracking error needs to be controlled. Therefore, the weighting functions w_i are determined to constraint $S(s)$, $T(s)$, $K(s)S(s)$. The relation between each sensitivity function and their corresponding frequency domain performance weights are given in the considering the maximum singular values of the sensitivity functions:

$$\begin{cases} \bar{\sigma}\big(S(s)w_1(s)\big) < \gamma \\ \bar{\sigma}\big(KS(s)w_2(s)\big) < \gamma \\ \bar{\sigma}\big(T(s)w_3(s)\big) < \gamma \end{cases} \qquad \textit{Eq. 3-14}$$

which a sufficient condition is:

$$\left\| \begin{matrix} w_1 S \\ w_2 KS \\ w_3 T \end{matrix} \right\|_{\infty} < \gamma \qquad \textit{Eq. 3-15}$$

The optimization problem can be solved via the resolution of Algebraic Ricatti Equation (ARE) or the linear matrix inequality (LMI) (Apkarian & Gahinet, 1994) (Doyle & Glover, 1988). Although those both options seem promising, ARE cannot handle any singular problem without adding extra dimension called “regularization”, where LMI does not introduce any regularization (Apkarian & Gahinet, 1994). In (Heuvel, 1997), a brief study can be found to compare these two methods. This study shows the higher complexity of LMI solutions compared to ARE method, resulting in an increase of computational time of synthesis, generally LMI performs two to six times slower than ARE optimizations. As both algorithms are based on finding an optimal γ via either the dichotomy (in the case of ARE) or the convex optimization (in the case of LMI), a tolerance is given to converge to suboptimal γ in both of these cases (Heuvel, 1997). Study also shows that the LMI can accept smaller tolerance than ARE method, thus the synthesis via LMI with smaller tolerance can result in better γ

than ARE. Moreover, the ARE solutions are numerically more stable than LMI in our study.

3.5 FEASIBILITY STUDY ON THE SIMPLIFIED MODEL

In this section, we will design the controller via the method explained in 3.4.2 on the simplified plant model of section 3.3.

3.5.1 Specifications of the closed-loop performance

Before proceeding to further development, we need to clarify the closed-loop systems requirement for the VTS. The tracking error must be in the range of $\pm 1\%$, which implies a total reduction of unexpected vibrations of the system, even at the neighborhood of lower and higher vibration modes. As explained in Figure 1-3, the reference amplitude has been manually lowered near the modes as well as at higher frequencies to reduce the vibration and overshoot of the system. Instead the new architecture shall assure the tracking performance with a constant reference without the need for any manual reduction. A frequency-domain analysis shall assure the internal and the input-output stability of the system within the studied frequency range (5 to 100 Hz). The electromagnetic actuator has a limit on acceleration, 75 g, the maximum frequency (at 0 dB) is 1700 Hz and the control effort shall not exceed this actuation limit. The closed-loop system shall reject the influence of the different noises in the system, especially those at high frequencies. Since the very large band functioning accelerometers would increase the cost, therefore the development shall focus on decreasing the noise filter bandwidth to have less expensive choice of accelerometers while keeping the required performance. Moreover, the controller has to be robust with respect to uncertainties of the system.

3.5.2 Synthesis problem formulation

As mentioned previously, one of the main advantages of mixed sensitivity based H_∞ controller is the generalization of optimization problems via frequency domain weights. At the same time, the success of synthesizing an H_∞ optimal control mostly depends on the choice of those appropriate weighting functions. In other words, the proper definition of frequency-domain constraints (Skogestad, 1991). The weight selection for a classical tracking problem defined by steady-state error, accepted overshoot and convergence time is very straightforward in the literature (Duc & Font, 1999) (Preumont, 2018). The difficulties occur in the weight selection, when the reference is a periodic signal and the convergence time needs to be very small so that the system tracks the periodic signal very rapidly. In this case, the performance must be verified by post-synthesis analysis via the time-domain simulations. In many papers (Balas, 1990) (Chaudhuri, et al., 2003), weighting functions are selected manually by understanding the specification of the closed-loop system or automatically via a systematic procedure. Moreover, some approaches in the literature explore a systematic way to achieve appropriate weight for a steady-state single-frequency periodic tracking controller (Shafai & Oloomi, 2003). However, those approaches are mostly suitable for some specific problems. In our study, the main difficulty of the VTS is that the reference signal is a pseudo-periodic signal with variable frequency. Therefore, the system would never reach steady state as the frequency changes constantly (Bettacchioli & Nali, 2015), so the classical weight definition of a tracking error formulation cannot be applied. This dynamic tracking error topic is rarely addressed in the literature (Bettacchioli & Nali, 2015), though the following section proposes a way to achieve the required performance through a manual choice of frequency domain weights. The weights mentioned here are the result of the best choices from combinations of different feasible solutions. Only the accepted set of constraints are given in the following section and the selection is made upon the performance measures as there is no possible way to quantify the dynamic tracking error. The chosen case of the plant dynamics is given by Figure 3-2, the mode frequency at 15 Hz represents the first mode of a typical geostationary commercial satellite and the mode damping is selected to be 1% corresponding to a worst-case scenario. In addition, the complexity of the controller depends on the complexity of the weights, therefore, it is necessary to keep the complexity of the augmented system (given by Figure 3-7) as small as possible. In this study, the S-DoF model contains only modal parameter information such as the mode frequency and damping. In the simplified dynamics, there is no information about the mass of the satellite, therefore, the study will limit to only the feasibility of vibration elimination and fine dynamic tracking. Though, the study of the next chapter will include constraint on the limitation of the actuator. $P(s)$ of Eq. 3-12 can be given by:

$$P = \begin{bmatrix} w_1 & -w_1 G \\ 0 & w_3 G \\ I & -G \end{bmatrix}$$

The augmented model of Figure 3-5 can be simplified to the following figure.

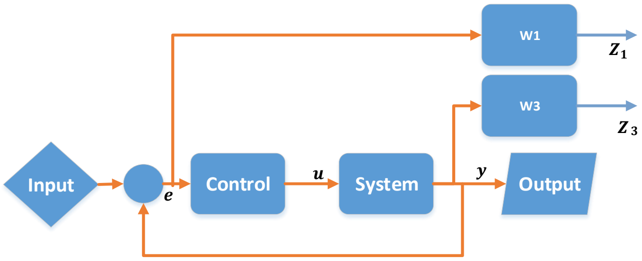

Figure 3-7 - Simplified augmented model with two weights

With the new definition of the exogenous output $Z = [z_1\ z_3]^T$ in Figure 3-7, without considering w_2. Moreover, the new simplified optimization criteria is:

$$\left\| \begin{matrix} w_1 S \\ w_3 T \end{matrix} \right\|_\infty < \gamma \qquad \textit{Eq. 3-16}$$

The detailed determination of the frequency weights is given below.

3.5.2.1 Dynamic tracking constraints

The tracking error is constrained via the weight $\frac{1}{w_1}$ (Apkarian, 1993). In the literature of robust tracking control, the tracking error is considered as a static error which tends to zero when the time tends to infinity. In addition, the response time, acceptable overshoot and the damping ratio of the control can be used to define the frequency domain constraint $\frac{1}{w_1}$. Therefore, the H_∞ controller satisfying the frequency domain constraint defined by $\frac{1}{w_1}$, will perfectly satisfy the time domain simulation in terms of error, response time and overshoot when the reference is a constant value. The exception can be found in the system with periodic reference tracking. In such system cannot be covered by only frequency domain verification as the error does not tend to zero when the time tends to infinity. Therefore, time domain verification is needed in addition to the frequency domain analysis to correlate the results assessing the tracking performance. In general, the periodic reference tracking controller must respond very fast compared to any static error compensation so that the closed-loop system remains steady to the periodic variation of the command. In addition to the periodicity of the reference, the $cola$'s frequency changes constantly. Therefore, the system stays in its transient state throughout the test. Note that the transient behavior becomes significant when taking into account the passage of mode frequencies, which introduces sudden but significant changes in terms of gain variation in the neighborhood of the modes. When the dynamics of the satellite contain lightly damped modes, it will further increase this gain variation. Therefore, the transient behavior of the closed-loop system gets even stronger. In order to address the varying frequency reference tracking issue via frequency domain weight, the bandwidth of the control has to be far superior than the tracking bandwidth, which signifies that the controller must respond very fast in the presence of tracking error. While varying the frequency of the reference, the lower frequencies need higher gain to keep the error below the specification. In fact, the periodic tracking can never tend to zero (Oloomi & Shafai, 2003) but the goal of the study is to keep under 1%. Therefore, the choice of weighting functions has to be verified in time domain simulation for performance satisfaction. The periodic tracking weight of mixed sensitivity H_∞ control can be chosen manually, though (Oloomi & Shafai, 2003) shows a systematic way to determine $\frac{1}{w_1}$ while tacking into account the acceptable error, maximize phase and gain margin. But this method cannot take into consideration the variable frequency tracking, furthermore, it can only be used for the specific plant dynamics and it cannot be taken as a generalized solution. Here we intend to evaluate the tracking error up to 20 Hz including the only mode at 15 Hz. Therefore, $\frac{1}{w_1}$ is chosen to constrain the magnitude near 20 Hz at approximately -20 dB (10% of the static tracking error), which satisfies the performance criteria of $\sim 1\%$ tracking error at 20 Hz (verified via time domain simulation). As mentioned earlier in this section, the tracking in lower frequencies will need high control gain, thus it seems appropriate to decrease the gain of $\frac{1}{w_1}$ towards the lower frequency direction. Therefore, the decreasing slope of the high pass filter $\frac{1}{w_1}$ contains the tracking error bandwidth, it reaches almost -31 dB at 5 Hz (which accounts for $\sim 3\%$ of static tracking error). Indeed, a magnitude of 3 to 10% of static error quantification through frequency domain weight results less than 1% of dynamic error in the system. By the definition of a slop of 6 dB/decade, covering the specific frequency interval (5 to 20 Hz) with specified error magnitude and a static gain magnitude of 1.4 (for better stability of the closed-loop system) results a frequency weight of bandwidth near 147 Hz. To summarize, a very fast response is needed to compensate dynamic tracking error compare to the static error as it can be stated in the weight $\frac{1}{\mathrm{w}_1}$, where the bandwidth of the control (147 Hz) is almost 7.5 times higher than the bandwidth of the tracking (20 Hz). Though this control bandwidth is chosen to be as small as possible (satisfying time domain error specification), since a higher corner frequency of $\frac{1}{\mathrm{w}_1}$ will result in a controller with high noise filtering bandwidth, resulting in bad noise filtering properties at lower frequencies. The weighting function is given by Eq. 3-17:

$$\frac{1}{w_1} = \frac{1.4s + 0.14}{s + 1571} \qquad \textit{Eq. 3-17}$$

Figure 3-8 illustrates the frequency response of the filter $\frac{1}{\mathrm{w}_1}$.

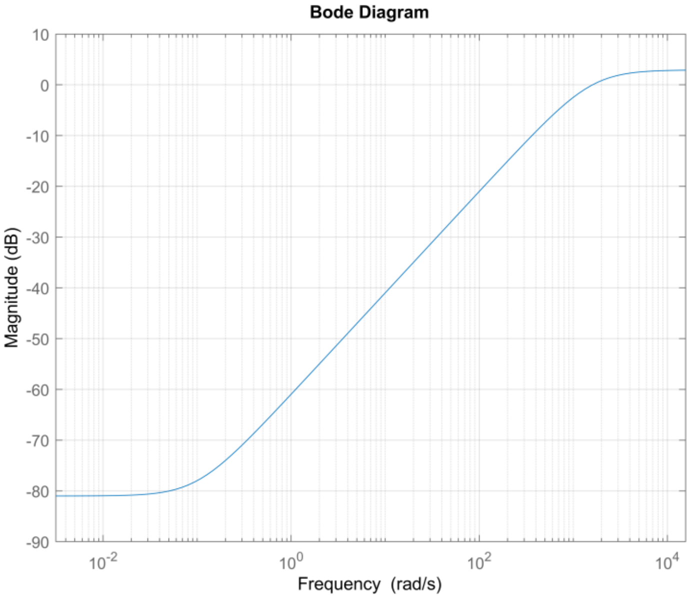

Figure 3-8 - Constraint on tracking error via sensitivity function

In Figure 3-8, the functioning frequency range of the dynamic tracking [5-20 Hz] is situated in the slop increasing at the rate of +6 dB. The main idea is to tackle the dynamic error via a dynamic frequency slope, where the lower frequency requires higher control gain to achieve the equal level of error correction for a system requiring long-range frequency tracking, thus the inverse of the $\frac{1}{w_1}$ will shape a controller having high gain at the beginning (low frequency) and decreasing with frequency. This point of view of treating the dynamic tracking error differs from classical tracking problems where the error can be constrained in terms of overshoot, response time and static error. Note that the complexity of the weighting filters is kept as minimum as possible as it will increase the complexity of the controller

3.5.2.2 Noise filtering constraints

In contrary to the last section where the classical notion of static tracking error can no longer restrain dynamic tracking issue, noise filtering can be done via the classical procedure. After restraining the tracking error via

$\frac{1}{\mathrm{w}_1}$, the noise filtering constraint $\frac{1}{\mathrm{w}_3}$ has to be fixed in regards to the first one. As explained in section 3.4.2.1, constraints on sensitivity function and complementary sensitivity function cannot be met at the same frequency. Therefore, the constraint on the complementary function focuses on the tracking bandwidth at low frequencies and the complementary sensitivity function for high frequency noises. In the feasibility point of view of the control system design, the criteria is to limit the bandwidth of the complementary sensitivity function as low as possible to filter as much sensor noises as possible. At the same time, we cannot lower this value arbitrarily as it will coincide with the bandwidth of tracking and the problem would not have any optimal solution (separation between sensibility and complementary sensibility function in section 3.4.2.1). In another word, we need a minimum bandwidth to keep the tracking error (due to noise) within the tolerance. So the bandwidth of this weight has been fixed at a minimum value in terms of achieving an optimal γ, which is 443 Hz, and its magnitude crosses 0 dB at 256 Hz to satisfy the H_∞ optimization criteria. A lower bandwidth of $\frac{1}{\mathrm{w}_3}$ will result more than 1% of dynamic tracking error. The low frequency gain of this weight has been fixed to 1.4 (more than 1) to maximize the stability margin.

$$\frac{1}{w_3} = \frac{2287s + 2.62 \times 10^8}{1.14 \times 10^5 s + 1.87 \times 10^8} \qquad \textit{Eq. 3-18}$$

Figure 3-9 illustrates the frequency response of the filter $\frac{1}{\mathrm{w}_3}$:

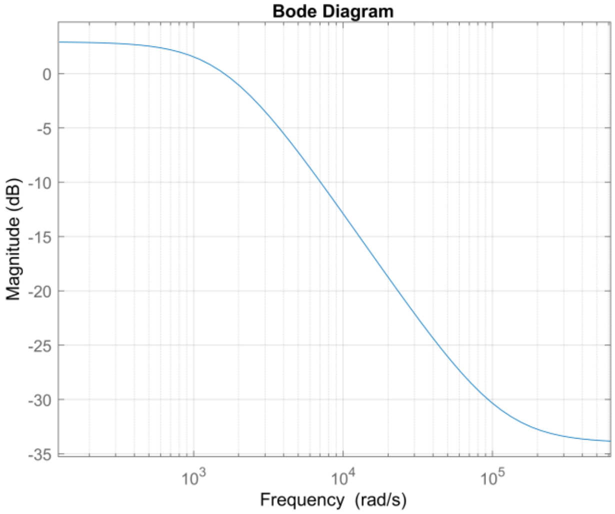

Figure 3-9 - Constraint on noise filtering via complementary sensitivity function

In Figure 3-9, the low-frequency component of the weight before passing below 0 dB concerns the tracking error bandwidth and the sensor does not induce noises. The bandwidth of this weight corresponds to the beginning of noise filtering frequency to be considered at higher frequencies compared to the error correction frequency. This noise filtering capacity can largely be satisfied using the current accelerometer. For example, the accelerometer PCB 356B21 can assure at least 1000 Hz without inducing any noise where the control design via $\frac{1}{\mathrm{w}_3}$ introduced in this chapter, can effectively filter noises from $\cong 147$ Hz (PCB 356B21, Website).

3.5.2.3 Constraint on the actuator capacity

The actuator saturation can be taken into account via the frequency domain constraint $\frac{1}{\mathrm{w}_2}$ on the sensitivity function KS. The simplified case of Figure 3-2 represents the satellite-interface dynamic where the only known information is the mode parameters (damping ratio and mode position). No additional information, such as the mass and inertia of the satellite is known for this case. Therefore, it is impossible to relate the actuation capacity and the satellite dynamics without this information. Due to this reason, no constraint on actuation has been imposed for this simplified case. But in the later chapter, it is included while studying the real identified satellite dynamics.

3.5.2.4 Synthesis result

Closed-loop specifications are given by frequency-domain constraints in the previous section and by using those constraints, the multi-objective mixed sensitivity H_∞ optimization has been solved via the ARE. Even though the LMI solutions are promising as stated in section 3.4.2.2 (Heuvel, 1997) and in our case study shows that the tolerance of the γ iteration is not a concern to obtain satisfactory performances (γ variation of a fraction does not significantly increase or decrease any performance, therefore, the advantage to augment a small fraction of γ is not suitable), ARE solution seems to be ideal. Moreover, the LMI solutions mostly provide numerically unstable controller during the study, which is unable to converge in the time domain simulations. The details of ARE based H_∞ optimization can be found in (Apkarian, 1993) (Zhou, et al., 1996). The synthesized controller corresponds to the optimization problem of Eq. 3-16 which does not take in consideration the actuator saturation.

The controller dynamics is given by:

$$K(s) = \frac{2.4 \times 10^{3}\ \mathrm{s}^{3} + 2.7 \times 10^{17}\ \mathrm{s}^{2} + 5.4 \times 10^{17}\ s + 2.4 \times 10^{21}}{\mathrm{s}^{4} + 1.6 \times 10^{9}\ \mathrm{s}^{3} + 3.3 \times 10^{14}\ \mathrm{s}^{2} + 1.5 \times 10^{18}\ s + 1.5 \times 10^{17}}$$

Figure 3-10 illustrates the frequency response of the H_∞ controller.

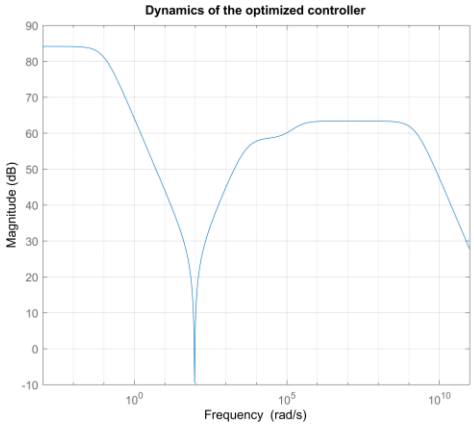

Figure 3-10 SISO H∞ Controller

The second-order plant dynamics combined with two first-order weights of each, the augmented model is a fourth-order dynamics and the synthesized control is as well fourth-order transfer function in terms of complexity. The dynamics of the satellite of Figure 3-2 has a low pass behavior after the mode frequency, therefore the control gain increases to frequencies after the mode to keep the dynamic error minimum. In addition, the controller is internally stable as the real part of the four poles are all negative ($-1.6 \times 10^9, -2 \times 10^5, -4.7 \times 10^3, -0.1$). As mentioned in literature (Alazard, et al., 1999) (Balas, 1990) (Apkarian, 1993), the controller of Figure 3-10 has anti-resonant dynamics which compensates exactly the dynamic of the vibration of Figure 3-2, known as pole-zero compensation.

3.6 DESIGN VALIDATION

This section is dedicated to the validation of the control design via frequency and time-domain simulations.

3.6.1 Frequency domain verification

The Figure 3-11 shows frequency response of the sensitivity and complementary sensitivity functions given by Eq. 3-17 and Eq. 3-18.

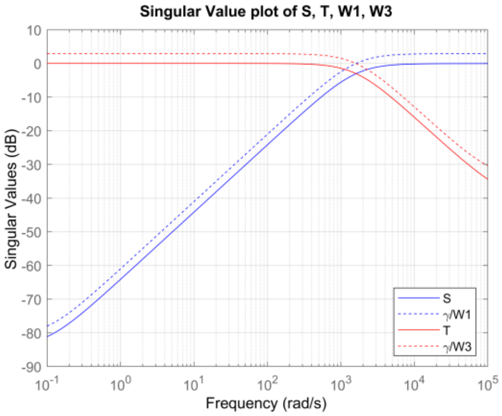

Figure 3-11 - Sensitivity and complementary sensitivity functions

The first attention of this optimization problem goes to the optimal γ value, which is equal to 0.97. Therefore, the optimization problem is solved with a very satisfactory solution for the given weights. In order to satisfy the tracking performance and noise filtering criterion, the open-loop dynamics must behave as an integrator (Skogestad & Postlethwaite, 2001) (Duc & Font, 1999). The low-frequency high gain above 0 dB corresponds to the error tracking and disturbance rejection while the high-frequency low gain which is below 0 dB corresponds to noise filtering. Figure 3-12 shows the open-loop $(G(s) * K(s))$ frequency response.

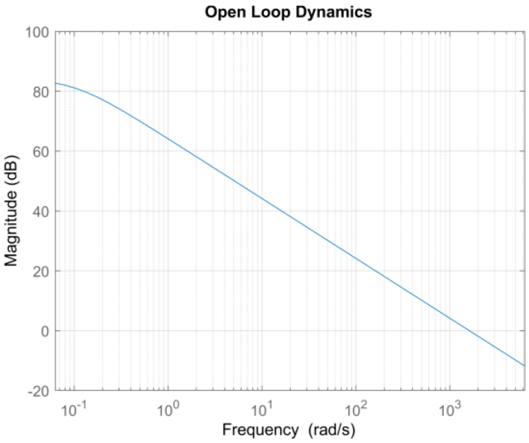

Figure 3-12 - Open loop behavior

The open-loop frequency response and the behavior is nominal according to loop shaping principals due to the fact that it behaves as an integrator (Duc & Font, 1999) (Skogestad & Postlethwaite, 2001). The H_∞ optimization increases the low-frequency gain of the plant by synthesizing a stable controller. In the Figure 3-12, the gain of the open-loop transfer function decreases at higher frequencies to filter noises.

The Nichols chart has been used to analyze the input-output stability criterion of an open-loop controlled system, Figure 3-13.

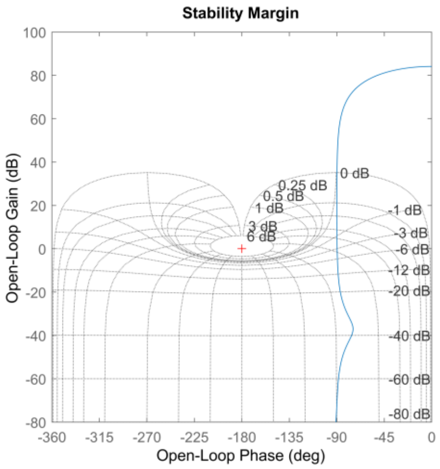

Figure 3-13- Nichols chart of the open loop system

By definition of an H_∞ control, the controller provides an internally stabilized system as the real part of closed-loop poles are negative (Zhou, et al., 1996). Figure 3-13 shows the Nichols chart of input-output stability margin of all frequencies, but the study concerns the range of frequency from 5 to 100 Hz, which corresponds to the right half of the plot and the corresponding Nichols critical point at the coordinate of $(0\,dB, -180°)$. The obtained SISO phase margin of the concerning frequency range is 90° at 1.6 kHz. This system is infinitely stabilized in terms of gain.

3.6.2 Time domain analysis

In order to verify the improvement of the designed controller, two different time-domain simulations have been performed. H_∞ control-based time-domain simulator is illustrated in Figure 3-3 and the current nonlinear control-based simulator is described in section 2.2.3. Figure 3-14 and Figure 3-15 illustrate the result obtained with the current nonlinear control strategy and with the H_∞ controller, respectively. The $cola$ signal is generated within the range of 5 to 30 Hz with an acceleration magnitude of $1\ g$. The satellite mode frequency is set at 15 Hz associated to 1% damping factor, same values as for the controller synthesis. The simulation is limited to 30 Hz as the study focuses on the behavior near the mode at 15 Hz, included in this range, and it shows the overall performance without excessively increasing the simulation time.

3.6.2.1 Performance of the nonlinear controller

The current nonlinear controller's performance is demonstrated in Figure 3-14 for a damping factor of 1%, sine sweep rate of 3 octave/min and compression factor of 20 (See section 2.2 for details about these parameters) using the simplified model of the satellite-interface given by Eq. 3-5. This is more likely to be the case of a real satellite, a maximum compression factor of 20 cannot even keep the error below the specification, and very high oscillations are observed.

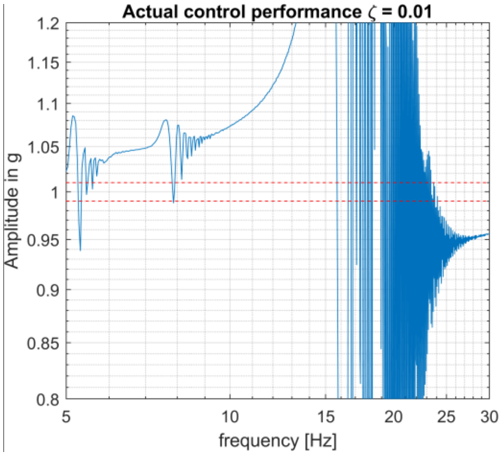

Figure 3-14 – Amplitude of the output acceleration of current control strategy with compression factor=20

Even though such severe uncontrolled amplitudes are rarely observed in real VTS, it does not contradict the current simulation result of Figure 3-14 as in the VTS, there is the possibility to fix different compression factors for different parts of the frequency range leading to a smoother tracking (generally, a higher compression factor in the passage of a mode and a smaller compression factor just after the mode to reduce the overshoot). In addition, the amplitude is manually reduced (known as a manual notch, see section 2.1.5) near high-frequency modes (In Figure 2-9, after 25 Hz, the reference (red dotted line) is reduced from 1g to 0.25g) to limit such oscillatory behavior.

3.6.2.2 H_∞ controller performance

3.6.2.2.1 Tracking performance

In this section, the tracking performance of the H_∞ controller is discussed. In this case, the configuration of the S-DoF dynamics is the same as the case explained in section 3.6.2.1 in order to compare both results. Figure 3-15 illustrates the obtained results between 5 to 30 Hz. The illustration states the amplitude of the pseudo periodic output acceleration.

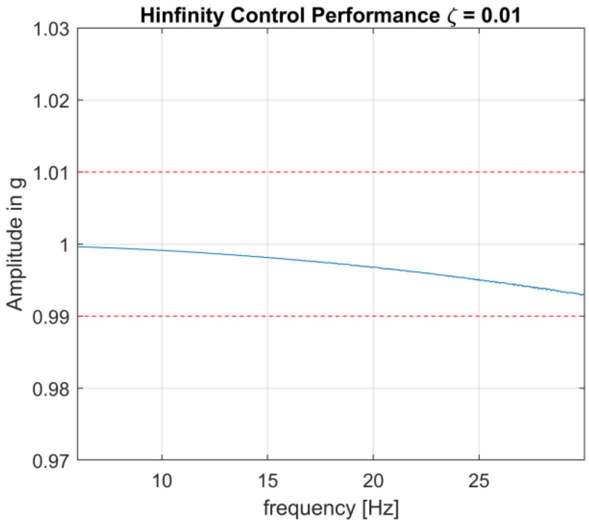

Figure 3-15 – Amplitude of the output acceleration with H_∞ controller

The obtained dynamic tracking error (error in amplitude) remains below $\pm 1\%$ and no oscillation at the neighborhood of the mode (15 Hz) is noticed. The tracking performance is far superior to the actual control method, though the tracking error can be further reduced by increasing the bandwidth of performance weight $\frac{1}{w_1}$. In that case, a slight increase of performance corresponds to demand of very high-performance sensors.

3.6.2.3 Robustness against time delay and damping factor

Some additional tests have been carried out to check the robustness of the proposed control strategy, illustrated in Figure 3-17 and Figure 3-18.

The time of the close-loop system corresponds to the time that a signal takes to enter into the amplifier and then its propagation to accelerometers. In the time domain simulator of the Figure 3-16, the delay is introduced by the factor of $e^{\tau s}$ where τ corresponds to the delay (in second), s is the Laplace variable. A first simulation considers the case where delay τ of 1 millisecond is introduced to the plant dynamics

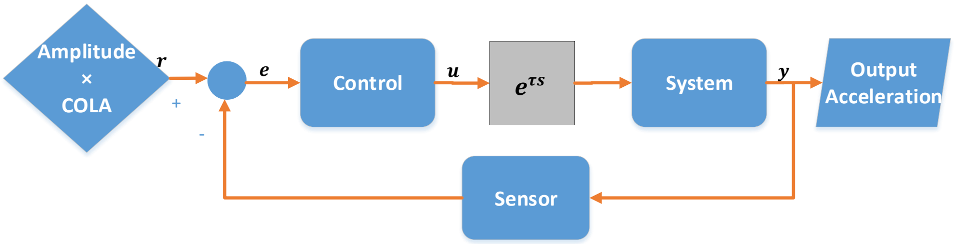

Figure 3-16 - Closed loop system with delay

In Figure 3-17, the output accelerations are zoomed at the end of the simulation (near 51.6 sec). The nominal plant is in red and the delayed plant corresponds to the blue dots. It can be noticed that the system remains robust and tracks the reference signal as the dispersed case follows the nominal plant without any visible delay, Figure 3-17.

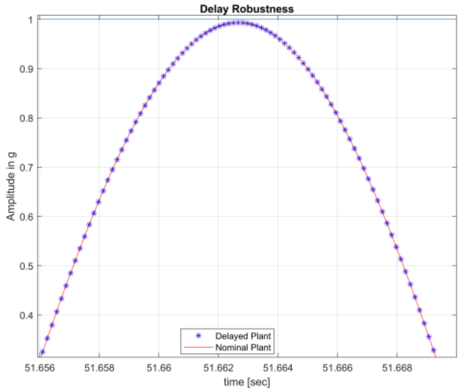

Figure 3-17- Robustness against delay (zoomed over a period)

In a second simulation, a mismatch of -15% on the damping factor is applied as a lighter damping factor leads to a worst-case of a vibration system. The obtained result is given in Figure 3-18 (blue line) and compared to the nominal case (orange line).

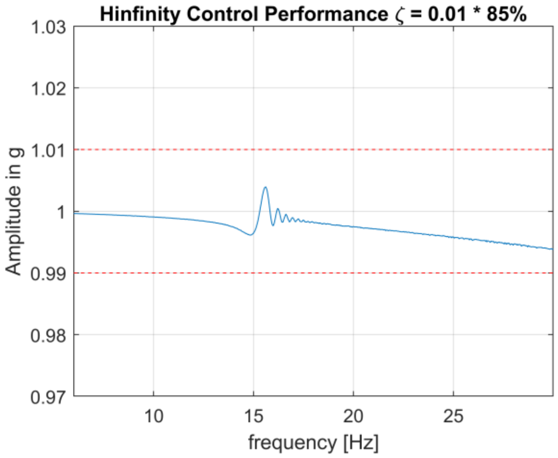

Figure 3-18- Robustness against the damping factor mismatch

The controller appears to be robust against the variation of the damping factor with an error below 1% in the whole range of the simulation. The variation of the damping factor introduces an oscillation of very small amplitude, though the very slight beating (0.1%) near 15.6 Hz is not an issue as the error amplitude is very small and it would not bring overstress to the structure. This preliminary study does not include the mode position variation, a detailed study will be carried out in the next chapter.

3.7 CONCLUSION

The research study of this chapter describes the first part of the thesis work where the state of art of vibration control, as well as different robust control methods, are analyzed to give a direction to further developments. The mixed sensitivity H_∞ control was selected and, before proceeding to advanced analysis for the perspective of a new VTS architecture, a feasibility study is carried on a simplified S-DoF model with a single vibrational mode, in order to validate the relevance of such optimal control strategy for further development of VTS on a real and more complex multi-degree of freedom (M-DoF) model. The main scientific contribution of this chapter is to introduce a systematic way to define frequency domain weights to limit dynamic tracking error eliminating vibration via robust control. Therefore, the results are optimistic as the performance of the proposed closed-loop system shows a very encouraging performance and a clear direction for the dynamic tracking control problem rarely addressed in the literature to our very best knowledge. In this chapter, our study focuses on satisfying the specification of precision tracking, although some robustness studies (delay and damping variation) are included. The mixed sensitivity H_∞ controller comes with pole-zero compensation phenomena, which is regarded to be very sensitive to the modal parameter variations. Therefore, no further study is conducted in case of mode frequency variation as it will result into strong vibration of the system in case of any mismatch between the mode resonance and controller anti-resonance of the closed-loop system. In the next chapter, the result of this chapter will be extended to a real identified model of satellite as well as the limitation of the optimal control in the specific case of modal parameter varying system with actuator saturation, and the chapter 5 will study the robustness issues. In the following chapters, further research work on a real satellite dynamic behavior will be developed based on the methods and strategies experienced from this feasibility study.

4 MODELING AND OPTIMAL CONTROL OF A REAL VTS

4.1 INTRODUCTION

The previous chapter detailed the application of an H_∞ optimal control on a newly proposed control architecture of VTS. In our feasibility study, the optimal control strategy applied on a simplified S-DoF model demonstrated a far superior performance than the actual control strategy. Therefore, the next step of the research focuses on real and more complex modeling of a satellite-shaker composite model and the application of the H_∞ optimal control strategy, experienced from the previous chapter. The frequency and time domain analyses are carried out to measure the performance of the newly proposed control scheme on a real model. Moreover, the developed control algorithm would go through specific tests in order to validate the robustness properties required for the VTS. The first part of this chapter details the modeling issues, and the last part describes the control strategy and the validation procedures.

4.2 MODELING OF A COMPOSITE

In this section, we are going to present a systematic way of achieving different models of the real satellite-actuator interface in perspective of control synthesis and validation of the closed-loop performance of a discrete-time model obtained through the pole-zero identification process.

4.2.1 Description of the dynamic model

Figure 4-1 illustrates the closed-loop architecture of the current vibration system architecture developed by LMS international. The system is briefly described with the VTS procedure in section 2.2.5. In this section, we will only describe the chosen model of the plant dynamics to be used later. The model is obtained from a very low-level vibration test of a typical commercial geostationary satellite, beginning at 5 Hz and ending at 100 Hz, where the data has been acquired from two points (Data 1 and Data

2 in Figure 4-1) of the closed-loop system. So, the acquired data includes a combined model of amplifier, actuator, satellite table and sensor dynamics between Data 1 and Data 2.

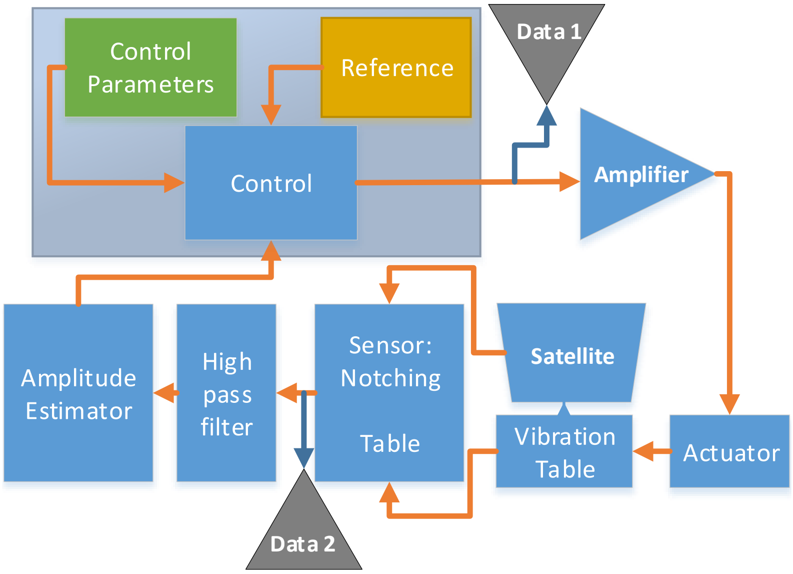

Figure 4-1 - Current system architecture

The command is an acceleration signal, and the output is the measured acceleration signal, therefore, the input and output of the identified plant model are both accelerations. Through an internal study at Thales Alenia Space (Erdavide, 2019), a 7th order discrete time model with a sampling frequency of 800 Hz has been achieved. The development of this model from data acquired through a low-level test is not the primary focus of this research work; thus, they are not detailed in the thesis work. The 7th order discrete time model is based on the estimation of poles and zeros, unlike the classical structural methods (Girard & Roy, 2010) where the mass, stiffness and damping matrices are directly identified depending on the number of degrees of freedom of the system. Therefore, the current estimation methods only provide the numerator and denominator coefficients of the transfer function, which is neither optimal in terms of complexity, nor the parametric equations are given. Thus, the plant order needs to be verified if any order reduction can be achieved to keep the complexity as low as possible. On the other hand, the synthesized model shall be derived by identifying modal parameters, so that the robustness analysis can be carried out against variations of these parameters. The estimated dynamical model represents the first two modes of the satellite from 5 to 50 Hz and the corresponding anti-resonances linked to these modes.

The first step consists in converting the discrete time model to a similar order continuous time model. The main reason for this conversion is the representativity of the real system via the MIL system, where the real physical system corresponds to a continuous-time model and the rest of the system is discrete. Therefore, a continuous-time plant dynamic replacing the physical system with a combination of discrete parts creates a similar condition of a real vibration test with the possibility to verify the numerical robustness through the real-time MIL closed-loop system. In addition, later in this chapter, the continuous-time model serves to achieve an analytical model with identified modal parameters for robustness analysis. There are several methods that enable this conversion, mainly the zero-order hold (ZOH) used for a case where the input of the system is a staircase, first-order hold (FOH) for a system of linear input, bilinear Tustin approximation for good matching of frequency domain discrete-continuous model, and pole-zero matching for also the frequency domain model matching, but only valid for SISO plants (Åström & Wittenmark, 1990) (Franklin, et al., 1997). Figure 4-2 illustrates the frequency responses of the discrete-time original estimated model with continuous time models obtained through the different conversion methods like ZOH, FOH, bilinear and matched transform. Figure 4-2 illustrates the frequency response in the range 5-40 Hz, the frequency range of interest for the study.

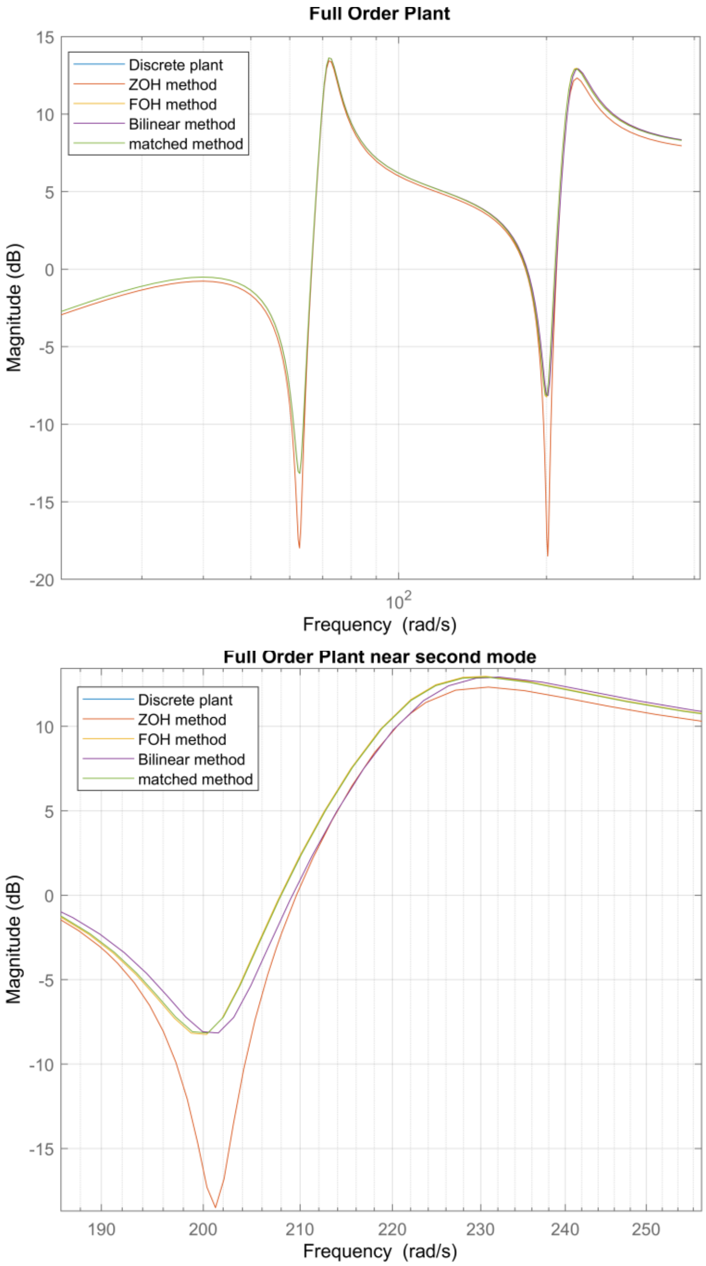

Figure 4-2 Full order discrete-time vs. continuous-time model (upper) and zoomed version near second anti-resonance(down)

Table 4-1 resumes the mismatch of models obtained from different methods.

Table 4-1 Mismatch among continuous-time models

Vib. modes	Impact points	Bilinear		ZOH		FOH		Matched	
Mode 1	Resonance	0 dB	0.15 Hz	0.2 dB	0.15 Hz	0 dB	0 Hz	0 dB	0 Hz
	Anti-resonance	0 dB	0.15 Hz	4.8 dB	0.15 Hz	0 dB	0 Hz	0 dB	0 Hz
Mode 2	Resonance	0 dB	0.31 Hz	0.7 dB	0.15 Hz	0.1 dB	0 Hz	0 dB	0 Hz
	Anti-resonance	0.01 dB	0.31 Hz	10.35 dB	0.15 Hz	0.09 dB	0 Hz	0 dB	0 Hz
5 Hz	Low freq.	0 dB	N.A	0.25 dB	N.A	0 dB	N.A	0 dB	N.A
50 Hz	High Freq.	0.06 dB	N.A	0.43 dB	N.A	0.05 dB	N.A	0 dB	N.A

In terms of the system robustness against the model mismatch, the robustness of the control system is determined by the small gain theorem. The point of impact of systems robustness depends on the maximum gap of gain of the estimated dynamic from the real system dynamic. Therefore, comparing of all these conversion methods (ZOH, FOH, bilinear and matched algorithms in Table 4-1), the mismatches from the original discrete model near the second anti-resonance are respectively by 10.35, 0.09, 0.01 and almost 0 dB. In addition, the bilinear transform and ZOH shifted the continuous-time model to 1 and 2 rad/sec at the left side. It can be stated that the matched transformation gives the best conversion without losing any significant information in the range of 5 to 50 Hz and the bilinear transformation gives a quasi-perfect matching with a very slight error, where the other two methods are far behind with a significant amount of error. The bilinear transformation is based on frequency domain matching between continuous-time and the discretized model, where the s-domain and z-domain transfer functions are related via the following relation:

$$z = e^{sT} \approx \frac{1 + sT/2}{1 - sT/2} \qquad \textit{Eq. 4-1}$$

where T is the sampling period. The matched conversion method computes the equivalent of the pole-zeros between the continuous and discrete-time system (Franklin, et al., 1997). Poles and zeros are related via the following equation:

$$z_i = e^{s_i T} \qquad \textit{Eq. 4-2}$$

where z_i and s_i are the i^{th} pole or zero of the discrete and continuous-time system. Details of these algorithms are given in appendix, 8.4. In the study case, the matched transformation performs slightly better than the bilinear one, as stated in literature (Yang, 2009). The identified plant model presented in this study corresponds to the SISO system, but an ongoing study aims to extend this model to the MIMO case at Thales (the identification problem is treated by another team, which is out of the scope of this thesis). Therefore, the bilinear procedure has been selected due to the option of extending to a MIMO plant where the matched transformation can be used only for a SISO dynamics (Franklin, et al., 1997) and the outcome of this study will be directly industrialized with choices made during this research without any further modification. Furthermore, this choice will let us verify the robustness of the whole industrialized procedure independent to any single method related to the process. In any case, the control synthesis shall include the modal parameter robustness to address these uncertainty issues due to the model mismatch.

4.2.2 Model reduction

The complexity of the synthesized controller depends on the complexity of the model, thus a reduced order model would induce a lower order controller (Alazard, et al., 1999). Therefore, the next step is to analyze the continuous-time model to possibly reduce the order of the dynamics without losing the dynamic characteristics of the original one. The order reduction is performed by considering the singular values of the full-order model by following a classical approach detailed in the sequel. In the literature (Glover, 1984) (Safonov & Chiang, 1989) (Zhou, 1993), two main methods are mostly used for order reduction, and multiplicative error balanced stochastic model truncation (BST) and the additive bound method (Balanced). The BST method tends to reduce the error between the original and reduced model within a specific frequency range; therefore, a model containing lightly damped modes is likely subject to have less error via BST reduction than the Balanced method in the neighborhood of a mode (Matlab Reduce, website). Details of these algorithms are given in section 8.4.5 of the appendix.

The additive bound method uses Hankel's singular values of the full-order model, which are the energy of the states of the model given by Figure 4-3.

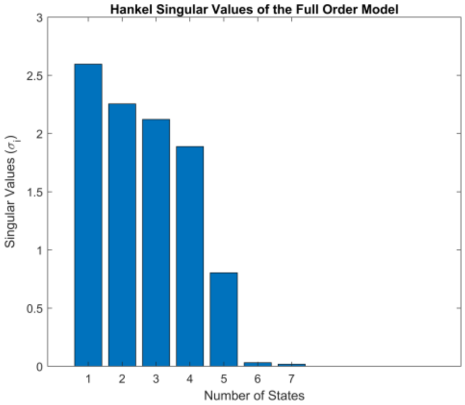

Figure 4-3 - Hankel's singular value plot

In Figure 4-3, Hankel’s singular values are ranked considering the energy of states (Glover, 1984). The main idea is to keep states with high energy and discard low energy states as states with low energy correspond to less significant characteristics (Skogestad, 1991). Suppose that the transfer function of the full model is given by G_{full} and the reduced order model is given by G_{red}. The Hankel’s singular values of the full order model are given by σ_i, i is the index of the total state n. Therefore, the error of the additive bound method is given by:

$$\left\|G_{full} - G_{red}\right\|_{\infty} \leq 2\sum_{1+k}^{n} \sigma_i \qquad \text{Eq. 4-3}$$

The main drawback of the Hankel’s theory-based additive bound method is that in some cases, the algorithm generates uncontrollable/ unobservable states (Safonov & Chiang, 1988). Therefore, the multiplicative error balanced stochastic model truncation (BST) computes the state energy based on the Hankel’s singular value of the phase matrix Φ of the full order model G_{full} (Safonov & Chiang, 1988).

$$\Phi = G_{full}(s){G_{full}}^{T}(s) \qquad \text{Eq. 4-4}$$

Figure 4-4 illustrates the energy of the states computed from the phase matrix.

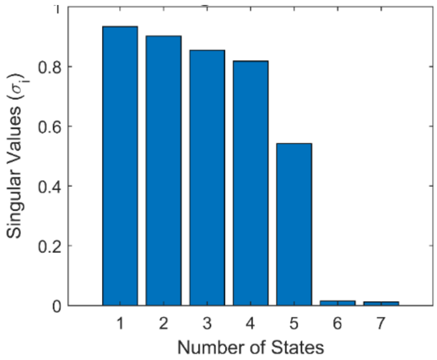

Figure 4-4 Multiplicative bound singular values of the full order model

Figure 4-4 illustrates the energy mapping of the full order dynamics, and like the additive bound method, it can be observed that the last two states are less significant. After obtaining Hankel's singular values of the phase matrix, the balanced stochastic model truncation guarantees the multiplicative relative error in infinity norm (Zhou, 1993), given by:

$$\left\| {G_{full}}^{-1}(G_{full} - G_{red}) \right\|_{\infty} \le \prod_{k+1}^{n} \left(1 + 2\sigma_i \left(\sqrt{1 + {\sigma_i}^2} + \sigma_i\right)\right) - 1 \qquad \textit{Eq. 4-5}$$

where n is the total order of the model G_{full}, k is the desired reduced order and $i \in [1, n]$.

Figure 4-5 illustrates the obtained 5th order reduced model via additive bound and balanced stochastic truncation methods.

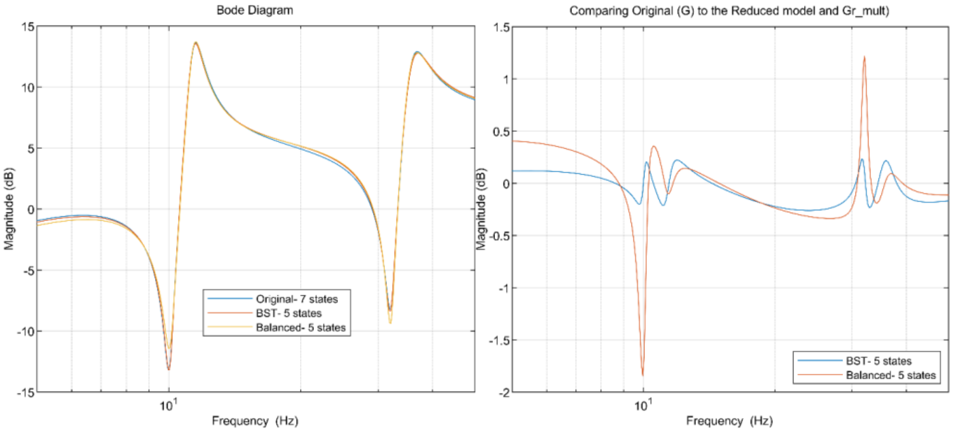

Figure 4-5 - Comparison of BST vs. balance method, model (left), error (right)

In Figure 4-5, the reduced model via BST, balanced method [left] and their corresponding errors from the full order model [right] are given. When comparing with the original 7 state continuous-time model, the reduced model via the balanced method resulted in maximum 1.8 dB of relative error near the first anti-resonance frequency, on the other hand, the BST method kept the error below 0.2 dB in the range of frequency [5, 50] Hz containing the two satellite modes and corresponding antiresonances. In this section, the mathematical methods are given, though the detailed algorithms of these order reduction technics are given in Appendix. Mentioned model reduction methods can be found in the latest versions of matlab (2017 and later), and they are directly used to reduce the model.

4.2.3 Modal parametarization

In modern control engineering, two models of plant dynamics are used. The simplified reduced order model also known as synthesis model is used for control design to keep the complexity of the controller as minimum as possible. The second one corresponds to the full order model without any reduction to verify the validity of the control design. Therefore, the next step of modeling consists in obtaining a synthesis model from the reduced five state satellite-interface-actuator optimal plant model by identification of modal parameters such as the mode frequency and damping ratio of corresponding two modes. Mainly, this synthesis model will be used for control design. Moreover, it will enable varying modal parameters to verify the robustness of the system against those parameter variations. In the following paragraph, we proceed to a general modal identification procedure from a standard coefficient based polynomial model of Eq. 4-6 without any regard to coefficient values (b_0,..., b_5 and $a_1, \ldots a_5$). This procedure can be used for any modal parameterization of a model, even with very high complexities. The general form of a fifth-order model can be written:

$$G_{red}(s) = \frac{b_5 s^5 + b_4 s^4 + b_3 s^3 + b_2 s^2 + b_1 s + b_0}{s^5 + a_1 s^4 + a_2 s^3 + a_3 s^2 + a_4 s + a_5} \qquad \textit{Eq. 4-6}$$

where s is the Laplace variable, $a_{1..5}$ and $b_{1..5}$ are the denominator and numerator coefficients ($b_\mathrm{i} \neq a_\mathrm{i}$). The partial fraction decomposition (Rao & Ahmed, 1968) of Eq. 4-6 leads to:

$$G_{red}(s) = \underbrace{\frac{R_1}{s - P_1} + \frac{R_2}{s - P_2}}_{1} + \underbrace{\frac{R_3}{s - P_3} + \frac{R_4}{s - P_4}}_{2} + \underbrace{\frac{R_5}{s - P_5}}_{3} + R_6 \qquad \textit{Eq. 4-7}$$

In Eq. 4-7, $P_1 .. P_5$ are the poles of the plant, $R_1 .. R_5$ complex coefficients of numerators, R_6 a real static gain. The model contains two modes, two pairs of conjugate poles for each mode and a real 5th pole. In Eq. 4-7, conjugate poles and numerators are regrouped in the following equation:

$$G_{red}(\mathrm{s}) = \frac{s(R_1 + {R_1}^*) - {R_1}^* P_1 - R_1 {P_1}^*}{s^2 - (P_1 + {P_1}^*)s + P_1 {P_1}^*} + \frac{s(R_3 + {R_3}^*) - {R_3}^* P_3 - R_3 {P_3}^*}{s^2 - (P_3 + {P_3}^*)s + P_3 {P_3}^*} + \frac{R_5}{\underbrace{s - P_5}_{3}} + R_6 \qquad \textit{Eq. 4-8}$$

Eq. 4-8 is a detailed form of Eq. 4-7, where the transfer function with conjugate poles are gathered together, * signifies the complex conjugate (each conjugate pairs are separated in Eq. 4-7), ${R_1}^* = R_2$, ${R_3}^* = R_4$, ${P_1}^* = P_2$, ${P_3}^* = P_4$. Then Eq. 4-8 can be rewritten by redefining variables to obtain modal parameters in view of a parametric model of the plant, as follows:

$$G_{red}(\mathrm{s}) = \frac{s(R_1 + {R_1}^*) - {R_1}^* P_1 - R_1 {P_1}^*}{s^2 + 2\Omega_1 \xi_1 s + {\Omega_1}^2} + \frac{s(R_3 + {R_3}^*) - {R_3}^* P_3 - R_3 {P_3}^*}{s^2 + 2\Omega_2 \xi_2\, s + {\Omega_2}^2} + \frac{R_5}{s + P_5} + R_6$$

In this equation, we can see the modal parameters such as the first mode angular frequency and damping, (Ω_1, ξ_1) and (Ω_2, ξ_2) for the second mode. They are obtained from Eq. 4-8 with the following variable change:

$${\Omega_1}^2 = P_1 {P_1}^*, {\Omega_2}^2 = P_3 {P_3}^*, \xi_1 = \frac{-(P_1 + {P_1}^*)}{2\Omega_1}, \xi_2 = \frac{-(P_3 + {P_3}^*)}{2\Omega_2}$$

The parametric model has to be represented mostly via modal parameters so that the variation of those parameters also results in varying all dependent variables of the model. The numerators of the first two transfer functions in the above equation can also be expressed in terms of modal parameters. As numerators contain the dynamics of anti-resonance, by expressing the numerators with modal parameters will vary them in case of mode variation in the model.

Let $R_1 = r_1 - ip_1$, $R_3 = r_2 - ip_2$, $P_1 = m_1 - in_1$, $P_3 = m_2 - in_2$ where $r_{1,2}$, $p_{1,2}$, $m_{1,2}$, $n_{1,2}$ are real coefficients.

$$G_{red}(s) = \frac{2sr_1 + 2(p_1\Omega_1\sqrt{(1+{\xi_1}^2)} + r_1\Omega_1\xi_1)}{s^2 + 2\Omega_1\xi_1 s + {\Omega_1}^2} + \frac{2sr_2 + 2(p_2\Omega_2\sqrt{(1+{\xi_2}^2)} + r_2\Omega_2\xi_2)}{s^2 + 2\Omega_2\xi_2\, s + {\Omega_2}^2} + \frac{R_5}{s+P_5} + K_S \qquad \text{Eq. 4-9}$$

In Eq. 4-9, modal parameters (Ω_1, ξ_1) and (Ω_2, ξ_2) can be expressed in terms of real coefficients $r_{1,2}$, $p_{1,2}$, $m_{1,2}$, $n_{1,2}$.

$$ {\Omega_1}^2 = {m_1}^2 + {n_1}^2, {\Omega_2}^2 = {m_2}^2 + {n_2}^2, \xi_1 = \frac{{m_1}^2}{\sqrt{{m_1}^2+{n_1}^2}}, \xi_2 = \frac{{m_2}^2}{\sqrt{{m_2}^2+{n_2}^2}}, K_S = R_6$$

The synthesized parametric model of Eq. 4-9 will be used for control synthesis and different analyses. The identified values of the first mode parameters are $\Omega_1 = 71.62\, rad/s$, $\xi_1 = 0.04$ and second mode parameters are $\Omega_2 = 224.94\, rad/s, \xi_2 = 0.06$, $R_5 = 89.03$, $P_5 = -42.16$, $K_S = -2.41$. The Figure 4-6 compares the fifth-order continuous model and the parametric model of Eq. 4-9.

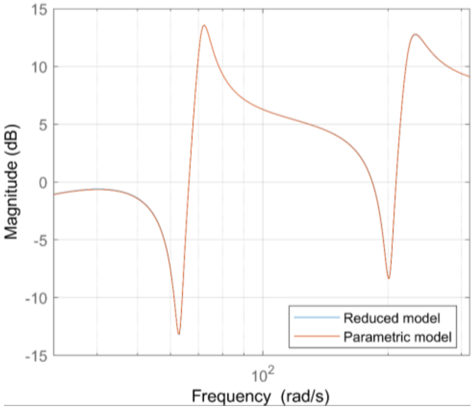

Figure 4-6 - Reduced model vs Parametric model

In Figure 4-6, the frequency response of the reduced model matches exactly the parametric model of Eq. 4-9. in the frequency range of [5,50] Hz. So, this parametric model bears similar characteristics to the reduced model, and it can be used for further analysis of these two modes of the satellite-interface-actuator plant. Note that the S-DoF model of Eq. 3-5 has a first-order numerator and second-order denominator. Here, the dynamics of Eq. 4-9 is the sum of two second-order transfer functions and a single-order transfer function, where each of those second-order transfer functions corresponds to one of the modes of the satellite. The form of each second-order dynamics is similar to the S-DoF given by Eq. 3-5. Therefore, the study on the real satellite dynamics corresponds to an extension of the study realized in the previous chapter. Moreover, the model of Eq. 4-9 contains two vibrational modes, therefore, their intersections create two anti-resonances. They are expressed in the function of mode parameters (the numerator of the first, second-order dynamics of Eq. 4-9). By consequence, the mode parameter variations will result in the variations in anti-resonance parameters. The detailed study is given in section 5.6.2.1 and Eq. 4-9.

4.3 STANDARD H_∞ CONTROL DESIGN OF A REAL COMPOSITE MODEL

This section develops a systematic H_∞ control design experienced from the feasibility study of the previous chapter while using the parametric satellite-interface-actuator plant of the Eq. 4-9. instead of the two degrees of freedom model.

4.3.1 Closed-loop formulation and requirements

The closed-loop system architecture is the same as in the feasibility study (Figure 3-3) where the system block containing S-DoF model is replaced by the parametric composite model (Eq. 4-9). Figure 4-7 shows the block diagram of the closed-loop system and will be used in the formulation of the mixed sensitivity H_∞ control problem and simulations.

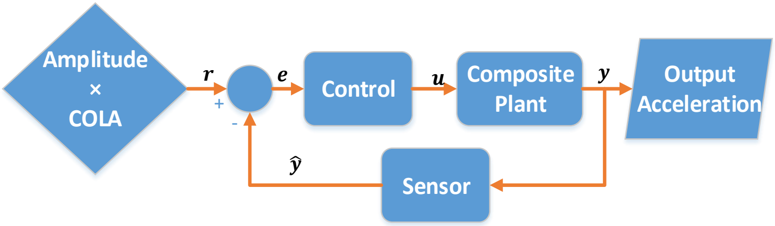

Figure 4-7 - System architecture with composite plant

The closed-loop specifications are already explained in section 3.5.1, and remain similar for this composite case. Though the feasibility study did not develop further analysis on the robustness against mode frequency variation except the robustness against delay and a slight damping ratio variation, in this current chapter, a detailed study will be carried out to determine the parameter sensitivity of the proposed control design. In general, the principal factor contributing to the modal parameter mismatch of the real system from the identified system is the fact that the plant dynamics, which is identified from a low amplitude level test will differ from the one identified from a high-level vibration test. Moreover, the modal parameter estimation procedure from the identified full order case will slightly mismatch from the real plant. In the case study, a $\pm 15\%$ of maximum mode frequency variation is considered, and the maximum damping ratio variation is $\pm 25\%$. The main contribution of these modal parameter variations comes from the model (Eq. 4-9) identified from very low-level amplitude differing from the model identified from qualification level amplitude, which accounts for $\pm 10\%$ of mode frequency variation and $\pm 20\%$ of damping ratio variation. The specification also accounts for the mismatch due to the difference between the reduced order model and the full order model. From the previous experience of the VTS for different commercial and scientific satellites, these values are sufficiently large to cover the robustness of the closed-loop system. The composite model identified from a very low-level test from 5 to 100 Hz range; therefore, Eq. 4-9 containing the real pole situated at 1.6 Hz is an approximation made by the identification algorithm, which is not subject to any variation. Neither the real gain K_S, as it does not vary from a very low-level test to qualification level test.

4.3.2 Problem formulation

As mentioned in the state of art of the VTS problem, the dynamic tracking control is uncommon in the literature of classical control engineering, and the feasibility study shows a systematic way to formulate control problems to address the dynamic tracking issues. Thus the control formulation in the feasibility study is based on fixing the frequency domain constraints manually and verifying the performance through the time domain simulation (see section 3.5). In this section, we introduce a systematic way to transform the industrial specifications of the closed-loop vibration testing system to frequency domain weights w_1, w_2 and w_3. The proposed constraints would satisfy the dynamic tracking problem criteria as the optimal γ value would signify the satisfaction of the frequency domain constraints. Moreover, it can be reproduced as the solution of similar problems corresponding to different satellites in the domain of optimal control. The main objective of this chapter is to expand the results of the previous chapter to the real identified composite model and complete the analysis with the modal parameter variations of the model for the first mode. In addition, the performance of the time domain simulation (Figure 4-12) shows the limitation of standard H_∞ control to tackle large spectral tracking control (5 to 100 Hz in the case of VTS). In this section, the analysis is restricted to just the first mode of the satellite, and the frequency domain synthesis criteria would be limited to 20 Hz. The chapter 6 will generalize the solution for all modes of the satellite between 5 and 100 Hz.

4.3.2.1 Dynamic tracking and noise filtering constraints

The frequency-domain dynamic tracking constraint is explained in section 3.5.2.1. The main objective of this constraint is to achieve a controller with a very high bandwidth compared to the static tracking error correction. In addition, noise filtering constraints are imposed to achieve the maximum filtering of high-frequency noises in regards to the sensor's characteristics and at the same time, assuring the dynamic tracking error requirement. Section 3.5.2.2 details this constraint. These constraints (see Figure 3-8 and Figure 3-9) are independent of the composite model; therefore, the same constraint will be used for the current case to achieve the same performance level as shown in the previous chapter.

4.3.2.2 Control effort constraints

The study of the previous chapter does not include any constraint on control effort as the characteristics of the satellite are not known. Therefore, the study only focused on the dynamic tracking and noise filtering constraints. In this chapter, the characteristics of real identified satellite model are known and it is essential to assess the capacity of the current actuator to cover the VTS while using robust control scheme.

The definition of the constraint $\frac{1}{\mathrm{w}_2}$ comes from the upper limit of the electromagnetic actuator (see section 2.1.1). The actuator can produce up to 75g of acceleration, and the operating frequency is limited to 1700 Hz. Therefore, the low-frequency amplitude has been set at the maximum value of acceleration (75g), and it reaches 0 dB at the maximum operating frequency (1700 Hz) of the vibrator. So the transfer function of the weight corresponds to a first-order low pass filter, given by:

$$\frac{1}{w_2} = \frac{1.04 \times 10^4 s + 1.08 \times 10^9}{1.04 \times 10^5 s + 1.43 \times 10^7} \quad \textit{Eq. 4-10}$$

Figure 4-8 illustrates the frequency response of the filter $\frac{1}{\mathrm{w}_2}$.

Note that the details of the frequency constraints $\frac{1}{\mathrm{w}_1}$ and $\frac{1}{\mathrm{w}_3}$ are given in section 3.5.2. Even though, both $\frac{1}{\mathrm{w}_1}$ and $\frac{1}{\mathrm{w}_3}$ are modeled as first-order low-pass filters, it can be noticed that the bandwidth of $\frac{1}{\mathrm{w}_2}$ is far greater than the noise filter, indicating that the actuator can compensate very high-frequency noise in case the design needs to release the bandwidth of noise filtering to a higher value.

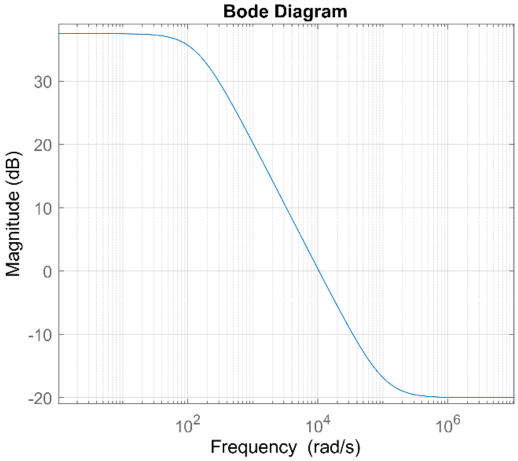

Figure 4-8 - Constraint on control effort

4.3.2.3 Control synthesis

The detail of the control formulation is explained in the feasibility study (section 3.4.1), the same procedure has been applied here. In addition, the LMI and ARE solutions showed the same properties as in the feasibility study, where ARE solutions seem to work without any numerical problem while the LMI solutions show numerical instabilities. Though each of these solutions appeared equivalent in frequency domain representation, the ARE solution appears to be more suitable since solutions are found systematically free from numerical instabilities while evaluating them through time-domain simulations. The synthesized H_∞ controller is given by:

$$K(s) = \frac{\begin{array}{c}-785.4s^7 - 1.7 \times 10^8 s^6 - 9.3 \times 10^{12} s^5 - 7.2 \times 10^{14} s^4 \\ -5.3 \times 10^{17} s^3 - 2.6 \times 10^{19} s^2 - 2.6 \times 10^{21} s - 1.0 \times 10^{23}\end{array}}{\begin{array}{c}s^8 + 2.4 \times 10^5 s^7 + 1.4 \times 10^{10}\, s^6 + 3.2 \times 10^{11} s^5 \\ +6.3 \times 10^{14} s^4 + 8.3 \times 10^{15} s^3 + 2.3 \times 10^{18} s^2 + 2.4 \times 10^{19} s + 2.3 \times 10^{1}\end{array}}$$

Eq. 4-11

The sum of plant model order (5th) with three frequency weights (1st order of each) gives the 8th order control of the *Eq. 4-11*. Considering the complexity of the system and requirements, the 8th order H_∞ controller is relatively simple to be implemented in a real-time framework. This low complexity is the result of minimizing the plant order, in addition to properly converting all necessary specifications without increasing the order of frequency weights. Figure 4-9 illustrates the frequency response of the synthesized controller.

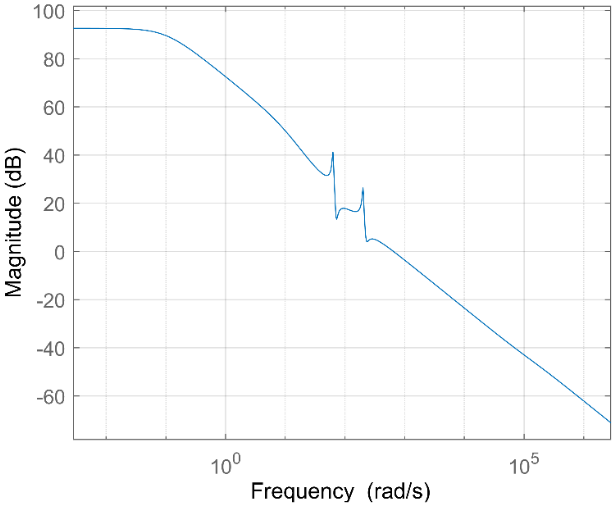

Figure 4-9 - Dynamics of the controller

The controller of Figure 4-9 increases the gain at low frequencies to properly reduce the tracking error while reducing the noise effects in higher frequencies; therefore, the low gain in higher frequencies is justified. The worst-case in the robust control strategies are based on the singular values of the system; therefore, the gain of the system is considered for assessing the sizing case, and the phase is not essential for the analysis. The poles of the controllers are given in Table 4-2.

Table 4-2 - Poles of the controller

Poles	Associated values	Frequency (rad/s)	Damping ratio
1	-1.4×10^5	2.15×10^4	1
2	-1.0×10^5	1.60×10^4	1
3	$-4.4 + 2 \times 10^2 i$	32	0.02
4	$-4.4 - 2 \times 10^2 i$	32	0.02
5	$-1.3 + 63i$	10.03	0.02
6	$-1.3 - 63i$	10.03	0.02
7	-10.4	1.66	1
8	-0.1	0.02	1

The real part of the poles of the controller is on the left side of the real-imaginary plane, leading to an internally stable dynamic. Two pairs of complex poles are responsible for the two resonances of the controller, which cancel the antiresonances of the system and antiresonances of the controller cancel the resonances of the system. This phenomenon is called pole-zero cancellation, also observed in the study of the previous chapter. The first two poles are at high frequencies, which mainly controls the high-frequency component (noise filtering) of the system. The two last frequencies are at low frequencies, which assures the dynamic tracking performance at the beginning of the test.

4.4 ANALYSIS AND VALIDATION

In this section, the design criterion and optimal controller will be analyzed through frequency and time domain simulations for validation.

4.4.1 Frequency domain analysis

4.4.1.1 *Stability analysis*

The Bode plot and black-Nichols diagram of the open-loop dynamics $G_{red}K$ are given in Figure 4-10.

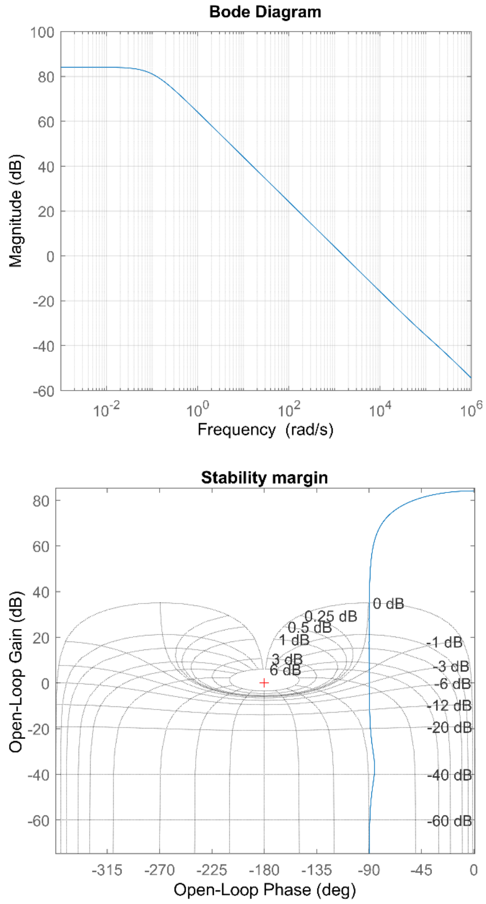

Figure 4-10- Open-loop Bode plot (top) and Black-Nichols plot (bottom) of the open-loop GK

The Bode plot (top) of the open-loop function shows an integral behavior in the control bandwidth, starting from 0.1 Hz to higher frequencies. It leads to nominal loop shaping behavior of the open-loop function in the bandwidth of the control (5 to 100 Hz), which is similar to the synthesis of the section 3.6.1. Moreover, the frequency response lacks the vibration resonance and anti-resonance as the optimal controller compensates these dynamics, and it will result in steady-state performance for the nominal plant. The Black-Nichols plot (bottom) shows the input-output stability of the open-loop system, where the system is stable with a phase margin of 90° and an infinite gain margin.

4.4.1.2 Sensitivity analysis

The optimization problem has been solved with an optimal $\gamma \sim 1$, meaning that the design criterion has been achieved perfectly. Figure 4-11 shows the singular value plot of the sensitivity function S, T, KS obtained for the achieved optimal controller. In general, upper singular values are the worst-case gain of the MIMO system. In a SISO system, the singular values are simply the gain of the transfer function.

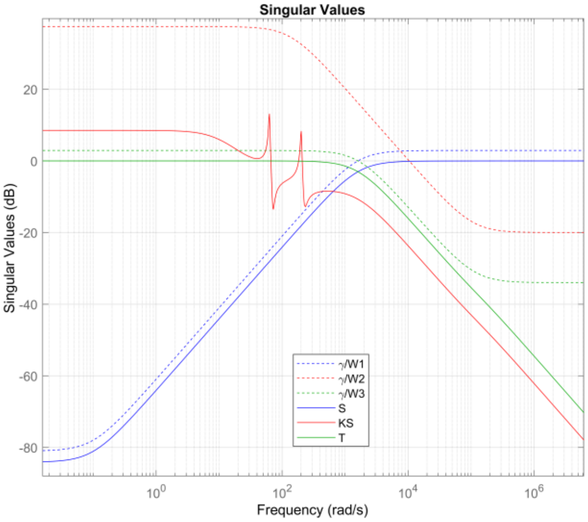

Figure 4-11 - Frequency weights vs. sensitivity functions

In Figure 4-11, the dotted lines correspond to the frequency weights and the continuous lines to the sensitivity functions. In the case where the H_∞ optimization synthesizes an optimal controller, the optimal sensitivity functions would stay below the corresponding frequency constraints. As it can be stated in Figure 4-11, each sensitivity function stays below its frequency weights (in the same color), leading to proper satisfaction of the frequency criterion. The sensitivity function stays below the $\frac{\gamma}{w_1}$ in the whole frequency range and the dynamics of the correction stays in the increasing slope, where the error gain is low in lower frequencies, leading to a high gain of control action in lower frequencies to satisfy the dynamic tracking control. The complementary sensitivity function behaves as desired through $\frac{\gamma}{w_3}$ (green). In addition, the control effort presents the resonance and anti-resonance to tackle the vibrational modes, and the gain of the control effort stays far below the frequency weights (red), meaning the respect of the limitation due to actuator saturation.

4.4.2 Time-domain analysis

The time-domain analysis assesses the performance of the closed-loop system and validates the assumptions made through frequency weights. Along with the tracking performance, modal parametric robustness also has to be considered. The simulations have been realized via the time domain simulator of Figure 3-3, with the parametric model of Eq. 4-9 by using the nominal values. Figure 4-12 illustrates the tracking performance of the standard H_∞ controller between 5 and 100 Hz, with a sweep rate of 3 octaves/minute.

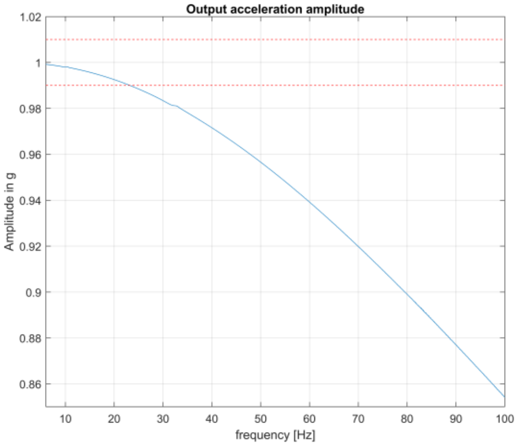

Figure 4-12 - Large spectral tracking via standard H_∞controller

Standard H_∞ controller keeps the error below 1% up to 25 Hz of the simulation. Therefore, in the following sections, we only focus on the first mode of the satellite (see section 4.3.2), with the range of the test between 5 to 20 Hz. This result is extended to the large spectral tracking control in the chapter 6.

4.4.2.1 Tracking performance

Figure 4-13 shows the comparison of the tracking performance of the current nonlinear control versus the H_∞ control. In the case of VTS, the frequency of the reference $cola$ is a function of time (see Eq. 2-2). Therefore, the time-domain performance of the following figures is shown as a function of frequency instead of time to analyze the influence of the mode frequencies on the system's performance.

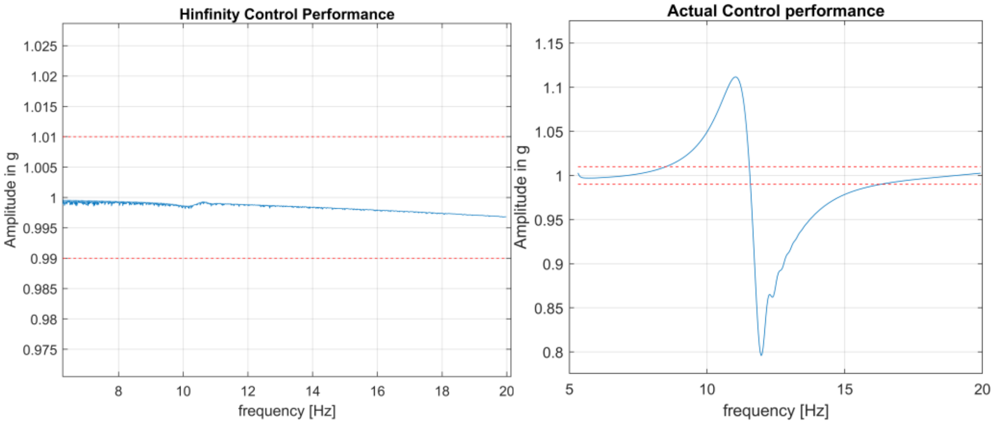

Figure 4-13 - Tracking performance comparison between nonlinear and H-infinity control

As observed in the feasibility study, the H_∞ control (left) shows very promising performance in the case of a real composite model. The tracking error is below 1%, while the nonlinear control (right) leads to a degraded performance with an overshoot of 11% and an undershoot of almost 20%. The $cola$ reference starts at 5 Hz and ends at 20 Hz, and the systems sampling frequency is set to 12k Hz. Therefore, the low-frequency periods of the signal contain more sampling points. While estimating the maximum amplitude of the result (left of Figure 4-13) at lower frequencies, the concentrated sampling points result in noises, though it is not from the closed-loop performance of the H_∞ control. Therefore, the tracking performance validates the frequency domain design criteria and so, the closed-loop requirement.

4.4.2.2 Control effort

Figure 4-14 shows the control effort needed to obtain satisfactory performance.

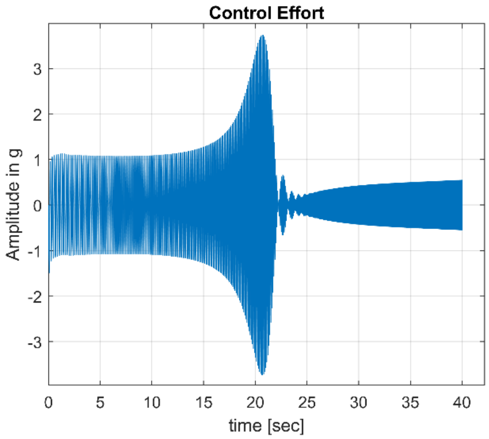

Figure 4-14 - Control effort

In the case of the real composite model, the control effort is remarkably small (max: 3.8g). The sensitivity analysis of the Figure 4-11 shows that the gain of the sensitivity loop KS is very low compared to the limit of 75g; therefore, the current simulation value (3.8g) justifies such a low gain. Even though the acceleration limit (75g) of the electromagnetic actuator seems very high compared to the demand (3.8g), it is important to note that the identified model of the satellite corresponds to the lightest among the Spacebus NEO product lines. Therefore, the heaviest of the same product line or scientific satellites/objects with onboard rovers would necessitate very high control effort. As a consequence, our study generalizes the procedure for all types of large space structures by attributing the control effort constraints in the design of the controller.

4.4.2.3 Parametric robustness

The parametric robustness is essential in an industrial system as the identification of the modal parameters is not perfect and comes with uncertainties. The VTS system needs to be robust, as explained in section 4.3.1 and the use of a reduced-order model also induces some mismatch with respect to the full order model (section 4.2). The reformulation of the model of Eq. 4-9 in terms of modes enables to vary parameters and observe the robustness of the H_∞ control. The first modal parameters (Ω_1, ξ_1) of the parametric model Eq. 4-9 will be considered for the study. The parameters are varied from a smaller value to a reasonable higher value to see the influence on the output acceleration.

4.4.2.3.1 Variation of the damping ratio

Firstly, a mismatch in the damping ratio is considered where the first mode damping ratio (0.04) is dispersed into the limit of $\pm 25\%$ in the parametric model of Eq. 4-9 given by the specification of section 4.3.1. Figure 4-15 illustrates the output acceleration evolution and thus the controller performance against damping ratio variation.

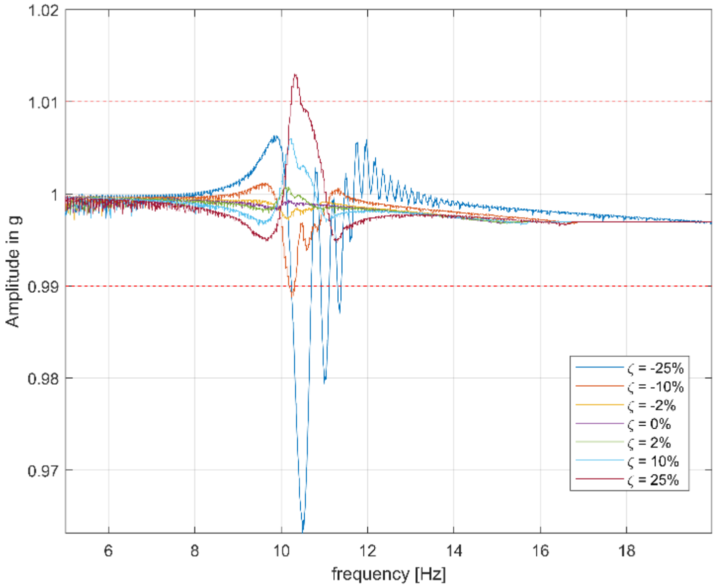

Figure 4-15 - Robustness against damping ratio variations

In Figure 4-15, the simulation result shows the influence of damping ratio variations, where the smaller damping means the worst case (-25%). The simulation result shows that the lightest damping factor (-25%, in blue) corresponds to an undershoot error of 4%, while -10% of dispersion (deep red) resulted in an overshoot slightly crossing the 1% limit, signifying that the lightest damping corresponds to the worst case. In the presence of other dispersion values, the output acceleration error is kept under 1%. In terms of robust control, the bigger the damping factor, the better is the scenario for robustness. Though results show overshoot (1.1%) and undershoot (4%) in case of damping ratio variation, it stays remarkably low compared to the performance of the current control algorithm for a nominal case (see Figure 4-13). Moreover, the results are also compatible with the performance obtained in the case of S-DoF (see 3.6.2.3), which illustrates the robustness of H_∞ controller against the damping ratio variation.

4.4.2.3.2 Variation of the natural frequency

Secondly, the robustness against the natural frequency variations of the mode position is assessed through the variation of Ω_1 in Eq. 4-9. The plant is dispersed very slightly as only $\pm 2\%$ of the nominal value (11.31 Hz), and the results are out of the accepted error specification (1%). Figure 4-16 illustrates the robust performance of the H_∞ controller.

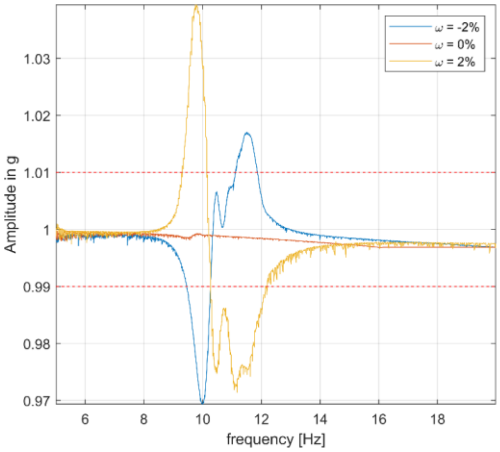

Figure 4-16 - Robustness against mode position uncertainties

As little as a $\pm 2\%$ of modal frequency variation results in degraded performance and in an output acceleration that crosses the limit of $\pm 1\%$ error required for the VTS. An industry-grade requirement (see section 4.3.1) where the mode position can vary up to $\pm 15\%$, the simulation results show the output acceleration getting far from the required accuracy; therefore, results are irrelevant to illustrate here. Consequently, the standard H_∞ control on a real composite model shows the high sensitivity of the control and conservatism, resulted in unacceptable performance. The pole-zero compensation of the H_∞ controller is the reason for this modal parameter sensitivity, also observed in the controller designed for the S-DoF model in the previous chapter. Therefore, the next chapter will tackle the robustness issue of the H_∞ mixed sensitivity control.

4.5 CONCLUSION

In this chapter, an optimal parametric model of the composite has been synthesized from a discrete-time full order estimated plant model. The parametric model lets us disperse modal parameters, and the optimal plant model ensures a minimal order controller. The main contribution of this chapter is to extend the result of the previous chapter treating the dynamic tracking error performance of the VTS along with other specifications of the system via general frequency domain weights on the real satellite-interface composite model. Therefore, the general definitions of these weights are used to generate a standard formulation of the H_∞ control problem. The time-domain simulation using a nominal plant model satisfies the required performance as described through frequency constraints, which validates the constraint definition for the dynamic tracking error. Yet, the standard H_∞ controller cannot guarantee the performance of large spectral dynamic tracking rather than a part of the frequency ranges. Therefore, the study of this chapter concerns 5 to 20 Hz of frequency of dynamic tracking satisfying the specification of the tracking accuracy, which includes the first mode of the satellite. The further development of the large spectral tracking issue is discussed in the chapter 6. Although, the standard H_∞ control seems to show a certain degree of robustness against the damping ratio variations, the closed-loop system exhibits a high sensitivity to variations of the modal frequency even in the case of slight variations. Therefore, the standard H_∞ control scheme cannot completely satisfy the industrial criteria of robustness against modal parameter variation, which motivates the development of a more robust strategy presented in the next chapter.

5 ROBUSTIFICATION OF VTS

5.1 INTRODUCTION

The previous chapters show a systematic way of addressing dynamic tracking error minimization on a real identified satellite-interface composite model through general frequency domain weights in a mixed sensitivity H_∞ synthesis framework. Considering the nominal plant without any mismatch on the process model provides satisfactory results. As stated in section 4.2, the dynamics of the identified system through low-level test would mismatch from a high-level test in accordance with the reference amplitude as the mode position would shift, and the damping ratio would be different according to the level of the reference amplitude (Bettacchioli & Nali, 2015). In addition, the reduced-order synthesis model would cause a mismatch from the full order estimated one (section 4.2.1). Therefore, the implemented control algorithm shall tackle these modal parameters uncertainties and provide satisfactory performance in a real-world VTS. Yet, the standard H_∞ synthesis shows poor performance when varying modal parameters (section 4.4.2.3). This chapter is dedicated to the development of a robust solution to the dynamic tracking problem in an industrial-level VTS.

5.2 LITERATURE REVIEW

In the literature, the robustness against modal parameter variations of a system, including lightly damped modes, has been hugely studied (Alazard, et al., 1999) (Balas, 1990). In the same literature, the mixed sensitivity solutions are addressed, which generally comes with a specific type of controller named central compensator, as it creates a resonance to cancel anti-resonance, and also the same dynamics of anti-resonance to cancel a resonance of a mechanical system. In Figure 3-10 and Figure 4-9, the synthesized controllers behave as stated in the literature. In other words, this problem is also known as pole-zero compensation by mixed sensitivity solutions (Tsai, et al., 1992) (Apkarian, 1993) and several publications also show possibilities to counter such issue. Firstly, the direct LMI based applications can solve the pole-zero compensation problem (Apkarian & Gahinet, 1994). Then the LMI based mixed H_2/H_∞ optimization gives the possibility to introduce an additional constraint on the poles and zeros of the closed-loop system to avoid synthesizing a central compensator by mainly increasing the damping factor of the controller (Chilali & Gahinet, 1995). These solutions work perfectly when the system tackles a regulation problem limited to disturbance and noise reduction. The increased damping factor of such controller would have the same properties as those of the central compensator for all frequency ranges except the neighborhood of the mode, where the constrained controller would have smaller resonance (or anti-resonance). The increase of the damping factor results in higher robustness against modal parameters, and at the same time, the loss of performance stays in the tolerable limit. In the case of tracking problems as in VTS, this increased damping factor results in a total loss of performance near the vibrational mode and consequently, these methods are not suitable for robustification of a VTS.

The H_∞ control is known to be conservative in terms of parametric stability and robust performance as it does not allow introducing structured uncertainties of the system (Skogestad & Postlethwaite, 2001). Some publications show prominent results of some control methods having the possibility to synthesize optimal controllers by introducing parametric uncertainties in the optimization process. (Alazard, et al., 1999) shows a parameter robust LQG (PRLQG), where the structured uncertainties are integrated within the synthesis procedure in a regulation problem. This study also shows the same regulation problem solved via μ-synthesis controller allowing also to integrate the parametric uncertainties in the optimization phase. As both are optimal controls based on H_2 and H_∞ optimization, the results seem to be very similar in terms of performance (Alazard, et al., 1999). Both of these control strategies address the structured uncertainties in the synthesis and create the worst-case scenario by varying modal parameters; therefore, the synthesized controller satisfies this worst case of the plant dynamics. These methods decrease the conservatism in the controller (Alazard, et al., 1999) of the mixed sensitivity H_∞ central-compensator by increasing damping factor of the corresponding resonances and anti-resonances. Though the solution satisfies the regulation problem, it will always tradeoff performance to reduce the conservatism. In (Balas, 1990), the study also shows a modal parameter robust μ-synthesis, which satisfies the criteria in a regulation problem but the performance is always degraded when comparing with H_∞ nominal case. The main difficulty of the studied case is the absence of literature on the application of parameter robust tracking control, as a little desensitization of the controller from the nominal H_∞ control would result in an important performance degradation of a rapid system like VTS.

At this stage, the first focus of this study is to extend the standard H_∞ problem to a μ-synthesis optimization in order to evaluate the performance of a desensitized control. As shown in (Alazard, et al., 1999), a correctly designed control by both μ-synthesis and PRLQG provides similar results; therefore, this PRLQG solution will not be developed in this study. In addition, if the system contains two modes sufficiently close to each other, in the set of plants (used for μ synthesis) where the modal frequency of the two modes are dispersed to their limit, the highest taken frequency dynamics of the first mode would coincide with the lowest taken frequency dynamics of the second mode; therefore, this structured uncertainty of frequency variation modeling will completely fail obtaining the worst-case scenario, and the desensitized μ controller will completely fail to perform desirably. The variation of this mode frequency is similar to the structural, mechanical term "pole-zero flip-flop" (Preumont, 2018), where the poles and zeros exchange the position due to the mode frequency uncertainty. Analytically, the exact solution of a high precision very fast-tracking problem with mode position uncertainty would necessitate a solution alike the mixed sensitivity H_∞ central-compensator, where the resonance and anti-resonance part of the central compensator would track appropriately in the case of a nominal plant, as shown further. In case where the mode position of the real plant mismatches from the nominal plant, the resonance/anti-resonance of H_∞ central-compensator will no longer compensate the anti-resonance /resonance of the real plant. The first approach goes to an H_∞ adaptive control in which the resonance/anti-resonance frequency changes to adapt to the real plant dynamics. Undoubtedly, this approach will require a real-time, very precise estimation of the mode position changes, ending up with an extremely high complexity of the closed-loop system. Another approach would consist of introducing an additional control gain to the central compensator, which can add an extra gain to the system in case of any frequency shift of the mode position in the real plant, which will result in tracking error reduction. In a tracking problem, the use of feedforward action is common in the literature (Tung & Tomizuka, 1993) (Ben-Gurion, Cousework) to anticipate the command, which lets the feedback control gain to reduce tracking error and noises. In addition, the two DoF feedforward control results in superior tracking performances (Vilanova, 2008) (Ling, et al., 2018), though neither the feedforward nor the 2 DoF feedforward control is addressed to tackle modal parametric uncertainties. In our research, the study develops a combined feedforward - 2 DoF feedback mixed sensitivity based H_∞ controller to tackle the very rarely addressed modal parameter robust tracking of VTS issue. In this chapter, the comparison between these two methods will demonstrate their advantages and disadvantages in order to select the most suitable one for real-time VTS.

5.3 SPECIFICATION & FREQUENCY DOMAIN CONSTRAINTS

In section 3.5.1, the description of the industrial specification was given, and in the previous chapter (section 4.3.2), frequency domain weights were introduced to address the dynamic tracking requirement and also the regulation issues. In this chapter, we extend the work of the previous chapter, and the main goal is to robustify the standard mixed sensitivity control against modal parameter variations. Therefore, an extended version of typically mixed sensitivity H_∞ control (see Figure 3-5) with feedforward and 2-DoF feedback structures introduced in this chapter in which the same generalized frequency domain weights can be used to achieve the robust performance of the system.

5.4 FEEDFORWARD-FEEDBACK CONTROL

The robustness against modal position variations in a tracking control is rarely studied in the literature, though the same issue in a regulation problem can be found in many references (Alazard, et al., 1999) (Apkarian, 1993) (Preumont, 2018). In our study, the mixed sensitivity H_∞ control seems to be promising for specifically the excellent precise tracking performance in a nominal case, though in the presence of modal position variation, the superior performance is completely degraded (section 4.4.2.3). The main motivation here is to anticipate the command as it will increase the rapidity of the closed-loop system. At the occasion of a mismatch of modal positions between the nominal plant and real plant, the feedback controller will be used to keep the dynamic error sufficiently small for precise tracking. Therefore, the proposed strategy consists of firstly anticipating the command via a feedforward control as feedforward controls are well known for rapid responsiveness. The feedforward control is taken into account in the H_∞ control synthesis in order to use the feedback gain only for dynamic error reduction. Before getting into the 2-DoF controller, a single DoF feedback-feedforward control structure has also been studied. The drawback of the a single DoF feedback-feedforward control system will later on, motivate the study a two DoF control scheme.

5.4.1 1-DoF Feedback architecture with Feedforward control

Figure 5-1 shows the architecture of such a control system used in the study.

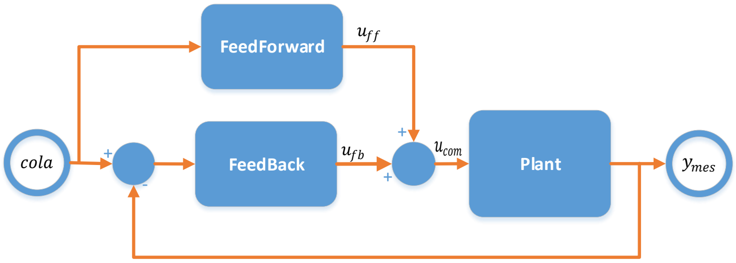

Figure 5-1 - Feedforward S-DoF feedback control system

Figure 5-1 shows the feedforward control, achieved from the reduced order plant model given by Eq. 4-9. The model of Eq. 4-9 is proper and zeros are stable, which let inverse the model to determine the feedforward controller K_{ff}, given by Eq. 5-2. The control effort u_{com} is the sum of feedforward effort u_{ff} and feedback effort u_{fb}. y_{mes} is the output measured acceleration.

5.4.2 H_∞ 1-DoF feedback control synthesis

In the following study, the control design follows the similar procedure as explained in the previous chapter, additionally the feedforward action is taken into account in the design (which is basically the inverse of the reduced nominal model of the system dynamics). Figure 5-2 illustrates the synthesis model.

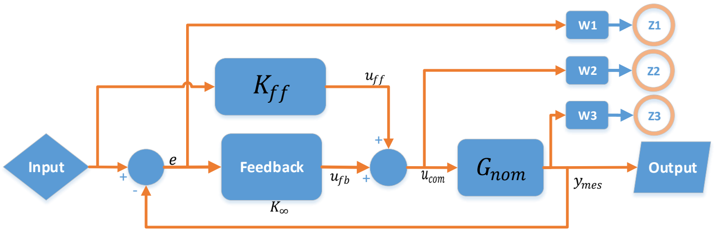

Figure 5-2 - 1-DoF synthesis model

Three generalized frequency domain design constraints w_1, w_2 and w_3 detailed in chapter 3 and 4 are used to constrain successively the dynamic tracking error, control effort limitation and noise filtering. The G_{nom} is the optimal order plant given by Eq. 4-9. The controller $K_\infty(s)$ has to satisfy performances induced by frequency domain weights. By taking out the controller from augmented model of Figure 5-2, the LFT is given by Eq. 5-1.

$$\begin{bmatrix} Z_1 \\ Z_2 \\ Z_3 \\ y \\ e \end{bmatrix} = \begin{bmatrix} (w_1 - w_1 G_{nom} K_{ff}) & -w_1 G_{nom} \\ w_2 K_{ff} & w_2 \\ w_3 G_{nom} K_{ff} & w_3 G_{nom} \\ G_{nom} K_{ff} & G_{nom} \\ (1 - G_{nom} K_{ff}) & -G_{nom} \end{bmatrix} \begin{bmatrix} R \\ u_{fb} \end{bmatrix} \qquad \textit{Eq. 5-1}$$

From Eq. 5-1, the procedure to formulate the H_∞ control problem is same as it is detailed in 3.4.2.2. A single DoF feedback control with feedforward action resulted a γ of 50, meaning the optimization criteria are far from satisfaction; therefore, the performances.

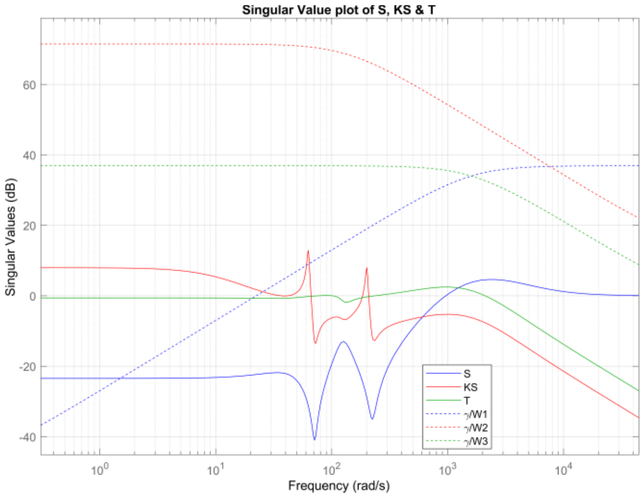

Figure 5-3 - Sensitivity functions vs frequency weights

Figure 5-3 shows the frequency responses of all three sensitivity functions (continuous lines) versus corresponding frequency weights in the same color (dotted lines). The optimized γ is 50, therefore, in Figure 5-3 the sensitivity functions are much lower than their corresponding weights, signifying that the obtained γ is not optimal. Therefore, the time domain performance is far from achieving the requirements, neither in the nominal cases nor it shows any robustness against modal position variation. The study of this control structure is summarized here without going into details as it does not fulfill the requirements, but it shows the way and motivation towards a 2-DoF controller. The 2 DoF feedback controller is addressed in the literature for precision control (Guo, et al., 2009), therefore, in our study, it seems to also help achieving the H_∞ optimal solution with an optimal γ.

5.4.3 Closed-loop system architecture in a 2-DoF formulation

The proposed architecture of Figure 5-4 uses an additional feedforward action, which is the inverse of the nominal plant model as explained in the previous section (see Eq. 5-2), to deliver an accurate anticipative command to the actuator. The multivariable two-input one output feedback controller is used to compensate tracking error, noise and disturbance. This structure will facilitate the design of the robust controller, leading to an increase in the system's robustness against modal parameter variations. In general, this strategy increases the bandwidth of the control through feedforward action and also the gain of correction via the second degree of freedom, solving the issue of pole-zero compensation of a lightly damped structure.

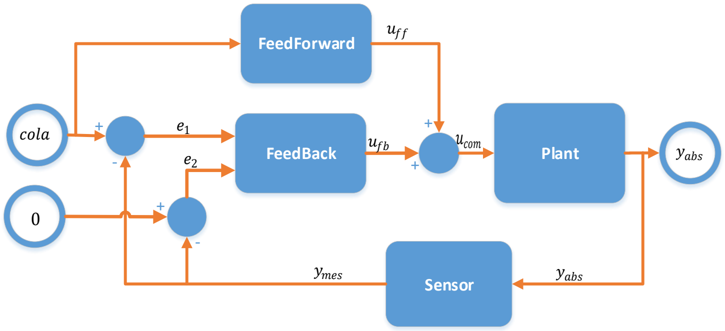

Figure 5-4 – Proposed 2-DoF closed-loop system architecture

The first reference input is $cola$ and the second one is a constant value of 0, which emphasizes the cancellation of the disturbance impact on the output. The errors associated to the references are denoted respectively by e_1 and e_2. The control effort, u_{com}, is the sum of the feedforward action, denoted u_{ff}, and the feedback action denoted u_{fb}. y_{abs} and y_{mes} are the real and measured output acceleration.

5.4.4 H_∞ 2-DoF feedback control synthesis

Firstly, the industrial specifications are transformed into generalized frequency domain weighting functions in order to derive an optimization problem formulation (section 4.3.2). Figure 5-5 defines the closed-loop synthesis model augmented from the basic model of Figure 5-4 with the definition of all necessary weights. The synthesis model of Figure 5-5 is the nominal one.

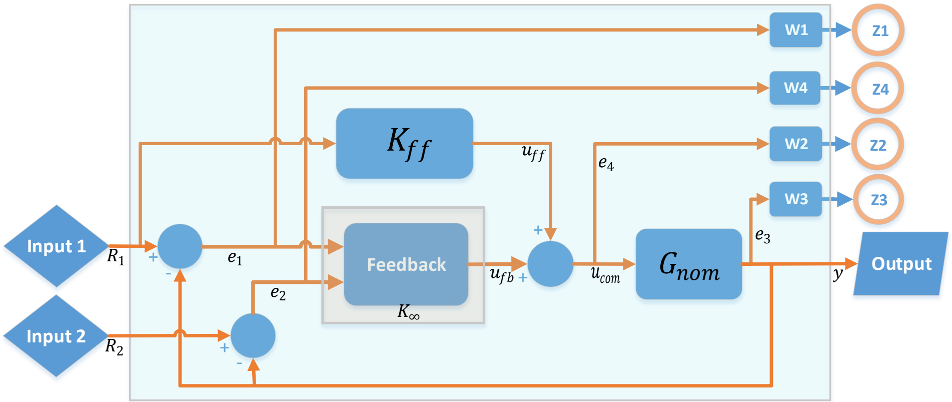

Figure 5-5 – 2-DoF synthesis model

In Figure 5-5, the output signal is $y = y_{mes}$. The frequency-domain constraints are imposed on the system via four weighting functions, denoted w_1, w_2, w_3 and w_4.

The feedforward controller $K_{ff}(s)$ is defined by:

$$K_{ff}(s) = G_{nom}(s)^{-1}$$

Eq. 5-2

where $G_{nom}(s)$ is the plant dynamics obtained from Eq. 4-9 with the nominal values of (Ω_1, ξ_1) and (Ω_2, ξ_2). As mentioned in the previous section, the model G_{nom} has stable poles and zeros and it is a proper order transfer function; therefore, K_{ff} is stable and proper. The feedback controller composed of two inputs and an output ($K_\infty = [K_{11} \quad K_{12}]$), the feedback control effort is given by following equation.

$$u_{fb}(s) = K_{11}e_1 - K_{12}y \qquad \text{Eq. 5-3}$$

5.4.4.1 Problem formulation

The controller $K_\infty(s)$ has to satisfy the performance criteria defined by frequency-domain weights. By separating the control block from the rest of the augmented model of Figure 5-5, we may obtain the lower LFT, Figure 5-6 illustrates the scheme of the LFT of the given problem.

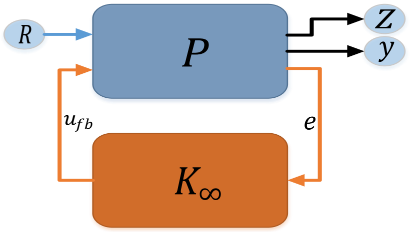

Figure 5-6- LFT model

In Figure 5-6, $R = [R_1 \;\; 0]^T = [cola \;\; 0]^T$ is the reference input, $e = [e_1 \;\; e_2]^T$ is the tracking error and $Z = [z_1 \;\; z_2 \; z_3 \; z_4]^T$ is the exogenous output. The LFT associated to Figure 5-6 can be written as:

$$\begin{bmatrix} Z \\ y \\ e \end{bmatrix} = P(s) \begin{bmatrix} R \\ u_{fb} \end{bmatrix} \qquad \text{Eq. 5-4}$$

The expression of $P(s)$ obtained from Figure 5-6, is given below.

$$P(s) = \left\{ \begin{matrix} (w_1 - w_1 G_{nom} K_{ff}) & 0 & -w_1 G_{nom} \\ w_2 K_{ff} & 0 & w_2 \\ w_3 G_{nom} K_{ff} & 0 & w_3 G_{nom} \\ -w_4 G_{nom} K_{ff} & w_4 & -w_4 G_{nom} \\ G_{nom} K_{ff} & 0 & G_{nom} \\ (1 - G_{nom} K_{ff}) & 0 & -G_{nom} \\ -G_{nom} K_{ff} & 1 & -G_{nom} \end{matrix} \right\} \qquad \text{Eq. 5-5}$$

P is the augmented model of Figure 5-6 and K_∞ is the feedback controller, then the LFT between P and K_∞ can be denoted by $F(P, K_\infty)$.

The main particularity of this problem formulation is to include the feedforward action in the control synthesis, and at the same time, the 2 DoF feedback control works as a multivariable two input one output controller. By considering two identical outputs and one input of the composite plant, $\mathbb{G} = [G \quad G]^T$, matched with the combined two inputs one output feedback controller $K_\infty = [K_{11} \quad K_{12}]$, the closed-loop system is a multivariable system, which will introduce similar sized sensitivity and complementary sensitivity matrices ($\mathbb{R}^{2\times2}$) to facilitate the analysis later on. Therefore, the sensitivity functions are transfer matrices.

5.4.4.1.1 Sensitivity matrix

The sensitivity matrix $S_2 \in \mathbb{R}^{2\times2}$ is given by:

$$S_2 = [I_2 + \mathbb{G} \times K_\infty]^{-1} = \left[\begin{bmatrix} 1 & 0 \\ 0 & 1 \end{bmatrix} + \begin{bmatrix} G \\ G \end{bmatrix} \times [K_{11} \quad K_{12}]\right]^{-1} \qquad \textit{Eq. 5-6}$$

In Eq. 5-6, I_2 is a 2×2 identity matrix, Eq. 5-6 can be simplified by determining the inverse matrix:

$$S_2 = \begin{bmatrix} S_{11} & S_{12} \\ S_{21} & S_{22} \end{bmatrix} = \frac{1}{1 + G(K_{11} + K_{12})} \begin{bmatrix} 1 + GK_{12} & -GK_{12} \\ -GK_{11} & 1 + GK_{11} \end{bmatrix} \qquad \textit{Eq. 5-7}$$

5.4.4.1.2 Complementary sensitivity matrix

The complementary sensitivity matrix $T_2 \in \mathbb{R}^{2\times2}$, is given by:

$$T_2 = I_2 - S_2 \qquad \textit{Eq. 5-8}$$

Eq. 5-8 can be written as:

$$T_2 = \begin{bmatrix} T_{11} & T_{12} \\ T_{21} & T_{22} \end{bmatrix} = \begin{bmatrix} \dfrac{-GK_{12}}{1 + G(K_{11} + K_{12})} & \dfrac{GK_{12}}{1 + G(K_{11} + K_{12})} \\ \dfrac{GK_{11}}{1 + G(K_{11} + K_{12})} & \dfrac{-GK_{11}}{1 + G(K_{11} + K_{12})} \end{bmatrix} \qquad \textit{Eq. 5-9}$$

5.4.4.1.3 Sensitivity related to the control effort

The sensitivity related to the control effort $K_\infty S_2 \in \mathbb{R}^{1\times 2}$, is given by:

$$K_\infty S_2 = \begin{bmatrix} K_{11} & K_{12} \end{bmatrix} \begin{bmatrix} S_{11} & S_{12} \\ S_{21} & S_{22} \end{bmatrix}$$

Eq. 5-10

The final expression is given in Eq. 5-11

$$K_\infty S_2 = \frac{1}{1 + G(K_{11} + K_{12})} \begin{bmatrix} K_{11} & K_{12} \end{bmatrix}$$

Eq. 5-11

Eq. 5-7, Eq. 5-9 and Eq. 5-11 give different sensitivity matrices for the MISO system, though we impose SISO criteria. Therefore, we only constrain one sensitivity function from each S_2, T_2 and $K_\infty S_2$. Definitions of different sensitivity functions of this specific synthesis case are given by:

- Sensitivity function S_{11} between e_1 and R_1, we restrain this function from minimizing the dynamic tracking error of the input $cola$ via the weight w_1
- Complementary sensitivity function T_{11} between e_3 and R_1 ($cola$), is used to constrain the effect of sensor noise via the weight w_3
- The first component of $K_\infty S_2$ (noted KS_1) between e_4 and $R_1(cola)$ is used to limit the control effort via the weight w_2
- The additional sensitivity functions for the second loop of the control system (Figure 5-5) between e_2 and R_2 are only used to achieve an optimal solution of the H_∞ problem, so the weight w_4 does not contain any frequency restriction and, is set to unity gain. In case the system requires more noise filtering, this second loop or second degree of freedom can be used to restrain further noise filtering on the sensor/estimator data via the weight w_4.

By the application of the small gain theorem (Zhou, et al., 1996), we can obtain the design criteria, as follows:

$$\begin{cases} \bar{\sigma}\big(S_{11}(s)w_1(s)\big) & < \gamma \\ \bar{\sigma}\big(KS_1(s)w_2(s)\big) & < \gamma \\ \bar{\sigma}\big(T_{11}(s)w_3(s)\big) & < \gamma \end{cases}$$

Eq. 5-12

where $\bar{\sigma}$ is the upper singular value and $\gamma > 0$. The H_∞ feedback controller is obtained by minimizing $\|F(P, K_\infty)\|_\infty$ for the set of $K_\infty(s)$ which stabilizes the internal states of the system. The minimum gain is called H_∞ optimal gain γ_{opt}. From Eq. 5-12, we deduce the sufficient condition of the optimization problem:

$$\|F(P,K)\|_\infty = \left\| \begin{matrix} S_{11}(s)w_1(s) \\ KS_1(s)w_2(s) \\ T_{11}(s)w_3(s) \end{matrix} \right\|_\infty < \gamma_{opt}$$

Eq. 5-13

In Eq. 5-13, the optimization problem is similar to the mono-variable control scheme of chapter 4, as the frequency domain constraint w_4 is not imposed. So, the multi-variable control problem has been optimized using the mono-variable weights.

5.4.5 Synthesized controller

The optimization problem has been solved with an optimal γ of 0.98, unlike the scheme containing the feedforward and single DoF feedback control, considering a very high γ (almost 50). The synthesized controller presents 13th order stable dynamic (real parts of poles are all negative) as the sum of orders of 5th order plant, 5th order feedforward control and three additional order from three weights of 1st order each. Figure 5-7 shows the frequency response of two-input single-output controller.

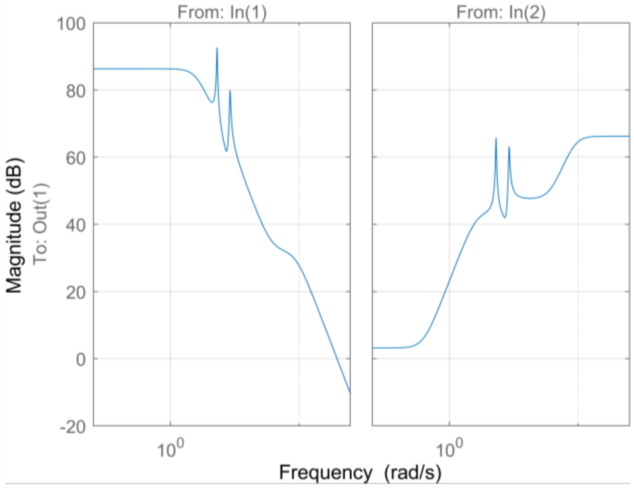

Figure 5-7 – First input vs. output (left), second input vs. output (right)

In Figure 5-7, the first input vs. output loop illustrates a similar dynamic as they are determined with the single DoF controller in chapter 4. The second input to output seems to be quite different from the first one; it basically helps solve the optimization problem by adding an extra gain to the command. Though it adds an extra gain to the command, the total command stays below the saturation (The constraint on the control effort is well respected). The controller can be represented by:

$$K_\infty = [K_{11} \quad K_{12}]$$

Eq. 5-14

Then the total feedback control effort u_{fb} can be written as a function of the error e_1 and e_2, given by:

$$u_{fb} = K_{11}e_1 + K_{12}e_2$$

Eq. 5-15

Without including the structured uncertainties of modal parameters, the second DoF adds gain in case an error occurred by any mismatch of real model from the nominal plant model. Therefore, the system is less sensitive to modal parametric variations, and the performance will be assessed in the time domain simulation later in this chapter. Table 5-1 gives the poles of the controller and associated frequencies and damping ratios.

In Table 5-1, the real parts of all poles are strictly negative; therefore; the controller dynamic is internally stable. When comparing to the one DoF controller deigned in previous chapter (see Table 4-2), the two DoF controller counts the feedforward action, adding 5 five more orders to the previous one. The fourth and fifth poles are same as the one DoF controller, but sixth and seventh poles are added to counter the second resonance of the feedforward action, tenth and eleventh are for the first mode.

Table 5-1 - Poles of the 2-DoF controller

Poles	Associated values	Frequency (r/s)	Damping ratio
1	$-1.1 \times 10^5 + 9.7 \times 10^3 i$	1.1×10^5	0.99
2	$-1.1 \times 10^5 - 9.7 \times 10^3 i$	1.1×10^5	0.99
3	-1.1×10^5	1.1×10^5	1
4	$-4.4 + 2 \times 10^2 i$	201	0.02
5	$-4.4 - 2 \times 10^2 i$	201	0.02
6	$-5.7 + 2 \times 10^2 i$	204	0.03
7	$-5.7 - 2 \times 10^2 i$	204	0.03
8	$-1.3 + 63i$	63.3	0.02
9	$-1.3 - 63i$	63.3	0.02
10	$-1.3 + 63i$	63	0.02
11	$-1.3 - 63i$	63	0.02
12	-10.4	10.4	1
13	-10.5	10.5	1

5.5 FREQUENCY DOMAIN ANALYSIS

In this section, the sensitivity analysis of 2-DoF H_∞ controller will show the satisfaction of frequency domain constraints versus the corresponding optimized sensitivity functions. In the case of 2 DoF multivariable controller, sensitivity functions (given by Eq. 5-7, Eq. 5-9, Eq. 5-11) and corresponding weights are given in Figure 5-8.

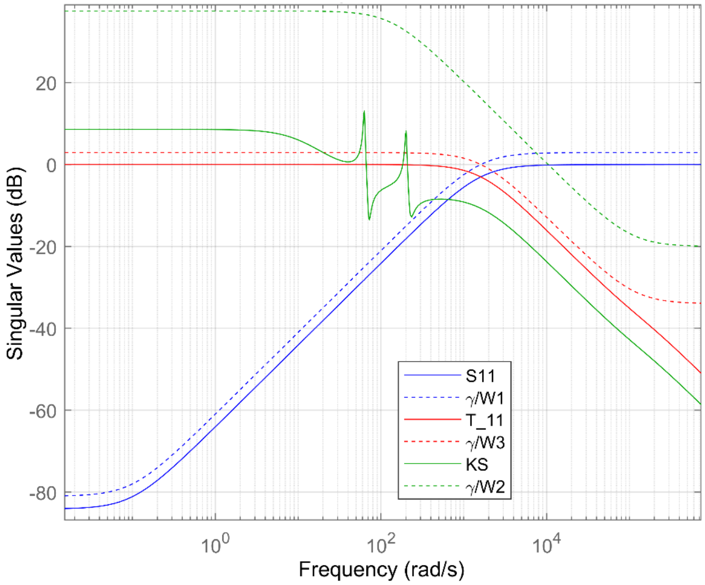

Figure 5-8 - Sensitivity functions (continuous) vs weights (dotted)

Figure 5-8 illustrates sensitivity functions (continuous line) versus the corresponding frequency-domain weights (dotted lines). The optimization has been solved with a satisfactory $\gamma = 0.99$, therefore, all sensitivity functions are below their weights, meaning a proper satisfaction of the specifications. Moreover, the $K_\infty S_2$ being much lower than the weight $\frac{\gamma}{W_2}$ signifies that the control effort will be much lower than the actuation capacity in the frequency range of error correction.

5.5.1 Stability margin assessment

The closed loop system architecture with two inputs and one output feedback controller studied in this chapter constitutes a multivariable loop where the system stability cannot be obtained through the approach of classical stability margins. In general, in the case of the multiloop control linear feedback system (Gahinet, et al., 2020), the stability margin can be obtained via the unstructured small gain theorem, which mainly computes the guaranteed stability of the multivariable closed-loop system. Stability margins are defined directly from the feedback-loop, where the feedforward controller does not participate in the margin computation. Figure 5-9 illustrates the feedback closed-loop system without the feedforward control.

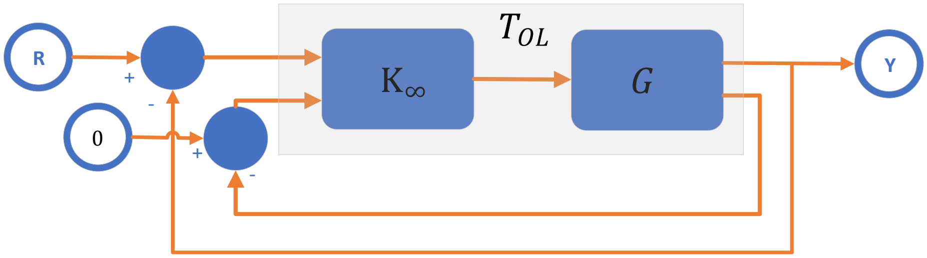

Figure 5-9 - Feedback loop

The open-loop two-input two-output function (gray rectangle in Figure 5-9) is given by:

$$T_{OL} = G\mathrm{K}_\infty$$

Eq. 5-16

In Eq. 5-16, $T_{OL} \in \mathbb{R}^{2\times 2}$ the open loop system, $G \in \mathbb{R}^{1\times 2}$ the plant model and $\mathrm{K}_\infty \in \mathbb{R}^{2\times 1}$ the feedback controller. The closed-loop transfer function $T_{CL} \in \mathbb{R}^{2\times 2}$ of this open-loop system (T_{OL}) can be expressed by:

$$T_{CL} = \ (I + T_{OL})^{-1}$$

Eq. 5-17

By using the unstructured small gain theorem, the guaranteed minimum margin of the two loops is given by:

$$\alpha_{max} = \frac{1}{\sup_{w} \overline{\sigma}(T_{CL})} \qquad \text{Eq. 5-18}$$

In Eq. 5-18, $\overline{\sigma}$ defines the pick singular value of all channels of the closed-loop transfer matrix T_{CL}, therefore the minimum margin α_{max} is the largest value of $\overline{\sigma}(T_{CL})$ over all frequencies. The guaranteed margin obtained via (Eq. 5-18) is $\alpha_{max} \cong 0.71$. α_{max} can be used to deduce the stability margin through the following relations:

$$\begin{cases} \dfrac{1}{1+\alpha_{max}} < GM < \dfrac{1}{1-\alpha_{max}} \\ |\varphi_i| < 2sin^{-1}(\dfrac{\alpha_{max}}{2}) \end{cases} \qquad \text{Eq. 5-19}$$

The stability margin of these methods is differently expressed from the classical margin. In this case, the gain margin is $(-4.4,10.7)_{dB}$ and the phase margin $\pm 41.4°$. The $(-4.4,10.7)_{dB}$ signifies that the closed-loop system can accept a gain reduction up to -4.4 dB or a gain augmentation up to 10.7 dB before being unstable and the same way, the phase margin $\pm 41.4°$ means that the closed-loop system can sustain a phase reduction up to $-41.4°$ and the phase augmentation up to $41.4°$ before being unstable.

5.5.1.1 Stability margin of SISO system

The studied closed-loop system can be considered as a SISO system if the loop is opened just after the control block. Figure 5-10 Illustrates such possibility.

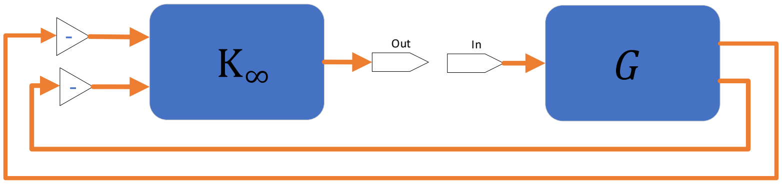

Figure 5-10 - Open-loop system for SISO stability

In Figure 5-10, the closed-loop system is opened just after the K_∞ block, where the transfer function between In and out port is used to evaluate classical gain margin. In Figure 5-11, the Nichols plot of this open-loop transfer function shows the classical gain margin of the system.

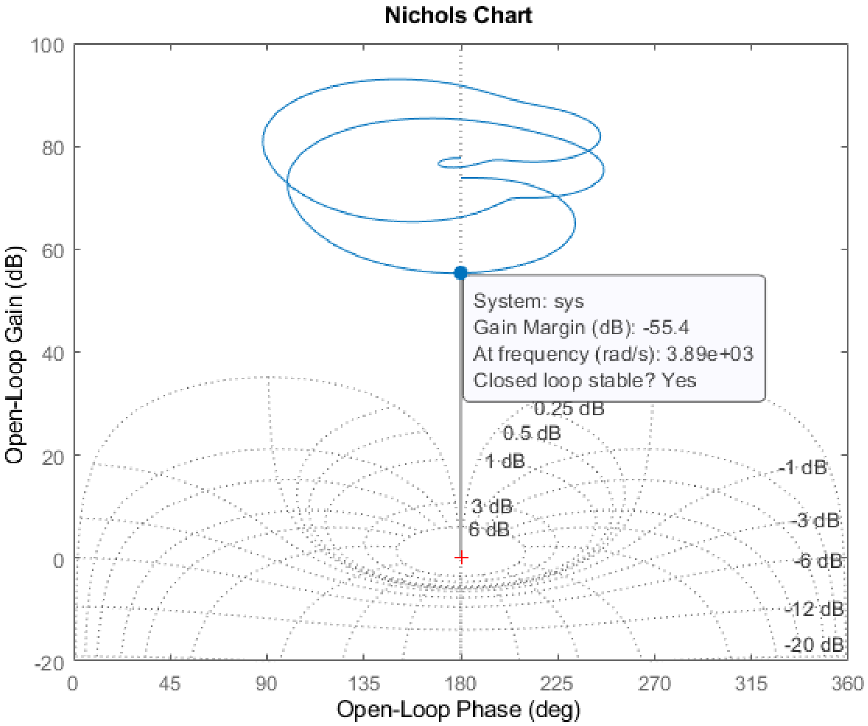

Figure 5-11 - SISO stability margin in nichols plot

In Figure 5-11, the Nichols plot illustrates the stability margin, where at low frequency the gain margin is 55.4 dB and at high frequency infinite, along with an infinite phase margin for all ranges of frequencies. The gain margin obtained from the unstructured small gain theorem is much smaller than the SISO margin, and it is due to the fact that the unstructured small gain theorem captures the worst case to determine the stability margin rather than the fixed gain and phase calculation in the classical stability margin. Therefore, the result obtained via unstructured small gain theorem is more representative than the SISO margin.

5.6 TIME-DOMAIN ANALYSIS

In this section, we assess the performance of the combined H_∞ control in a nominal case as well as the robust performance against the modal parametric uncertainty. The identified composite plant given by Eq. 4-9 already contains the delay from the command signal to the measurement signal (Figure 4-1). Therefore, no additional test has been carried out with regards to additional delay. In this part, we will only limit the study to the first mode and so, the simulations are limited to 20 Hz. The next chapter will generalize the result obtained from this chapter, to several modes.

5.6.1 Performance of the nominal case

5.6.1.1 Tracking performance

The nominal case is obtained from Eq. 4-9 with nominal values of modal parameters identified from Eq. 4-9. Simulations are obtained for the nominal value of the sweep rate 3 oct/min. The combined H_∞ control architecture is given in the Figure 5-4 and Figure 5-12 shows the simulation results.

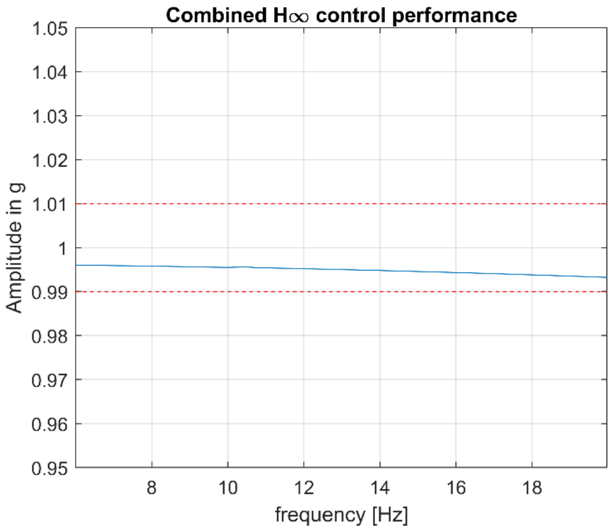

Figure 5-12 - nominal performance of 2-DoF H_∞ control – output acceleration

As shown in chapter 4, the nominal performance of the H_∞ 2 DoF control (Figure 5-12) is similar to the standard H_∞ feedback control (Figure 4-13). In both cases, the output accelerations are within the specification of $\pm 1\%$ tracking error and at the same time, vibrations are completely suppressed from the system. The simulation results along with the optimal H_∞ solution ($\gamma \cong 1$) validate the definition of the frequency domain weights in case of a dynamic tracking correction of lightly damped structures.

5.6.1.2 Control effort

Figure 5-13 illustrates the total control effort (sum of feedforward and feedback) demanded by H_∞ controller. Figure 5-13 shows that H_∞ controller starts without any noticeable initialization phase. It is due to the fact that the 2-DoF feedback controller is more rapid than one DoF controller. The high demand of control effort near 21 sec is due to the antiresonance dynamic, where the controller gain is very high compensating the low gain of the dynamics. Just after the antiresonance, near 23 sec, the control effort decreased enormously as iy passes through the first mode of the satellite, needing very small control effort contrary to antiresonance. The control effort of Figure 5-13 is the sum of feedforward and feedback actions, in the next chapter, these actions are detailed individually.

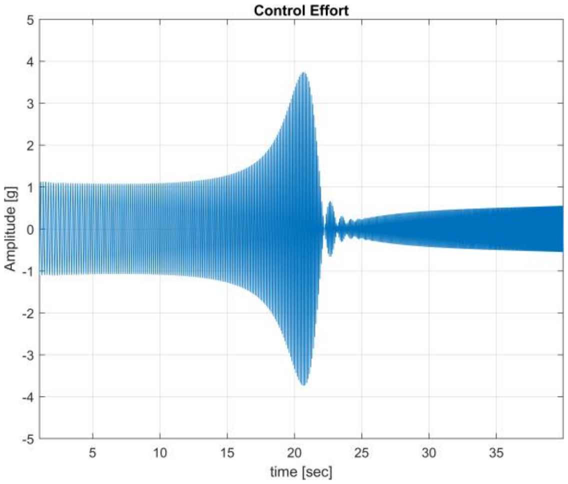

Figure 5-13 - Control effort on demand by H_∞ controller

5.6.2 Robust tracking performance

5.6.2.1 Worst case scenario via scattering at the limit of interval

In this section, the robustness against the modal parameter variations are obtained by varying the first mode parameters (Ω_1, ξ_1) in Eq. 4-9 according to the industrial specifications (see section 2.2.5 and 4.3.1). The robustness analysis has been conducted on the first mode of the satellite to obtain the performance of the different control structures, the next chapter will generalize the solution for all modes of the composite model. Simulations are obtained for the nominal value of the sweep rate 3 oct/min. The first mode frequency is varied up to $(\pm 15\%)$ and the corresponding damping ratio is varied up to $\pm 25\%$. The worst-case scenario of mode position mismatch can be expressed by the case, representing the most frequency shift of the mode to the right/left in frequency domain representation. Therefore, the worst case can be considered to the scenario with maximum mode frequency shift from the nominal position in the frequency domain representation of the composite, without regard to the sign of the variation (both cases of $\pm 15\%$). In case of damping factor variation, the lightly damped dynamics correspond to a higher pick gain of the mode; therefore, the worst-case correspond to -25% of damping variation. As the extreme values of those modal parameters correspond to the worst case, it is unnecessary to take intermediate values of dispersion to obtain robust performances of the system.

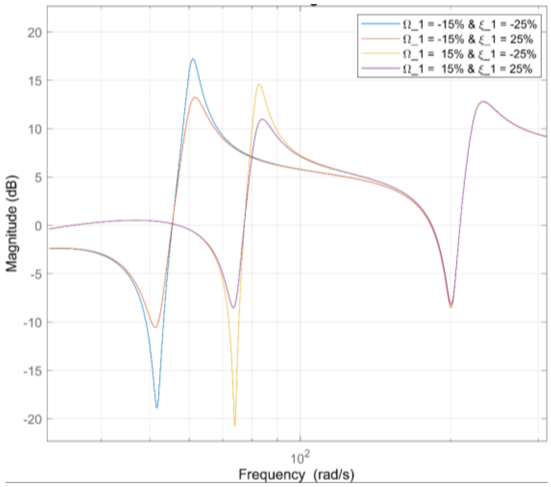

Figure 5-14 - Scattered dynamics

Figure 5-14 illustrates 4 scattered dynamics for extreme modal parameter variations ($\Omega_1 = \pm 15\%, \xi_1 = \pm 25\%$). The modal frequency shift accounts for 9.65 Hz (-15%) and 13.05 Hz (15%), accounting 3.4 Hz of distance of those extreme cases. The corresponding damping factor variations of -25% (of the case where the mode frequency is shifted to the left by -15%) result in a peak gain variation of 3.8 dB at mode frequency. These cases are largely sufficient to analyze the necessary robustness of the VTS.

5.6.2.2 Robust performance of $\mathbf{2}$ $\boldsymbol{DoF}$ $\boldsymbol{H}_{\infty}$ control

Figure 5-15 shows the robust performance of 2-DoF feedforward feedback control system against modal parameter variations. This controller is obtained for the same frequency domain constraints as the one DoF controller and for the nominal plant dynamics, without any structured uncertainties in the model.

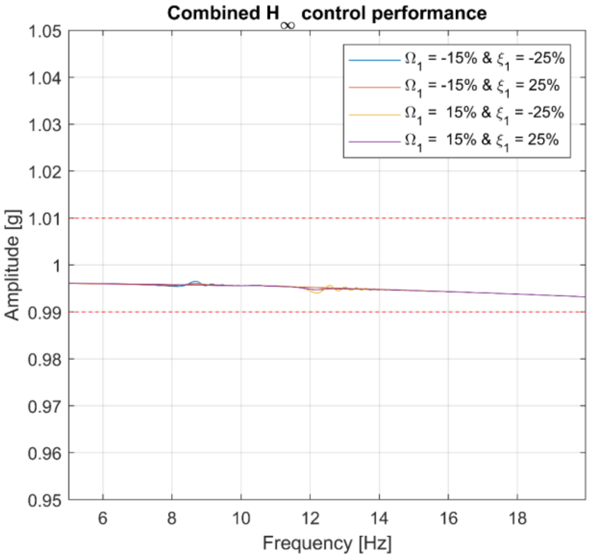

Figure 5-15 - Robust tracking performance of combined H_∞ control - output acceleration

In our case study, the combined H_∞ control shows total respect of specification (output acceleration is inside 1% error, red dotted lines) in every case of scattered dynamics. As these cases correspond to the worst-case scenario, no intermediate values of modal parameters are needed to analyze further robustness. In the neighborhood of the first mode, the blue case ($\Omega_1 = -15\%, \xi_1 = -25\%$) shows a slight oscillation near the anti-resonance frequency (between 8 and 9 Hz) and the yellow case ($\Omega_1 = 15\%, \xi_1 = -25\%$) also shows a very tiny oscillation near the resonance (12 to 13 Hz), though the amplitude of the oscillations in these cases is almost 0.1%, and it can be neglected compared to $\pm 1\%$ of accepted error.

5.6.2.3 Worst-case scenario via uniform distribution

It is not always evident that worst-case performance lies when varying the modal parameters at their limits. Therefore, it is also captious to scatter all parameters at any values between the intervals of interest. At a second time, the two modal parameters (Ω_1, ξ_1) are scattered uniformly between their dispersion range, which is $[-25\%, 25\%]$ for damping ratio and

$[-15\%,15\%]$ for resonant frequency. For each parameter, a series of 50 parameters are generated to create 50 dynamics for the simulation. Figure 5-16 illustrates the robust performances

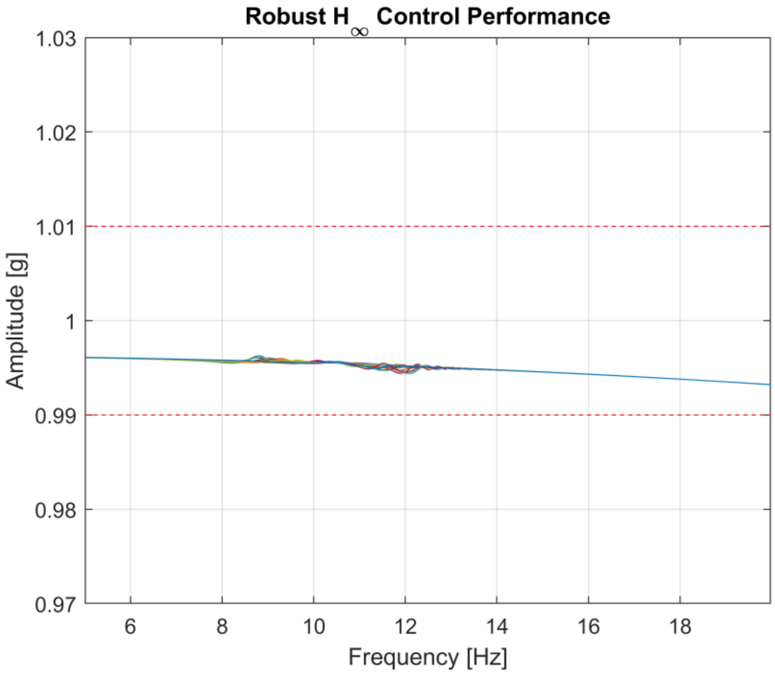

Figure 5-16 - Robust performance of 50 uniformly distributed cases

In Figure 5-16, the result of uniformly distributed parameters can be observed. As the mode positions are distributed all over the frequency interval of interest, the performance degradation due to the frequency shift can be observed all around the frequency between 8 to 13 Hz. In the case of the dispersion in two values (maximum and minimum frequency), the tracking error degradation is concentrated around two main points (In Figure 5-15, around 8 and 13 Hz). In both cases, the robust performances in terms of tracking error are equivalent and tracking error stays below 1% of the reference signal.

5.7 CONCLUSION

Chapter 4 presents a systematic way of introducing frequency domain weights to consider the dynamic tracking control problem via standard feedback H_∞ control scheme. The standard solution illustrates the superior performance in a nominal case, but completely fails to satisfy robustness against structured uncertainty. This chapter extends the preliminary control study to include robustness features to modal parametric variations. The research work was conducted to analyze two control strategies. Firstly, the one DoF H_∞ controller with feedforward action, resulted in non-optimal solution of the problem leading non-respect of the design criteria. Secondly, a feedforward two DoF multivariable H_∞ controller is synthesized, based on the approach of increasing the gain of correction via the second DoF of the controller along with the feedforward action for faster responses of the controller, in case of modal parameter variation. The combined H_∞ controller shows very prominent performance with regards to the modal parametric uncertainties. Therefore, the perspective of the research is to accommodate the combined feedforward 2-DoF H_∞ control architecture in the VTS. The study up to the current chapter includes a simulation interval of 5 to 20 Hz to only focalize the first mode of the satellite. Figure 5-17 shows the result of simulation from 5 to 100 Hz of frequency range using the 2-DoF controller.

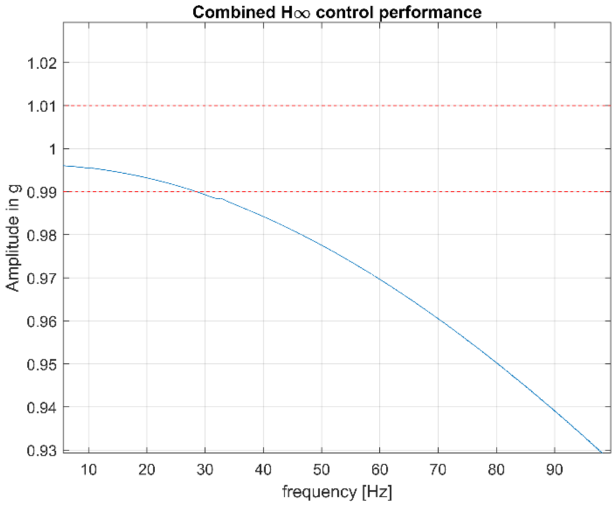

Figure 5-17 - Large spectral Simulation [5 100 Hz]

The 2 DoF controller behaves similar to the feedback controller given by Figure 4-12. The next chapter will generalize the 2-DoF control strategy for all modes of the satellite to adapt it up to 100 Hz, and a model in the loop architecture will be used for different types of simulations to validate the control structure for industrial use.

6 VTS ROBUSTNESS & VALIDATION CAMPAIGN

6.1 INTRODUCTION

The chapters 3 and 4 show the generalized frequency domain weights to address the dynamic tracking error and the chapter 5 extends the standard feedback H_∞ control in order to address the robustness against modal parameter uncertainties in a tracking problem. The feedback two DoF multivariable system shows a prominent performance against structured parametric variation. In this chapter, we extend the solution of the last chapter (concerns 5 to 20 Hz) to give a perspective of the large frequency band tracking problem of VTS (tracking in the interval of 5 to 100 Hz). In the modern era, the progress of numerical calculation allows to complexify the closed-loop system architecture and create more realistic scenarios of the system. Therefore, the industrial approach to validate the control system architecture through robustness campaign is hugely spread in the aerospace, aeronautics, automobile and defense industries. The validation campaign consists of realistic simulations alike the real system, not only estimates the performance of the system, but also helps to manage the specific topics like the precision control, system non-linearity management, noise reduction. Moreover, the frequency domain simulation guarantees the stability and so, the security of the closed-loop system. In this chapter, we introduce more realistic architecture of VTS for the robustness campaign. The concept is to launch a series of complex sizing scenarios to validate the closed-loop system, through automated predetermined frequency and time-domain simulations, also known as the virtual shaker test in the literature (Cozzani & Appolloni, 2007) (Bettacchioli, 2014b). Therefore, the campaign result validates the system design and the VTS can be launched once at the qualification level amplitude of the reference $cola$ without the necessity of traditional lengthy four stage VTS campaign.

6.2 SWITCHING CONTROL FOR LARGE SPECTRAL TRACKING

Mechanical systems with the necessity of controlling several vibrational modes are quite common in regulation and tracking problems (Balas, 1990). Most of the tracking problems alike the VTS, where the main challenge is the precision control within the frequency spectral (5 to 100 Hz) of the pseudo-periodic signal $cola$ (in which the spacecraft model contains four vibrational modes), are controlled by separating a single controller for each of the modes via classical control methods found in the literature of structural mechanics (Preumont, 2018). Though, the same problem is rarely treated through modern optimal control strategies. In the literature of optimal control, the behavior of the H_∞ control shows prominent tracking performance at a certain frequency spectral rather than a very large spectral like the VTS as it focuses on minimizing the maximum gain of the system at a certain frequency (Shukla, et al., 2016). In the issue of large spectral tracking, the H_2 solution addresses a whole range of frequency spectral as it minimizes the energy of states independent from the frequency interval, though it lacks robustness (Shukla, et al., 2016). Figure 5-17 illustrates the simulation result of combined multivariable feedforward 2DoF feedback H_∞ control scheme derived in section 5.4.4. In the study until this section, simulations are realized for the first mode of the satellite in between the frequency range of 5 to 20 Hz, but here, Figure 5-17 shows the simulation results within the full spectrum (5 to 100 Hz) of the VTS, which contains 4 satellite modes and it can be remarked that the tracking error increases with frequencies (frequency increases with time) and after 25 Hz, the error goes out of specification. As shown in Figure 4-12, this controller behaves similar to the feedback controller derived in chapter 4, resulting in a superior performance for a short range of frequencies. Therefore, it demonstrates the exactitude of the literature (Shukla, et al., 2016) about the behavior of H_∞ synthesis.

6.2.1 Gain scheduling control (Rugh & Shamma, 2000)

In our study, we need the robustness properties of the H_∞ control and, therefore, the necessity to overcome this issue to properly track the full frequency range of $cola$ signal. In our research, we introduce a model-based combined H_∞ synthesis, based on the gain scheduling principles. So two to three sets of generalized frequency weights can be defined for the model-based combined H_∞ synthesis, where each set of weights is used to synthesize a controller for a given range of frequency interval. In our case, the dynamic model provided by Thales Alenia Space provides first two modes at ~11 and ~35 Hz of the composite, and up to 40 Hz of the model assures the exactitude of the model to the real satellite. So that we limit the simulation at 40 Hz containing both modes. If intended to extend the result up to 100 Hz with a model corresponding the exactitude of the whole range (5 to 100 Hz), the similar approach demonstrated in this section, can be used. Figure 5-17 shows that the error stays below 1% up to 25 Hz; therefore, the first synthesized control is valid for 5 to 20 Hz range, then a second controller synthesized with the second set of frequency weights can cover the range from 20 to 50 Hz. The switching between controllers need an observable variable to switch between two feedback control laws (Rugh & Shamma, 2000), therefore the switching condition of these two switched feedback controllers is the frequency increase function of the reference $cola$ defined by the Eq. 2-2. Figure 6-1 shows the scheme of the gain scheduling.

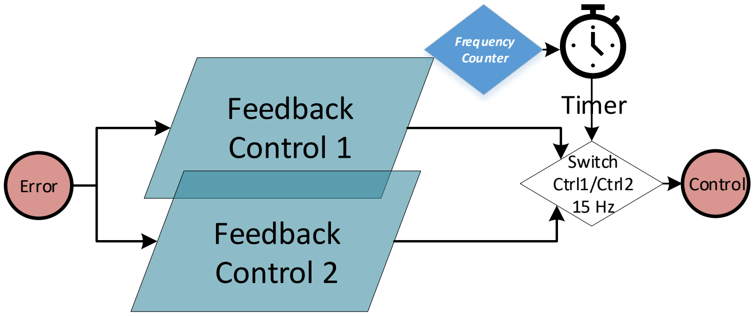

Figure 6-1 - Gain scheduling feedback control strategy of VTS

Figure 6-1 shows the schematized function of the proposed control block, where a frequency counter function computes the increment of the $cola$ frequency in function of simulation run time by using Eq. 2-2. Once it attains a preconfigured frequency, the switch function shifts control 1 to control 2 (next section details the design of these two feedback control laws). In our study, the switch is preconfigured at ~15 Hz, just after passing the first anti-resonance and first mode frequency. In order to smoothen the transition between the two controllers and reduce the transient error, the proposed strategy consists of activating the second controller much before the transition to overcome the controller initialization error, during the time of transition.

6.2.2 Model-based combined $\boldsymbol{H}_\infty$ control synthesis

Chapter 5 presented the architecture of the combined two DoF multivariable H_∞ control synthesis procedure based on the generalized frequency domain weights defined in chapter 3, which satisfies the industrial criteria for the frequency interval between 5 (31.4 Hz) to almost ~15 Hz (94.25 Hz) with the minimum bandwidth of noise cancellation. Eq. 3-17 and Eq. 3-18 gives the frequency constraints of the first controller, where the tracking constraint magnitude attains -20dB at 20 Hz (125.60 Hz) with a decrease of -6 dB/decade (with frequency decrease) and -31 dB at 5 Hz to keep the dynamic error below 1% between 5 to almost 20 Hz of the reference. In this part, we introduce another set of frequency weight to target higher frequency intervals of tracking, starting from ~15 up to 40 Hz (251.20 Hz). The controller switching frequency is chosen to be 15 Hz (<20 Hz), such that the tracking error between two controllers are minimum, mainly in order to avoid the transient effects. The principal ideas are the same as the first set of weights described in section 4.3.2, though the frequency bandwidth of the w_1 and w_3 weighting functions is moved to higher frequencies. The second controller constraint given by Eq. 6-1, where the error magnitude is almost -18 dB at 40 Hz and decreases at -20 dB/decade (with frequency decrease). It passes by -26.6 dB at 15 Hz. At the same time, the noise filtering weight w_3 needs to be readjusted according to the new w_1. So the new w_3 shift to the right and passes 0 dB at 685 Hz (4301.80 Hz) where the first one is at 254 Hz (1595.93 Hz). Time domain simulation validates the tuning of these frequency weights. The following transfer functions are taken as weights for the second controller:

$$\begin{cases} \dfrac{1}{w_1} = \dfrac{1.4s + 7}{s + 2827} \\ \dfrac{1}{w_3} = \dfrac{6158s + 7.6 \times 10^8}{1.2 \times 10^5 s + 5.4 \times 10^8} \end{cases} \qquad \text{Eq. 6-1}$$

In Figure 6-2, the illustration shows these two sets of frequency weights given by Eq. 3-17, Eq. 3-18 and Eq. 6-1. As the actuation limitation is equal for all cases, the frequency constraint w_2 is not mentioned here.

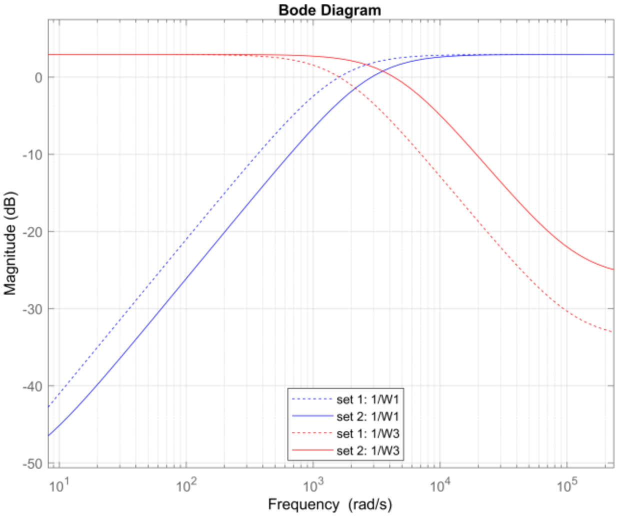

Figure 6-2 - Two sets of weighting functions

Figure 6-2 shows the clear partition between the two designs where the lower bandwidth frequency weights (dotted lines) focus on the lower part of the correction; therefore, the intersection point between the $\frac{1}{w_1}$ and $\frac{1}{w_3}$ of set 1 is lower than set 2.

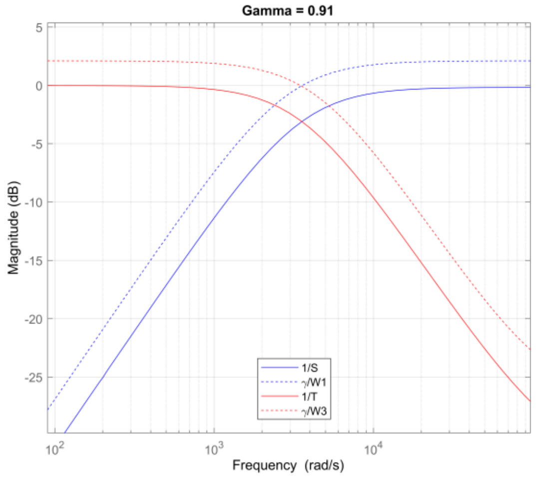

Figure 6-3 - Second sets of frequency constraints vs sensitivity functions

The given frequency weight sets are considered for the two H_∞ optimizations with optimal $\gamma_1 = 0.99$ and $\gamma_2 = 0.91$. The second set of constraints has met the specifications slightly better than the first set as the γ_2 is slightly smaller than γ_1, and both of them are less than 1. The second constraint sets are better optimized as the $\frac{1}{w_3}$ is shifted to right and the high-frequency noise filtering weight is set to -26 dB instead of -34 dB. In general, the implication of this weight is that the second controller will be more sensitive to sensor noises. The high frequency noises can be tackled by using the high-performance larger band accelerometers and the switching strategy using the first controller at low frequencies will increase the overall closed-loop system performance against noises. Later in this chapter, performances of both controllers against the sensor noises are illustrated (see section 6.3.2.1.5). Another strategy of having a very large band measurement from current accelerometers is to combine the acceleration measurement from several of them (PCB 356B21, Website). While switching between the two-feedback controller, the feedforward controller stays the same one given by Eq. 5-2 for the whole frequency range.

6.3 VALIDATION OF THE CONTROL ARCHITECTURE

Modern-day control systems used in the space, automotive and robotic industry highly depend on the analysis and performance assessment, before the use of such system in the real world. The validity of those assessments mostly depends on the numerical modeling of the physical system bearing the characteristics of the real physical model. Though, it is impossible to achieve a model which completely matches to the physical model in all frequency ranges, it should behave identically at least in the control bandwidth of the system to assess the system's performance (Skogestad & Postlethwaite, 2001). The remaining error between those models shall be taken as a modeling error during the control synthesis. Moreover, the assessment must take into account different possible scenarios so that the outcome of the performance assessment guarantees the well-functioning of the system. In VTS literature (Naisse & Bettacchioli, 2012) (Cozzani & Appolloni, 2007) (Nali & Bettacchioli, 2014a), several simulation studies have been conducted in prior to vibration testing campaign to predict the performance of the system, called virtual shaker. Since the work is based on a model-based control synthesis for vibration testing system, it is essential to validate the system through a validation campaign in a virtual shaker, corresponding to a numerical model of the composite and the closed-loop control system as well as different possible scenarios to estimate the system's performance. In this part, we propose a numerical model of the close loop system (see section 6.3.2 for details) and a plan of campaign for the validation purpose, also by introducing frequency domain analysis to assess the stability margins. This way, the virtual shaker testing would reduce the four-level testing to just a single test campaign, validated via numerical simulations.

6.3.1 Frequency domain validation

One of the main motivations of introducing linear control on the VTS is the possibility of assessing the stability of the control system prior to the real test. The case of a satellite is extremely sensitive due to the risk of structural fatigue and the lack of stability assessment in the current nonlinear control law leads to the four-stage VTS campaign (Bettacchioli, 2014b). The new control structure lets us define the stability margins of the system, though the classical stability margin cannot be used in the case of the multivariable control structure. There are several ways to determine the stability of such systems, mainly by using unstructured small gain theorem for a nominal plant, structured singular values for robust stability or μ analysis (Zhou, et al., 1996). Each of these methods determines the smallest stability margin from a multiple loop system; therefore, the structured analysis extends the unstructured small gain theorem to the case of structured or parameter uncertainties for the stability of a whole range of parameter dispersions (Zhou, et al., 1996). In this section, two distinct methods are used for the stability analysis, which will be compared in order to give a perspective for the VTS.

6.3.1.1 Stability analysis via unstructured small gain theorem

In section 5.5.1, the stability margin is obtained via the unstructured small gain theorem, which mainly computes the guaranteed stability of the multivariable linear closed-loop system. In our case study, Figure 5-9 illustrates the closed-loop system, and by using successively Eq. 5-16, Eq. 5-17 and Eq. 5-18, the stability margin α_{max} can be determined. The minimum margin α_{max} is the largest value of $\overline{\sigma}(T_{CL})$ over all frequencies, where $\overline{\sigma}$ represents the upper singular value of the multivariable closed-loop transfer matrix T_{CL}. Stability margins are defined directly from the feedback-loop, where the feedforward controller does not participate in the margin computation. Two different margins have been assessed for two separate feedback controllers. The unstructured small gain theorem cannot distinguish between two controllers and $\alpha_{max} \cong 0.71$. By using Eq. 5-19, the stability margins can be assessed from α_{max}. As mentioned in previous chapter, the gain margin is $(-4.4{,}10.7)_{dB}$ and the phase margin $\pm 41.4°$, meaning that the system is stable for a gain reduction up to $-4.4\ dB$ ($-\ 41.4°$ for phase) and up to $10.7\ dB$ ($41.4°$ for phase) in case of augmentation. In the case of the classical margin, the phase margin is computed by fixing the gain at 0 dB and the gain margin by fixing the phase at $-180°$. The method presented in this section uses the unstructured small gain theorem to assess the minimum margin that makes the system unstable and this is valid for a SISO as well as a MIMO system. Though this method shows conservatism due to the use of unstructured small gain theorem, which does not take into consideration the simultaneous gain-phase variation in the multivariable multiloop system (Gahinet & Apkarian, 2011). The next section introduces a method to remedy this issue.

6.3.1.2 Stability analysis via disk margin

The limitations of classical stability margins are largely studied in the literature (Gahinet, et al., 2020). The real system often differs from its mathematical model in both magnitude and phase simultaneously, which cannot be measured by the classical stability analysis. Moreover, a small plant perturbation can cause robustness issues in a system with a very high gain and phase margin (Gahinet, et al., 2020). The stability margin via unstructured small gain theorem introduced in the previous section can determine the stability margin of a MIMO system, but it does not capture the simultaneous variation of phase and gain perturbation in the stability of the closed-loop system. In order to address these issues, several options can be found in the literature (Zhou, et al., 1996) (Alazard, et al., 1999). (Gahinet, et al., 2020) extends the unstructured small gain theorem to structured uncertainty analysis in order to address the stability issue, in which the perturbations are introduced both at the input and output of the plant to measure the effect of simultaneous perturbation in both input and output of the plant. Additionally, the perturbations are taken in the form of phase and gain variation, which can be modeled as structured uncertainties to address the issues of simultaneous perturbation in a multivariable system. Therefore, the μ analysis generalizes the stability margin in case of simultaneous independent variation of perturbation in each loop to capture the worst case. Due to the simultaneous individual loop variation in a multivariable closed-loop system, the results are less conservative than the method in section 6.3.1.1. In this part, we introduce disk margin to deduce the guaranteed stability region of the VTS system.

6.3.1.2.1 Closed-loop system modeling

Like in the previous section, we model the closed-loop feedback system without the feedforward controller for stability assessment. The one input and two identical output full order plant model is given by G (Eq. 6-15), the 2 DoF H_∞ feedback controller K_∞. The closed loop system contains an input perturbation dynamic f_{in} and an output perturbation dynamic f_{out}. The size of perturbations $f_{in} \in \mathbb{C}^{1\times 1}$ and $f_{out} \in \mathbb{C}^{2\times 2}$ are taken accordingly, where the input perturbation is a SISO dynamics and the output perturbation f_{out} is MIMO to capture the multiloop variation. In Figure 6-4, the input and output perturbations (f_{in} and f_{out}) are modeled to vary the gain and phase at input and output of the plant dynamics of the closed-loop system, in order to capture the simultaneously gain-phase variations. In reality, the plant input perturbation (f_{in}) corresponds to disturbance due to command (mainly due to actuator dynamics), and the plant output perturbation (f_{out}) corresponds to noises due to measurement (mainly due to sensor dynamics). Figure 6-4 illustrates the closed-loop model with input and output perturbation.

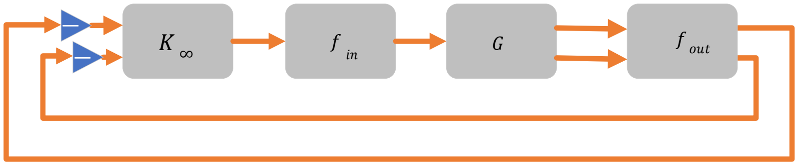

Figure 6-4 - Closed-loop model with perturbation dynamics

The main idea is to model the f_{in} and f_{out} in a way that we can vary both the phase and gain as perturbation at the input and output of the plant simultaneously, and also in each individual loop of a multivariable system in order to capture the worst stable case.

6.3.1.2.2 Perturbation introduction

This section is dedicated to modeling the input and output perturbation in terms of the gain and phase variation, which can be achieved by taking a complex dynamic of the perturbation where the real part corresponds to the gain variation of the system and the imaginary part is for phase variation (Gahinet, et al., 2020). In a general term, the perturbation model can be expressed by the following relation:

$$f \in D(\alpha,\sigma) = \frac{1 + \frac{(1-\sigma)}{2}\delta}{1 - \frac{(1+\sigma)}{2}\delta} \; with\, \sigma \in R, \delta \in C, |\delta| < \alpha \qquad \textit{Eq. 6-2}$$

The expressions used in the Eq. 6-2 can be defined by:

- α: Size of the disk, including all coordinates of simultaneous gain and phase variation (see Figure 6-5).
- σ : The skew factor, which is used to move the whole disk position to the right or left if there is any offset gain or phase variation in the real system not accounted in the plant model (see Figure 6-5).

The variation addressed by Eq. 6-2 is illustrated below.

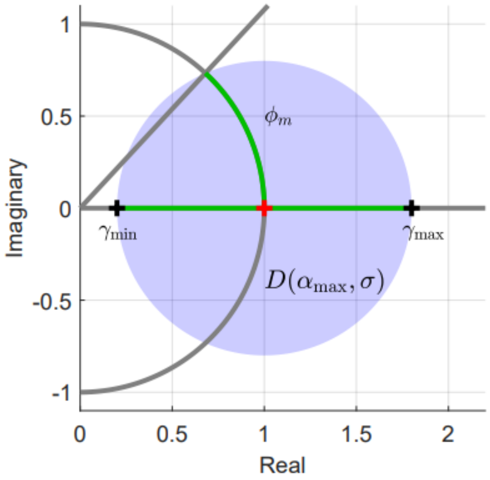

Figure 6-5: Definition of disk margin (Gahinet, et al., 2020)

In Figure 6-5, $D(\alpha,\sigma)$ is the disk margin where the stable gain variation is limited within $[\gamma_{min}\, \gamma_{max}]$ on the real axis and the phase variation corresponds to the angle $\pm\, \varphi_m$ between the real axis and the maximum attainable imaginary coordinate variation from the real axis. To be noted that $\sigma\; = 0$ signifies a $\gamma_{max} = \frac{1}{\gamma_{min}}$, and therefore, the disk margin α_{max} is the biggest value of α such that the closed loop system stays stable as stated in Eq. 6-2, disk margin gives the stable region inside the disk and is represented by the open interval $|\delta| < \alpha$. The intersection with real axis on the perimeter of the disk, the open interval becomes equality given by $\delta = \pm\alpha_{max}$. We can now use the value of δ in Eq. 6-2 to determine the disk parameters $(\gamma_{min}, \gamma_{min})$:

$$\begin{cases} \gamma_{min} = \dfrac{2 - \alpha_{max}(1-\sigma)}{2 + \alpha_{max}(1+\sigma)} \\ \gamma_{max} = \dfrac{2 + \alpha_{max}(1-\sigma)}{2 - \alpha_{max}(1+\sigma)} \end{cases} \qquad \text{Eq. 6-3}$$

φ_m is the phase margin, which intersects the boundary of the disk $D(\alpha_{max}, \sigma)$. The origin (0,0i), the intersection point and the center of the disk $D(\alpha_{max}, \sigma)$ form a triangle. By applying the cosine law, we can write:

$$r^2 = 1 + C^2 - 2Ccos(\varphi_m) \qquad \text{Eq. 6-4}$$

In Eq. 6-4, r the radius and C is the center of the disk $D(\alpha_{max}, \sigma)$. The phase margin φ_m can be determined from Eq. 6-4.

$$cos(\varphi_m) = \frac{1 + C^2 - r^2}{2C} \qquad \text{Eq. 6-5}$$

The center C and the radius r of the disk are given by:

$$\begin{cases} C = \dfrac{1}{2}(\gamma_{min} + \gamma_{max}) \\ r = \dfrac{1}{2}(\gamma_{max} - \gamma_{min}) \end{cases} \qquad \text{Eq. 6-6}$$

Example of a simplified SISO system

Firstly, we introduce a simplified case study of a SISO system to understand the concept, then it will be applied to the real system. Let's define the open-loop dynamics by $L = K \times G$ (where G is the plant dynamics and K is the controller) and the perturbation by f. f brings the phase and gain variation to the closed-loop system, generalizing the perturbation in the closed-loop system, which can either be the error in the model or any disturbances that reduce the stability margin. The closed-loop system is given in the following figure.

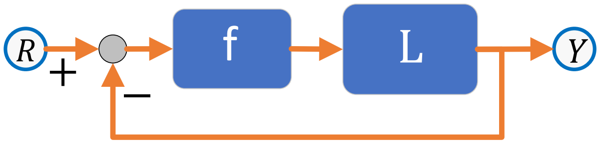

Figure 6-6 - Closed-loop SISO with input perturbation

The closed-loop system between the reference R and output Y, while introducing dynamics of the perturbation in the loop, can be written by:

$$\frac{Y}{R} = \frac{fL(jw)}{1 + fL(jw)} \qquad \textit{Eq. 6-7}$$

Suppose that the perturbation $f = f_0 \in D(\alpha, \sigma)$ shifts a pole of the closed-loop system to the imaginary axis at $s = jw_0$, if and only if the $(1 + f_0\, L(jw_0)) = 0$, where $f_0 = \frac{2+(1-\sigma)\delta_0}{2-(1+\sigma)\delta_0}$ for $\delta_0 \in C\ et\ |\delta_0| < \alpha$.

By the definition of the sensitivity function $S = \frac{1}{1+L}$ and replacing f_0 by its value in the stability condition $(1 + f_0\, L(jw_0)) = 0$, let us write:

$$\left(S(jw_0) + \frac{\sigma - 1}{2}\right)\delta_0 = 1 \qquad \textit{Eq. 6-8}$$

Similar to Eq. 5-18 of the unstructured small gain theorem, the disk margin α_{max} can be defined as the biggest value for which the closed-loop system remains stable.

$$\alpha_{max} = \frac{1}{\left\| S + \frac{\sigma - 1}{2} \right\|_{\infty}} \qquad \text{Eq. 6-9}$$

Extension of the disk margin to our study case

The input and output perturbation of Figure 6-4, can be defined as:

$$\begin{cases} f_{in} \\ f_{out} = \begin{bmatrix} f_{out1} & 0 \\ 0 & f_{out2} \end{bmatrix} \end{cases}$$

Figure 6-4 can be represented as $M - \Delta$ structure, where M is known and Δ is the structured (model) uncertainties induced by the perturbations (Green & Limebeer, 2012) (Skogestad & Postlethwaite, 2001).

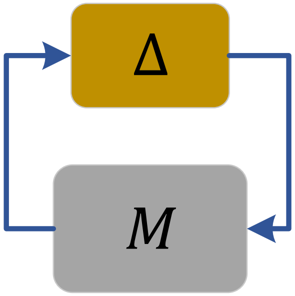

Figure 6-7 – Structure $M - \Delta$

In Figure 6-7, Δ contains the unknown part of the input and output perturbation such that $f_{in} : \delta_{in} \in \mathbb{C}$ and $f_{out} : \delta_{out\_j \in [1,2]} \in \mathbb{C}$. Therefore, the variable structure Δ can be written as:

$$\Delta = \begin{bmatrix} \delta_{in} & 0 & 0 \\ 0 & \delta_{out\_1} & 0 \\ 0 & 0 & \delta_{out\_2} \end{bmatrix} \qquad \text{Eq. 6-10}$$

By using the similar approach as Eq. 6-8 and the corresponding SISO plant of Eq. 6-15, the system M can be defined as a function of sensitivity function S:

$$M = \left(S(jw_0) + \frac{\sigma - 1}{2}\right) \qquad \textit{Eq. 6-11}$$

and the stable region can be defined as:

$$F_j \in D(\alpha, \sigma) = \frac{1 + \frac{\alpha(1-\sigma)}{2}\delta_j}{1 + \frac{\alpha(1+\sigma)}{2}\delta_j} \ : \ |\delta_j| < 1 \qquad \textit{Eq. 6-12}$$

In Eq. 6-12, $\delta_j \in \Delta$ is the normalized structured uncertainty due to phase and gain variation of the input and output perturbation of the j^{th} channel of the multi-variable system, modeled by F_j. Similar to the Eq. 6-8, in the case of MIMO, the system can have poles on an imaginary axis for $\det(I - M\Delta) = 0$. In this case, α_{max} is the biggest value for which the system described by $M\Delta$ stays stable.

$$\alpha_{max} = \frac{1}{\mu_\Delta(S + \frac{\sigma - 1}{2})} \qquad \textit{Eq. 6-13}$$

In Eq. 6-13, μ_Δ is the structured singular value of Δ in Figure 6-7. The skew factor σ moves the disk at right or left and this parameter is used to introduce an offset in the closed-loop system. In the perturbation dynamics F_j, δ_j ($|\delta_j| < 1$) is the variable part to vary the phase and gain simultaneously among different channels of the multivariable system.

The maximum of μ_Δ in all frequencies can be expressed by:

$$\|\mu_\Delta\|_\infty = \max_{w \in R} \mu_\Delta(jw) \qquad \textit{Eq. 6-14}$$

The disk margin $\alpha_{\max}$ can be achieved by Eq. 6-13 and then, Eq. 6-3 can be used to determine the guaranteed gain margin $[\gamma_{min}, \gamma_{max}]$ and phase margin ($\pm\varphi_m$) as well as the stable region, in case of simultaneous phase gain variation in the input and output perturbation.

6.3.1.2.3 Stability margin

The studied system can be represented by Figure 6-8 to determine the disk margin. The input perturbation $f_{in} \in \mathbb{C}^{1\times1}$, output perturbation $f_{out} \in \mathbb{C}^{2\times2}$ is diagonal, $G_{full} \in \mathbb{R}^{2\times1}$ is the full-order plant dynamics given by Eq. 6-15 and $K_\infty \in \mathbb{R}^{1\times2}$ is the feedback controller designed in section 6.2.2.

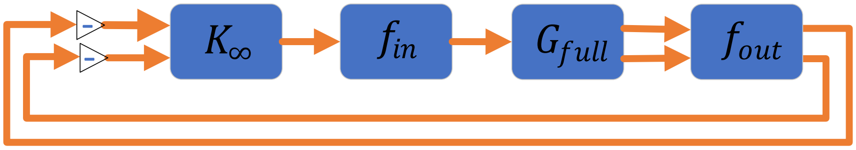

Figure 6-8 - Closed-loop multivariable system with input and output perturbation

The study case includes two switching controllers for two ranges of frequencies; therefore, we deduce two different disk margins for the stability assessment illustrated in Figure 6-9 and given by Figure 6-1. The computation of these disk margins are realized via integrated Matlab functions. Though, the difference of stability margins is very small as illustrated in the figure below.

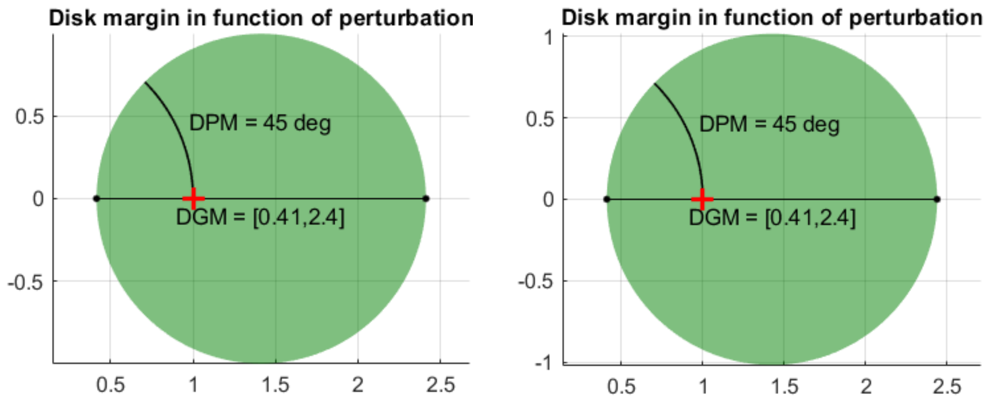

Figure 6-9 - Disk margin associated to two feedback controllers

Figure 6-9 shows the rounded values for stability margin which does not show any difference between two controllers. Non rounded values are presented in Table 6-2.

Table 6-1 - Stability via disk margin

Stability Criterion	FB control 1	FB control 2
Gain stability	$[-7.65, 7.65]_{dB}$	$[-7.75, 7.75]_{dB}$
Phase stability	$\pm 44.97°$	$\pm 45.48°$
Disk margin α_{max}	0.83	0.84

Figure 6-9 gives the disk margin $\boldsymbol{\alpha_{max}}$ along with the gain and phase margins obtained via Eq. 6-3 and Eq. 6-5, which is slightly different from one controller to another. The difference can be stated in gain and phase margins as well, where the first controller (second controller respectively) guarantees a variation of $[-7.65, 7.65]$dB ($[-7.75, 7.75]$dB respectively) of gain and $\pm 44.97°$ ($\pm 45.48°$ respectively) of phase from the nominal plant before being unstable. The second controller shows a better stability margin than the first one, which can be linked to the design where the second controller was optimized with a smaller γ than the first one (see section 6.2.2). Though, the difference in stability between two controllers are very small and both of those strategies show required industrial level of stability margin considered to be at least 6dB of gain and 30° of phase margin.

6.3.1.3 Validation of frequency domain analysis

The stability of VTS is assured as the real part of the closed-loop poles are strictly negative in both controllers. The obtained margin via unstructured small gain theory is 0.71 and no difference has been observed in both controllers. Moreover, stability is achieved by determining the highest unstructured gain of the closed-loop system in overall frequency ranges (See section 6.3.1.1). This method is an extension of the classical gain and phase margin to a multivariable system, though it cannot consider the simultaneous variation of gain and phase in the system. Therefore, the second method takes all these limitations into account and the phase and gain variations have been taken into account via structured singular values (parametric uncertainties) to lessen the conservativeness of the result (Gahinet, et al., 2020) (Skogestad & Postlethwaite, 2001). Compared to the stability margin 0.71 obtained via unstructured small gain theorem, the disk margin gives a higher stability margin (0.83 for the controller-1 and 0.84 for controller-2) and it is due to the reduction of the conservatism of the system using structured singular values. Moreover, the disk margin distinguishes the differences of the stability margin between two controllers, which shows the sensitivity of the method in case of a very small difference in the closed-loop system. As per consequence, the disk margin is an appropriate choice for the stability assessment of the VTS.

6.3.2 MIL architecture

The model in the loop system is basically an automated numerical system that corresponds to the model related to the real-world system (Albrecht, et al., 2012). These models generally correspond to a discrete numerical part and a real physical continuous model. Figure 6-10 shows the new MIL architecture of the VTS introduced for the virtual shaker testing campaign.

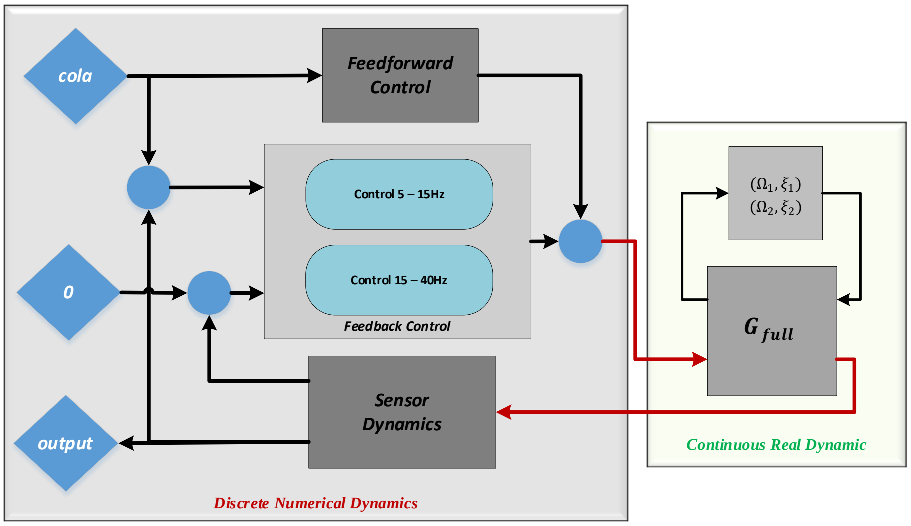

Figure 6-10 - MIL architecture for virtual shaker testing

The MIL architecture contains two blocks, the discrete part of the system containing the sensor dynamics, feedback and feedforward control, as well as reference generation. The feedback control contains the switching controlstrategy explained in section 6.2. Though, the feedforward controller given by Eq. 5-2 is unique for all ranges of the reference frequencies. On the other hand, the block in the right corresponds to the physical system, unlikely the optimal order synthesis model given by Eq. 4-9; this is a full order continuous model (7th order model, explained in section 4.2.1) to assess the robust performance of the optimal order controller in case of modeling error due to model reduction. In the virtual shaker, the discrete part generates the reference, which goes through the control block to generate the command for the continuous block containing the composite model of the actuator, shaker and satellite, then the sensor samples the output acceleration via measurement. The following part of this chapter is dedicated to specific simulations using this virtual shaker, and the simulations are conducted via intel fourth-generation $I3$ processor of 3.4 Mhz clock speed. The simulation comprises the 5 to 40 Hz frequency range to cover the first two modes and their corresponding anti-resonances.

6.3.2.1 Nominal case validation

6.3.2.1.1 Nominal simulation

In this part, the virtual shaker test will demonstrate the performance of the proposed control system without any parameter variation. Therefore, in the first test scenario, all parameters are taken in their nominal values and the full order (7th order model) continuous model is described in section 4.2. Though, the 13th order feedback controller is designed on a reduced-order system given by Eq. 6-15. As described in section 6.2.1, the controller switch is activated at 15 Hz. The Figure 6-11. gives the output acceleration and different commands. The output acceleration (upper left) stays below 1% of error, satisfying the criteria of tracking accuracy and no vibration has been remarked. Moreover, the control system shows the appropriate robustness to comply with full order continuous system. The other three plots of Figure 6-11 correspond to the total control effort (upper right) delivered to the system, which is the sum of the feedforward action (lower left) and the feedback action (lower right).

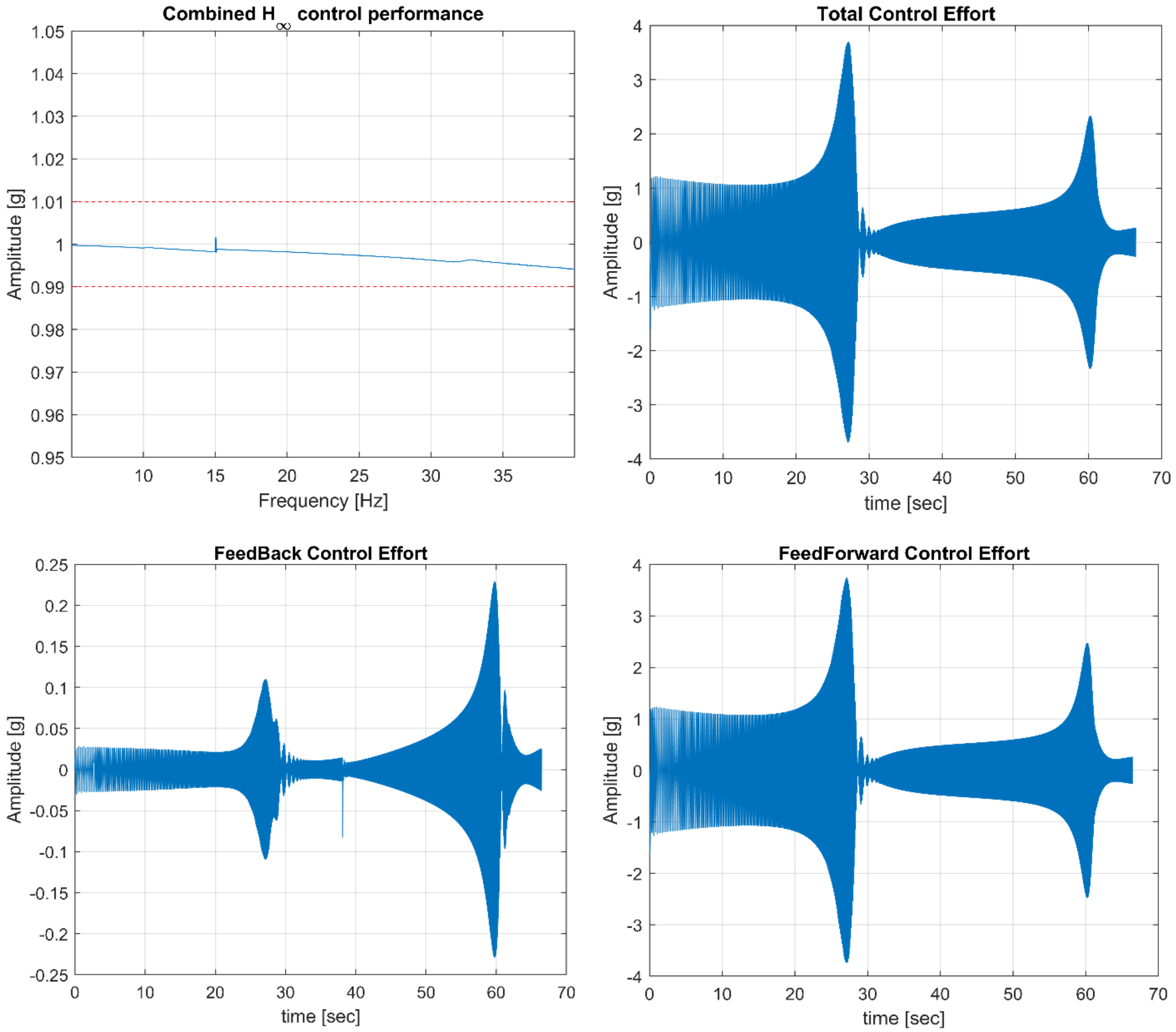

Figure 6-11 - Control system performance of a nominal scenario

The total control effort rarely attains 4g remaining far below the maximum actuation capacity 75g, as predicted from the frequency domain constraint in Figure 6-11. While analyzing the behavior of the feedforward control, it contributes to the maximum control effort to the total effort.

As the feedforward control is the inverse of the system dynamics and it is commanded directly, contrary to the feedback controller, which needs updates at the end of each loop. Therefore, the response is faster than the feedback system as it predicts the command. The feedback command is used to compensate for the error in the closed-loop system due to model error, tracking error, parameter variation as well as noise filtering. The feedback control effort remains below 0.25g near the second antiresonance frequency; this corresponds to the higher need of control action, dedicated to the vibration suppression of the system in higher frequencies unlike the lower frequency dynamics, which need higher amplitude of control action through feedforward action for error correction. The acceleration output near 15 Hz contains a spike due to switch between two controllers (see section 6.2.1). Though the strategy of initializing the second controller before switching to it, keeps the error below 1%. It is mainly possible due to the rapid response from the control system and this initialization error is compensated by the feedback controller. Therefore, the initialization error can be observed in the feedback action in Figure 6-11 (lower left); which is present at 38 sec of the simulation showing a spike just below -0.1g. In summary, the nominal result of gain scheduling control shows the satisfaction of the control performance in the presence of full order system dynamics.

6.3.2.1.2 Sweep rate variation

In the current system, sweep rate is a sizing criterion as the higher sweep rate means that the system will stay in higher transient modes. Consequently, it increases the transient state behavior of the closed-loop system such as oscillations and decreases with lower sweep rate, but in that case, the system will stay longer in each vibration mode bringing the fatigue to the structure (Soucy & Coté, 2002) (Bettacchioli & Nali, 2015). In this simulation, we define two tests with the extreme values of the sweep rate, the lower rate is 2 Octave/min, and 5 Octave/min is the higher one; these values correspond to scenarios that can be demanded for the satellite qualification (Nali & Bettacchioli, 2014a). Figure 6-12 illustrates the output acceleration and control effort in the two corresponding cases.

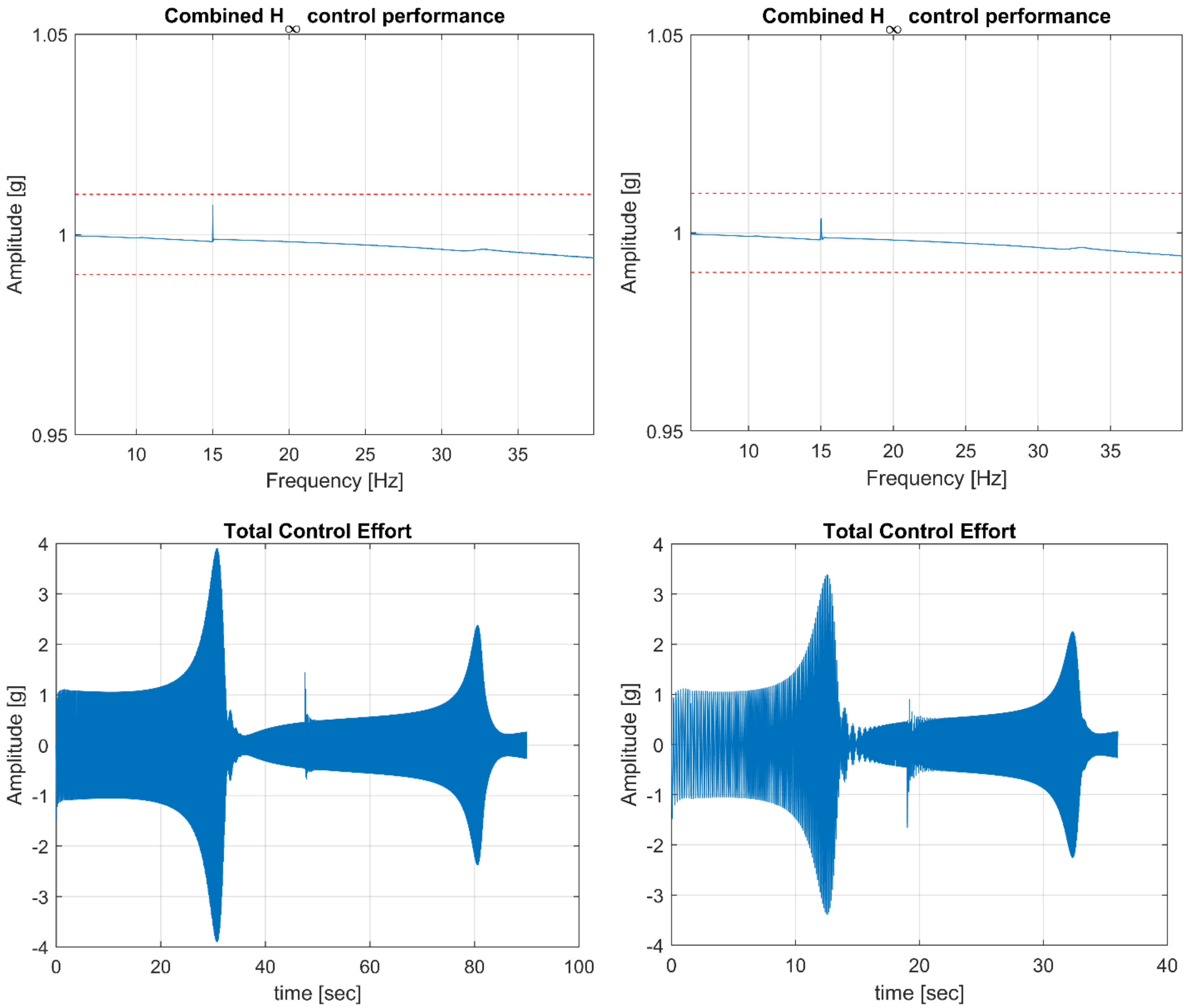

Figure 6-12 - Control performance with a sweep rate of 2 OCT/min (left) vs. 5 OCT/min (right)

The left column of Figure 6-12 shows the acceleration performance remaining below 1% limit, though the spike due to frequency shift increased. The effect can be observed in the control effort, where the spike near 45 sec of simulation is higher (more than 1g) compared to the nominal case (0.1g). Though, the overall result remains satisfactory. The case of 5 octave/min (right column) also shows very satisfactory tracking performance as the spike gets smaller and the high transient effect due to higher sine sweep speed can be seen in the total control effort, as it contains more oscillations near modes and during the controller switching, compared to the other one. In the case of sweep rate variations, the proposed control system gives satisfactory performance compared to the performance degradation in a VTS with an actual control algorithm (section 2.4.3).

6.3.2.1.3 Varying amplitude

In the VTS, the amplitude of the $cola$ signal is often different in different ranges of frequencies, specifically, in the neighborhood of the modes in order to reduce the risk of overshoot (see section 2.2.5). So, the scenario of the virtual shaker must comply with the variation of the amplitude. In this simulation case, we generate a unit $cola$ signal (1g) but it decreases almost 25% near the first mode frequency, while the sweep rate is nominal (3 octave/minute). Figure 6-13 shows the closed-loop system performance. In the upper plot of Figure 6-13 shows the periodic output acceleration where the amplitude between 28 to 40 sec during the simulation gets to the desired 0.75g. Unlike the current control performance (section 2.2.5), the robust control system follows the varying amplitude precisely without any oscillation, overshoot or undershoot. The control switch happens just after the amplitude variation near the first mode and it can be remarked in the lower plot of Figure 6-13 where the spike in control effort reaches near -4g, which remains acceptable with regards to the actuation limit.

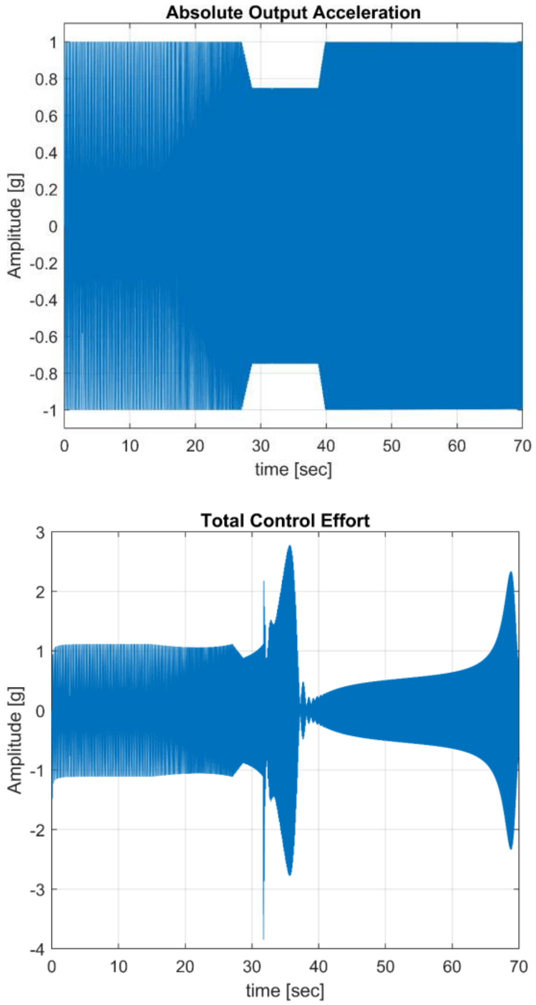

Figure 6-13 - Control performance with varying cola amplitude

The maximum control effort near the first mode (in Figure 6-13, 2.75g) is lower than for the constant amplitude case (Figure 6-11, 3.80g), though the effect of amplitude change can be remarked just before the first mode compared to the constant amplitude case. The control effort near the second mode stays identical in both cases.

6.3.2.1.4 Low level to qualification level test

The previous cases test different scenarios with 1g of amplitude, though different levels of tests are conducted from very low amplitude to qualification level amplitude of $cola$, mostly between 0.25g to 2g. In this part, we will test the MIL architecture to respond in case of different levels of amplitudes. Figure 6-14 illustrates such simulations.

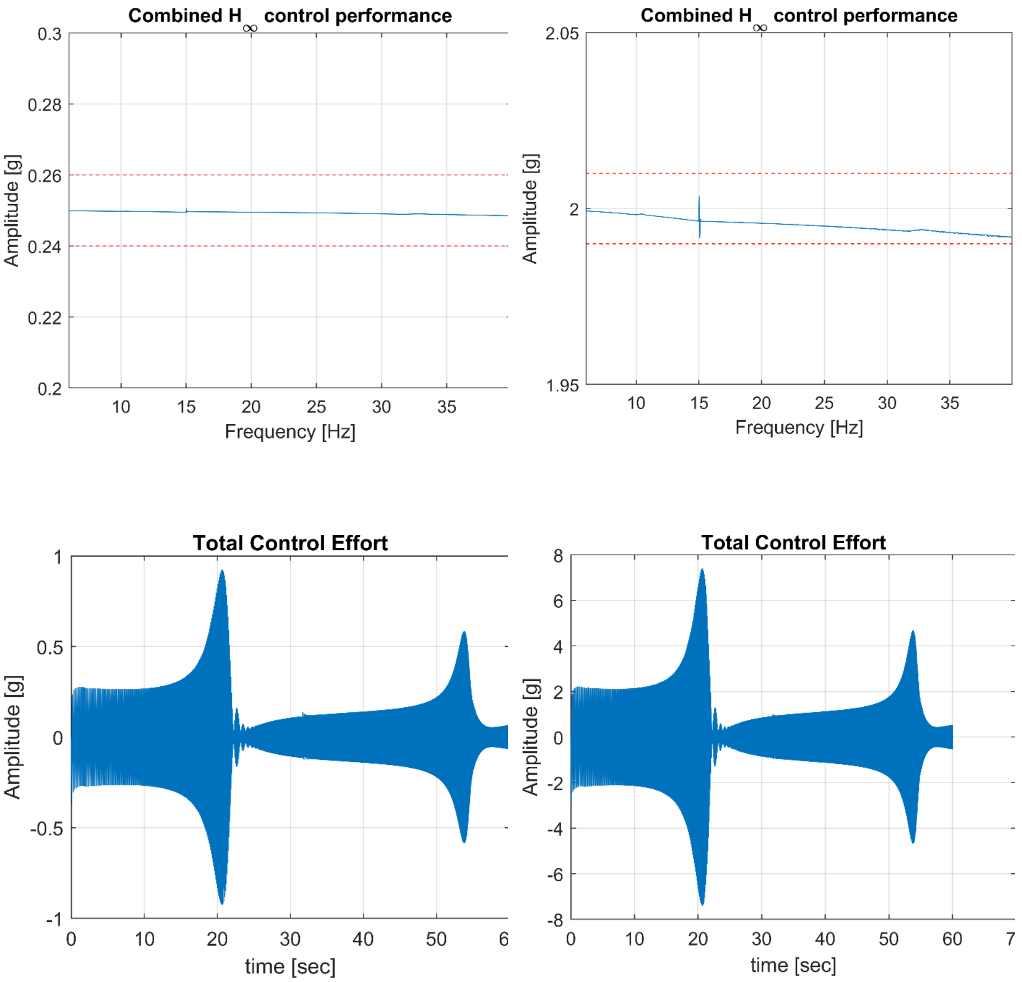

Figure 6-14 – Response to 0.25g (left column) and 2g (left column) amplitudes

Figure 6-14 shows the simulation result of 0.25 g (left column) and 2g (right column) of the amplitude of $cola$. The output acceleration in the case of low amplitude level case is better (stays below -0.1%) than the high amplitude level (almost -0.8% at the end of the simulation), though both satisfy the criteria of 1% error. For low amplitude case, the switching effect between controllers is quasi invisible, where the high amplitude level increases the transient spike. At the same time, the demand of control effort at low-level test is 1/8th of the high-level test as expected. Though the results of all cases are within the satisfactory level, main attention goes to the fact that the dynamic error correction is different in different amplitude levels and results in this section show that of the error gets higher when the amplitude level rises. The present result of these cases validates the proposed control system performances in different $cola$ amplitude level and motivates the test run via a unique step instead of the four-step VTS campaign.

6.3.2.1.5 Noise filtering performance

The accelerometer measurements are considered to be perfect in the control bandwidth to precisely track the reference and it may induce noise in high frequencies, although in the reality, the measurements are not perfect. In the accelerometer’s datasheet, different ways of installation are mentioned (PCB 356B21, Website) which can significantly reduce the noise. The single head measurement shows reduced spectral functioning point (up to 1000 Hz), which can be increased largely by assembling several heads of the measurement accelerometers for a given axis. The upper limit of current noise amplitude is 0.1% of the magnitude of the output signal attainable by using several heads for the measurement of the piezoelectric accelerometers such PCB, Endevco, DJB, Bruel, Kjaer etc. These accelerometers can measure a single to three-axes at the same time. Moreover, each of them has different properties to be used in different needs, starting from mainly measurement, control or noise reduction (PCB 356B21, Website). The modeling of a sensor in a MIL architecture consists of sampling the signal from the continuous output of the system at 12 kHz, then adding appropriate measurement noise to the sampled output data. The noise can be additive or multiplicative, though additive noise corresponds to the random noise, which does not depend on the state equation of the system. On the other hand, the multiplicative noise is correlated to the system, mainly used to represent the noise related to the system dynamics (Nicholson & Kaipio, 2020). In the case of accelerometer measurement noise, it is modeled as additive noise to the system as it is totally decorrelated from the system equation. In the literature (Dilhaire & Maillet, 2015), the measurement noises are often modeled as white noise as the property of the white noise shows that it has constant energy around all frequency bands and, consequently, unlimited energy. Therefore, in reality, the measurement noises are spread through all frequency bands of the system (Dilhaire & Maillet, 2015). In our case, the high-frequency noises are randomly spread around the absolute acceleration, so it can be modeled as a zero-mean gaussian noise which can go up to the interval of $[-0.001g, 0.001g\ ]$ corresponding 0.1% of the signal.

As mentioned in section 6.2.2, the second controller of the switched control system has a filtering bandwidth at much higher frequencies than the first controller. Therefore, the optimal noise reducing performance of this controller supposed to situate at higher frequencies as H_∞ controllers in general tend to maximize the performance near control bandwidth. So far it moves from this frequency, the performance degrades. Before testing the switching strategy, the second controller is tested for the performance assessment. The simulation has been realized under nominal parameters of the MIL structure considering noisy measurement. In Figure 6-15, the performance of the controller 2 is given from 5 to 40 Hz.

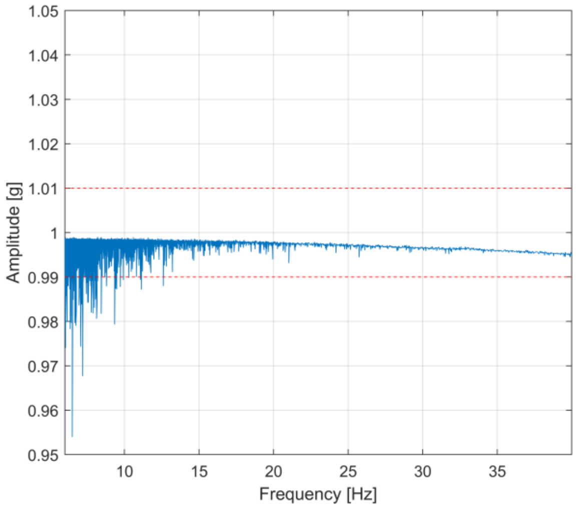

Figure 6-15 - Performance of controller-2 against sensor noises

Figure 6-15 shows the performance of the controller 2, where the performance degrades at lower frequencies as stated previously. The tracking error reaches almost -5% near 5 Hz, though the performance gets better with frequency increase. From 5 to 14 Hz, the tracking error is higher than the specification of $\pm 1\%$.

In the second scenario, MIL structure considers both controllers as well as the switching strategy mentioned previously. Figure 6-16 gives the set of output performances from 5 to 40 Hz. Figure 6-16 shows the maximum output amplitude with measurement noises (left plot), the controller keeps the error under the specification. The right plot of Figure 6-16 gives total control effort.

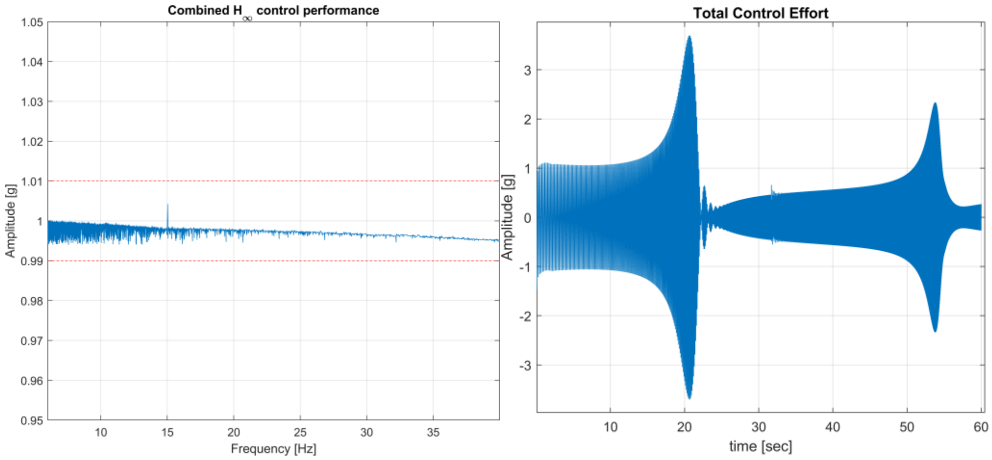

Figure 6-16 - Max amplitude (left) and total control effort (right)

The proposed control structure satisfies the specification even in the presence of noise in the system. In addition, the spike observed near 15 Hz is due to the change of controller which stays below the specification as the nominal case. The mean amplitude and the standard deviation of the output acceleration are 0.998g and 0.014g; therefore, the mean error of the output is 0.002. Statistically, the mean error is below the specification of $\pm 1\%$ with a very low standard deviation. While taking into account sensor noises, total control effort stays below the saturation. Small amplitude of gaussian noises demands very low control effort compared to the amplitude of the total control effort; therefore, its effects are not noticeable.

6.3.2.2 Robustness campaign via Monte-Carlo simulation

The main objective of this section is to assess the performance of the MIL system in the presence of a mismatch of the real system from the optimal order synthesis model. Additionally, the mismatch can happen due to modeling errors, loss of characteristics of the real system in the reduced-order synthesis model, nonlinear modal parameter variations linked to different amplitudes of excitation, which are not included in the linear reduced-order model of Eq. 4-9 (see the section 2.3, and 4.2). In the previous chapter, the robustness of the controller is validated by varying the modal parameters of the synthesized model in Eq. 4-9. In reality, the robustness assessment shall be generalized for the full-order satellite model without any model reduction to validate the behavior of the optimal order controller synthesized from the reduced order plant model in a full order system. In our study, the generalization of the variations of the full order model are obtained via the variations of each mode frequency and damping independently within a given limit. The proposed approach will vary the modal parameters of two separate satellite modes with the condition of a sufficient number of scattered cases. This can be carried out through a Monte-Carlo simulation, which is hugely used in modern control architecture validation and performance assessment (Harrison, 2010). The main objective of the Monte-Carlo simulations is to statistically verify the performance of the system in terms of random parametric variations achieved by a sufficient number of simulation cases. However, it does not necessarily call for the worst-case scenario. An analysis has been realized in chapter 5 to assess the worst-case performance for the validation of the control strategy (see section 5.6.2.1). Each mode of the system (2 mode frequencies) is scattered normally with a standard deviation of 6 Hz, which assures a centered normal distribution of the modes in the interval between $[-15\%, 15\%]$. In addition, each damping of 2 modes is scattered normally with a standard deviation of 10 which assures an centered normal distribution of the modes in the interval between $[-25\%, 25\%]$. Here, by following the procedure introduced in section 4.2, we separate the 7th order model into the sum of 3 parts corresponding two conjugate pairs of poles corresponding each to one of the two satellite modes. Then three additional poles for the three rest of the system. The model is given below:

$$G_{red}(\mathrm{s}) = \frac{2sr_1 + 2(p_1\Omega_1\sqrt{(1+{\xi_1}^2)} + r_1\Omega_1\xi_1)}{s^2 + 2\Omega_1\xi_1 s + {\Omega_1}^2} + \frac{2sr_2 + 2(p_2\Omega_2\sqrt{(1+{\xi_2}^2)} + r_2\Omega_2\xi_2)}{s^2 + 2\Omega_2\xi_2\, s + {\Omega_2}^2} + \frac{R_5}{s+P_5} + \frac{R_6}{s+P_6} + \frac{R_7}{s+P_7} + K_S \quad \textit{Eq. 6-15}$$

In Eq. 6-15, parameters (Ω_1, ξ_1), (Ω_2, ξ_2), $r_{1,2}$, $p_{1,2}$, K_s, R_5, P_5 are the same as explained in Eq. 4-9. Additional, R_6, R_7, P_6, P_7 are added to take into account the 2nd order dynamics to form the full order model. In our simulation, each mode of the satellite (Ω_1, Ω_2) are scattered individually, as well as the two corresponding damping ratios (ξ_1, ξ_2). Figure 6-17 shows the histogram of the mode and damping ratio scattering.

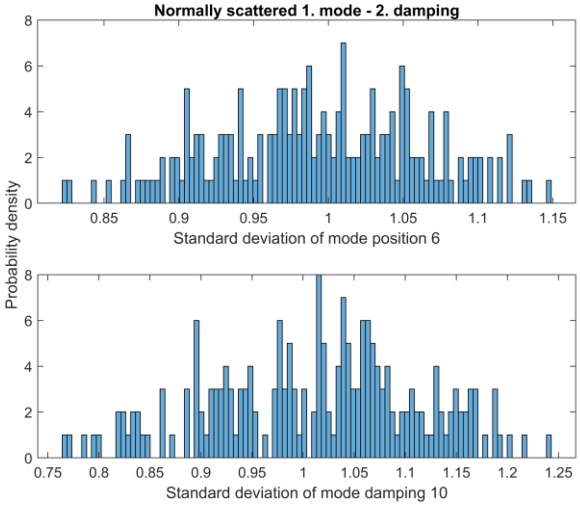

Figure 6-17 - Scattered modes (upper) and damping (lower)

Figure 6-17 shows the histogram of the mode and damping scattering, which contains 100 cases for each mode and damping. Therefore, the histogram contains 200 scattered modes and 200 damping ratios distributed normally in the given standard deviation. By using these modes and damping in Eq. 6-15, 100 scattered dynamics are created for simulation, given in Figure 6-18.

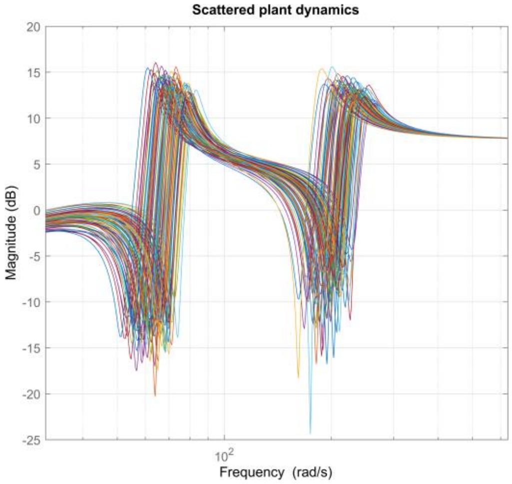

Figure 6-18 – 100 scattered full order plants

Figure 6-18 plots 100 cases of scattered dynamics with the scattered mode-damping given by Figure 6-17. Table 6-2 shows the obtained dispersion of different parameters.

Table 6-2 – Parameter scattering

Parameter	Lowest	Highest
Mode 1	- 18%	13%
Mode 2	- 15%	15%
Damping of mode 1	- 23%	24%
Damping of mode 2	- 24%	22%

In Table 6-2, the standard deviation of 6 for each mode variation results $\sim \pm 15\%$ of frequency variability of both modes of the satellite. On the other hand, the variability of the damping factor expressed by the standard deviation of 10, accounts for almost $\pm 25\%$ of nominal values.

Therefore, the random dispersion covers the specification given in 5.3.

Figure 6-19 illustrates the performance of 100 scattered cases through Monte-Carlo simulations.

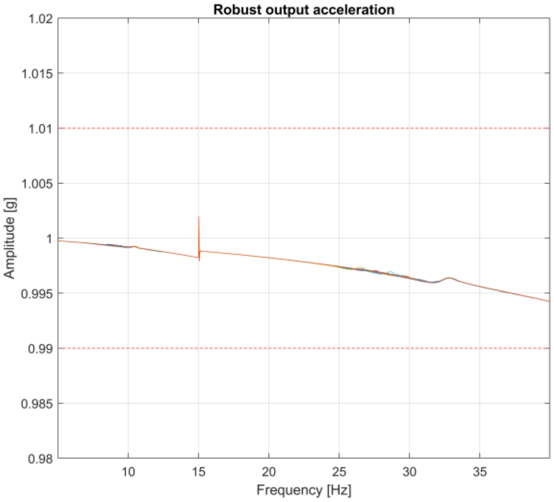

Figure 6-19 - Robust performance

Figure 6-19 shows the output acceleration of 100 scattered cases in which the simulation up to 15 Hz is realized using the first feedback controller, then the small spike due to the switching of controller dynamics and later, the second feedback controller continues for the rest of the test. Table 6-3 give us the statistical performance of the monte-carlo simulation.

Table 6-3 - Statistical Performance of the Monte-Carlo simulation

Error Criterion	FB control 1	FB control 2	Switch
Avg. Max	- 0.03%	- 0.18%	0.18%
Std. Max	2.47e-5	8.01e-6	5.95e-6
Avg. Min	- 0.18%	- 0.4%	- 0.42%
Std. Min	9.27e-6	8.15e-6	7.99e-6

The first feedback controller keeps the extreme error below 0.18% and the performance of the second controller is degraded (can reach 0.42%) compared to the first one. As Figure 6-19 illustrates, the switching stage induces the highest error (0.42%), although in all cases, the error remains below $\pm 1\%$.

In this section, simulations on a nominal plant model for different scenarios such as the $cola$ amplitude level variations, sweep rate variations and also sensor noises validate the overall closed-loop MIL architecture for required tracking performance along with the control effort. In addition, the Monte-Carlo simulations generalize the model mismatch issue via mode-damping variations on a full order model and illustrate the proposed MIL being statistically reliable with the random variations of the system dynamics with respect to the limitation where the poles stay in the left half-plane on the complex plane.

6.4 CONCLUSION

This chapter generalizes the robust control of VTS described in the previous chapter for the whole range of frequencies via two switching controllers (5 to 40 Hz for the given satellite composite model). The validation of the system has been achieved by introducing a MIL architecture containing the full order continuous plant versus the optimal order discrete controllers. The diverse results illustrate the good performance of the control system in case of noise, variation of the speed and amplitude of the reference $cola$. Time-domain Monte Carlo simulations show the robustness of the architecture in case of any variation in the system including mode-damping variation of the full order composite plant model. The frequency-domain analysis via disk margin allows us to determine the stability of the system and gives us the measure of the minimum perturbation, which leads the system to instability.

7 CONCLUSIONS AND PERSPECTIVES

The Ph.D. research introduces a new control structure of the vibration testing system, which can achieve precise tracking performance while attenuating the beating phenomenon observed during the mechanical qualification of a spacecraft. In order to compare the performance, the research focuses on a brief analysis of the current nonlinear control algorithm via the constructor's manual and literature review. The real-world experience of several commercial and scientific satellite testing campaigns, such as Inmarsat GX5, Konnect, Exomars, etc., has been analyzed in order to evaluate all flaws and advantages of the current control architecture and the real-time solutions based on the experience of the AIT architects. A simulator based on the current control architecture has also been developed to evaluate the current control performance regarding the different configurations of the control system. Based on the identified problems and issues, a literature review has been conducted in the domain of active vibration control and robust control strategies highlighting sliding mode control, state feedback, robust and optimal control for possible directions of the study.

At the beginning, the research focuses on studying robust control algorithms on a simplified single degree of freedom dynamic system representing the actuator-satellite-interface composite as a first step towards the appropriation of the industrial specifications for the control design paradigm. This preliminary study shows superior performance compared to the current control structure evaluated via simulation, which gives the direction of research for detailed industrialization of the solution.

Therefore, the next step considered the elaboration of a real multi-degree of freedom satellite model from a very low-level vibration test. This study provided a minimum order satellite model from a higher-order identified model together with the modal parametric variables-based model for robust control design and robustness analysis purposes. The result of the preliminary study has been extended to the real identified case and, is completed with the whole industrial scenario by taking into account the actuator dynamics in controller design. Based on this identified model, the industrialization of the developed control strategies has been introduced via virtual shaker testing. The virtual shaker consists of a time-domain simulator based on a model in-the-loop architecture corresponding to the real-time closed-loop system with an identified actuator-satellite-interface composite dynamical model. The virtual shaker test focuses on the real testing scenario where the optimal order discrete-time controller tackles the full order non-reduced continuous-time dynamical composite model. This scenario illustrates the robustness of the control architecture against the neglected dynamics of the composite plant. The Monte-Carlo simulations conducted by scattering each mode and damping individually to demonstrate the robustness of the control system, not limited to only modal parameter variations but also against all types of possible significant model mismatches of the full order system. Though the current industrial specification only requires the vibration cancellation by precisely tracking the reference signal, in this study, the frequency domain simulation points out the stability margins of the closed-loop system and the monte-carlo simulations illustrate the robustness of the control architecture against parameter variations, which suggests the feasibility of a single-run vibration test instead of a four-level time-consuming current campaign. However, the validation of the findings of this research depends on implementation and prototyping on the vibration testing system via real-time control architecture.

7.1 SCIENTIFIC PRODUCTION

The current vibration testing architecture has some uniqueness in the domain of control systems engineering. The investigation on actual nonlinear control systems concludes that these control schemes are prominent in the literature of robust control, though it seems inadequate for vibration testing system. The control laws based on amplitude estimation require a full period of signal to estimate the amplitude. Therefore, the control law responds slowly as it is able to update only after a full period and within this period of time, the quick change of gain in the closed-loop system due to the passage of lightly damped modes takes the error far from the specification. In addition, the pseudo-periodic reference signal starts at a lower frequency and ends at a higher frequency; therefore, the nonlinear controller mainly tuned for the low frequency of the reference is not optimal for higher frequency error compensation, which needs a faster response of the controller. The consequence of this control scheme leads to very bad reference tracking, oscillations and overshoots of the current vibration testing system, in particular, when the reference moves towards higher frequencies, the performance continues to degrade.

Moreover, the nonlinearities of the command add the disturbances in the output acceleration. The first challenge of the study is to reshape the control structure to accommodate the robust control scheme, which updates the command at each sampling period. In chapter 3, a new feedback H_∞ based control structure shows superior performance than the actual system on the simplified S-DoF satellite model. This new control loop responds faster than the current system, where the correction is updated at each pseudo-period of the reference. As the frequency of the reference changes constantly, the transient state becomes permanent. Therefore, the definition of tracking error convergence based on the final value theorem can no longer satisfy the error compensation criteria. In this research, a systematic way of addressing this issue called dynamic tracking via frequency domain weights has been presented, and it seems to keep the error of the tracking within the desired limit for both simplified dynamics and real more complex cases. In chapter 4, the same strategy is applied to a real identified M-DoF satellite model. Though, it seems to satisfy only the nominal case of the plant dynamics, the optimal H_∞ control seems to be sensitive in terms of modal parameter variations because of the pole-zero simplification of mixed sensitivity-based control design. Though the problem can be solved via some existing strategies for a regulation problem, yet the tracking control with the same issue can rarely be found in the literature. In chapter 5 of this manuscript, a combined feedforward-feedback robust control scheme shows an effective way to address this issue, which satisfies the industrial criteria and shows a very prominent result in case of modal parameter variations. In contrast to existing but more complex methods such as adaptive control or higher-order sliding mode control, the introduced control scheme results in a minimum order controller with a similar control design procedure as the basic version of mixed sensitivity-based robust control.

Nonetheless, it appears to overcome the pole-zero compensation issue, increasing all types of model mismatch from the synthesis model, including the unstructured and structured uncertainties. In addition, the industrialization of the control scheme validation procedure encompasses the random and independent variation of each mode position and damping of the plant model, which generalizes the model mismatch issue for all uncertainties. Moreover, the stability analysis based on robust analysis methods decreases the system's conservatism and increases the control structure's viability.

7.2 PERSPECTIVES

The current study assures superior tracking performance in comparison with the existing control algorithms. Though, some points are still open to further discussion.

From a theoretical point of view:

One of the main issues concerns the assessment of the stability of the closed-loop system during the controller switch. In the simulation, the overshoot due to the initialization of the second controller stays below the requirement for a very short period of time, within only two to three samples of the 12kHz sampling frequency of the system. Compared to the current system's performance, the performance of the extended switching H∞ controller is far better, even in the presence of this overshoot. Therefore, this issue which was not tackled in this work can be taken into account, needing further investigation in the future. The stability of an LPV system is hugely studied in the literature. The switching controllers seem to vary the control gain simultaneously with regard to the LPV model variation, and the stability in such a variable system seems to match the switching strategy used in this study. Therefore, the stability study can be realized via existing methods found in LPV system literature.

Moreover, the study of this thesis mainly concerns an extension of mixed sensitivity H∞ control, though other possibilities can still be considered. When studying the linear control methods, µ-synthesis based control comes first as it will be the extension of nominal H_∞ control, to desensitize the nominal controller to parametric variations of the plant via D-K iterations. Another direction is related to the current SMC structure that can be subject to further study in order to take into account the recent advances in the domain of non-linear control. Notably, the higher-order sliding mode controls are very prominent as they can reduce the chattering phenomena of classical sliding mode control systems. It will result in a significant noise reduction of the actual VTS, observed mainly when the reference goes to higher frequencies. Moreover, the main advantage of such control algorithms is that a group of SMC called model free-SMC can work without any prior knowledge of the plant model, unlike most control algorithms, which need a good knowledge of the plant dynamics. Such algorithms depend on state observers to estimate the system's state vector, even in a very fast system like VTS. This strategy can totally eliminate the step of dynamic model identification in the VTS process.

From an experimental point of view:

The thesis concerns the theoretical development of a new VTS control architecture, providing satisfactory results via virtual shaker simulation. In order to implement the current solution to the existing VTS, the first concern goes to the sensors, actuators and the numerical system. This study takes into account the existing sensors and actuators of a typical vibration testing system; therefore, the proposed control structure can be accommodated in the current hardware perimeter.

From the theoretical achievements to the experimental proof of concept, the main task will be prototyping the simulation-based virtual shaker to its implementation. The first step toward the physical implementation consists of using a test of hardware in the loop in parallel with the current model in the loop simulation on a dummy satellite with features corresponding at least to the modal parameters of the satellite. The requirement of this parallel testing strategy is to be able to compare the real-world test and simulation results. Undoubtedly, it will validate the exactness of the simulation as well as the real-time closed-loop performance of the onboard computer in terms of complexity management. After validation of the model in the loop structure, the robustness definition has to be defined. The parallel testing must assure the worst-case scenario to verify the feasibility range of the new control structure. After prototyping, the next step concerns implementing the existing numerical system based on LMS provided software package. The new closed-loop architecture has to be added to the existing real-time software. Once the robustness is defined and it complies with the real testing scenario, industrialization of the whole procedure would allow the user-friendliness of the whole procedure for AIT engineers and technicians.

8 APPENDIX

8.1 LINEAR ALGEBRA

8.1.1 Eigenvalue:

Eigenvalue of the matrix $A \in \mathbb{C}^{n\times n}$ is the root of the equation $\det(\lambda I - A) = 0$, noted by $\lambda_i(A)$, the i^{th} eigenvalue.

8.1.2 Vector norm

Let X be a vector space, the norm related to this space X defined by $\|.\|$ verifies:

- Positivity: $\|x\| \geq 0$
- Positive definite: $\|x\| = 0 \; if \; and \; only \; if \; x = 0$
- Homogeneity: $\|\alpha x\| = |\alpha|\|x\|, \text{where } \alpha \text{ is a scalar}$
- Triangular inequality: $\|x + y\| \leq \|x\| + \|y\|$

where $x, y \in X$.

Let $x \in \mathbb{C}^n$, p-norm of x can be written as:

$$\|x\|_p = \left(\sum_{i=1}^{n} |x_i|^p\right)^{\frac{1}{p}} \qquad \textit{Eq. 8-1}$$

Then the norm $1, 2 \text{ and } \infty$ can be given using *Eq. 8-1*.

$$\|x\|_1 = \sum_{i=1}^{n} |x_i|$$

$$\|x\|_2 = \sqrt{\sum_{i=1}^{n} |x_i|^2}$$

$$\|x\|_\infty = \max_{1\le i\le n} |x_i|$$

8.1.3 Matrix norm

Suppose that $A = \left[a_{ij}\right] \in \mathbb{C}^{m\times n}$, the p-norm of matrix A induced by a vector x is defined as:

$$\|A\|_p = \sup_{x\neq 0} \frac{\|Ax\|_p}{\|x\|_p}$$

The norm $1, 2$ and ∞ can be given as:

$$\|A\|_1 = \max_{1\le j\le n} \left|a_{ij}\right|$$

$$\|A\|_2 = \sqrt{\lambda_{max}(A^*A)}$$

where λ_{max} the highest eigenvalue of the matrix A and A^* is the complex conjugate matrix of A (Zhou, et al., 1996).

$$\|A\|_\infty = \max_{1\le i\le m} \sum_{j=1}^{n} \left|a_{ij}\right| \quad \{row\ sum\}$$

8.1.4 Singular Value

The i^{th} singular value of the matrix $A \in \mathbb{R}^{m\times n}$ is the square root of the i^{th} eigenvalues of the matrix A^TA for $m > n$ (or AA^T if A is a row matrix). i^{th} singular value is noted $\sigma_i(A)$, $\overline{\sigma}(A)$ and $\underline{\sigma}(A)$ are respectively the biggest and smallest singular values of matrix A.

8.1.5 Singular value decomposition

Any matrix $A \in \mathbb{R}^{m \times n}$ $(m \geq n)$ can be written as:

$$A = U\Sigma V^T$$

where U, V are orthogonal matrices of dimension $m \times m$ and $n \times n$ respectively, $\Sigma \in \mathbb{R}^{m \times n}$ is in form:

$$\Sigma = \begin{pmatrix} \operatorname{diag}(\sigma_1, \dots, \sigma_n) \\ 0 \end{pmatrix}$$

Properties of singular value:

- $\sigma_i(A) = \lambda_i(AA^*)^{\frac{1}{2}} = \lambda_i(A^*A)^{\frac{1}{2}}$
- $\overline{\sigma}(A) = \sup\limits_{\|x\|=1} \|Ax\|$
- $\underline{\sigma}(A^{-1}) = \frac{1}{\overline{\sigma}(A)}$
- $\overline{\sigma}(A^{-1}) = \frac{1}{\underline{\sigma}(A)}$
- $\underline{\sigma}(A) \leq |\lambda_i(A)| \leq \overline{\sigma}(A)$
- $\overline{\sigma}(.)$ is a matrix norm, which inherits all properties of a norm as $\overline{\sigma}(AB) \leq \overline{\sigma}(A)\overline{\sigma}(B)$
- $rank(A)$ is the number of total non-zero singular values
- $\overline{\sigma}(VAU) = \overline{\sigma}(A)$, $\forall U, V$ unity matrix

$\underline{\sigma}$ and $\overline{\sigma}$ represent the smallest and biggest singular values of a matrix.

8.2 LINEAR TIME-INVARIANT CONTINUOUS-TIME DYNAMICAL SYSTEMS

The Laplace transformation of a time domain causal signal $x(t)$ sur $(0,+\infty)$ is the function $X(s) = \mathcal{L}(x(t))$ of the Laplace variable s defined by:

$$X(s) = \int_{0}^{+\infty} x(t)e^{-st}dt$$

The main characteristics of the Laplace transformation are:

- $\mathcal{L}[x(t+\tau)] = e^{s\tau}X(s)$
- $\mathcal{L}\left[\frac{dx}{dt}\right] = sX(s) - x(0)$
- $\mathcal{L}\left[\int_0^t x(u)du\right] = \frac{X(s)}{s}$
- Time domain convolution product: $\mathcal{L}[x * y] = X(s)Y(s)$
- Initial value theorem: $\lim_{t\to 0} x(t) = \lim_{s\to +\infty} sX(s)$
- Final value theorem: $\lim_{t\to +\infty} x(t) = \lim_{s\to 0} sX(s)$

8.2.1 Transfer function

Let $g(t)$ be the impulse response of the linear time invariant system, where input $u(t) = \delta(t)$. The relation between the input and output in time domain is the convolution product between g and u.

$$y(t) = g(t) * u(t) = \int_{-\infty}^{+\infty} g(t-\tau)\mathrm{x}(\tau)d\tau$$

- In case of causal system, $g(t) = 0$ for all $t < 0$

$$y(t) = g(t) * u(t) = \int_{0}^{t} g(t-\tau)\mathrm{x}(\tau)d\tau \qquad \textit{Eq. 8-2}$$

The Laplace transformation let us write:

$$Y(s) = G(s)U(s)$$

The Laplace transformation $G(s)$ of the impulse response $g(t)$ is called transfer-function or frequency response of the system. In the case of finite dimension system, $G(s)$ is a rational function. The transfer functions are illustrated via bloc diagram:

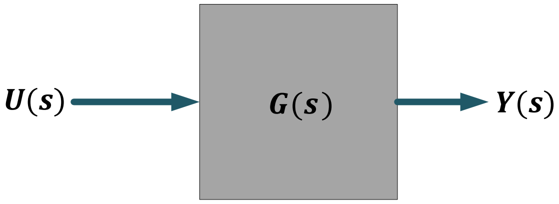

Figure 8-1 - Representation of a transfer function

8.2.2 State space representation

A linear time invariant finite dimensional dynamical system (LTI) can be described by the following differential equation:

$$\begin{cases} \dot{x}(t) = Ax(t) + Bu(t), \ \ x(t_0) = x_0 \\ y(t) = Cx(t) + Du(t) \end{cases} \qquad \textit{Eq. 8-3}$$

where $x(t) \in \mathbb{R}^n$ is the state vector, $x(t_0)$ the initial condition of the system, $u(t) \in \mathbb{R}^m$ the system input, $y(t) \in \mathbb{R}^P$ the system output. A, B, C and D are real constant matrices. A single input ($m = 1$) and single output system ($p = 1$) is known as SISO, otherwise MIMO. The transfer matrix from u to y is defined as:

$$Y(s) = G(s)U(s)$$

$U(s)$ and $Y(s)$ are the Laplace transformation of $u(t)$ and $y(t)$ with zero initial condition. The system matrix $G(s)$ can be written in terms of state matrices:

$$G(s) = C(sI - A)^{-1}B + D$$

Given the initial condition $x(t_0)$, the response of the dynamical system for $t \geq t_0$ can be defined by:

$$x(t) = e^{A(t-t_0)}x(t_0) + \int_{t_0}^{t} e^{A(t-\tau)}Bu(\tau)d\tau$$

$$y(t) = Cx(t) + Du(t)$$

The input and output relation can be described via the convolution product given by *Eq. 8-2*.

8.2.3 Controllability and observability of a LTI system

The pair (A, B) of the dynamical system is controllable if there exists an input $u(.)$ such that the solution of *Eq. 8-3* satisfies $x(t_1) = x_1$. The controllability of a system can be verified through following algebraic criteria:

The pair (A, B) is controllable in an LTI SISO and MIMO system, equivalent to the following conditions:

- The matrix $W_c(t) = \int_0^t e^{A\tau}BB^*e^{A^*\tau}d\tau$ is positive definite for any $t > 0$
- The controllability matrix $\mathcal{C} = [B \quad AB \quad A^2B \quad \dots \quad A^{n-1}B]$ has full row rank
- The matrix $[A - \lambda I,\ B]$ has full row rank for all λ in $\mathbb{C}$

The pair (C, A) of the dynamical system (defined in *Eq. 8-3*) is observable if for any $t > 0$, the initial state $x(0) = x_0$ can be determined from the input $u(t)$ and the output $y(t)$ in the interval of $[0, t_1]$. The observability of a system can be verified through following algebraic criteria:

The pair (C, A) is observable, equivalent:

- The matrix $W_0(t) = \int_0^t e^{A\tau} CC^* e^{A^*\tau} d\tau$ is positive definite for any $t > 0$
- The controllability matrix:

$\mathcal{O} = [C^T \quad (CA)^T \quad (CA^2)^T \quad \dots \quad (CA^{n-1})^T]^T$ has full column rank

- The matrix $\begin{bmatrix} A - \lambda I \\ C \end{bmatrix}$ has full column rank for all λ in $\mathbb{C}$

8.2.4 Stability and stabilizability of a LTI system

An unforced dynamical system described by $\dot{x} = Ax$ is called stable if all Eigenvalues of the matrix A are in the open left half plane, $Re\lambda(A) < 0$.

8.2.5 Linear Fractional transformation

The linear Fractional transformation are used to model and control dynamic systems, mainly:

- Formulation of control problem of $H_\infty/H_2/\mu$ of the augmented plant via LFT
- Structured uncertainties via LFT

Suppose a matrix P and K of appropriate dimension and their inverse exist, P partitioned as follows:

$$P = \begin{bmatrix} P_{11} & P_{12} \\ P_{21} & P_{22} \end{bmatrix}$$

The upper LFT F_u and lower LFT F_l can be defined as follows:

$$F_u(P, K) = P_{22} + P_{21}K(I - M_{11})^{-1}P_{12}$$

$$F_l(P, K) = P_{11} + P_{12}K(I - P_{22})^{-1}P_{21}$$

Upper and lower LFT representations are given in Figure 8-2.

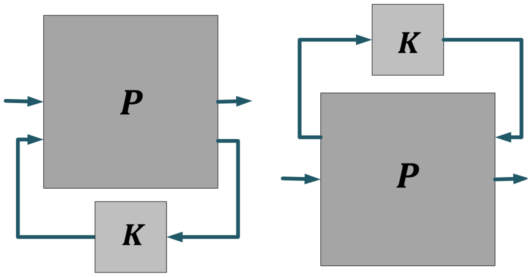

Figure 8-2 - Lower (left) and Upper LFT (right)

8.3 H_2 AND H_∞ NORMS

8.3.1 $\mathcal{L}_2$ and H_2 space

$\mathcal{L}_2(j\mathbb{R})$ is a Hilbert space of matrix-valued function, which consists of complex function of matrix G such that the following function stays bounded.

$$\int_{-\infty}^{\infty} Trace[G^T(jw)G(jw)]dw < \infty$$

H_2 norm is a subspace of $\mathcal{L}_2(j\mathbb{R})$, the H_2 norm of a matrix function $G(s)$ is given by:

$$\|G\|_2{}^2 = \frac{1}{2\pi}\int_{-\infty}^{\infty} Trace[G^T(jw)G(jw)]dw$$

8.3.2 $\mathcal{L}_\infty$ and H_∞ space

$\mathcal{L}_\infty(j\mathbb{R})$ is a Banach space of matrix-valued function, G is a complex-matrix function such that the following function stays bounded on $j\mathbb{R}$.

$$\|G\|_\infty = \sup_{w\in\mathbb{R}} \bar{\sigma}[G(jw)]$$

H_∞ norm is a subspace of $\mathcal{L}_\infty$, for all complex matrix function G are in the open right half plane in the norm H_∞.

$$\|G\|_\infty = \sup_{Re(s)>0} \bar{\sigma}[G(s)]$$

Performance specification via H_2 and H_∞ norm:

Suppose input u of size q and output v of size p linear finite dimensional system of the Figure 8-1, where the transfer matrix $G \in H_\infty$. The system transfer matrix G of size $p \times q$ can be written as:

$$G(s) = \begin{pmatrix} G_{11}(s) & \cdots & G_{1q}(s) \\ \vdots & \ddots & \vdots \\ G_{p1}(s) & \cdots & G_{pq}(s) \end{pmatrix} = \begin{pmatrix} G_1(s) \\ \cdot \\ \cdot \\ G_p(s) \end{pmatrix}$$

Norms are used to determine the systems performance. Generally, inducing a norm to a system matrix G is equivalent to say that an operator (norm) relating the input to output signals which determines the achievable performance of the system for given input signals.

8.3.3 Signal and System

8.3.3.1 Signal

Suppose the x and y are two signals on $\mathcal{L}_2$ space. The scalar product of these two signals are given by:

$$\langle x, y \rangle = \int_{0}^{+\infty} x(t)y(t)dt$$

The instantaneous power of the signal is $x(t)^2$, then the energy of the signal can be expressed by the H_2 norm:

$$\|x\|_2 = (\int_{0}^{+\infty} \|x(t)\|^2 dt)^{\frac{1}{2}}$$

The ∞ norm of a signal is given by the following equation:

$$\|x\|_\infty = \sup_t |x(t)|$$

8.3.3.2 System

Let $G(s)$ be the transfer function of a system. The 2-norm of the system is given by:

$$\|G\|_2 = (\int_{-\infty}^{+\infty} |G(jw)|^2 dt)^{\frac{1}{2}} = (\frac{1}{2\pi} \int_{-\infty}^{\infty} Trace[G^T(jw)G(jw)]dw)^2$$

$$= \sup_{U(s)\in H_\infty} \frac{\|Y(s)\|_2}{\|U(s)\|_\infty}$$

The physical signification of the 2-norm of a system is the energy of the system output in case of a Dirac input.

The ∞-norm of the system:

$$\|G\|_\infty = \sup_{w\in[-\infty,\infty]} |G(w)| = \sup_{U(s)\in H_2} \frac{\|Y(s)\|_2}{\|U(s)\|_2}$$

8.3.3.3 $\|H\|_\infty$ norm and control synthesis

There are several methods to compute the $\|H\|_\infty$ norm of a standard control problem explained in 3.5.2.4. Here, we exploit the solution of $\|H\|_\infty$ problem by solving Riccati equation, which is the mostly used approach in robust control literature. At first, the control problem is defined in Figure 8-3.

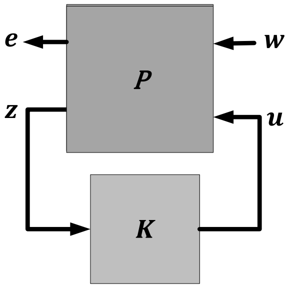

Figure 8-3 – Standard $\|H\|_\infty$ problem

The transfer matrix $K(s)$ is the controller to be determined, $P(s)$ represents the dynamic between external two input block, w (reference, disturbance etc..) and u control effort, two output blocks, z corresponds to the measure and e is for error signal. $P(s)$ can be partitioned in such way that the dynamics of input and output can be modeled as follows:

$$\begin{bmatrix} E(s) \\ Z(s) \end{bmatrix} = \begin{bmatrix} P_{\mathrm{ew}}(s) & P_{\mathrm{eu}}(s) \\ P_{\mathrm{zw}}(s) & P_{\mathrm{zu}}(s) \end{bmatrix} \begin{bmatrix} W(s) \\ U(s) \end{bmatrix} \qquad \textit{Eq. 8-4}$$

Replacing the expression of $Z(s)$ in $E(s)$ of *Eq. 8-4*, the following relation can be obtained.

$$E(s) = \left(P_{\mathrm{ew}}(s) + P_{\mathrm{eu(s)}}K(s)(I - P_{\mathrm{zu}}(s)K(s))^{-1}P_{\mathrm{zw}}(s)\right)W(s)$$

Then the $E(s)$ can be written in the form of lower LFT, as illustrated in Figure 8-3.

$$E(s) = \boldsymbol{F_l}(\boldsymbol{P}(\boldsymbol{s}), \boldsymbol{K}(\boldsymbol{s}))W(s)$$

8.3.3.3.1 Definition of the problem

If there exists a $\gamma > 0$, determine the $K(s)$ which internally stabilizes the closed loop system of Figure 8-3 by assuring $\|F_l(P(s), K(s))\|_\infty < \gamma$. The optimal $K(s)$ is the one assuring the smallest value of γ.

8.3.3.3.2 Significance of the $\|\boldsymbol{H}\|_\infty$ norm:

The transfer function from each component of the vector w to each component of the vector e will have $\|H\|_\infty$ norm and it will stay below γ (as $\|F_l(M(s), K(s))\|_\infty < \gamma$, where P is replaced by M for the rest of this section, as P is introduced in Riccatti equation, which is different than the augmented matrix M). The significance of this norm is that we can impose specifications of closed-loop system via appropriate filters on the transfer function from w to e in order to obtain the desired response of the closed-loop system.

Computation of the $\|H\|_\infty$ norm via Riccati equation:

This approach is known as Glover-Doyle in the literature (Doyle, et al., 1989). *Eq. 8-4* can be written in state space form by partitioning the transfer matrix to proper channel:

$$\begin{bmatrix} \dot{x}(t) \\ e(t) \\ z(t) \end{bmatrix} = \begin{bmatrix} A & B_w & B_u \\ C_e & D_{ew} & D_{eu} \\ C_z & D_{zw} & D_{zu} \end{bmatrix} \begin{bmatrix} x(t) \\ w(t) \\ u(t) \end{bmatrix}$$

with $x \in \mathbb{R}^n$, $w \in \mathbb{R}^{n_w}$, $u \in \mathbb{R}^{n_u}$, $e \in \mathbb{R}^{n_e}$ and $z \in \mathbb{R}^{n_z}$. Let matrices $P \in P^T$,

$Q \in Q^T$ have the same dimension as A. Let the following Riccati equation such that the real part of the eigen values of the matrix $A - PX$ are strictly negative:

$$XA + A^T X - XPX + Q = 0 \qquad \textit{Eq. 8-5}$$

If the solution of *Eq. 8-5* exists, it would be symmetric and expressed by:

$$X = Ric\begin{pmatrix} A & -P \\ -Q & -A^T \end{pmatrix}$$

The following hypotheses have to be satisfied in order to solve the standard $||H||_\infty$ problem:

1. The pair (A, B_u) is stabilizable and (C_z, A) is detectable. This hypothesis is common in all state feedback control system for the assurance of the stability of the closed-loop system.

2. $rank(D_{eu}) = n_u$ and $rank(D_{zw}) = n_z$. The complete rank of D_{eu} signifies that all variables of the vector e are controlled. This hypothesis also implicitly supposes that $n_e \geq n_u$ and $n_w \geq n_z$.

3. $\forall\, w \in \mathbb{R}$, $rank\begin{pmatrix} A - jwI_\mathrm{n} & -B_\mathrm{u} \\ C_\mathrm{e} & D_\mathrm{eu} \end{pmatrix} = n + n_u$. It implies that $P_{eu}(s)$ does not have any zero on the imaginary axis.

4. $\forall\, w \in \mathbb{R}$, $rank\begin{pmatrix} A - jwI_\mathrm{n} & -B_\mathrm{w} \\ C_\mathrm{z} & D_\mathrm{zw} \end{pmatrix} = n + n_z$. Like the previous hypothesis, it implies that $P_{zw}(s)$ does not have zero on the imaginary axis.

Under these hypotheses, the standard $||H||_\infty$ problem admits a solution if and only if:

5. $H_\infty = \begin{bmatrix} A & \gamma^{-2} B_\mathrm{w} {B_\mathrm{w}}^T - B_\mathrm{u} {B_\mathrm{u}}^T \\ -{C_\mathrm{e}}^T C_\mathrm{e} & -A^T \end{bmatrix}$ does not have strict imaginary eigenvalue.

6. There exists a matrix $X_\infty = Ric(H_\infty) \geq 0$
7. $J_\infty = \begin{bmatrix} A^T & \gamma^{-2}{C_\mathrm{e}}^T C_\mathrm{e} - C_\mathrm{z}{C_\mathrm{z}}^T \\ -B_\mathrm{w}{B_\mathrm{w}}^T & -A \end{bmatrix}$ does not have strict imaginary eigenvalue.
8. There exists a matrix $Y_\infty = Ric(J_\infty) \geq 0$
9. $\rho(X_\infty Y_\infty) < \gamma^2$, where ρ is the biggest eigenvalue.

The second condition of this theorem assesses the resolution of a Riccati equation, where the last condition introduces a coupling of two Riccati solutions. Lastly, the following theorem states the solution of the problem:

Under condition from one to four, the rational controller $K(s)$ stabilizes the system and satisfies $\|F_l(M(s), K(s))\|_\infty < \gamma$. Then the rational controller $K(s)$ can be given by the following LFT form of two transfer matrix $K_a(s)$ and $\Phi(s)$.

$$K(s) = F_l\big(K_a(s), \Phi(s)\big)$$

Where $\Phi(s) \in \mathbb{R}H_\infty$ is a $n_u \times n_z$ transfer matrix verifying $\|\Phi\|_\infty < \gamma$, and $K_a(s)$ is given by following state space representation.

$$\begin{bmatrix} \dot{x}_a(t) \\ u(t) \\ u_a(t) \end{bmatrix} = \begin{bmatrix} \hat{A}_\infty & Z_\infty Y_\infty {\mathrm{C}_z}^T & Z_\infty B_\mathrm{u} \\ -{\mathrm{B}_u}^T X_\infty & 0 & I_{\mathrm{n}_u} \\ -C_\mathrm{z} & I_{\mathrm{n}_z} & 0 \end{bmatrix} \begin{bmatrix} x_a(t) \\ z(t) \\ z_a(t) \end{bmatrix}$$

$$\hat{A}_\infty = A + \gamma^{-2} B_\mathrm{w} {B_\mathrm{w}}^T X_\infty - B_\mathrm{u} {B_\mathrm{u}}^T X_\infty - Z_\infty Y_\infty {\mathrm{C}_z}^T C_\mathrm{z}$$

$$Z_\infty = (I_\mathrm{n} - \gamma^{-2} Y_\infty X_\infty)^{-1}$$

Practically, the controller can be achieved by firstly obtaining the optimal value of γ through the formulation 5 to 9, called γ iteration. Then the theorem $\|F_l(M(s), K(s))\|_\infty < \gamma$ let us compute the controller.

8.3.4 Robustness

Previous synthesis methods introduce the control based on the nominal plant model. A real physical system presents significant difference from the modeled plant. We can categorize these differences into two types of uncertainties. Firstly, the unstructured uncertainties account for the neglected or unknown dynamics in higher or lower frequencies outside the control bandwidth. Secondly, the structured uncertainties address the parameter variation of the plant model. Standard H_∞ method can be used for elaborating the unstructured uncertainties into synthesis, though the structured uncertainties need to be defined through structured singular value known as μ. In this part, we introduce the μ-analysis to assess the closed-loop systems robust stability in case of parameter variation.

8.3.4.1 Structured vs unstructured singular values

Structured values are the generalization of the singular values when the system matrix is not constant. Suppose the following $M-\Delta$ interconnection of Figure 8-4. In the robust stability analysis, main idea is to assess the largest value of Δ without destabilizing the closed-loop system. The closed loop system becomes unstable for $\det(I-M\Delta)=0$. Let α be a scalar value such that the closed loop system is stable for all $\|\Delta\|_\infty < \alpha$. Let increase α up to α_{max} when the system becomes unstable, α_{max} is called the robust stability margin.

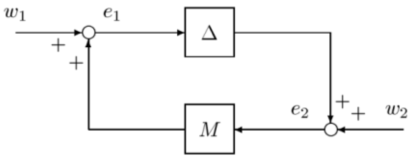

Figure 8-4 - M-Δ structure

By the application of small gain theory, we may obtain the α_{max}:

$$\alpha_{max} = \frac{1}{\|M\|_\infty} = 1/\sup_{w} \bar{\sigma}(M(jw))$$

8.3.4.2 Singular value

When the Δ is unstructured, small gain theorem let us write $\bar{\sigma}(M(jw)$ as:

$$\bar{\sigma}(M(jw) = \frac{1}{min\{\bar{\sigma}(\Delta)\ such\ that\ \det(I - M\Delta) = 0\}}\quad where\ \Delta\ is\ unstuctured$$

8.3.4.3 Structured singular value (SSV)

When Δ is structured, small gain theorem let us define the structured singular value μ:

$$\mu_\Delta\big(M(s)\big) = \frac{1}{min\{\bar{\sigma}(\Delta)\ such\ that\ \det(I - M\Delta) = 0\}}\quad where\ \Delta\ is\ structured$$

Which is the largest singular value of $M(s)$ with respect to structured Δ. In this case, the robust stability can be defined as:

$$\alpha_{max} = \frac{1}{\sup\limits_{w} \mu_\Delta(M(jw))}$$

8.3.4.4 μ analysis

Here, we use the properties of structured singular value μ to analyze the robustness of the closed loop system. Firstly, we have to define the standard LFT form of the closed-loop system as illustrated in Figure 8-5.

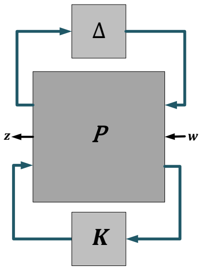

Figure 8-5 - General structure

Suppose that $P(s)$ is the nominal plant matrix, K the controller dynamics and Δ the uncertainty block, let $P(s)$ be the following matrix.

$$P(s) = \begin{bmatrix} P_{11}(s) & P_{12}(s) & P_{13}(s) \\ P_{21}(s) & P_{22}(s) & P_{23}(s) \\ P_{31}(s) & P_{32}(s) & P_{33}(s) \end{bmatrix}$$

The model of Figure 8-5, can be presented as a combination of one upper and one lower LFT.

$$z = F_u(F_l(P, K), \Delta)w$$

The next step of the robust analysis of a LPV system consists of introducing the standard $M - \Delta$ form of the previous Figure, where we separate the known part of the system from the uncertain part. M is defined as:

$$M(s) = F_l(P(s), K(s)) = \begin{bmatrix} M_{11}(s) & M_{12}(s) \\ M_{21}(s) & M_{22}(s) \end{bmatrix}$$

M contains the known part where we regroup P and K with above relation, Δ structure contains the variable part of the system. Figure 8-6 illustrates the $M - \Delta$ structure.

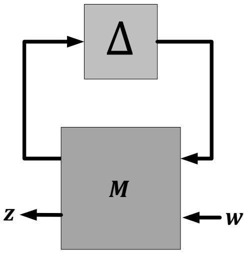

Figure 8-6 - Standard M-Δ structure for μ analysis

The transfer function from w to z can be given by:

$$z = F_u(M, \Delta)w = [M_{22} + M_{21}\Delta(I - M_{11}\Delta)^{-1}M_{12}]w \qquad \textit{Eq. 8-6}$$

The state space representation of a LPV system of *Eq. 8-6* can be written in the following standard form, where z corresponds to the output y and w corresponds to the input u of Figure 8-6:

$$\begin{cases} \dot{x} = \left(A_0 + \sum_i A_i \delta_i\right) x + \left(B_0 + \sum_i B_i \delta_i\right) u \\ y = \left(C_0 + \sum_i C_i \delta_i\right) x + \left(D_0 + \sum_i D_i \delta_i\right) u \end{cases}$$

$\delta_i \in [-1,1]$ represents the normalized i^{th} parameter variation, we can define the uncertainty block $\Delta = diag\{\delta_1 I_{r_1}, \dots \dots, \delta_r I_{r_r}\}$; $\delta_i \in \mathbb{R}$. In here, the block M and Δ have the same dimension, r is the total number of structured uncertainties. The robust stability defines the minimum stability margin while varying Δ bloc. If real parts of all poles of $M(s)$ are strictly negative, the system of *Eq. 8-6* is stable for all uncertainties of $\Delta(s)$ such that $\|\Delta(s)\|_\infty < \alpha$ if and only if

$$\mu_\Delta\big(M(s)\big) \le \alpha^{-1} \; \forall w$$

α is then the robust stability margin. Practically, for a set of w we assess the max value of μ considering the variation defined by Δ. So, the SSV $\mu_\Delta\big(M(jw)\big)$ (Apkarian, 1993) (Duc & Font, 1999) would be computed for a finite number of $w_{i\in[1,N]}$ and the robustness margin α_{max}:

$$\alpha_{max}{}^{-1} = \max_{i\in[1,N]} \mu_\Delta\big(M(jw_i)\big)$$

In order to achieve better results, the values of w has to be dense in the given range. In addition, we can evaluate the robust performance via μ-analysis, but it is not needed for the thesis work, so the description is limited to the robust stability analysis.

The details of these methods can be found in (Skogestad & Postlethwaite, 2001) (Alazard, et al., 1999) (Duc & Font, 1999) (Apkarian, 1993).

8.4 DISCRETE AND CONTINUOUS MODEL

8.4.1 Zero Order Hold

ZOH generates the continuous time signal $u(t)$ by keeping the discrete time signal $u(k)$ for a sampling time T_s.

$$u(t) = u(k) \quad for \quad kT_s \leq t \leq (k+1)T_s$$

Converting a discrete system $H_d(z)$ to the continuous time system $H(s)$ by ZOH, where the $H(s)$ matches $H_d(z)$.

8.4.2 First-Order Hold

The FOH differs from ZOH as in FOH, the output of the system is no longer a constant value, rather than the interpolation between two points. To convert a discrete signal $u(k)$ to continuous time signal $u(t)$, the FOH interpolation can be given by the following expression:

$$u(t) = u(k) + \frac{t - kT_s}{T_s}(u(k+1) + u(k)) \quad for \quad kT_s \leq t \leq (k+1)T_s$$

Compared to ZOH, FOH results more accurate and smoother dynamics.

8.4.3 Bilinear Approximation

The bilinear approximation consists of relating the s-domain and z-domain transfer function by the following approximation:

$$z = \; e^{sT_s} \; \approx \; \frac{1 - \frac{sT_s}{2}}{1 - + \frac{sT_s}{2}}$$

An explicit continuous-time state space model ($where\ the\ matrix\ E = I$), the state vector $w(k)$ of the discretized model is linked to the continuous-time state vector $x(t)$ by following equation:

$$w(kT_s) = \left(1 - A\frac{T_s}{2}\right)x(kT_s) - \frac{T_s}{2}Bu(kT_s)$$

8.4.4 Zero-Pole Matching equivalents

The conversion between continuous and discrete-time system by computing the equivalent of pole-zero, which can be given by:

$$z_i = e^{s_i T_s}$$

$$z_i : i^{th}\ pole\ or\ zero\ of\ the\ of\ discrete - time\ system$$

$$s_i : i^{th}\ pole\ or\ zero\ of\ the\ of\ the\ continuous - time\ system$$

The details of this method can be found in (Franklin, et al., 1997) (Matlab Reduce, website).

8.4.5 Model reduction

8.4.5.1 Hankel Singular Values

Hankel singular values (HSS) of a system matrix define the energy of each state of the system. The larger energy states correspond to the most characteristics of the system. A stable system is defined by state matrices (A, B, C, D), where the Hankel singular values are given by following equation:

$$\sigma_H = \sqrt{\lambda_i(PQ)}$$

P and Q are controllability and observability grammians of the system (A, B, C, D) defined in next section.

8.4.5.2 Balanced model truncation via square root method

A full order model of the system is given by G_{full}, where (A, B, C, D) are the associated state-space matrices and the reduced version of G_{full} is G_{red}. This method assures an additive error bound in infinity norm given by the following equation:

$$\left\| G_{full} - G_{red} \right\|_{\infty} \leq 2 \sum_{1+k}^{n} \sigma_i$$

where n is the total order of the model G_{full}, k is the desired reduced order and $i \in [1, n]$.

Algorithm:

Given the state-space model (A, B, C, D) and k the order of the reduced model, the following algorithm provides the reduced-order model G_{red}.

P and Q are controllability and observability grammians of the system (A, B, C, D), which satisfy:

$$AP + PA^T = -BB^T$$

$$A^T Q + QA = -C^T C$$

1) Step 1: Compute the SVD of the controllability and observability grammians (P, Q):

$$P = U_P \Sigma_P {V_P}^T$$

$$Q = U_q \Sigma_q {V_q}^T$$

with (U_P, U_q) the left eigenvectors, (V_P, V_q) the right eigen vectors, (Σ_P, Σ_q) the singular value matrices.

2) Step 2: Compute the square root of grammians:

$$L_P = U_P {\Sigma_P}^{\frac{1}{2}}$$

$$L_q = U_q {\Sigma_q}^{\frac{1}{2}}$$

3) Step 3: Compute the SVD of $({L_q}^T L_P)$:

$${L_q}^T L_P = U \Sigma V^T$$

4) Step 4: The left and right transformation of the final k^{th} order reduced model:

$$S_{L,BIG} = L_q U(:,1:k)\Sigma(1:k,1:k)^{-\frac{1}{2}}$$

$$S_{R,BIG} = L_p V(:,1:k)\Sigma(1:k,1:k)^{-\frac{1}{2}}$$

5) Step 5: The reduced order state space matrices $(\hat{A},\hat{B},\hat{C},\hat{D})$ are given by:

$$\begin{bmatrix} \hat{A} & \hat{B} \\ \hat{C} & \hat{D} \end{bmatrix} = \begin{bmatrix} {S_{L,BIG}}^T A S_{R,BIG} & {S_{L,BIG}}^T B \\ C S_{R,BIG} & D \end{bmatrix}$$

8.4.5.3 Balanced stochastic model truncation via Schur method

A model of the system given by G_{full}, where (A,B,C,D) the associated state space matrices and the reduced version is G_{red}. The balanced stochastic model truncation guarantees the multiplicative relative error in infinity norm:

$$\left\| {G_{full}}^{-1}(G_{full} - G_{red}) \right\|_\infty \leq \prod_{k+1}^{n} \left(1 + 2\sigma_i \left(\sqrt{1 + {\sigma_i}^2} + \sigma_i\right)\right) - 1$$

where n is the total order of the model G_{full}, k is the desired reduced order and $i \in [1,n]$.

Algorithm:

Given the state space model (A,B,C,D) and k the order of the reduced model, the following algorithm provides the reduced order model G_{red}.

1) Step 1: Solve the following equation to compute controllability and observability grammians (P,Q) of the system (A,B,C,D), which satisfy:

$$AP + PA^T = -BB^T$$

$$A^T Q + QA = -C^T C$$

2) Step 2: Compute an orthogonal real matrix V such that $VPQV^T$ is upper triangular.

3) Step 3: Find the Schur decomposition for PQ in both ascending (V_A) and descending (V_D) order:

$$V_A{}^T PQV_A = \begin{bmatrix} \lambda_{A_n} & \cdots & * \\ \vdots & \ddots & \vdots \\ 0 & \cdots & \lambda_{A_1} \end{bmatrix}$$

$$V_D{}^T PQV_D = \begin{bmatrix} \lambda_{D_1} & \cdots & * \\ \vdots & \ddots & \vdots \\ 0 & \cdots & \lambda_{D_n} \end{bmatrix}$$

4) Step 4: Partition V_A and V_D as follows:

$$V_A = \left[\overbrace{S_{L,SMALL}}^{n-k} \quad \overbrace{V_{L,BIG}}^{k} \right]$$

$$V_D = \left[\overbrace{S_{R,BIG}}^{k} \quad \overbrace{V_{L,SMALL}}^{n-k} \right]$$

5) Step 5: Find the SVD of $(V_{L,BIG}{}^T V_{R,BIG})$

6) Then step 6 and 7 are alike the step 4 and 5 of the previous method.

The details of this method can be found in (Zhou, 1993) (Safonov & Chiang, 1988) (Safonov & Chiang, 1989).

9 REFERENCES

Glover, K., 1984. All Optimal Hankel Norm Approximation of Linear Multivariable Systems, and Their L∝-error Bounds. *Int. J. Control,* pp. 1145-1193.

Zhou, K., 1993. Frequency-weighted model reduction with L∞ error bounds. *Syst. Contr. Lett.*.

Achiezer, N. I., 1956. *Theory of approximation.* New York: Frederick Ungar Publishing Co..

Alazard, D. et al., 1999. *Robustesse et commande optimale.* Toulouse: Cépadués-Editions.

Alazard, D., De Lafontaine, J. & Kron, A., 2003. Robust 2-DOF H-infinity Controller for Highly Flexible Aircraft : Design Methodology and Numerical Results. *Canadian Aeronautics and Space Journal,* pp. 19-29.

Alazard, D., Jeanneau, M. & Mouyon, P., 1999. A semi-adaptive frequency control law for flexible structures - On the way to adaptive Q-LQG control. *American Institute of Aeronautics and Astronautics.*

Albrecht, A., Frémovici, M., Gaid, M. B. & Grise, C., 2012. *Multi-Model Integration from MiL to HiL: A New Simulation Approach to address the Modern Powertrain Development Challenges.* Sao Paulo, s.n.

Apkarian, P., 1993. *Élément de la commande robuste.* [Online] Available at: http://pierre.apkarian.free.fr/COURS/polysae.pdf

Apkarian, P. & Gahinet, P., 1994. A linear matrix inequality approach to H∞-control. *Int. J. Robust and Nonlinear Control,* p. 421–448.

Apkarian, P., Noll, D. & Pellanda, P. C., 2005. *Nonsmooth H∞ Synthesis.* Rio de Janeiro, IEEE.

Arefin, S., 2020. *Sine Sweep Tracking Control of a Lightly-Damped Spacecraft.* s.l., IEEE.

Arefin, S., 2021. *Robust Dynamic Tracking Control of a Modal Parameter Varying Spacecraft avoiding Vibration.* s.l., IEEE.

Arianespace, 2011. *Ariane 5 User's Manual.* s.l.:Arianespace.

Aström, K. J. & Murray, R. M., 2009. *Feedback Systems An Introduction for Scientists and Engineers.* s.l.:PRINCETON UNIVERSITY PRESS.

Åström, K. & Wittenmark, B., 1990. *Computer-Controlled Systems: Theory and Design.* s.l.:Prentice-Hall.

Aubrun, J. & Margulies, J., 1982. *Low-Authority Control Synthesis for Large Space Structures,* California : Lockheed Missiles and Space Company, Inc..

Balas, G., 1990. *Robust control of flexible structures: theory and experiments,* California: California Institute of Technology.

Balas, G. J. & Doyle, J. C., 1990. *Collocated versus Non-collocated Multivariable Control for Flexible Structure.* San Diego, IEEE.

Bandyopadhyay, B., Deepak, F. & Kim, K.-S., 2009. *Sliding Mode Control Using Novel Sliding Surfaces.* Bombay: Springer.

Barrera-Cardenas, R. A. & Molinas, M., 2012. Optimal LQG Controller for Variable Speed Wind Turbine. *Energy Procedia.*

Bartolini, G., Fridman, L., Pisano, A. & Usai, E., 2008. *Modern Sliding Mode Control Theory.* s.l.:Springer.

Bartoszewicz, A., 2011. *Robust Control, Theory and Applications.* Rijeka: InTech.

Ben-Gurion, Cousework. *Feedforward Control.* [Online] Available at: https://www.bgu.ac.il/chem_eng/pages/Courses/oren%20courses/Chapter_9.pdf

Bettacchioli, A., 2014b. *Simulation of Satellite Vibration Test.* Braunschweig, ESA Communications, p. 46.

Bettacchioli, A., 2018. Feasibility study of the beating cancellation during the satellite vibration test. *Advances in aircraft and spacecraft science,* pp. 225-237.

Bettacchioli, A. & Nali, P., 2015. *Common issues in S/C sine vibration testing and a methodology to predict the sine test responses from very low level* *run*. Los Angeles, s.n.

Brennan, M., n.d. *Vibration testing,* s.l.: Institute of sound and vibration research, University of Southampton.

Calvi, A. & Nali, P., 2007. *Some remarks on the reduction of overtesting during base-drive sine vibration tests of spacecraft.* Rethymno, ECCOMAS.

Charles, C., n.d. *Synthèse d'un correcteur robuste pour le contrôle des battements lors des essais en vibration des satellites,* Cannes: Thales Alenia Space Confidential Document.

Chaudhuri, G. et al., 2003. Mixed-sensitivity approach to H∞ control of power system oscillations employing multiple FACTS devices. *IEEE Transactions on Power Systems.*

Chilali, M. & Gahinet, P., 1995. H∞ Design with Pole Placement Constraints: An LMI Approach. *IEEE Trans. Aut. Contr.,* p. 358–367.

Cozzani, A. & Appolloni, M., 2007. *Virtual testing simulation tool for the new quad head expander electrodynamic shaker.* s.l., ESA-ESTEC.

Dilhaire, S. & Maillet, D., 2015. *Dealing with the measurement noise of a sensor.* [Online]
Available at: https://www.sft.asso.fr/Local/sft/files/101/Text-L4-M6.pdf

DJB A/131/V, n.d. [Online]
Available at: https://www.trinstruments.cz/imported/files/Sn%C3%ADma%C4%8De/Sn%C3%ADma%C4%8De%20vibrac%C3%AD%20a%20r%C3%A1z%C5%AF/IEPE%20akcelerometr%20A-131-V/A-131-V%20datasheet.pdf

Doherty, M. J. & Tolson, R. J., 2013. *Input Shaping to Reduce Solar Array Structural Vibrations.* s.l.:Biblioscholar.

Doyle, J., Francis, B. & Tannenbaum, A., 1990. *Feedback control theory.* s.l.:Dover Publications.

Doyle, J. & Glover, K., 1988. State-space formulae for all stabilizing controllers that satisfy an H∞ norm bound and relations to risk sensitivity. *Systems & Control Letters,* pp. 167-172.

Doyle, J., Glover, K., Khargonekar, P. & Francis, B. A., 1989. State Space Solution to Standard H2 and H∞ Control Problem. Volume 34, pp. 831-847.

Duc, G. & Font, S., 1999. *Commande H∞ et μ-analyse.* Paris: Hermes Sciences publications.

Dulau, M. & Oltean, S.-E., 2020. *The Effects of Weighting Functions on the Performances of Robust Control Systems.* Târgu Mureș, MDPI.

ECSS, 2013. *Spacecraft mechanical loads analysis handbook.* s.l.:European Cooperation for Space Standardization.

Ellero, N., 2014. *Identification des fonctions de transfert multi-variables pour la simulation des essais d'environnement vibratoire des satellites,* Cannes: Thales Alenia Space Internal document.

Endevco 2222C, n.d. [Online] Available at: https://buy.endevco.com /contentstore/mktgcontent/endevco/datasheet/5002.pdf

Erdavide, T., 2019. *Synthèse identification NARMAX essai vibration,* Cannes: Thales Alenia Space Restricted Document.

Ewins, D., 2000. *Modal Testing: theory, practice and application.* s.l.:Research Studies Press.

Fleming, A. J. & Yik, T., 2014. *Active damping control using optimal Integral Force Feedback.* s.l., s.n.

Franklin, G., Powell, D. & Workman, M., 1997. *Digital Control of Dynamic Systems.* s.l.:Prentice Hall.

Fuller, C. C., Elliott, S. J. & Nelson, P. A., 1997. *Active Control of Vibration.* s.l.:Academic Press Inc.

Gabbert, U., Köppe, H. & Nestorović-Trajkov, T., 2006. Active vibration control using optimal LQ tracking system with additional dynamics. *International Journal of Control,* pp. 1182-1197.

Gagne, J.-P., Thomas, M. & Bensoussan, D., 1995. *Active control of vibrations by low-pass filter and state feedback on a flexible structure.* Montreal, IEEE.

Gahinet, P. & Apkarian, P., 2011. *Decentralized and fixed-structure H∞ control in MATLAB.* Orlando, IEEE.

Gahinet, P., Packard, A. & Seiler, P., 2020. An Introduction to Disk Margins. *IEEE Control Systems,* p. IEEE.

Genta, G., 2009. *Vibration Dynamics & Control.* Torino: Springer.

Girad, A. & Roy, N., 2012. *Revisiting The Effect Of Sine Sweep Rate On Modal Identification.* Noordwijk, ESTEC.

Girard, A. & Roy, N., 2007. *Structural Dynamics in Industry.* New Jersey: Wiley-ISTE.

Girard, A. & Roy, N., 2010. *Structural Dynamics in Industry.* s.l.: Wiley-ISTE.

Giuliano, F., 2019. *Robust attitude control of a spacecraft with flexible dynamics,* Stockholm: KTH ROYAL INSTITUTE OF TECHNOLOGY.

Glover, K., Sefton, J. & Mcfarlane, D., 1990. A Tutorial on Loop Shaping using H-Infinity Robust Stabilization. *IFAC Proceedings Volumes,* 23(8), pp. 117-126.

Green, M. & Limebeer, D. J., 2012. *Linear Robust Control.* s.l.:Dover Publications Inc..

GU, D., Petkov, P. & Konstantinov, M., 2013. *Robust Control Design with Matlab.* s.l.:Springer.

Guo, D. et al., 2009. Investigation of 2-DOF Precision Positioning System for IC Packaging. *Materials Science Forum,* pp. 628-629.

Habtour, E., Dasgupta, A. & Vantadori, S., 2017. *Cross-Axis Coupling and Phase Angle Effects Due to Multiaxial Vibration.* s.l., Springer, pp. 95-97.

Harrison, R. L., 2010. Introduction To Monte Carlo Simulation. *PubMed,* pp. 17-21.

Hernández, D., Castanos, F. & Fridman, L., 2014. *Pole-Placement in Higher-Order Sliding-Mode Control.* Cape Town, s.n.

Heuvel, I. v. d., 1997. *H-infinite controller design: algebraic Riccati equalities versus Linear Matrix Inequalities,* Eindhoven: Technische Universiteit Eindhoven.

Holterman, J. & Vries, T. J. D., 2001. *Active and passive damping based on piezoelectric elements, Controllability issues.* Enschede, s.n.

Jain, N. & Alleyne, A. G., 2009. *Comparison of SISO and MIMO Control Techniques for a Diagonally Dominant Vapor Compression System.* St. Louis, IEEE.

Jatunitanon, P., Srivongsa, T. & Meckl, P., 2009. Reference Input Shaping to Reduce Move Time of a Very Flexible One-Link Manipulator. *Kasetsart Journal - Natural Science,* p. 43.

Kacprzyk, J., 2019. *Variable-Structure Systems and Sliding-Mode Control From Theory to Practice.* Warsaw: Springer.

Khan, Y. & Khot, S., 2015. *Simulation of Active Vibration Control of a Cantilever Beam using LQR, LQG and H-∞ Optimal Controllers.* s.l., s.n.

Lalanne, C., 2014. *Mechanical Vibration and Shock Analysis, Sinusoidal Vibration, 3rd Edition.* New Jersey: Wiley-ISTE.

Le Ballois, S., 1994. *Commande Hoo multivariable d'un satellite par les facteurs premiers, assurant la robustesse vis à vis des modes souples.* Gif Paris: Université Paris XI.

Lee, H. & Utkin, V., 2006. *Chattering Problem in Sliding Mode Control Systems.* Alghero, IEEE.

Leguiller, Q., 2015. *Synthèse d'un correcteur robuste pour le contrôle des battements lors des essais en vibration,* Cannes: Thales Alenia Space Confidential.

Ling, J., Feng, Z. & Ming, M., 2018. Precision contour tracking using feedback-feedforward integrated control for a 2-DOF manipulation system. *International Journal of Robotics and Automation.*

Liu, J. & He, W., 2019. *Active Vibration Control and Stability Analysis of Flexible Beam Systems.* s.l.:Springer.

Liu, J. & Wang, X., 2011. *Advanced Sliding Mode Control for Mechanical Systems Design, Analysis and MATLAB.* Beijing: Springer.

LMS FAQ, n.d. *Frequently Asked Question : What's the theory behind Sine*

Control Testing, Luven: LMS Thales internal document.

Lundstrøm, P., Skogestad, S. & Wang, Z.-Q., 1991. Performance Weight Selection for H-Infinity and µ-Control Methods. *Transactions of the Institute of Measurement and Control ,* pp. 241-252.

Mahmoud, M. S. & Xia, Y., 2012. *Applied Control Systems Design.* London: Springer.

Masani, P. & Wiener, N., 1957. *The prediction theory of multivariate stochastic processe.* s.l.:Acta Math.

Matlab Reduce, website. *reduce.* [Online] Available at: https://fr.mathworks.com/help/robust/ref/lti.reduce.html

McConnell, K., 1995. *Vibration Testing: Theory and Practice.* s.l.:Wiley.

Miljković, D., 2009. *Review of Active Vibration Control.* Opatija, MIPRO.

Moon, R. J. et al., 2017. *Selection of Positive Position Feedback Controllers for Damping and Precision Positioning Applications.* Singapore, Springer, pp. 289-301.

Naisse, C., 2012. *Modélisation et atténuation du phénomène de battements lors des essais de qualification des satellites en vibration,* s.l.: Thales Alenia Space confidential document.

Naisse, C. & Bettacchioli, A., 2012. *Simulation des essais en vibrations de satellites à partir de l'analyse modale d'une réeponse bas niveau.* s.l., s.n.

Nali, P. & Bettacchioli, A., 2014a. *Beating phenomena in spacecraft sine tests and an attempt to include the sine sweep rate effect in the test-prediction.* Braunschweig, ESA SP-727.

Nelson, G. & O'Malley, L. J., 2014. *Comparison of Multi-Axis and Single Axis Testing on Plate Structures.* s.l., s.n.

Newman, M., 2020. *Vibration Avoidance in Industrial Robots Using Input Shaping and Learning-Based Structural Models.* s.l.:Department of Mechanical Engineering, University of Manitoba.

Nicholson, R. & Kaipio, J. P., 2020. An Additive Approximation to Multiplicative Noise. *Springer Nature.*

Nonami, K. & Ito, T., 1997. Sliding Mode Control with Frequency Shaping to Suppress Spillover. *Transactions of the Japan Society of Mechanical Engineers Series C.*

Oloomi, H. & Shafai, B., 2003. *Weight selection in mixed sensitivity robust control for improving the sinusoidal tracking performance.* Maui, IEEE.

Pai, M. & Sinha, A., 2011. Increasing Robustness of Input Shaping Method to Parametric Uncertainties and Time-Delays. *Journal of Dynamic Systems Measurement and Control,* p. 133.

PCB 356B21, Website. [Online] Available at: https://www.pcbpiezotronics.fr/wp-content/uploads/356B21.pdf

PLM Software, 2013. *PLM Thales Cannes Configuration.* s.l.:Siemens.

PLM Software, 2015. *LMS Test.lab Sine Vibration Control.* s.l.:Simens AG restricted document.

Preumont, A., 2018. *Vibration Control of Active Structures.* 4th ed. s.l.:Springer International Publishing.

Rao, K. R. & Ahmed, N., 1968. Recursive techniques for obtaining the partial fraction expansion of a rational function. *IEEE Trans. Educ..*

Reinfrank, M., Hellendoorn, H. & Driankov, D., 1993. *An Introduction to Fuzzy Control.* s.l.:Springer.

Ross, W. T. & Cima, J. A., 2000. *The Backward Shift on the Hardy Space.* s.l.:American Mathematical Society.

Rugh, W. & Shamma, J., 2000. *Research on Gain Scheduling.* s.l.:Automatica.

Sabanovic, A., Kaynak, O. & Erbatur, K., 1999. A study on robustness property of sliding-mode controllers: A novel design and experimental investigations. *IEEE Transactions on Industrial Electronics,* pp. 1012-1018.

Safonov, M. & Chiang, R., 1989. A Schur Method for Balanced Model Reduction. *IEEE Trans. on Automat. Contr..*

Safonov, M. G. & Chiang, R. Y., 1988. *Model Reduction for Robust Control: A Schur Relative-Error Method.* s.l., IEEE.

Seto, K. & Preumont, A., 2008. *Active Control of Structures*. Chichester: A John Wiley & Sons, Ltd, Publication.

Shafai, B. & Oloomi, H., 2003. Weight selection in mixed sensitivity robust control for improving the sinusoidal tracking performance. *42nd IEEE International Conference on Decision and Control*.

Shahravi, M. & Azimi, M., 2014. *A comparative study for collocated and non-collocated sensor/actuator placement in vibration control of a maneuvering flexible satellite*. s.l., s.n.

Shukla, P., Ghodki, D., Manjarekar, N. S. & Singru, P. M., 2016. A Study of H infinity and H2 synthesis for Active Vibration Control. *Elsevier*.

Simcenter Control, 2019. *Sine Control: Closed Loop Control Parameters*. [Online]
Available at: https://community.sw.siemens.com/s/article/sine-control-closed-loop-control-parameters

Simcenter Estimation, 2019. *Sine Control: Amplitude Estimation Methods*. [Online]
Available at: https://community.sw.siemens.com/s/article/sine-control-amplitude-estimation-methods

Simcenter Notching, 2019. *Sine Control: Notching*. [Online]
Available at: https://community.sw.siemens.com/s/article/sine-control-notching

Sinha, A., 2007. *Linear Systems Optimal and Robust Control*. s.l.:CRC Press.

Skogestad, S., 1991. Performance Weight Selection for H-Infinity and μ-Control Methods. *Transactions of the Institute of Measurement and Control*.

Skogestad, S. & Postlethwaite, I., 2001. *Multivariable Feedback Control Analysis and design*. s.l.:JOHN WILEY & SONS.

Soucy, Y. & Coté, A., 2002. Reduction of overtesting during vibration tests of space hardware. *Canadian Aeronautics and Space Journal,* p. Vol 48.

SUA, S., 2017. *Contrôle optimale d'un pont vibrant pour la réduction de battements,* Cannes: Thales Alenia Space Confidential document.

Tewari, A., 2002. *Modern Control design with MATLAB and SIMULINK.* s.l.:John Wiley & Sons Ltd..

Tliba, S. & Abou-Kandil, H., 2003. *H∞ Controller Design for Active Vibration Damping of a Smart Flexible Structure Using Piezoelectric Transducers.* s.l., Elsevier.

Tsai, M., Geddes, E. & Postlethwaite, I., 1992. Pole-zero cancellations and closed-loop properties of an $H\infty$ mixed sensitivity design problem. *Automatica.*

Tung, E. & Tomizuka, M., 1993. Feedforward Tracking Controller Design for High-Speed Motion Control. *IFAC Proceedings Volumes,* pp. 299-302.

Vilanova, R., 2008. Reference controller design in 2-DOF control. *Electrical Engineering,* pp. 275-281.

Wijker, J., 2004. *Mechanical Vibrations in Spacecraft Design.* s.l.:Springer.

Wijker, J. J., 2007. *Spacecraft Structures.* 1st ed. Leiden: Springer.

wikipedia Hinfinity, n.d. *H-infinity methods in control theory.* [Online] Available at: https://en.wikipedia.org/wiki/H-infinity_methods_in_control_theory

Xia, Y. & Mahmoud, M. S., 2012. *Applied Control Systems Design.* s.l.:Springer.

Xing, G. & Bainum, P., 2012. H-infinity robust controller design and comparison with LQG, PID controllers for an expendable launch vehicle. *American Institute of Aeronautics and Astronautics.*

Xue, D., Chen, Y. & Atherton, D. P., 2007. *Linear Feedback Control Analysis and Design with MATLAB.* Philadelphia: Society for Industrial and Applied Mathematics.

Yang, W. Y., 2009. *Signals and Systems with MATLAB.* s.l.:Springer.

Yasuo, N., Sato, D., She, J. & Miyamoto, K., 2018. Automatic determination of LQR weighting matrices for active structural control. *Engineering Structures,* pp. 308-321.

Youla, D. C., Jabri, H. A. & Bongiorno, J. J., 1976. Modern Wiener-Hopf design of optimal controllers. *IEEE Trans. Automat. Contr.,* p. 319–338.

Zames, G., 1981. Feedback and optimal sensitivity: Model reference transformations, multiplicative seminorms, and approximate inverses. *IEEE Transactions on Automatic Control.,* pp. 301-320.

Zenga, A. L. Y., 2005. *Iterative SISO Feedback Design For an Active Vibration Isolation System,* Eindhoven: Technische Univererseit Eindhoven.

Zhang, J., He, L., Wang, E. & Gao, R., 2008. *A LQR Controller Design for Active Vibration Control of Flexible Structures*. Wuhan, IEEE.

Zhou, K., Doyle, J. C. & Glover, K., 1996. *Robust and Optimal Control*. s.l.:PRENTICE HALL.

10 SYNTHÈSE EN FRANÇAIS

La qualification des très grandes structures spatiales telles que des satellites artificiels nécessite de nombreux tests, parmi lesquels le test en vibration a pour objectif de valider la résistance mécanique du satellite devant lui permettre de survivre à des conditions de lancement très sévères. La qualification démontre la capacité de la navette spatiale à résister aux contraintes qu'elle subira lors du lancement surdimensionné 1,25 fois l'amplitude de lancement, tandis que l'acceptation est seulement limitée à la valeur attendue du vol. Lors d'une campagne d'essais vibratoires, le niveau de qualification ou d'acceptation n'est jamais appliqué immédiatement sur le satellite mais en quatre étapes partant d'une faible amplitude de référence pour atteindre successivement des niveaux d'amplitude plus élevés. La principale raison pour laquelle ce test en vibration se réalise en quatre étapes est le comportement de l'architecture de commande non linéaire actuelle, qui présente des oscillations et, par conséquent, un suivi imprécis. L'oscillation s'intensifie en passant par les modes mécaniques du satellite et les antirésonances correspondantes. En passant par un très bas niveau d'amplitude permet de fixer les paramètres de commande plus aisément vu que ce niveau d'amplitude ne causera pas la fatigue structurelle de satellite. Ainsi, la stratégie actuelle valide l'exactitude de la campagne avec une très faible excitation et augmente successivement l'amplitude de l'excitation jusqu'à atteindre le niveau de la qualification.

De plus, l'architecture actuelle du système ne permet pas d'évaluer les marges de stabilité avant le lancement de la campagne. Par conséquent, il est très risqué de mettre le satellite à un niveau d'amplitude élevée pendant le test de vibration car cela pourrait induire des dommages modérés à graves au niveau de la structure du satellite.

Le but de ces travaux est, partant de l'étude de la structure de commande actuelle et du phénomène de battement associé, de développer une nouvelle architecture de commande pour le système d'essai en vibration, qui soit capable d'éliminer les oscillations du système pendant l'essai en vibration et d'assurer également la stabilité du système en boucle fermée, tout en fournissant une évaluation des marges de stabilité garanties.

10.1 ANALYSE DU SYSTEME ACTUEL

Le système d'essais vibratoires de Thales Alenia Space est développé par LMS Siemens. Il se compose d'un actionneur électromécanique alimenté par un courant alternatif très intense atteignant jusqu'à 3000 A délivrant en sortie un signal en accélération. Un système de refroidissement par eau déminéralisée (pour éviter le court-circuit électromagnétique) assure le bon fonctionnement du banc. Le satellite est fixé à l'actionneur via 2 configurations différentes. La figure ci-dessous montre la configuration longitudinale et transversale de l'installation.

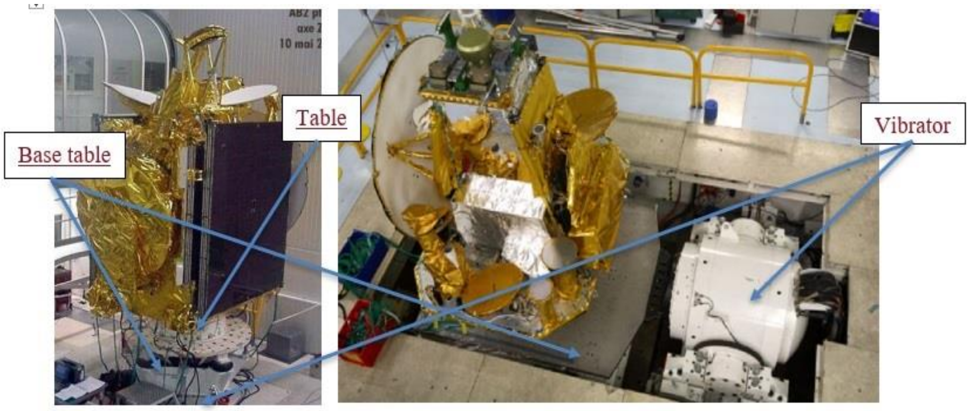

Figure 10:1 - Configuration longitudinale et transversale du vibreur

Dans une configuration longitudinale, (à gauche sur la Figure 10:1), le satellite est attaché directement sur le vibreur alors qu'en configuration transversale (à droite sur la Figure 10:1), le satellite est placé sur une table qui est fixée au vibreur. L'ensemble de la configuration actionneur-table est installé sur une masse sismique (~150 tonnes) qui est montée sur des boîtes à ressort pour isoler le bâtiment des vibrations produites. La plage de fonctionnement de cette installation est comprise entre 5 et 1700 Hz, l'actionneur pouvant délivrer les caractéristiques de la Table 10-1.

Table 10-1 Caractéristiques de l'actionneur

Type de Vibration	Effort max.(kN)	Accélération max. (g)
Aléatoire	267	60g
Sinusoïdale	289	75g
Choc	801	180g

L'amplificateur établit un pont entre la sortie de la commande numérique et l'entrée de l'actionneur. La sortie de commande est un signal en accélération, qui doit donc être converti en un signal électrique approprié pour commander l'actionneur, ce qui est essentiellement effectué par l'amplificateur. Un ensemble de très grands amplificateurs est nécessaire pour convertir la tension de sortie analogique (±10 V crête) du système de commande en un courant proportionnel de plusieurs milliers d’ampères (3000 A crête).

La mesure d'un test en vibration s'effectue via plus de 400 accéléromètres, jusqu'à 640, et bien plus encore avec la nouvelle gamme de satellites. Parmi ce grand ensemble de canaux, pas plus de 128 peuvent être dédiés à la commande. Ils sont approximativement répartis en trois groupes : un tiers (~40 canaux ou moins) pour le contrôle de l’essai sur l'axe z longitudinal du satellite, un autre tiers pour l'axe transversal x et le dernier tiers pour l'axe transversal y. Dans chaque groupe, quatre canaux sont dédiés à la commande de la table vibrante et les autres sur le satellite pour mesurer l’accélération locale du satellite. Quatre accéléromètres placés sur la table du vibreur sont des capteurs triaxiaux et, lors d'un essai, seuls les quatre canaux orientés de manière identique sont utilisés. Ces quatre mesures permettent le contrôle à la base du satellite.

Les autres capteurs sont placés à des endroits clés de la structure du satellite, généralement là où les modes de structure sont les plus critiques. Ces capteurs sont appelés "accéléromètre notch". Ils permettent de vérifier que les excitations locales des équipements ou des structures sont toujours dans un domaine sûr. Lors du test en vibration, lorsque la fréquence de référence atteint une fréquence correspondant à celle d'un mode du satellite, l'amplitude de l'accélération de sortie mesurée par les capteurs notch dépasse les capteurs de contrôle. Dès qu'il atteint le seuil fixé pour le mode donné, l'effort de commande est alors calculé à partir des données mesurées des accéléromètres notchs. L'objectif principal de cette stratégie est de limiter les vibrations du satellite près des modes afin de le protéger de la fatigue structurelle ou de tout dommage.

La Figure 10:2 suivante illustre l'architecture actuelle des systèmes de commande.

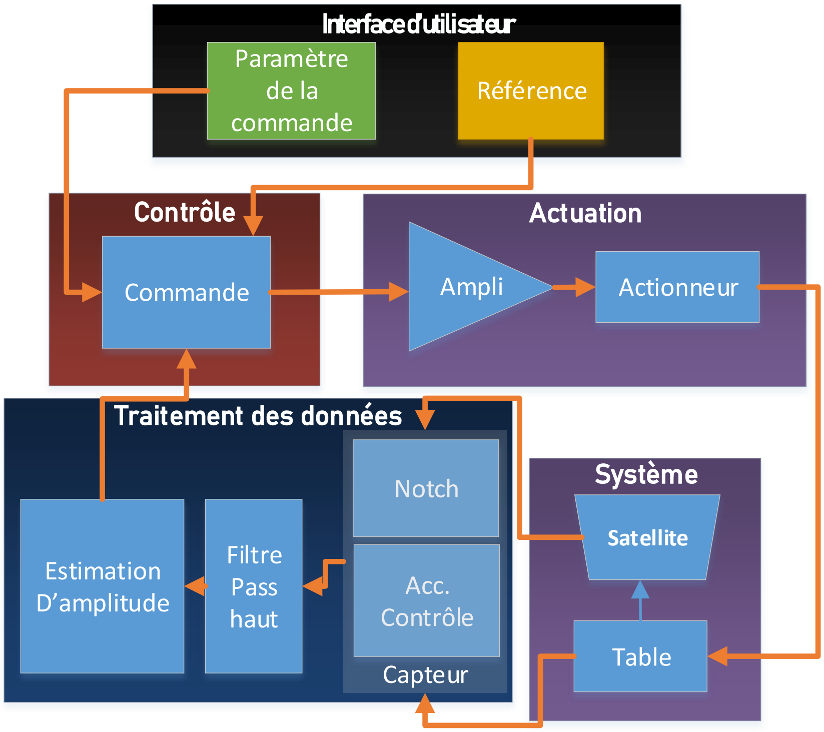

Figure 10:2 - Architecture du système de test en vibration

La référence du système est un signal pseudo-périodique pour lequel, comme indiqué ci-dessus, la fréquence augmente (ou diminue) pendant toute la durée du test, qui est envoyé au bloc réalisant la commande. Le bloc de commande génère l'effort de commande nécessaire pour alimenter l'amplificateur, puis l'amplificateur convertit le signal numérique en un signal analogique et l'amplifie si nécessaire pour piloter l'actionneur électromécanique. Le bloc actionneur génère l'accélération faisant vibrer la structure du satellite et des accéléromètres de contrôle ainsi que des accéléromètres notch mesurent respectivement l'accélération de la table du vibreur et du satellite. Un filtre passe-haut coupe alors les composantes en basse fréquence de l'accélération mesurée (généralement inférieure à 0,5 Hz). Un estimateur d'amplitude estime l'amplitude maximale de chaque pseudo-période, qui est ensuite comparée à l'amplitude d'accélération de référence pour générer un signal d'erreur. Enfin, le bloc de commande met à jour la commande à chaque pseudo-période de la référence.

La structure de la commande de ce vibreur est assez différente d'une commande classique car elle ne s'effectue pas sur une erreur de position (ou de vitesse ou d'accélération directement) mais sur une erreur définie comme le rapport de l'amplitude de référence et de l'amplitude réelle. La figure ci-dessous illustre le système en boucle fermée actuel.

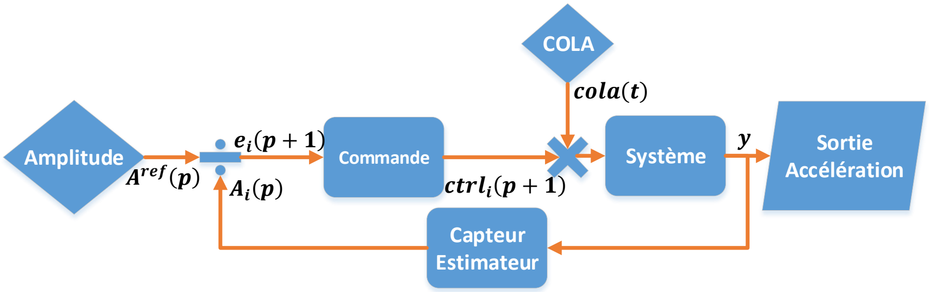

Figure 10:3 - Architecture de la commande actuelle

La Figure 10:3 représente l'architecture numérique simplifiée du système en boucle fermée de la loi de commande actuelle. $A^{ref}, A, e, ctrl, cola$ et y correspondent respectivement à l'amplitude de référence, l'amplitude mesurée, l'erreur, la référence périodique et l'accélération de sortie où p représente la « $p^{ème}$ » pseudo-période, i l'indice du capteur. Le signal de référence appliqué au système est une accélération pseudo-sinusoïdale, il comporte deux parties distinctes, l'amplitude du signal sinusoïdal exprimée en "g" (la constante gravitationnelle) et sa fréquence qui varie avec le temps dans un intervalle donné et à une vitesse donnée, notée vitesse de balayage exprimée en octave par minute. La figure suivante illustre le signal ≪cola≫.

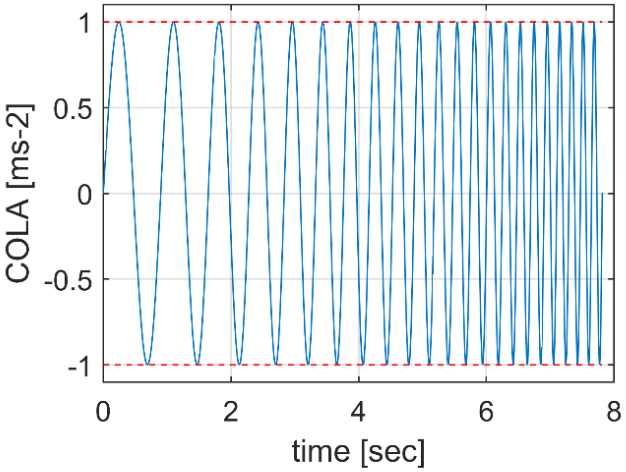

Figure 10:4 - Signal typique <<cola>>

La Figure 10:4 illustre bien que la fréquence au départ est petite, puis elle croit en fonction du temps. La commande génère alors des signaux en tenant compte du fait que l'amplitude de cette erreur est inférieure ou supérieure à 1. De plus, un paramètre intitulé "facteur de compression" permet d'ajuster la dynamique de la boucle de commande : plus ce facteur est petit, plus la commande est réactive au prix d'un risque plus important d'instabilité, plus il est grand et plus le système est stable, mais la dynamique est plus lente. La figure suivante montre les performances de suivi en boucle fermée d'un test en vibration typique d'un satellite.

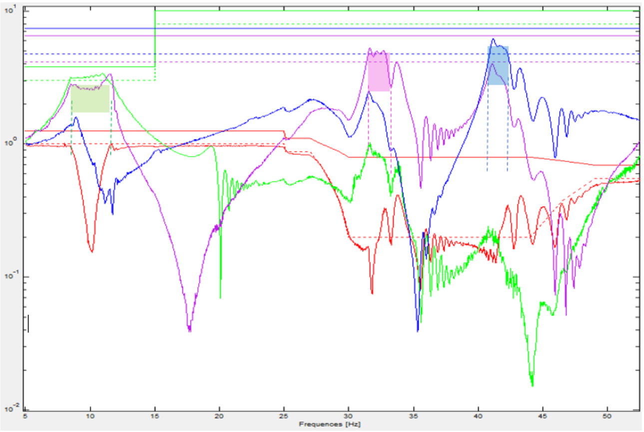

Figure 10:5 - Réponse fréquentielle du satellite avec accélération de référence

La Figure 10:5 montre la réponse des trois accéléromètres de mesure (en vert, violet et bleu), la vibration imposée au satellite via la table vibrante (en rouge) captant l'accélération de sortie d'un satellite géostationnaire entre 5 et 60 Hz où des oscillations non désirées sont observées dans toutes les gammes de fréquences. Les signaux de référence pour chaque accélération de sortie sont donnés dans la même couleur tandis que les lignes pointillées représentent les références de suivi correspondantes et les lignes droites sont la limite supérieure connue sous le nom <<abort>>. Les blocs vert, violet et bleu correspondent respectivement au suivi des positions du pont terrestre, du réservoir supérieur et inférieur. La figure illustre le dépassement au voisinage des modes et les oscillations pendant et après les fréquences de mode. Lors de l'analyse de la commande en vibration (en pointillé rouge), la commande de sortie suit idéalement de 5 à 25 Hz et limite l'amplitude du premier mode en dessous d'abort. Après 25 Hz jusqu'à la fin du test, l'amplitude du signal de référence est réduite de manière significative afin de limiter le dépassement et l'oscillation des deuxième et troisième modes (en violet et bleu). Dans le scénario idéal, le signal de référence serait une valeur avec une unique amplitude et le correcteur devrait générer une commande telle que l'accélération de sortie ait un suivi précis tout en évitant les dépassements et les oscillations.

10.2 LES DEFIS SCIENTIFIQUES

Ce système de commande non linéaire actuel peut être considéré comme une commande par mode glissant non linéaire sans modèle, où la surface de glissement est en 1 et l'erreur glisse sur cette surface. Deux lois de commande existent, la première est appliquée lorsque le signal d'erreur est supérieur à un et la seconde s'applique sinon. Ce système présente également deux particularités.

La première est le fait que le système bouclé possède deux périodes d'échantillonnage différentes. Les capteurs échantillonnent le système à 12 kHz puis l'estimateur estime l'amplitude à chaque pseudo-période du signal. Ensuite, le signal d'erreur est généré à chaque pseudo-période de référence, et par conséquent la commande est mise à jour à chaque pseudo-période de la référence. Comme la référence varie de 5 à 150 Hz maximum, la commande se met à jour au même rythme. La fréquence de référence excite successivement quatre modes du satellite, qui sont très faiblement amortis, généralement de 1 à 3% pour un engin spatial géostationnaire typique incluant son énorme masse de charge utile. Par conséquent, les modes légèrement amortis entraînent des variations rapides du gain du système dans un temps très court. Le système de commande avec ses mises à jour de la commande très lentes ne peut pas faire face à la variation rapide de gain causée par les modes légèrement amortis du satellite. Il résulte que le système en boucle fermée présente principalement de fortes oscillations à proximité des modes propres du satellite en raison de la réponse plus lente de la commande. De plus, la fréquence de référence se déplace vers les hautes fréquences lors du test, des phénomènes de « chattering » de la commande par mode glissant apparaissent. Comme indiqué dans la littérature dans le domaine des modes glissants, le phénomène de « chattering » est très courant pour un tel système en raison des non-linéarités de l'effort de commande généré, provoquant une non-régularité dans la sortie du système, contribuant à l'erreur de suivi et aux oscillations à hautes fréquences.

La deuxième particularité est le signal d'erreur, qui comme indiqué ci-dessus est le rapport entre le signal de référence et le signal estimé, contrairement au système de commande classique où le signal d'erreur est la différence entre la référence et la sortie (ici estimée). Ceci est imposé pour prendre en compte la valeur « 1 » de la surface de glissement, de sorte que le signal d'erreur (rapport entre la référence et l'estimation) peut prendre une valeur supérieure à un ou inférieure ou égale à un.

Les commandes par mode glissant semblent attractives pour les systèmes de suivi pour lesquels les problèmes de robustesse sont importants. En effet, le système de test en vibration a besoin d'un certain niveau de robustesse vis-à-vis des variations des paramètres modaux, car la fréquence et l'amortissement du mode changent de manière non linéaire avec l'amplitude du signal de référence. Ce type de commande semble donc intéressant pour le système de test de vibration mais comme il est déjà mentionné précédemment, le signal de référence pseudo-périodique évolue de basse à haute fréquence, créant les phénomènes de « chattering ». Malgré les progrès actuels des commandes non linéaires, ces problèmes demeurent.

D’autres stratégies doivent dès lors être étudiées. Plusieurs algorithmes de commande trouvés dans la littérature dans le domaine de la mécanique soit traitent le problème de régulation en augmentant le facteur d'amortissement via un correcteur robuste, soit ne traitent tout simplement pas les problèmes de robustesse dans un cadre de suivi, ce qui est essentiel dans un système de test en vibration. L'application de stratégies de commande linéaires robustes se rencontre dans la littérature portant sur la commande active de vibrations, par exemple la commande linéaire quadratique (LQ), la commande linéaire quadratique gaussienne (LQG) ainsi que des commandes de type H_∞. Les deux premières stratégies fournissent de bonnes performances dans un cas nominal, mais manquent de robustesse du fait de l'utilisation de la norme H_2. D'autre part, la commande H_∞ a vu son intérêt grandir dans le domaine de la commande active de vibrations car elle permet de convertir les spécifications industrielles en contraintes dans le domaine fréquentiel, avec à la clé un problème d'optimisation à résoudre pour synthétiser la commande. De plus, la nature des correcteurs H_∞ est intrinsèquement considérée comme robuste en raison de l'utilisation du théorème du petit gain. Au final, compte tenu de cette étude, les travaux se sont orientés vers l'étude des performance potentielles d'un schéma de commande H_∞.

10.3 ELABORATION DE STRATEGIES DE COMMANDE ROBUSTE DE TYPE H-INFINI

La première contribution de ces travaux concerne l'élaboration d'une commande H_∞ par sensibilité mixte. Son développement impose préalablement que l'architecture de commande actuelle soit modifiée pour s'adapter au schéma classique de commande robuste, comme indiqué dans la Figure 10:6.

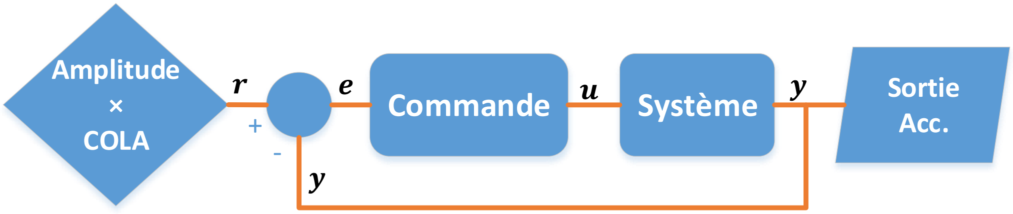

Figure 10:6 - Système en boucle fermée pour vibreur

Dans cette figure, r, e, u et y sont respectivement la référence, l'erreur, la commande et l'accélération de sortie. La dynamique du système considéré est un système monovariable (SISO) contenant un seul mode propre. L'objectif principal de ce chapitre est de mener une étude préliminaire de conception de cette commande sur un système simplifié afin d'évaluer la faisabilité de la suppression des vibrations via une commande de type H_∞.

Le premier défi de la conception d'un tel système concerne la compréhension du problème industriel et la conversion de ses contraintes dans le domaine fréquentiel sous la forme de fonctions de pondération. L'erreur de suivi doit être de l'ordre de ± 1%, ce qui implique une réduction totale des vibrations du système, même au voisinage des modes de vibration. Comme expliqué sur la Figure 10:5 l'amplitude de référence a été abaissée manuellement près des modes ainsi qu'à des fréquences plus élevées pour réduire les vibrations et le dépassement du système. Au lieu de cela, la nouvelle architecture assurera les performances de suivi avec une référence constante sans nécessiter de réduction manuelle. Une analyse dans le domaine fréquentiel doit assurer la stabilité interne et en même temps, la stabilité entrée-sortie du système dans la gamme de fréquences étudiée (5 à 100 Hz). L'actionneur électromagnétique a une limite d'accélération de 75 g, la fréquence maximale (à 0 dB) est de 1700 Hz et l'effort de commande ne doit pas dépasser cette limite d'actionnement. Le système en boucle fermée doit rejeter l'influence des différents bruits du système, en particulier ceux à hautes fréquences. Étant donné que les accéléromètres fonctionnant à très large spectre augmenteraient le coût, le développement doit donc se concentrer sur la diminution de la bande passante du filtre de bruit pour avoir un choix d'accéléromètres moins coûteux tout en conservant les performances requises. De plus, le correcteur doit être robuste vis-à-vis des incertitudes du système.

La fréquence du signal de référence évoluant avec le temps, le système en boucle fermée n'atteint jamais le régime statique, restant dans un état transitoire. Il convient donc d’observer avant tout les comportements transitoires du système en boucle fermée tels que le dépassement et les oscillations. Cette contrainte de suivi ne peut pas être abordée par la définition classique du gain statique, du temps de réponse et du dépassement, car le système nécessite une réponse très rapide de la commande. L'apport principal de cette partie est de pouvoir définir ce type particulier de suivi appelé poursuite dynamique, via des contraintes dans le domaine fréquentiel. De plus, le poids du filtrage du bruit est également imposé en fonction des caractéristiques des accéléromètres. Les résultats de cette étude montrent des performances supérieures de la commande H_∞ par rapport au système de commande actuel, en termes d'erreur de suivi, de robustesse vis-à-vis d’éventuels retards, ainsi qu’en présence de variations de l'amortissement du mode. Cette étude portant à ce stade sur un système simplifié du satellite contenant un seul mode propre sans aucune antirésonance doit être élargie à la prise en compte de modèles plus complets.

Pour cette raison, un modèle d'ordre supérieur incluant plusieurs modes est introduit. Il comprend une dynamique du 7ème ordre avec deux modes propres et les antirésonances correspondantes. Une première étape consiste à convertir ce modèle en un modèle à temps continu par une transformation de type bilinéaire, fournissant la meilleure correspondance dans le domaine fréquentiel et permettant une extension à une dynamique MIMO. Dans une deuxième étape, le modèle d'ordre complet à temps continu est réduit pour obtenir une dynamique d'ordre réduit utilisable pour la synthèse de la commande, de sorte à conserver des ordres de correcteur acceptables. La procédure de réduction du modèle commence par le calcul de l'énergie des états en fonction de la valeur singulière de Hankel de la matrice de phase du modèle d'ordre complet. L'énergie des états indique le niveau d'importance de chaque état dans le comportement dynamique du modèle. L'idée principale est de conserver l'état à haute énergie et d'éliminer les états à basse énergie. Cette élimination est réalisée par la méthode BST (Balanced stochastic model truncation) tout en garantissant l'erreur multiplicative ($\|G_{red} - 1(G_{full} - G_{red})\|_{\infty}$, ici, G_{full} : dynamique d'ordre complet et G_{red} : dynamique réduite) définie par la norme infinie. La forme finale du modèle d'ordre réduit est une dynamique du cinquième ordre, assurant l'erreur minimale entre le modèle d'ordre complet et le modèle d'ordre réduit. Enfin, la fonction de transfert de la dynamique du cinquième ordre est paramétrée de sorte à faire apparaitre explicitement les modes propres. Cette forme permettra par la suite une analyse plus approfondie en faisant varier les paramètres modaux du système. Les pondérations fréquentielles définies précédemment sur le modèle très simple à un seul mode sont utilisées pour concevoir un correcteur H_{∞} sur le modèle d'ordre réduit. Les performances du système nominal s'avèrent supérieures à la loi de commande actuelle de type mode glissant. Cependant, la commande H_{∞} fondée sur la sensibilité mixte génère un type particulier de correcteur, appelé compensateur central. Ce correcteur compense la résonance avec l'anti-résonance et l'anti-résonance avec la résonance, appelée compensation des pôles-zéros. Ce phénomène réduit drastiquement la robustesse du système en boucle fermée lorsque les paramètres modaux du système varient. De plus, si le système contient des modes légèrement amortis, le compensateur central ne présente aucune robustesse. Par conséquent, il est essentiel de surmonter les problèmes de compensation pôle-zéro afin de renforcer la robustesse de la loi de commande, ce qui est essentiel pour la mise en œuvre.

D’où l’extension proposée de la commande H_∞ standard par feedback à un schéma de commande à 2 degrés de liberté par feedback H_∞ et correcteur feedforward. Le correcteur feedforward est l'inverse du modèle nominal, la conception de la commande H_∞ à deux degrés de liberté résout le problème d'optimisation avec succès avec les pondérations fréquentielles introduites précédemment. La Figure 10:7 illustre l'architecture du système en boucle fermée.

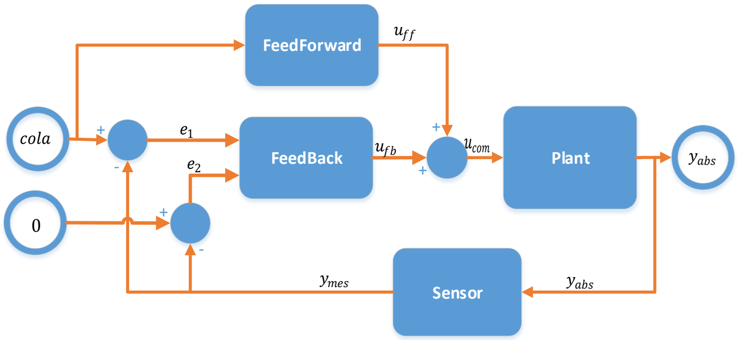

Figure 10:7 - Système en boucle fermée avec commande à deux degrés de liberté

Dans cette figure, la première entrée est le signal de référence pseudo-périodique, la deuxième entrée est mise à zéro, l'effort de commande u_{com} est la somme de l'effort issu du bouclage u_{fb} et de l'effort issu de l’anticipation u_{ff}, y_{abs} est la sortie en accélération, mesurée par des capteurs (y_{mes}). La particularité de cette procédure de conception est que la dynamique du correcteur feedforward est incluse dans la procédure de conception du correcteur feedback. Le deuxième degré de liberté est ajouté pour obtenir une solution appropriée de l'optimisation car, avec un seul degré de liberté, le système ne peut pas le résoudre de manière satisfaisante. La simulation dans le domaine temporel de ce système en boucle fermée montre la robustesse aux variations des paramètres modaux, de ± 15 % pour la position du mode et de ± 25 % pour l'amortissement du mode. Pour les simulations, ces paramètres ont été modifiés via une dispersion uniforme. La figure ci-dessous illustre la performance robuste de 50 cas dispersés.

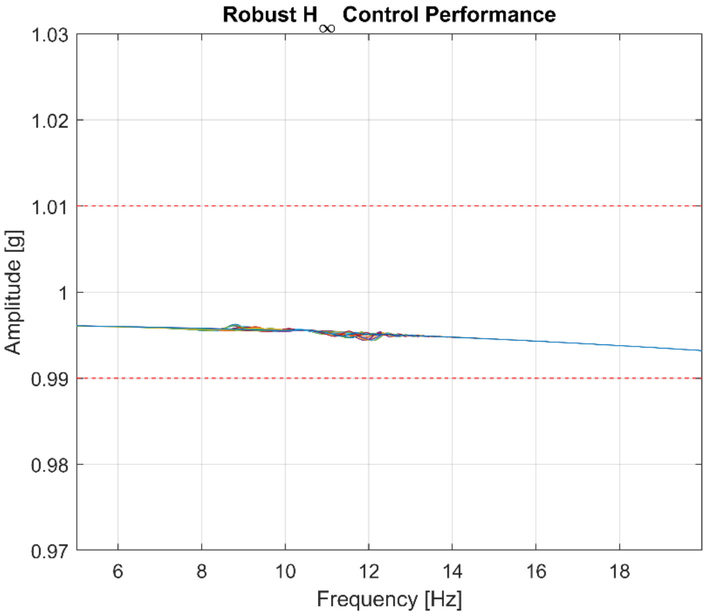

Figure 10:8 - Performance robuste de l'architecture développée

La Figure 10:8 montre la performance robuste vis-à-vis de variations modales, l'erreur dynamique reste inférieure à 1%, malgré les incertitudes. Le système ne produit aucune vibration. L'idée principale de cette architecture est d'augmenter le gain de la commande via deux canaux d'entrée du correcteur, car le gain total est la somme des deux canaux afin de compenser la variation rapide du système en boucle fermée causée par l'erreur de suivi et la variation des paramètres modaux. Par conséquent, le contrôleur anticipatif fournit l'effort de commande nécessaire pour piloter l'actionneur, tandis que le correcteur feedback gère les problèmes d'erreur de suivi et de robustesse.

Cependant, la limitation principale du correcteur H_∞ est le fait qu'il minimise le gain maximal du système à une certaine fréquence seulement. Dès lors, les performances en suivi ne sont pas identiques sur toute la plage de fréquences, mais plutôt sur un intervalle de fréquences restreint. Globalement donc, le correcteur H_∞ ne peut pas maintenir l'erreur de suivi en dessous de la spécification industrielle pour toute la gamme de fréquences allant de 5 à 40 Hz. Pour contrer ce problème, deux correcteurs feedback sont synthétisés, l’un pour le suivi de 5 à 15 Hz, puis le second pour le suivi de 15 à 40 Hz. Ceci est réalisé par deux synthèses H_∞ séparées, pour lesquelles les contraintes de suivi sont situées à des fréquences différentes. Dans le même temps, les fonctions de pondération de filtrage du bruit sont ajustées en fonction des contraintes de suivi pour créer un problème H_∞ optimisable répondant à la configuration existante de l'accéléromètre du VTS. Par ailleurs, la contrainte limitant l'effort de commande reste la même pour les deux conceptions du fait que la limitation sur l'actionneur électromagnétique est la même. La mise en œuvre de deux correcteurs feedback avec la commande anticipatrice unique est réalisée via une fonction d'incrémentation de fréquence, qui calcule l'augmentation de fréquence de la référence en fonction du temps. Lorsque le signal de référence passe par 15 Hz, le premier correcteur passe le relais au second.

10.4 VALIDATION DES STRATEGIES DE COMMANDE DEVELOPPEES

Une procédure de validation est introduite à la fois dans le domaine temporel et fréquentiel afin de valider la stabilité et les performances du système en boucle fermée. L'analyse du domaine fréquentiel comprend deux méthodes différentes pour évaluer la stabilité du système multivariable. La première stratégie consiste à utiliser le théorème du petit gain non structuré. La deuxième stratégie est appelée « marge de disque », où la perturbation est introduite dans le système via une fonction complexe dans laquelle le gain et la phase peuvent varier simultanément parmi toutes les chaines du système multivariable en boucle fermée pour obtenir la combinaison pire cas pour l'évaluation de la marge de stabilité minimale. Cette stratégie utilise la $\mu - \text{analyse}$ pour prendre en compte la variation simultanée de phase et de gain du système, donc les incertitudes structurées réduisent le conservatisme par rapport aux incertitudes non-structurées et représentent une marge de stabilité garantie. Contrairement aux simulations en temps discret précédentes, cette partie introduit une architecture MIL comme indiqué Figure 10:9.

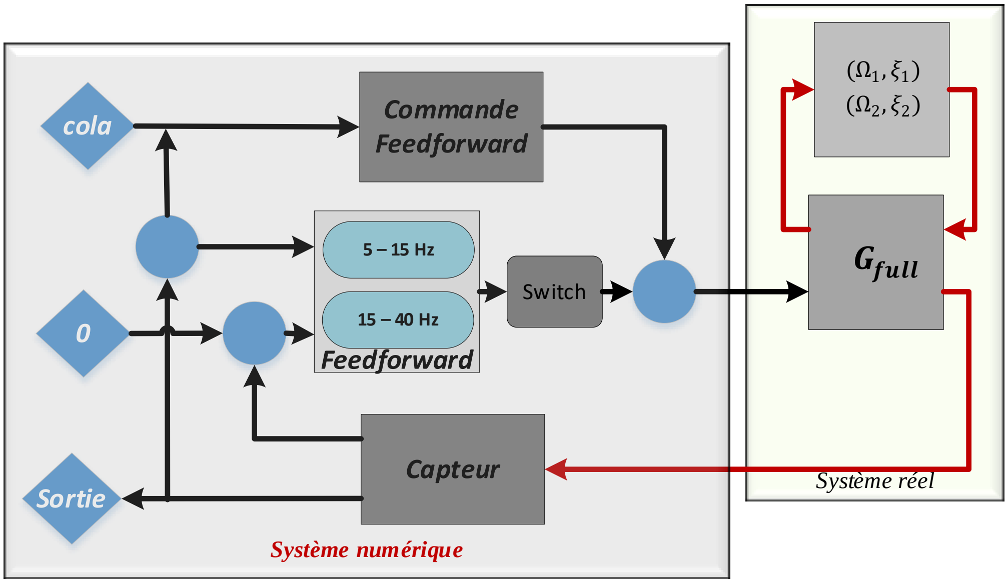

Figure 10:9 - Architecture MIL d'un vibreur

Dans cette figure, l'architecture MIL représente le système en boucle fermée, comportant deux blocs. Le bloc de gauche correspond au calcul numérique, tel qu'il sera utilisé dans le système en boucle fermée en temps réel. Ensuite, le bloc de droite contient le modèle à temps continu d'ordre complet G_{full} avec la possibilité de faire varier la fréquence du mode et son amortissement. Le premier avantage de la combinaison entre modèle discret et temps continu est de pouvoir vérifier la robustesse numérique de l'architecture en boucle fermée en temps réel via la simulation MIL. Deuxièmement, la dynamique introduite du satellite G_{full} est le modèle d'ordre complet tandis que les correcteurs sont synthétisés sur le modèle d'ordre réduit, permettant de valider la performance du correcteur optimal vis-à-vis des dynamiques négligées lors de la réduction du modèle. Les bruits des accéléromètres sont modélisés par un bruit blanc additif avec une amplitude de bruit définie par le fabricant des capteurs. Le système de commande fonctionne de manière satisfaisante contre les bruits du capteur sans affecter la commande de l'actionneur.

Globalement, le MIL crée un système en boucle fermée en temps réel remplaçant la dynamique physique du système par son modèle à temps continu pour estimer des performances réalistes à partir de la simulation numérique. Les scénarios de simulation incluent tout d'abord les performances d'un système nominal sans aucun type de variations au niveau de la référence, ni dans le modèle dynamique. Ensuite, la variation de vitesse de balayage de la référence est introduite. Une vitesse de balayage plus élevée augmente le comportement transitoire du système, et une vitesse de balayage inférieure diminue le comportement transitoire mais la référence reste plus longtemps dans les fréquences de résonance du modèle. On remarque que l'architecture développée permet de maintenir les performances dans la limite spécifiée dans tous les cas de variations de la vitesse de balayage.

Le processus de la campagne d'essais vibratoires commence par une très faible amplitude de l'accélération de référence et augmente progressivement son niveau d'amplitude pour atteindre le niveau de qualification pour la condition de lancement. Par conséquent, le scénario de test utilisé ici inclut également une amplitude de niveau très bas évoluant jusqu'au niveau requis du signal de référence pour la qualification et les performances dans tous les cas sont conformes à la spécification requise. Finalement, une simulation Monte-Carlo est présentée pour évaluer les performances robustes du système en boucle fermée par rapport à la variation des paramètres modaux. Des centaines de cas de dynamiques différentes sont générés en dispersant les paramètres modaux, ils sont introduits de manière aléatoire dans le MIL et tous les cas de simulation sont conformes à la spécification requise pour le système en boucle fermée. La complexité de ce système se résume à l'introduction d'un correcteur feedforward d'ordre 5 et deux correcteurs feedbacks d'ordre 5 pour chacun. Les tests ont été réalisés dans un ordinateur standard contenant un processeur Intel I3 de 4éme génération et l'échantillonnage est fixé à sa valeur maximale 12kHz. Nous avons pu constater le bon fonctionnement lors des simulations sans avoir de difficultés en termes de retards en boucle fermée, ni de convergence numérique en temps réel, ce qui indique la faisabilité de cette architecture en question dans le logiciel de LMS-Siemens.

10.5 CONCLUSIONS ET PERSPECTIVES

L'architecture développée du VTS montre des performances en simulation supérieures à celles obtenues avec la commande non linéaire actuelle. Les travaux développent non seulement la procédure de synthèse du correcteur, mais fournissent également un moyen pour valider l'architecture de commande via une simulation réaliste réalisée avant la campagne d'essais en vibration, appelée « virtual shaker test ». L'un des principaux résultats de ces travaux est tout d'abord de démontrer la faisabilité de la définition de contraintes dans le domaine fréquentiel pour la commande permettant le suivi dynamique, nécessaires à la conception d'une commande H_∞ optimale robuste, rarement étudiée dans la littérature. Un autre résultat concerne les problèmes de robustesse de la commande H_∞ lorsque la dynamique contient des modes faiblement amortis provoquant une compensation pôle-zéro par le correcteur nominal. Ce problème est résolu en étendant le correcteur feedback simple à un correcteur feedback à 2 degrés de liberté combiné à une dynamique de correction par anticipation. Le système de commande développé est capable de suivre la référence sur une très grande gamme de fréquence, ce qui est également rarement étudiée dans la littérature. La robustesse aux variations d'amplitude de la référence ainsi que les variations des paramètres modaux et la marge de stabilité garantie ouvrent la possibilité d'exécuter directement le test en vibration à un niveau de qualification.

Le développement actuel peut être étendu en utilisant d'autres types de systèmes de commande, en particulier tout d'abord la commande par mode glissant. Le principal avantage de ce type de système de commande est la possibilité d'obtenir des lois de commande sans modèle ou avec une très faible connaissance de celui-ci. Le système de commande actuel utilisé dans le VTS est fondé sur la SMC, induisant des phénomènes de « chattering ». Or les progrès récents de la SMC devraient permettre de réduire les phénomènes de « chattering » en introduisant des lois de commande d'ordre supérieur.

Plusieurs recherches traitent également de l'évaluation de la stabilité d'un tel système non linéaire via la preuve de la convergence temporelle. De plus, les résultats de simulation de la stratégie avec commutation entre deux correcteurs feedback présentent un très faible dépassement, qui reste inférieur à la limite demandée par les spécifications industrielles dans tous les cas de simulation. Bien qu'il soit nécessaire d'évaluer la marge de stabilité d'un tel système, il n'est pas abordé ici. L'une des principales perspectives pour une analyse plus approfondie est d'étudier ce problème de stabilité et de l'intégrer dans le système actuel. Les recherches futures peuvent également étendre cette architecture actuelle à une procédure de conception de commande fondée sur la µ-synthèse pour désensibiliser le correcteur vis-à-vis des variations des paramètres modaux. Dans la littérature, les correcteurs issus de la µ-synthèse montrent une performance robuste très importante dans un problème de régulation, mais rarement étudiée dans un problème de suivi. D'un point de vue académique, il serait intéressant d'évaluer les performances de ce type de correcteur dans une telle problématique de commande.

Les travaux portent sur le développement théorique d'une nouvelle architecture de commande VTS, fournissent des résultats satisfaisants via la simulation par « virtuel shaker ». Afin de mettre en œuvre la solution actuelle au sein du VTS existant, la première préoccupation concerne les capteurs, les actionneurs et la commande numérique. Cette étude prend en compte les capteurs et actionneurs existants d'un système de test en vibration typique ; par conséquent, la structure de commande proposée peut être directement adaptée dans le cadre du périmètre matériel actuel.

Des réalisations théoriques à la preuve de concept expérimentale, la tâche principale sera le prototypage du « virtual shaker » fondé sur la simulation jusqu'à sa mise en œuvre. La première étape vers l'implémentation physique consiste à utiliser un test du matériel dans la boucle en parallèle avec le modèle courant dans la simulation de la boucle sur un satellite (ou un objet de même caractéristique modale) avec des caractéristiques correspondant au moins aux paramètres modaux du satellite. L'exigence de cette stratégie de test est de pouvoir comparer les résultats des tests et des simulations en temps réel. Cela validera alors la justesse de la simulation ainsi que les performances temps réel en boucle fermée via le calculateur embarqué, en termes de gestion de la complexité. Après la validation du modèle en boucle fermée, la définition de la robustesse doit être précisée. Les tests parallèles doivent garantir le scénario le plus défavorable pour vérifier la plage de faisabilité de la nouvelle structure de commande. Après le prototypage, la prochaine étape concerne la mise à jour du système numérique existant fondé sur le progiciel fourni par LMS Siemens. La nouvelle architecture en boucle fermée doit être intégrée au logiciel temps réel existant. Une fois la robustesse définie et sa conformité au scénario de test réel validée, l'industrialisation de l'ensemble de la procédure doit permettre son utilisation simple pour les ingénieurs et techniciens d’assemblage, intégration et tests (AIT), qui ne sont pas tous spécialistes des commandes avancées.